AIX-MARSEILLE UNIVERSITÉ

Ecole Doctorale 352 : Physique et Sciences de la Matière

Faculté des Sciences

Centre de Physique des Particules de Marseille (CPPM)

Thèse présentée pour obtenir le grade universitaire de docteur

Discipline : Physique et Sciences de la Matière
Spécialité : Physique des Particules et Astroparticules

Robert WOLFF

Searches for $t\bar{t}H$ and flavour-changing $t \rightarrow Hq$ productions in multileptonic final states with the ATLAS detector

Soutenue le 20/09/2018 devant le jury composé de :

Sandra KORTNER	MPP, Munich, Allemagne	Rapporteur
Yves SIROIS	LLR, Palaiseau, France	Rapporteur
Martin ALEKSA	CERN, Genève, Suisse	Examinateur
Andreas HOECKER	CERN, Genève, Suisse	Examinateur
Cristinel DIACONU	CPPM, Marseille, France	Directeur de thèse
Emmanuel MONNIER	CPPM, Marseille, France	Directeur de thèse

Numéro national de thèse/suffixe local : 2018AIXM0304/031ED352

Contents

Synthèse en français

Le Modèle Standard (SM) de la physique des particules est une théorie cohérente des particules élémentaires et de leurs interactions. Il décrit les interactions électromagnétique, faible et forte dans une théorie de jauge unifiée. La force gravitationnelle beaucoup plus faible n'est pas prise en compte par le SM.

Ses prédictions théoriques sont vérifiées par de nombreuses expériences de haute précision depuis les années 1960. La dernière pièce manquante a été trouvée en 2012, quand les collaborations ATLAS et CMS ont annoncé la découverte d'un boson scalaire d'une masse d'environ 125 GeV [1, 2].

Cette particule a été prédite par le mécanisme Brout-Englert-Higgs qui explique l'origine des masses des particules élémentaires. Les bosons vecteurs d'interaction faible (bosons W et Z) obtiennent leur masse par leur interaction avec le champ de Higgs. Les couplages de Yukawa des particules de matière (fermions) déterminent leurs masses et leurs forces d'interaction avec le boson de Higgs.

Néanmoins, le modèle standard n'a pas de réponse à plusieurs questions ouvertes en physique des particules. Il ne peut pas décrire l'asymétrie observée de la matière et de l'antimatière dans l'univers. Il n'a pas non plus d'explication pour la matière noire, qui est prédite à partir d'observations cosmologiques. Les théories de grande unification (GUT), celle avec des particules partenaires supersymétriques (SUSY) ou avec des champs de Higgs supplémentaires sont des extensions du SM qui peuvent résoudre de tels problèmes.

Les nouveaux modèles physiques sont limités par les expériences précédentes, en particulier à des échelles de masse allant jusqu'à quelques 100 GeV. Parce que le quark top est le fermion du SM le plus lourd, la mesure de son couplage de Yukawa est d'un intérêt particulier.

Avec les collisions proton-proton produites entre 2010 et 2013 (Run 1) par le grand collisionneur de hadrons (LHC) au CERN et enregistrées par le détecteur ATLAS, ce couplage a été mesuré avec une précision de 15% [3]. La production du boson de Higgs et ses modes de désintégration où le quark top contribue aux boucles de particules ont donc été étudiés mais indirectement. La nouvelle physique peut se manifester par des boucles de particules supplémentaires dans cette mesure.

La production de boson de Higgs associé à une paire de quarks tops ($t\bar{t}H$) est le meilleur moyen de faire cette mesure directe, parce que le couplage Yukawa du quark top entre directement au niveau de l'arbre. Alors qu'au Run 1 du LHC cette mesure était statistiquement limitée, avec les données produite entre 2015 et 2018 au Run 2, une aug-

mentation d'énergie du centre de masse $\sqrt{s}$ de 8 TeV à 13 TeV et une luminosité intégrée de 25 fb^{-1} à 150 fb^{-1}, sont attendues correspondant a une production de vingt fois plus d'événements $t\bar{t}H$.

Cette thèse de doctorat présente la recherche du signal $t\bar{t}H$ dans les états finaux avec au moins deux leptons, en utilisant 36,1 fb^{-1} de données du Run 2 enregistrées par le détecteur ATLAS entre 2015 et 2016 [4]. Sept canaux sont catégorisés suivant le nombre de leptons légers ($\ell = e$ ou μ) et de leptons taus en décomposition hadronique (τ_{had}). Ils sont illustrés dans la figure 0.1 (à gauche). La figure 0.1 (à droite) montre les fractions
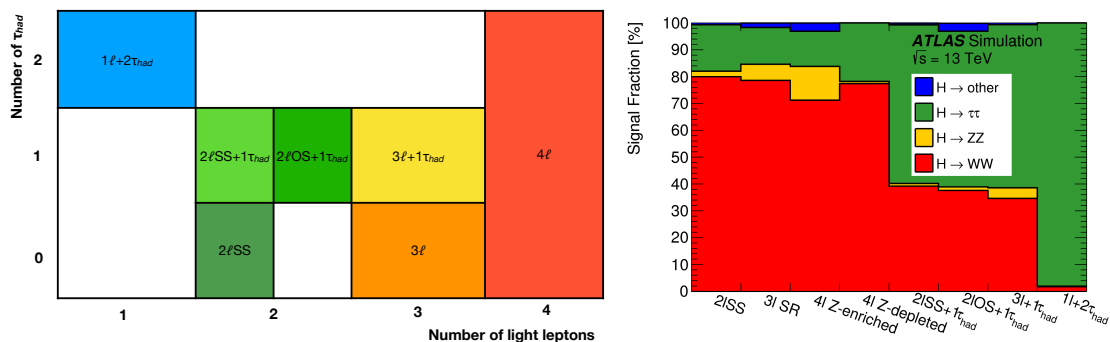
Figure 0.1.: Classification des sept canaux d'analyse par τ_{had} et multiplicités de leptons légers (à gauche) et fraction des désintégrations du boson de Higgs dans le signal $t\bar{t}H$ dans les régions du signal (à droite) [4].

du signal par modes de désintégration du boson de Higgs pour les différentes régions du signal (SRs).

Les canaux les plus significatifs ont deux leptons légers avec la même charge électrique (2ℓSS) ou trois leptons légers (3ℓ) et aucun τ_{had} dans leur état final avec 80% des désintégrations du boson de Higgs à W bosons ($H \to WW$).

Les leptons légers non-prompts provenant de la désintégration de hadron b dans la production $t\bar{t}$, qui a une section efficace 1600 fois plus grande que celle du signal, et ceux des conversions de photons sont les principales sources de bruit de fond dans ces canaux, suivis par la production de bosons vectoriels associés à une paire de quarks tops ($t\bar{t}V$), qui a des états finaux similaires à ceux du signal $t\bar{t}H$. Les propriétés cinématiques sont exploitées pour distinguer le signal et le bruit de fond avec une analyse multivariée.

J'ai travaillé en particulier sur l'optimisation de la séparation dans le canal 3ℓ. Dans ce canal les événements avec exactement trois leptons légers reconstruits et zéro τ_{had} sont sélectionnés. La somme des charges des leptons légers doit être ± 1 comme prévu dans le processus de signal. Les leptons de même charge (ℓ_1 et ℓ_2) sont choisis avec des contraintes très serrées et un $p_T > 15$ GeV. Le lepton de charge opposée (ℓ_0) est choisi avec des contraintes lâches, isolé et qui passe les critères de l'algorithme d'arbre de décision forcé (BDT) non-direct (prompt), algorithme qui a été développé pour réduire ce type de bruit de fond. Le bruit de fond $t\bar{t}Z$ est réduit par un veto Z, éliminant les événements avec des paires de leptons de mêmes saveurs et de charges opposées (MSCO) avec une masse invariante dans une fenêtre de 10 GeV autour de la masse du

boson $Z : |m(\ell^+\ell^-) - 91{,}2\,\mathrm{GeV}| > 10\,\mathrm{GeV}$. Les résonances de faible masse sont supprimées par l'exigence d'un minimum de $m(\ell^+\ell^-) > 12\,\mathrm{GeV}$ pour toutes les paires des leptons MSCO. Le bruit de fond potentiel de $Z \to \ell\ell\gamma^* \to \ell\ell\ell'(\ell')$, où un lepton a un quantité de mouvement très faible et n'est pas reconstruit, est enlevé en appliquant le veto Z sur la masse invariante des trois leptons : $|m(3\ell) - 91{,}2\,\mathrm{GeV}| > 10\,\mathrm{GeV}$. Un BDT à cinq dimensions discrimine différentes catégories de cibles par rapport à tous les autres événements. Ces catégories cibles sont le signal $t\bar{t}H$ et les quatre processus de bruit de fond de production $t\bar{t}W$, $t\bar{t}Z$, $t\bar{t}$ et dibosons (VV). Les variables les plus importantes pour le BDT sont les multiplicités de jets et de jets étiquetés provenant d'un quark b, les quantités de mouvement transverses des leptons et les distances angulaires des leptons aux jets les plus proches ou à ceux étiquetés provenant d'un quark b.

Dans la classification standard [4], cinq régions orthogonales sont créés pour les cinq catégories cibles. J'ai proposé dans cette thèse une classification alternative avec deux régions orthogonales. Dans la région de signal (SR appauvrie en Z), on oppose un veto aux événements qui ont une paire de leptons MSCO avec une masse invariante de $|m(\ell^+\ell^-) - 91{,}2\,\mathrm{GeV}| \leq 10\,\mathrm{GeV}$. Cette région a un rapport signal sur bruit de fond d'environ 9,1%. La deuxième région (CR enrichie en Z) sélectionne des événements qui ont une paire de leptons MSCO avec une masse invariante dans une fenêtre de 10 GeV autour de la masse du boson Z. La figure 0.2 montre les distributions discriminantes pour ces deux régions avant l'extraction des résultats. On observe un bon accord entre
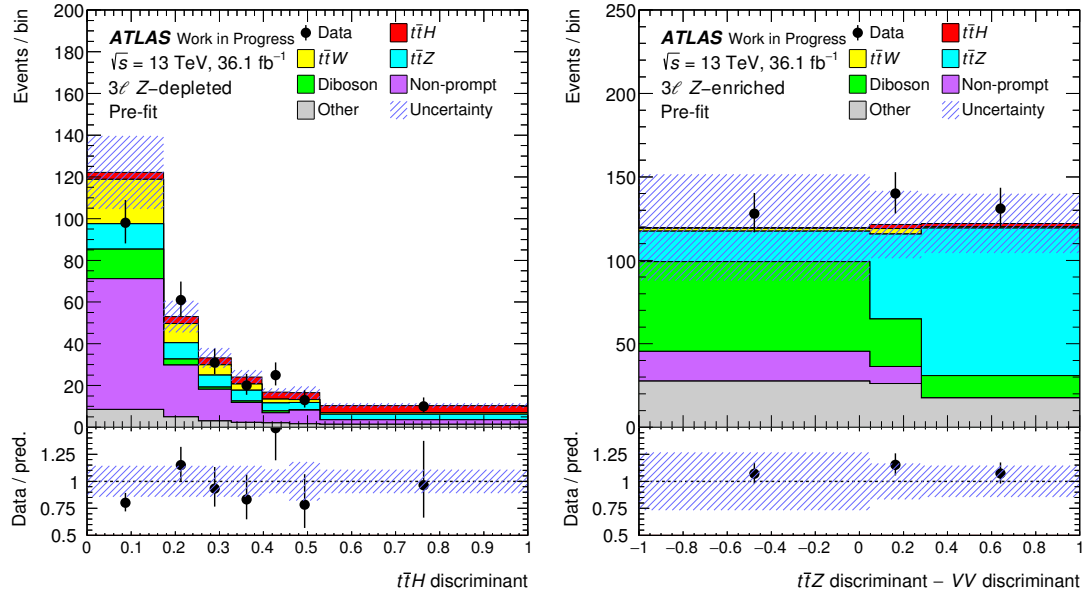
Figure 0.2.: Distributions discriminantes dans (à gauche) la région de signal appauvrie en Z : $t\bar{t}H$ discriminant et (à droite) la région de contrôle enrichie en Z : ($t\bar{t}Z$ discriminant $-$ VV discriminant) avant l'extraction des résultats.

les données et les prévisions. La différence des BDTs utilisée dans la CR enrichie en Z

sépare bien le bruit de fond $t\bar{t}Z$ à droite du bruit de fond VV à gauche.

Une analyse statistique est utilisée pour extraire la quantité de signal $t\bar{t}H$ en comparant le nombre d'événements de donnée observés par rapport à ceux attendu pour les bruits de fonds et le signal dans le cadre du SM. La quantité mesurée est le rapport entre le signal observé et le signal attendu $\mu_{t\bar{t}H}$. Les incertitudes systématiques sont attribuées à toutes les variables d'entrées et j'ai étudié leur impact sur les résultats de l'analyse. Parce qu'elles contribuent à différents processus et canaux, une attention particulière est accordée à leurs corrélations dans la combinaison de tous les canaux.

Dans la classification alternative du canal 3ℓ la valeur mesurée est :

$$\mu_{t\bar{t}H} = 1.37 \,^{+0.56}_{-0.52}\,(\text{stat.}) \,^{+0.52}_{-0.45}\,(\text{syst.}) = 1.37 \,^{+0.76}_{-0.69}, \tag{0.1}$$

compatible avec l'espérance SM de $\mu_{t\bar{t}H} = 1$. La signification observée (prévue) de cet excès par rapport au bruit de fond attendu est de 2,06 (1,53) écarts-types. Les distributions après l'extraction des résultats sont illustrées dans la figure 0.3. Un meilleur accord
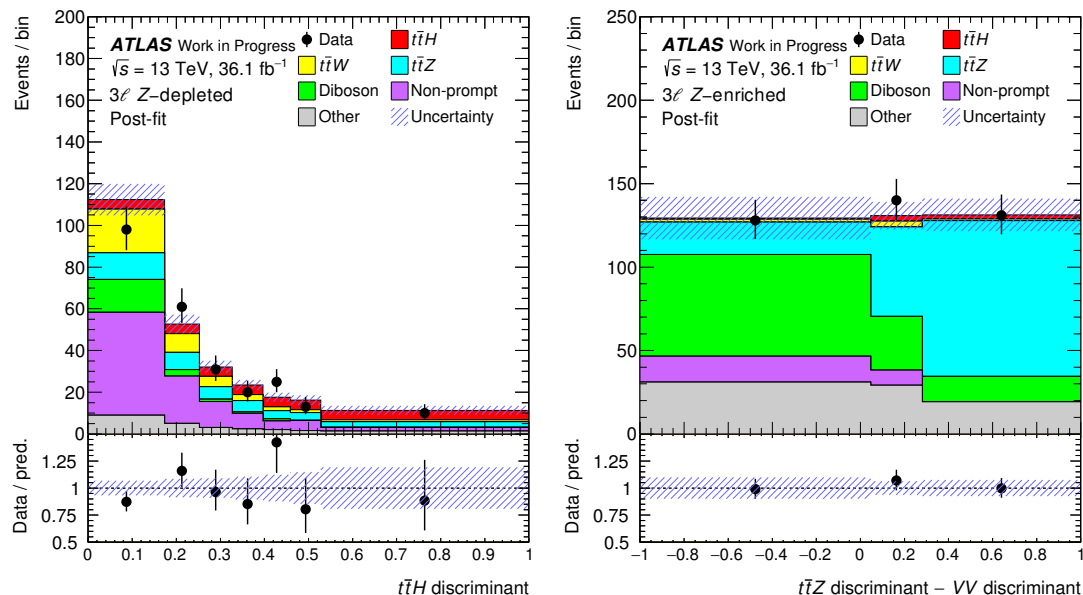
Figure 0.3.: Distributions discriminantes dans (à gauche) la région de signal appauvrie en Z : $t\bar{t}H$ discriminant et (à droite) la région de contrôle enrichie en Z : ($t\bar{t}Z$ discriminant $-$ VV discriminant) après l'extraction des résultats. La zone hachurée en bleu indique les incertitudes systématiques totales y compris l'incertitude observée sur $\mu_{t\bar{t}H}$.

entre les données observées et celles prédites est observé après l'extraction des résultats de l'ajustement de $\mu_{t\bar{t}H}$ et de toutes les paramètres avec leurs incertitudes.

L'analyse présentée dans [4] n'inclut pas ce résultat de la classification alternative des événements dans 3ℓ, mais la classification standard des événements. La valeur observée

de cette classification est :

$$\mu_{t\bar{t}H} = 1.76 \,^{+0.61}_{-0.57} \,(\text{stat.}) \,^{+0.60}_{-0.50} \,(\text{syst.}) = 1.76 \,^{+0.86}_{-0.76}, \qquad (0.2)$$

avec une signification du signal observé (attendu) de 2,38σ (1,48σ).

Alors que la classification standard vise à séparer simultanément le signal $t\bar{t}H$ et les quatre processus de bruit de fond de $t\bar{t}W$, $t\bar{t}Z$, VV et $t\bar{t}$ les uns des autres avec une grande pureté dans chacune des cinq régions, la classification alternative ne comporte que deux régions et utilise ces discriminants comme séparateurs. Dans le cas d'une normalisation flottante simultanément sur $t\bar{t}Z$ et $t\bar{t}W$, la classification alternative donne de meilleurs résultats dans la signification du signal $t\bar{t}H$, mais la force du signal mesurée $t\bar{t}W$ est peu fiable, bien que compatible avec l'espérance d'un signal SM. Parce que la classification standard inclut une région de contrôle dédiée au $t\bar{t}W$, le $\mu_{t\bar{t}W}$ mesuré est plus raisonnable dans ce cas.

Les deux classifications ont des performances similaires. Un avantage de la classification alternative est qu'elle inclut l'espace de phase complet de la présélection 3ℓ, ce qui est utile en cas de réinterprétation pour de nouvelles recherches physiques, effectuées en dehors de la collaboration ATLAS.

En combinaison avec les six autres canaux de l'analyse $t\bar{t}H \rightarrow$ multilepton, une valeur de :

$$\mu_{t\bar{t}H} = 1.56 \,^{+0.30}_{-0.29} \,(\text{stat.}) \,^{+0.39}_{-0.30} \,(\text{syst.}) = 1.56 \,^{+0.49}_{-0.42} \qquad (0.3)$$

est observée avec une signification du signal observé (attendu) de 4,1σ (2,8σ). Les incertitudes les plus importantes sont celles liées à la section efficace du signal $t\bar{t}H$, à l'échelle de l'énergie des jets et aux estimations du bruit de fond des leptons non-direct (dit non prompt). La figure 0.4 montre les valeurs mesurées pour la production de $t\bar{t}H$ dans les sept canaux individuels et la combinaison. Elles sont en accord entre elles et avec la prédiction du SM de $\mu_{t\bar{t}H} = 1$. Les canaux 2ℓSS et 3ℓ sont les plus sensibles dans l'analyse $t\bar{t}H \rightarrow$ multilepton.

Plusieurs autres recherches de la production $t\bar{t}H$ ont été effectuées par la collaboration ATLAS. En combinant avec les résultats de recherches $H \rightarrow b\bar{b}$ à 36,1 fb^{-1} et $H \rightarrow \gamma\gamma$ et $H \rightarrow ZZ \rightarrow 4\ell$ à 79,8 fb^{-1} une section efficace de $670 \pm 90 \,(\text{stat.}) \,^{+110}_{-100} \,(\text{syst.})$ fb [5] a été mesurée, ce qui est compatible avec la prédiction théorique du SM de $507 \,^{+35}_{-50}$ fb [6]. Cela correspond à une signification observée (attendue) de 5,8σ (4,9σ), ce qui est la première observation, par ATLAS, de la production de $t\bar{t}H$. Le couplage de Yukawa entre le boson de Higgs et le quark top est mesuré ainsi avec une précision meilleure que 10%.

Bien que la production de $t\bar{t}H$ ait été trouvée en accord avec les prédictions, la nouvelle physique peut se cacher dans un espace de phase différent. Les courants neutres, qui changent de saveur (FCNC), ne sont pas autorisés dans le SM au premier niveau de développement de la théorie, dit niveau de l'arbre. Par exemple, la désintégration du quark top en un boson de Higgs et un quark léger ($t \rightarrow Hq$) est fortement supprimée par le mécanisme de GIM. Son rapport d'embranchement prédit est de $\mathcal{B}(t \rightarrow Hc) \sim 3 \times 10^{-15}$ [7]. Un nouveau modèle physique à deux doublets de Higgs (2HDM) ajoute un champ de Higgs supplémentaire au SM et peut prédire des rapports d'embranchement de
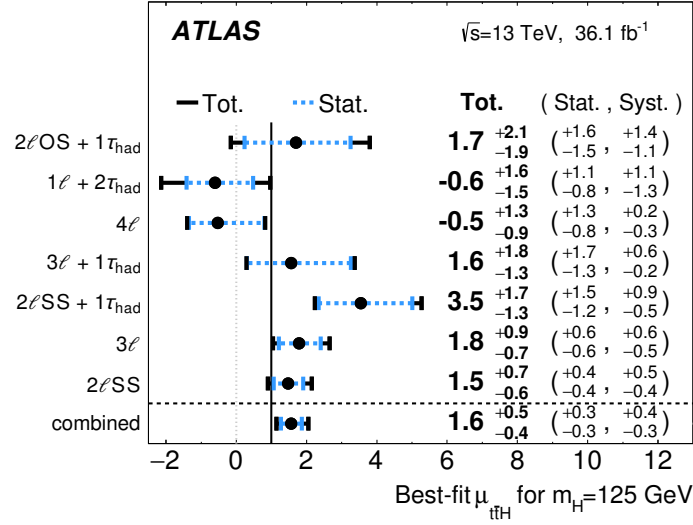
Figure 0.4.: Valeurs de $\mu_{t\bar{t}H}$ mesurées dans les sept canaux individuels et la combinaison [4].

désintégration $t \to Hc$ d'environ 0,15% [7]. Les meilleures limites sur la recherche du boson de Higgs se désintégrant en photons ($H \to \gamma\gamma$) par la collaboration ATLAS sont proches de cette valeur [8]. Dans cette thèse de doctorat, une recherche avec 36.1 fb^{-1} de collisions proton-proton est décrite [9]. Les mêmes canaux 2ℓSS et 3ℓ que dans la recherche de production $t\bar{t}H$ sont utilisés, en exploitant les similitudes des états finaux pour les différents signaux et les synergies des analyses. La production de $t\bar{t}H$ est ici considérée comme un bruit de fond SM supplémentaire et une analyse multivariée est mise en œuvre pour distinguer le signal FCNC des bruits de fond SM. Puisque moins de quarks d'état final sont attendus dans le signal FCNC que dans le signal $t\bar{t}H$, l'estimation basée sur les données de bruit de fond des leptons non-prompt a été adaptée pour cette analyse.

Les distribution des discriminants dans le cas de désintégration $t \to Hc$ sont illustrées par la figure 0.5 pour les deux régions du signal 2ℓSS et 3ℓ. Parce que la valeur mesurée de $\mathcal{B}(t \to Hc) = -0,07 \pm 0,08\%$ est négative, la contribution du signal $t \to Hc$ n'est pas quantifiable dans les histogrammes. On observe un bon accord entre les données et les prédictions. Dans les deux cas de $t \to Hc$ et $t \to Hu$ la valeur mesurée est cohérente avec l'hypothèse d'absence de signal.

Les limites supérieures des rapports d'embranchement à 95% degré de confiance (CL) sont calculées et présentées dans la figure 0.6. Pour la combinaison de $t \to Hu$ et de $t \to Hc$, les limites supérieures sur $\mathcal{B}$ attendues sont de 0,15%. Des limites supérieures attendues similaires ont été publiées dans la recherche de $t \to Hq$ avec $H \to \gamma\gamma$. Les limites supérieures observées sont de 0,19% et 0,16% pour $t \to Hu$ et $t \to Hc$, respectivement. Ce sont les meilleures limites expérimentales, à ce jour, sur cette désintégration
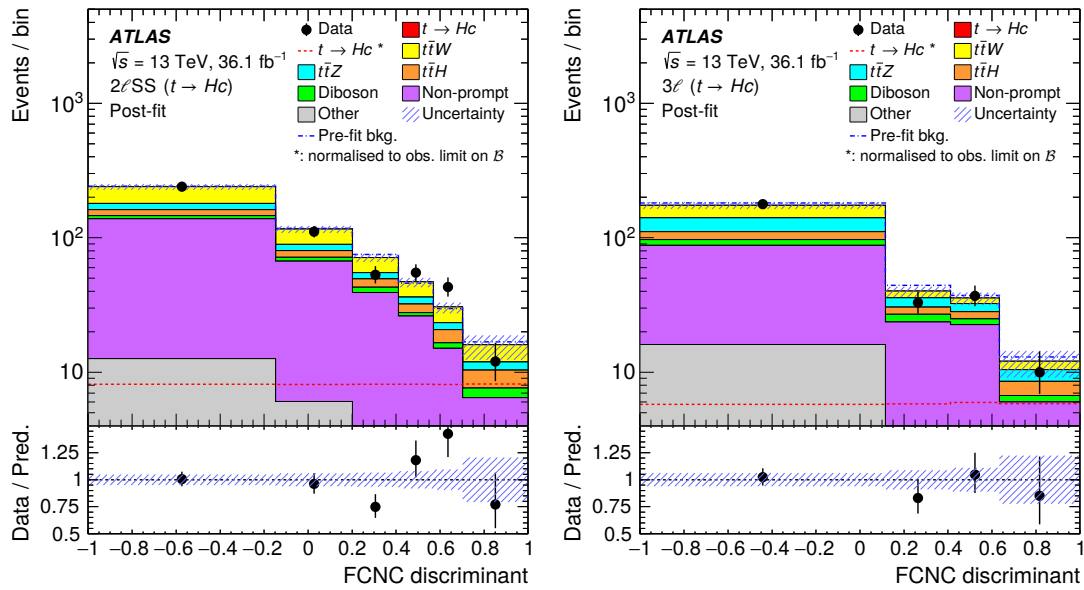
Figure 0.5.: Distributions discriminantes dans le cas de désintégration $t \rightarrow Hc$ pour (à gauche) la région de signal 2ℓSS et (à droite) la région de signal 3ℓ après l'extraction des résultats. La zone hachurée en bleu indique les incertitudes systématiques totales y compris l'incertitude observée sur $\mathcal{B}(t \rightarrow Hc)$ [9].
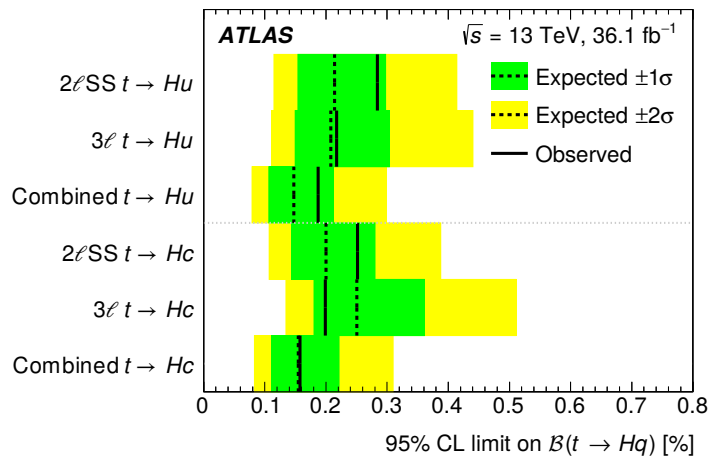
Figure 0.6.: 95% CL limites supérieures sur le rapport d'embranchement de $t \rightarrow Hq$ dans les canaux individuels et la combinaison [9].

de quark top avec changement de saveur.

Après le Run 2, le complexe d'accélérateurs du LHC et les expériences associées seront l'objet d'un ambitieux plan de mise à niveau pour fonctionner à une luminosité et une énergie dans le centre de masse accrue au Run 3 et au-delà. Le remplacement du système de déclenchement du calorimètre à Argon Liquide d'ATLAS introduira une granularité dix fois supérieure pour les informations envoyées au premier niveau de sélection d'événements (trigger). Cela permettra de maintenir des seuils d'énergie de déclenchement acceptable pour continuer à sélectionner au mieux les objets intéressants tout en maintenant une bande passante de déclenchement limitée. La performance d'un système de démonstration, en fonctionnement depuis 2015 au détecteur ATLAS, est étudiée et présenté dans cette thèse.

La mesure, par le démonstrateur du nouveau système de déclenchement, des impulsions électroniques envoyées par la carte d'étalonnage est illustré sur la figure 0.7 (à gauche) pour une super cellule du démonstrateur. Une bonne linéarité est observée jus-
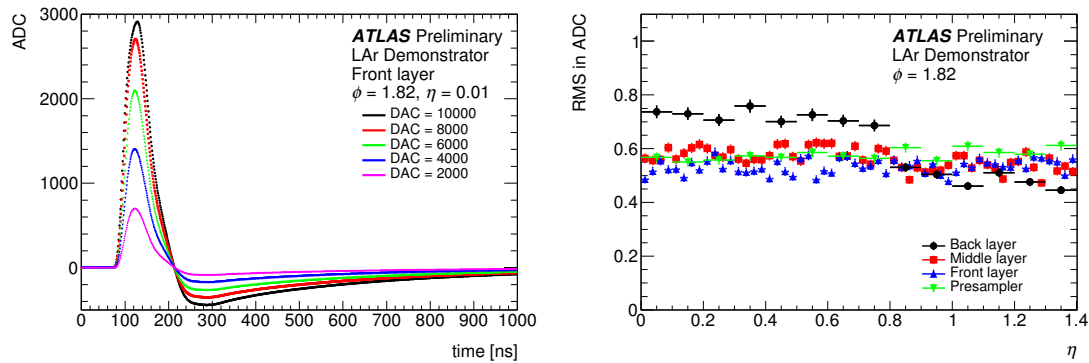
Figure 0.7.: Formes d'impulsions envoyées par le système d'étalonnage et lues par le démonstrateur pour une super cellule à différentes valeurs DAC (à gauche) et niveau de bruit pour les différentes super cellules (à droite) [10].

qu'à une certaine valeur où la saturation analogique apparaît. De plus, le niveau de bruit de différentes super cellules, illustré à la figure 0.7 (à droite), est bien inférieur à 1 ADC et est en accord avec les mesures effectuées sur banc d'essai.

Après l'étalonnage réussi du système, les données recueillies par le démonstrateur lors des collisions proton-proton ont pu être analysées et comparées avec la lecture principale du détecteur ATLAS. J'ai contribué à l'analyse en comparant les hauteurs d'impulsion des données de collision initiales. La figure 0.8 montre un exemple de collision proton-proton enregistrée en 2015. Un bon accord est observé entre les deux types de lectures. De plus, des gerbes de particules isolées et identifiées dans les événements lus par le démonstrateur ont pu être comparées avec succès aux mêmes objets reconstitués à partir de la lecture principale d'ATLAS. Plus tard, l'analyse a été améliorée en utilisant, pour la mesure des énergies transverses des super cellules, la même procédure de filtrage optimal [11] que dans la reconstruction standard.

Une version améliorée de ce démonstrateur avec le prototype final a été installée début
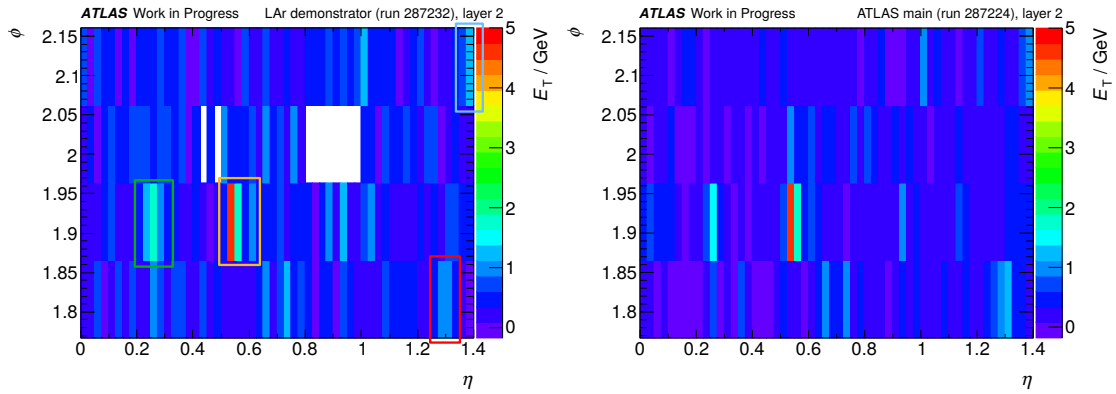
Figure 0.8.: Distribution des énergies transverses des super cellules du démonstrateur pour un événement pris en 2015 avec des collisions proton-proton (à gauche) et somme des énergies transverses des cellules LAr constituantes de la lecture principal d'ATLAS (à droite). Les zones colorées indiquent les régions où les électrons et les photons sont reconstruits sur la lecture principal d'ATLAS.

2018 et ses élémemts sont en cours de test pour préparer l'installation complète sur le détecteur en 2019-2020.

La mise à niveau Phase 2 prépare le LHC pour sa phase à haute luminosité, qui vise une luminosité intégrée totale de $3000\,\mathrm{fb}^{-1}$ à une énergie du centre de masse de $14\,\mathrm{TeV}$. Cela permettra d'améliorer la précision des mesures de couplage du boson de Higgs. Jusqu'à présent, la nouvelle physique est restée cachée et n'a pas été encore trouvée, mais les recherches futures pourraient le révéler. Une extrapolation préliminaire des analyses $t\bar{t}H \rightarrow$ multilepton et $t \rightarrow Hq \rightarrow$ multilepton permet d'espérer une amélioration d'un facteur deux de l'incertitude sur la section efficace et sur les limites des rapports d'embranchement.

Introduction

The Standard Model (SM) of particle physics is a coherent theory of the elementary particles and their interactions. It describes the electromagnetic, weak and strong interaction, in a unified gauge theory. The much weaker gravitational force is not considered by the SM. Its theoretical predictions are verified by many experiments with high precision since the 1960s. The last missing piece has been found in 2012, when the ATLAS and CMS collaborations announced the discovery of a scalar boson with a mass of about 125 GeV [1, 2].

This particle has been predicted by the Brout-Englert-Higgs mechanism, which explains the origin of masses of the elementary particles. The vector bosons of weak interaction (*W* and *Z* bosons) obtain their mass due to interaction with the Higgs field. The Yukawa couplings of the matter particles (fermions) determine their masses and their interaction strengths with the Higgs boson.

Nevertheless the Standard Model has no answers to several open questions in particle physics. It cannot describe the observed asymmetry of matter and antimatter in the universe. It has also no explanation for dark matter, which is predicted from cosmological observations. Theories with grand unification (GUT), supersymmetric particle partners (SUSY) or additional Higgs fields are extensions of the SM that may solve such issues.

New physics models are constrained by previous experiments in particular at mass scales up to few 100 GeV. Because the top quark is the heaviest SM fermion, the measurement of its Yukawa coupling is of special interest. With the proton-proton collisions in 2010–2013 (Run 1) of the Large Hadron Collider (LHC) this coupling has been measured with a precision of 15% [3]. Therefore Higgs boson production and decay modes have been exploited, where the top quark contributes in particle loops. New physics can manifest itself by additional particle loops in this indirect measurement. The associated Higgs boson production with a pair of top quarks ($t\bar{t}H$) is the best way for the direct measurement, because the top quark Yukawa coupling enters at tree-level. While in Run 1 of the LHC this measurement has been statistically limited, in 2015–2018 (Run 2) an increase of the center-of-mass energy $\sqrt{s}$ from 8 TeV to 13 TeV and of the integrated luminosity from 25 fb^{-1} to expected 150 fb^{-1} delivers more than twenty times more events for the $t\bar{t}H$ production.

This doctoral thesis presents the search for the $t\bar{t}H$ signal in final states with at least two leptons, using 36.1 fb^{-1} of Run 2 data, recorded by the ATLAS detector in 2015–2016 [4]. Seven channels are categorised by the number of light leptons ($\ell = e$ or μ) and hadronically decaying tau leptons (τ_{had}). They aim for different Higgs boson decay modes and

have different dominant background contributions. The most significant channels have two light leptons with same electric charge (2ℓSS) or three light leptons (3ℓ) and no τ_{had} in their final states with 80% of Higgs boson decays to W bosons ($H \rightarrow WW$). The non-prompt light leptons from b-hadron decays in $t\bar{t}$ production, which has 1,600 times the signal cross section, and those from photon conversions are the major background sources in these channels, followed by associated vector boson production with a pair of top quarks ($t\bar{t}V$), which has similar final states as the $t\bar{t}H$ signal. Kinematic properties are exploited to distinguish the signal from the background events in a multivariate analysis. I worked in particular on the optimisation of the separation in the 3ℓ channel. A statistical analysis is used to extract the amount of $t\bar{t}H$ signal by comparing the observed number of data events with the SM expectation for the backgrounds and the signal. Systematic uncertainties are assigned to all inputs and I studied their impact on the analysis results. Because they contribute to different processes and channels, particular attention is given to their correlation in the combination of all channels.

Flavour-changing neutral currents (FCNC) are not allowed in the SM at tree-level. E.g. the decay of the top quark into the Higgs boson and a light up-type quark is strongly suppressed by the GIM mechanism. Its predicted branching ratio is 3×10^{-15} [7]. The new physics model of two Higgs doublets (2HDM) adds an additional Higgs field to the SM and can predict branching ratios for the $t \rightarrow Hc$ decay of about 0.15% [7]. The best limits from the search in Higgs boson to photons ($H \rightarrow \gamma\gamma$) decay by the ATLAS collaboration are close to that value [8]. In this doctoral thesis a search aiming for the $H \rightarrow WW$ decay in 36.1 fb^{-1} of proton-proton collisions is described [9]. The same 2ℓSS and 3ℓ channels as in the search for $t\bar{t}H$ production are used, exploiting the similarity of the final states in the different signals. Therefore the $t\bar{t}H$ production is considered as an additional SM background and a multivariate analysis is implemented to distinguish the FCNC signal from the SM backgrounds. Because less final state quarks are expected in the FCNC signal than in the $t\bar{t}H$ signal, I adapted the data-driven estimate of the non-prompt light lepton estimate for this analysis.

After the Run 2 of the LHC the collider facilities and the experiments undergo an ambitious upgrade plan to run with increased luminosity in Run 3 and beyond. The replacement of the ATLAS Liquid Argon Calorimeter readout will introduce a ten times increase of granularity in the input to the first level of event selection (trigger). This allows to maintain low energy thresholds for interesting objects at limited trigger bandwidth. The performance of a demonstrator system, running since 2015 at the ATLAS detector, is presented.

This document is structured as follows: Chapter 1 introduces the theory of the SM, the Higgs boson properties and FCNC in the SM and in new physics models. Chapter 2 contains a description of the ATLAS detector at the LHC and its performance of particle reconstruction. Chapters 3 and 4 describe the searches for $t\bar{t}H$ production and flavour-changing $t \rightarrow Hq$ decays, respectively. Chapter 5 contains an overview of foreseen upgrades of the ATLAS Liquid Argon Calorimeter readout and performance studies on the demonstrator system.

1. Theory of Particle Physics

This chapter gives an overview of the theory of particle physics. Section 1.1 introduces the Standard Model (SM), which is a gauge theory, explaining three of the four fundamental interactions. The principal of a gauge theory is described at the example of electromagnetic interaction in section 1.1.1. It is expanded on the full electroweak interaction in section 1.1.2. This theory does not explain masses for the gauge bosons and thus the Brout-Englert-Higgs mechanism is needed. It introduces a spontaneous symmetry breaking of the electroweak gauge symmetries and can explain particle masses. It is described in section 1.1.3. A specific kind of particles is interacting strongly, which is theorised by an additional gauge symmetry group in section 1.1.4.

The Brout-Englert-Higgs mechanism does not only explain masses, but also introduces a new scalar boson, called the Higgs boson. It has been discovered in 2012 and this thesis presents a study of its interaction with the top quark. Therefore section 1.2.1 describes its properties of production and decay channels at hadron colliders and section 1.2.2 its experimental discovery at the LHC experiments of ATLAS and CMS.

Despite the SM has been very successful in describing many phenomena observed in the last decades, several unresolved questions remain. Some of them are summarised in section 1.3.1. Section 1.3.2 describes the theory of flavour-changing neutral currents (FCNC) which are strongly suppressed in the SM, but can be enhanced up to discoverable ranges in new physics models.

1.1. Standard Model

The Standard Model (SM) of particle physics, introduced in the 1960s by S. Glashow [12], A. Salam [13] and S. Weinberg [14], is very successful in describing the electromagnetic, weak and strong interactions of the fundamental particles, summarised in figure 1.1 with their properties of mass, charge and spin. It is build by three generations of matter containing each two quarks and two leptons which have spin $^1/_2$ (fermions). Each fermion has a partner with opposite electric charge and same mass, which is called antiparticle. Their interactions are mediated by the gauge bosons with spin 1.

It follows the principle of gauge invariance under certain local gauge transformations in the symmetry group of

$$\mathrm{SU}(3)_C \otimes \mathrm{SU}(2)_L \otimes \mathrm{U}(1)_Y \tag{1.1}$$
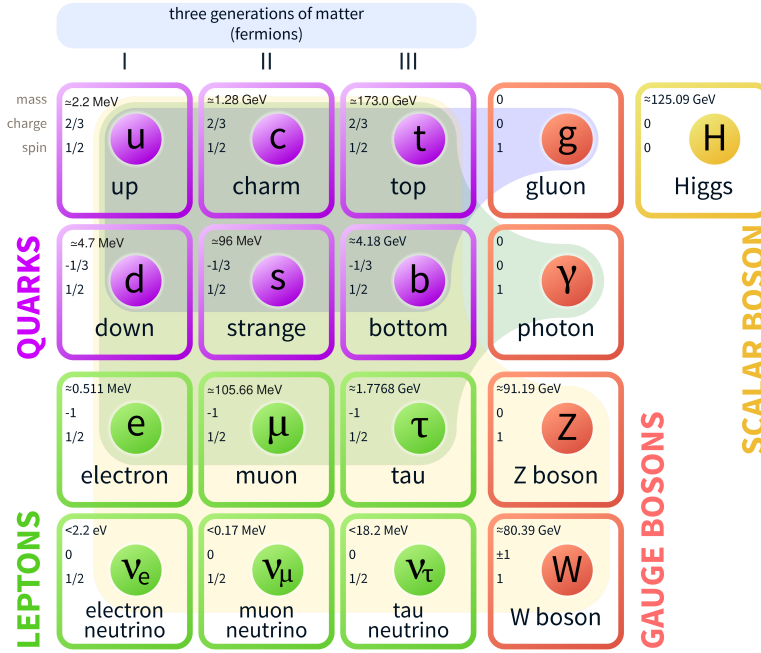
Figure 1.1.: Elementary particles in the Standard Model (derivative of [15]/public domain).

where $SU(3)_C$ and $SU(2)_L \otimes U(1)_Y$ represent the symmetry groups of strong and electroweak interaction, respectively.

1.1.1. Gauge theory of electromagnetic interaction

Free fermions are described by the Dirac Lagrangian density

$$\mathcal{L} = \bar{\psi} \left(i\gamma^\mu \partial_\mu - m \right) \psi \tag{1.2}$$

where ψ is the wave function of the fermion represented in form of a Dirac spinor, m is its particle mass and γ^μ are the Dirac matrices fulfilling the anticommutation relation $\{\gamma^\mu, \gamma^\nu\} = \gamma^\mu \gamma^\nu + \gamma^\nu \gamma^\mu$ ($\mu, \nu = 0, 1, 2, 3$). For simplicity, natural units are chosen with the velocity of light $c = 1$ and the Planck constant $\hbar = 1$. The adjoint spinor is $\bar{\psi} = \psi^\dagger \gamma^0$ where $\psi^\dagger$ is the conjugate transpose ψ.

Under a $U(1)_q$ transformation of $\psi \to \psi' = e^{-iq\Lambda}\psi$ with a constant charge q and a parameter Λ the Lagrangian is invariant if Λ is independent of the space-time x (global invariance). However if $\Lambda = \Lambda(x)$, the Lagrangian becomes not invariant because

$$\begin{aligned}
\mathcal{L} \to \mathcal{L}' &= e^{iq\Lambda}\bar{\psi} \left(i\gamma^\mu \partial_\mu - m \right) e^{-iq\Lambda}\psi \\
&= \mathcal{L} - q\bar{\psi}\gamma^\mu \partial_\mu \Lambda \psi.
\end{aligned} \tag{1.3}$$

The invariance under local gauge transformation can be introduced by the covariant

derivative $D_\mu = \partial_\mu + iqA_\mu$ with a vector field A_μ, which is transforming as $A_\mu \to A'_\mu = A_\mu + \partial_\mu\Lambda$. Then the Lagrangian becomes

$$\mathcal{L} = \bar{\psi}\left(i\gamma^\mu D_\mu - m\right)\psi = \bar{\psi}\left(i\gamma^\mu\partial_\mu - q\gamma^\mu A_\mu - m\right)\psi \tag{1.4}$$

and transforms under $\mathrm{U}(1)_q$ as

$$\begin{aligned}
\mathcal{L} \to \mathcal{L}' &= e^{iq\Lambda}\bar{\psi}\left(i\gamma^\mu\partial_\mu - q\gamma^\mu A_\mu + q\gamma^\mu\partial_\mu\Lambda - m\right)e^{-iq\Lambda}\psi \\
&= \mathcal{L} - q\bar{\psi}\gamma^\mu\partial_\mu\Lambda\psi + q\bar{\psi}\gamma^\mu\partial_\mu\Lambda\psi = \mathcal{L}.
\end{aligned} \tag{1.5}$$

Therefore, the Lagrangian in equation 1.4 describes the interaction of the vector field A_μ with a fermion of charge q, and can be interpreted as electromagnetic interaction with a massless photon (γ), represented by the vector field A_μ.

1.1.2. Electroweak interaction

In the 1950s–60s Lee, Yang and Wu observed parity violation in beta decays, which are charged current decays of $d \to ue\bar{\nu}_e$, where $\bar{\nu}_e$ is the anti-particle of the electron neutrino, expressed via charge conjugation [16]. It has been shown, that only left-handed electrons e_L couple to left-handed neutrinos $\nu_{e,L}$ in this process.

The left-handed SM fermions (neutrinos N, charged leptons E, up-type quarks U and down-type quarks D) can be represented in doublets of $\mathrm{SU}(2)_L$ by

$$\begin{aligned}
L_L &= \begin{pmatrix} N \\ E \end{pmatrix}_L = \begin{pmatrix} \nu_e \\ e \end{pmatrix}_L, \begin{pmatrix} \nu_\mu \\ \mu \end{pmatrix}_L, \begin{pmatrix} \nu_\tau \\ \tau \end{pmatrix}_L, \\
Q_L &= \begin{pmatrix} U \\ D' \end{pmatrix}_L = \begin{pmatrix} u \\ d' \end{pmatrix}_L, \begin{pmatrix} c \\ s' \end{pmatrix}_L, \begin{pmatrix} t \\ b' \end{pmatrix}_L,
\end{aligned} \tag{1.6}$$

where the down-type quarks are denoted with a prime because of flavour mixing in the quark sector, described by the Cabibbo-Kobayashi-Maskawa (CKM) mixing matrix $\mathcal{V}$ in

$$\begin{pmatrix} d' \\ s' \\ b' \end{pmatrix} = \mathcal{V}\begin{pmatrix} d \\ s \\ b \end{pmatrix}. \tag{1.7}$$

The right-handed components of the SM fermions can be represented as singlets

$$\begin{aligned}
L_R &= e_R, \mu_R, \tau_R, \\
U_R &= u_R, c_R, t_R, \\
D_R &= d_R, s_R, b_R.
\end{aligned} \tag{1.8}$$

Massless gauge fields W^a_μ ($a = 1, 2, 3$) and B_μ are introduced for $\mathrm{SU}(2)_L$ and $\mathrm{U}(1)_Y$ symmetry groups, respectively. Similarly to the electromagnetic case described in the previous section, the covariant derivative acting on left-handed doublets ψ_L and right-

handed singlets ψ_R is

$$D_\mu \psi_L = \left(\partial_\mu + ig \frac{\tau_a}{2} W_\mu^a + ig' \frac{Y_L}{2} B_\mu \right) \psi_L$$

$$D_\mu \psi_R = \left(\partial_\mu + ig' \frac{Y_R}{2} B_\mu \right) \psi_R \tag{1.9}$$

where g and g' are the coupling constants of the $SU(2)_L$ and $U(1)_Y$, respectively, $Y_{L(R)}$ is the weak hypercharge for left-(right-)handed particles and τ_a are the Pauli matrices, which are infinitesimal generators of the $SU(2)_L$:

$$\tau_1 = \begin{pmatrix} 0 & 1 \\ 1 & 0 \end{pmatrix}, \tau_2 = \begin{pmatrix} 0 & -i \\ i & 0 \end{pmatrix}, \tau_3 = \begin{pmatrix} 1 & 0 \\ 0 & -1 \end{pmatrix}. \tag{1.10}$$

They act only on the weak isospin doublets and in the following return zero when applied on right-handed singlets. The electroweak hypercharge is defined as $Y = 2(Q - I^z)$ with the electric charge Q and the third component of the weak isospin I^z, which is $+1/2$ $(-1/2)$ for the upper (lower) components of the left-handed doublets ψ_L and 0 for the right-handed singlets ψ_R. Table 1.1 summarises the quantum numbers for left- and right-handed fermions.

Table 1.1.: SM fermion quantum numbers of electric charge Q, third component of weak isospin I^z and electroweak hypercharge Y. *) Right handed neutrinos do not exist in the SM.

	Left-handed fermions				Right-handed fermions			
	N_L	E_L	U_L	D_L	N_R^*	E_R	U_R	D_R
Q	0	-1	$+2/3$	$-1/3$	$-$	-1	$+2/3$	$-1/3$
I^z	$+1/2$	$-1/2$	$+1/2$	$-1/2$	$-$	0	0	0
Y	-1	-1	$+1/3$	$+1/3$	$-$	-2	$+4/3$	$-2/3$

The full Lagrangian of electroweak interaction can be expressed as

$$\mathcal{L}_{EW} = \sum_\psi \bar{\psi} \gamma^\mu \left(i\partial_\mu - g \frac{\tau_a}{2} W_\mu^a - g' \frac{Y}{2} B_\mu \right) \psi - \frac{1}{4} W_a^{\mu\nu} W_{\mu\nu}^a - \frac{1}{4} B^{\mu\nu} B_{\mu\nu} \tag{1.11}$$

with field strength tensors

$$B_{\mu\nu} = \partial_\mu B_\nu - \partial_\nu B_\mu \tag{1.12}$$

and

$$W_{\mu\nu}^a = \partial_\mu W_\nu^a - \partial_\nu W_\mu^a - g\epsilon_{bc}^a W_\mu^b W_\nu^c, \tag{1.13}$$

where ϵ_{abc} is the Levi-Civita symbol which is $+1$ (-1) for even (odd) permutations of the indices a, b and c and zero for repeated indices. The weak gauge fields of charged

W bosons are a linear combination of W^1_μ and W^2_μ:

$$W^\pm_\mu = \frac{W^1_\mu \mp iW^2_\mu}{\sqrt{2}}, \tag{1.14}$$

and the weak neutral field of the Z boson (Z^0_μ) and the electromagnetic photon are obtained by the rotation in space

$$\begin{pmatrix} Z^0_\mu \\ A_\mu \end{pmatrix} = \begin{pmatrix} \cos\theta & -\sin\theta \\ \sin\theta & \cos\theta \end{pmatrix} \begin{pmatrix} W^3_\mu \\ B_\mu \end{pmatrix} \tag{1.15}$$

with the Weinberg angle θ, which is defined by

$$g\sin\theta = g'\cos\theta \equiv e \tag{1.16}$$

with the electromagnetic coupling e. In the electroweak Lagrangian in equation 1.11 the last two terms correspond to the gauge boson self interaction and the terms with W^a_μ and B_μ to the interaction of the fermions with the gauge bosons. The latter can be written as

$$\mathcal{L}^{\text{matter}}_{\text{EW}} = -\frac{g}{2}\left(J^\mu_{\text{CC}}W^+_\mu + J^{\mu\dagger}_{\text{CC}}W^-_\mu\right) - \frac{g}{2\cos\theta}J^\mu_{\text{NC}}Z^0_\mu - eJ^\mu_{\text{em}}A_\mu \tag{1.17}$$

introducing the weak charged current J^μ_{CC}, the weak neutral current J^μ_{NC} and the electromagnetic current J^μ_{em} for the fermion interaction with the W bosons, the Z boson and the photon, respectively.

The currents can be derived using the electroweak hypercharges Y for left- and right-handed fermions and the definitions in equations 1.14–1.16. For quarks the currents are

$$J^\mu_{\text{CC}} = \sqrt{2}\,\bar{U}_L\gamma^\mu D'_L, \tag{1.18}$$

$$J^\mu_{\text{NC}} = \left(1 - \tfrac{4}{3}\sin^2\theta\right)\bar{U}_L\gamma^\mu U_L - \tfrac{4}{3}\sin^2\theta\bar{U}_R\gamma^\mu U_R$$
$$\qquad - \left(1 - \tfrac{2}{3}\sin^2\theta\right)\bar{D}_L\gamma^\mu D_L + \tfrac{2}{3}\sin^2\theta\bar{D}_R\gamma^\mu D_R \text{ and} \tag{1.19}$$

$$J^\mu_{\text{em}} = \tfrac{2}{3}\bar{U}\gamma^\mu U - \tfrac{1}{3}\bar{D}\gamma^\mu D. \tag{1.20}$$

This leads to the following conclusions:

- In the weak charged current with the emission of a charged W boson the quark alters between up- and down-type quark, which is a flavour-changing interaction (e.g. $d \to u + W^-$ in the β^- decay of the hadron). Because of the flavour mixing in the quark sector, the generation can be changed, too. This explains CP violation in neutral kaon decays, which have been seen for the first time in 1964 [17].

- Both the weak neutral and the electromagnetic current have only interaction terms with same-flavour quarks. This means, that neither transitions in flavour nor in generation are predicted by SM at tree-level for neutral currents.

- The strength of the electromagnetic current scales with the electric charge of the particles ($Q_U = +2/3$, $Q_D = -1/3$) as expected by the classical theory of electromagnetism. The charge q introduced in section 1.1.1 corresponds to $q = Q \cdot e$ with electric charge quantum number Q and electromagnetic coupling strength e.

1.1.3. Spontaneous symmetry breaking and particle masses

The Lagrangian presented so far assumes massless particle fields, because explicit terms for fermion masses like in equation 1.2 violate the chiral symmetry and gauge boson mass terms violate the gauge symmetry. The Brout-Englert-Higgs mechanism [18–22] solves this problem by introducing the (so called Higgs) scalar field

$$\phi = \begin{pmatrix} \phi^+ \\ \phi^0 \end{pmatrix} = \frac{1}{\sqrt{2}} \begin{pmatrix} \phi_3 + i\phi_4 \\ \phi_1 + i\phi_2 \end{pmatrix}, \tag{1.21}$$

defined a weak isospin doublet like for left-handed fermions with $I^z = +1/2$ for the charged and $I^z = -1/2$ for the neutral complex scaler field. The Lagrangian term associated to this scalar field is

$$\mathcal{L}_{\text{Higgs}} = (D_\mu \phi)^\dagger D^\mu \phi - V(\phi) = \left| \left(\partial_\mu + i \left(g \frac{\tau_a}{2} W_\mu^a + g' \frac{Y}{2} B_\mu \right) \right) \phi \right|^2 - V(\phi), \tag{1.22}$$

where the first term describes the kinetic energy of the field and the second term is the Higgs potential

$$V(\phi) = \mu^2 \phi^\dagger \phi + \lambda \left(\phi^\dagger \phi \right)^2. \tag{1.23}$$

with parameters λ and μ^2. Only positive values of $\lambda > 0$ are allowed to provide a stable global minimum. Figure 1.2 shows the Higgs potential for fixed ϕ^+ in dependency of the real and imaginary parts of the neutral scalar field ϕ^0. For values of $\mu^2 \geq 0$ the minimum
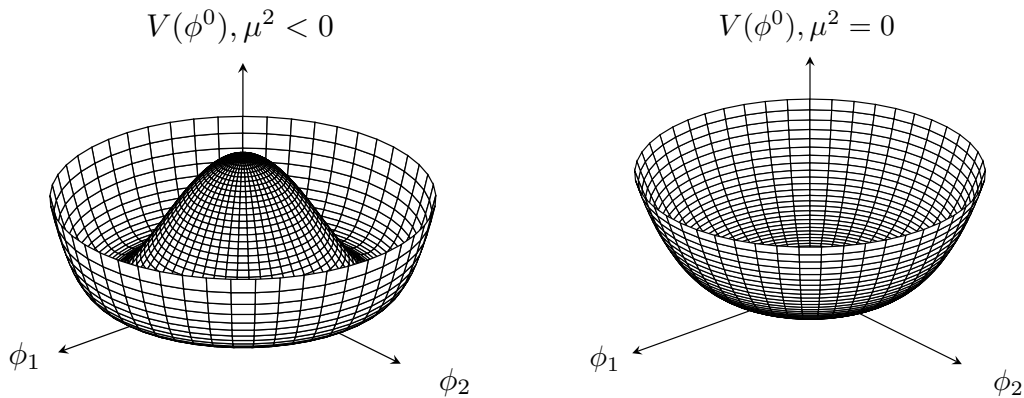

Figure 1.2.: Higgs potential $V(\phi^0)$ with $\lambda > 0$ as a function of real (ϕ_1) and imaginary (ϕ_2) part of the neutral complex scalar field ϕ^0 for (left) $\mu^2 < 0$ and (right) $\mu^2 = 0$.

of the potential is at $\phi_1 = \phi_2 = 0$. At values of $\mu^2 < 0$ the potential has a continuous minimum at

$$\left|\phi^0\right| = \sqrt{\frac{\phi_1^2 + \phi_2^2}{2}} = \sqrt{\frac{-\mu^2}{\lambda}} \equiv \frac{v}{\sqrt{2}}, \tag{1.24}$$

defining the vacuum expectation value (VEV) v. An arbitrary ground state can be chosen at $\phi_1 = \sqrt{2}v$ and $\phi_2 = 0$. Because this state is not invariant under $\mathrm{SU}(2)_L \otimes \mathrm{U}(1)_Y$ transformation, the process of changing sign from μ^2 is called spontaneous symmetry breaking. The expansion of the field around the ground state can be expressed as

$$\phi = \frac{1}{\sqrt{2}} \begin{pmatrix} \eta_3 + i\eta_4 \\ v + \eta_1 + i\eta_2 \end{pmatrix} \tag{1.25}$$

with small perturbations η_j to the vacuum state. Then the Lagrangian becomes

$$\mathcal{L}_{\text{Higgs}} = \frac{1}{2} \sum_{j=1}^{4} D_\mu \eta_j D^\mu \eta_j + \mu^2 (\eta_1)^2 + \frac{\lambda v^4}{4} + \mathcal{O}(\eta_1, \eta_2, \eta_3, \eta_4)^3. \tag{1.26}$$

The second term of this expression corresponds to a mass term for the η_1 with a mass of

$$m_H = \sqrt{-2\mu^2} = \lambda v. \tag{1.27}$$

It can be interpreted as the physical field of the Higgs boson $H \equiv \eta_1$ with the mass m_H. The other three perturbations are massless fields, which can be associated to Goldstone bosons. In gauge theory they can be removed by proper gauge choice. This transformation leads to masses of three of the vector bosons of electroweak interaction, the charged W bosons and the Z boson:

$$m_W = \frac{gv}{2}, m_Z = \frac{v}{2}\sqrt{g^2 + g'^2} = \frac{m_W}{\cos\theta}. \tag{1.28}$$

The VEV is experimentally determined with a value of $v = 246\,\text{GeV}$. Masses for the charged fermions can be generated by additional, under $\mathrm{SU}(2)_L \otimes \mathrm{U}(1)_Y$ transformation invariant coupling terms of the Higgs field and the fermion fields from equations 1.6 and 1.8. The corresponding Yukawa Lagrangian is

$$\mathcal{L}_{\text{Yukawa}} = -\lambda_{ab}^L \bar{L}_L^a \phi L_R^b - \lambda_{ab}^D \bar{\tilde{Q}}_L^a \phi \tilde{D}_R^b - \lambda_{ab}^U \bar{\tilde{Q}}_L^a i\tau_2 \phi^* \tilde{U}_R^b + \text{h.c.} \tag{1.29}$$

with coupling matrices λ and generation indices $a, b = 1, 2, 3$. Here both the down- and up-type quarks are given in their flavour eigenstates $\tilde{Q}_L$, $\tilde{D}_R$ and $\tilde{U}_R$.

The Yukawa coupling matrix for leptons is diagonal and e.g. the term for electrons with electron Yukawa coupling $\lambda_e \equiv \lambda_{11}^L$ becomes under expansion of the Higgs field

around the ground state in Higgs boson direction

$$\mathcal{L}_{\text{Yukawa},e} = -\frac{\lambda_e}{\sqrt{2}} \left(\begin{pmatrix} \bar{\nu}_e & \bar{e} \end{pmatrix}_L \begin{pmatrix} 0 \\ v+H \end{pmatrix} e_R + \bar{e}_R \begin{pmatrix} 0 & v+H \end{pmatrix} \begin{pmatrix} \nu_e \\ e \end{pmatrix}_L \right)$$

$$= -\frac{\lambda_e}{\sqrt{2}} \left(\bar{e}_L \left(v+H \right) e_R + \bar{e}_R \left(v+H \right) e_L \right)$$

$$= -\frac{\lambda_e v}{\sqrt{2}} \bar{e}e - \frac{\lambda_e}{\sqrt{2}} \bar{e}He. \tag{1.30}$$

The first term corresponds to the mass term for electrons with the mass $m_e = \frac{\lambda_e v}{\sqrt{2}}$ and the second term can be interpreted as interaction of the Higgs boson with the fermion via direct Yukawa coupling λ_e.

In case of the quarks the complex mass matrices $m^U = \frac{v}{\sqrt{2}} \lambda^U$ and $m^D = \frac{v}{\sqrt{2}} \lambda^D$ for up- and down-type quarks, respectively, are not diagonal. They can be diagonalised by the transformations

$$V_L^U m^U V_R^{U\dagger} = \text{diag}(m_u, m_c, m_t),$$
$$V_L^D m^D V_R^{D\dagger} = \text{diag}(m_d, m_s, m_b) \tag{1.31}$$

with four arbitrary matrices V_L^U, V_R^U, V_L^D and V_R^D which transform flavour to mass eigenstates $U_{L/R} = V_{L/R}^U \tilde{U}_{L/R}$ and $D_{L/R} = V_{L/R}^D \tilde{D}_{L/R}$ with $V_{L/R}^U V_{L/R}^{U\dagger} = V_{L/R}^D V_{L/R}^{D\dagger} = \text{diag}(1,1,1)$. The CKM matrix, introduced in section 1.1.2 to explain flavour mixing in the electroweak charged currents, is then

$$\mathcal{V} = V_L^U V_L^{D\dagger} \tag{1.32}$$

connecting the left-handed up-type with the left-handed down-type quarks.

Following the Higgs field expansion around the ground state, the matrices λ^U and λ^D are diagonalised for the quark mass terms and the interaction terms with the Higgs boson simultaneously, as shown here for the Yukawa Lagrangian of the up-type quarks,

$$\mathcal{L}_{\text{Yukawa},U} = -\frac{\lambda_{ab}^U}{\sqrt{2}} \bar{\tilde{U}}_L^a \left(v+H \right) \tilde{U}_R^b + \text{h.c.}$$

$$= - \left(1 + \frac{1}{v} H \right) \bar{U}_L^k \left(V_L^U \right)_k^a m_{ab}^U \left(V_R^{U\dagger} \right)_l^b U_R^l + \text{h.c.}$$

$$= - \left(1 + \frac{1}{v} H \right) \bar{U}^a \left(\text{diag}(m_u, m_c, m_t) \right)_{ab} U^b$$

$$= -m_u \bar{u}u - m_c \bar{c}c - m_t \bar{t}t - \frac{\lambda_u}{\sqrt{2}} \bar{u}Hu - \frac{\lambda_c}{\sqrt{2}} \bar{c}Hc - \frac{\lambda_t}{\sqrt{2}} \bar{t}Ht \tag{1.33}$$

with the quark Yukawa couplings $\lambda_q = \frac{\sqrt{2}m_q}{v}$. Because only terms with same-flavour quarks remain after the diagonalisation, flavour-changing neutral currents involving the Higgs boson are not allowed at tree-level.

The experimental discovery of neutrino oscillation requires masses for neutrinos which

are not predicted by the classic minimal SM. The seesaw mechanism adds heavy right-handed neutrinos with Majorana mass $m_{M,R} \sim 10^{15}$ GeV at grand unification scale. With a Dirac mass of e.g. $m_D \sim 10^2$ GeV for the coupling of left- and right-handed neutrinos the left-handed neutrinos can have a Majorana mass of $m_{M,L} = \frac{m_D^2}{m_{M,R}} \sim 10^{-2}$ eV, which is within the expected order of magnitude range.

1.1.4. Strong interaction

Quantum chromodynamics (QCD) is a gauge theory of $SU(3)_C$ colour symmetry and describes the strong interaction of the quarks and the massless gluons. Its Lagrangian can be written

$$\mathcal{L}_{\text{QCD}} = \sum_f \bar{q}_f \left(i\gamma^\mu (\partial_\mu + i g_s G_\mu^a T_a) - m_f \right) q_f - \frac{1}{4} G_{\mu\nu}^a G_a^{\mu\nu} \tag{1.34}$$

where q_f are the quark fields with flavour f in colour 3-vectors, g_s is the coupling strength of the strong interaction, G_μ^a are the gauge fields for the eight gluons ($a = 1, \ldots, 8$), T_a are the generators of the $SU(3)_C$ group, e.g. represented by 3×3 Gell-Mann matrices and $G_{\mu\nu}^a$ are the field strength tensors for the gluon-gluon self-interaction

$$G_{\mu\nu}^a = \partial_\mu G_\nu^a - \partial_\nu G_\mu^a - g_s f_{bc}^a G_\mu^b G_\nu^c \tag{1.35}$$

where f_{abc} are the structure constants of the $SU(3)_C$ group with $[T_a, T_b] = 2i f_{abc} T^c$.

The term for quark masses is usually included in the electroweak sector, namely in the Yukawa Lagrangian in equation 1.29. The strong interaction is neither coupled to the colourless leptons nor to the Higgs boson and the electroweak gauge bosons. The $SU(3)_C$ is an unbroken symmetry and thus the gluons are massless.

The coupling constant $\alpha_s = \frac{g_s^2}{4\pi}$ is decreasing logarithmically with the energy scale q^2. At low energies $q^2 \to 0$ or equivalently long distances the coupling constant diverges. This behaviour forbids free single gluons or quarks and is called confinement. Due to that, only hadrons can be observed in experiments, which are colour singlets, e.g. mesons ($\bar{q}_{f,i} q_{f',i}$) with electric charges of -1, 0 or $+1$ and baryons ($\epsilon^{ijk} q_{f,i} q_{f',j} q_{f'',k}$). Here f, f' and f'' are the quark flavours and i, j and k are the quark colours, which can be red, green or blue.

1.2. Higgs Boson

1.2.1. Production and decay properties at hadron colliders

The Higgs boson production at the LHC is dominated by four modes which are gluon-gluon fusion (ggF), vector boson fusion (VBF), associated production with a W or Z boson (VH with $V = W$ or Z) and associated production with a pair of top- or bottom-quarks ($t\bar{t}H$ or $b\bar{b}H$). The leading order Feynman diagrams of these processes are shown

in figure 1.3.
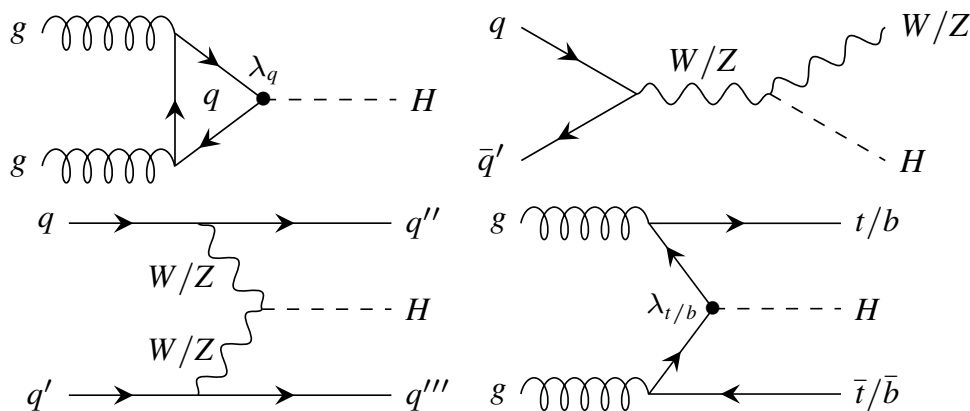
Figure 1.3.: Leading order Feynman diagrams for Higgs boson production in (top left) gluon-gluon fusion, (top right) associated production with a vector boson, (bottom left) vector boson fusion and (bottom right) associated production with pair of top- or bottom-quarks. The quark Yukawa coupling, entering in the gluon-gluon fusion is marked with λ_q. The $t\bar{t}H$ ($b\bar{b}H$) production gives direct access to the top (bottom) Yukawa coupling $\lambda_{t(b)}$.

In the ggF the Higgs boson is produced via virtual quark loop where mainly the top quark is contributing due to its highest Yukawa coupling λ_t. With a cross section of 48.5 pb at a center-of-mass energy of $\sqrt{s} = 13$ TeV for a Higgs boson mass of $m_H = 125$ GeV, it dominates the Higgs boson production mainly due to the large amount of gluons in proton-proton collisions [6].

The second largest production mechanism is the VBF with a cross section of 3.78 pb, where in leading order two vector bosons produced from incoming quarks fuse to the Higgs boson [6]. This process is used to access the coupling between the Higgs boson and the vector bosons.

The *VH* production with a cross section of 2.25 pb is the third largest contribution to the Higgs boson production [6]. Because the Higgs boson is radiated from a vector boson produced by fusion of a pair of quarks in the leading order tree-level contribution, this process is also known as Higgs strahlung.

The $t\bar{t}H$ and $b\bar{b}H$ production have a smaller cross section of 507 fb and 486 fb, respectively [6]. The measurement of the $t\bar{t}H$ production is the best way to directly unambiguously determine the size of the coupling of the top quark to the Higgs boson. In the SM the $t\bar{t}H$ production cross section is in leading order proportional to the square of the top Yukawa coupling $\sigma_{t\bar{t}H} \propto \lambda_t^2$.

The associated production modes with a single top and additional quarks (*tHqb*) or a *W* boson (*tHW*) have a negligible total cross section of about 80 fb [6].

Figures 1.4 (left) and (right) summarise the different production cross sections as a function of center-of-mass energy and Higgs boson mass, respectively.
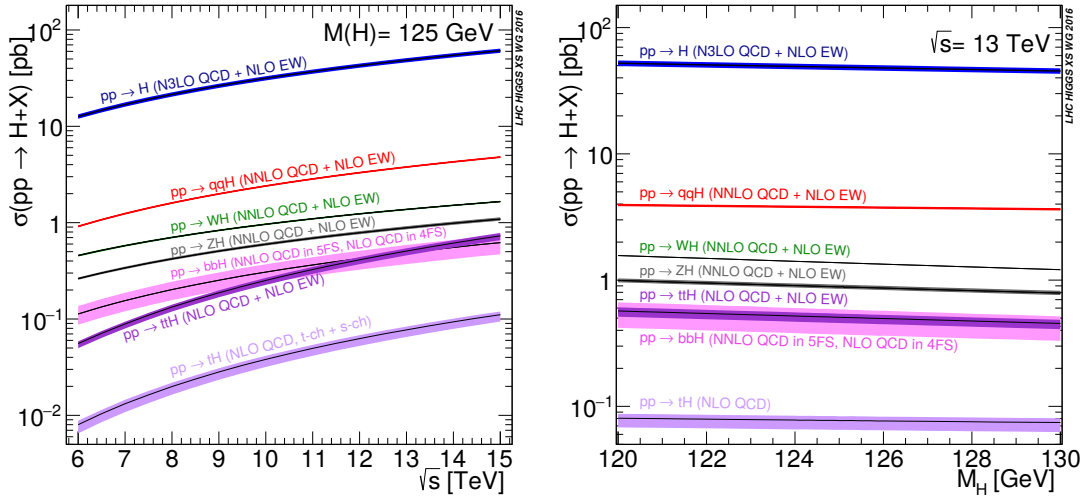
Figure 1.4.: LHC Higgs boson production cross section (left) at Higgs boson mass $m_H = 125\,\text{GeV}$ as a function of the center-of-mass energy and (right) at $\sqrt{s} = 13\,\text{TeV}$ as a function of the Higgs boson mass m_H [6].

The Higgs boson is unstable and decays at tree-level into pairs of fermions or vector bosons. Figure 1.5 shows the leading order Feynman diagrams of the different decay modes. The decays to a pair of photons or a photon and a Z boson have loops of W bosons
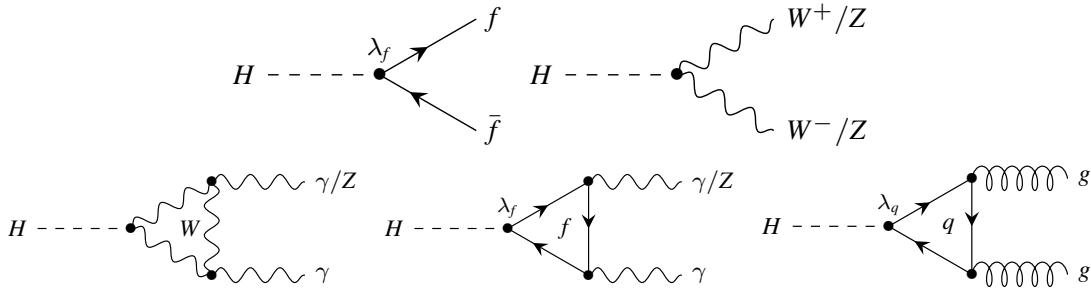
Figure 1.5.: Leading order Feynman diagrams for Higgs boson decay in (top left) a pair of fermions, (top right) a pair of vector bosons, (bottom left and middle) a pair of photons or a photon and a Z boson and (bottom right) a pair of gluons. The fermion Yukawa coupling is marked with λ_f. In the case of $H \rightarrow gg$ only the quarks contribute in the loops.

or fermions at leading order and the decays to gluons are possible due to quark loops.

The decay branching ratios as a function of the Higgs boson mass are shown in figure 1.6. At $m_H = 125\,\text{GeV}$ the leading decay mode is the decay to a pair of bottom-quarks with a branching ratio of 58.1%, followed by the decay to W bosons with a branching ratio of 21.5%. The most significant discovery channels of the Higgs boson have much smaller branching ratios of 2.64% for the decay to Z bosons and 0.227% for the decay to
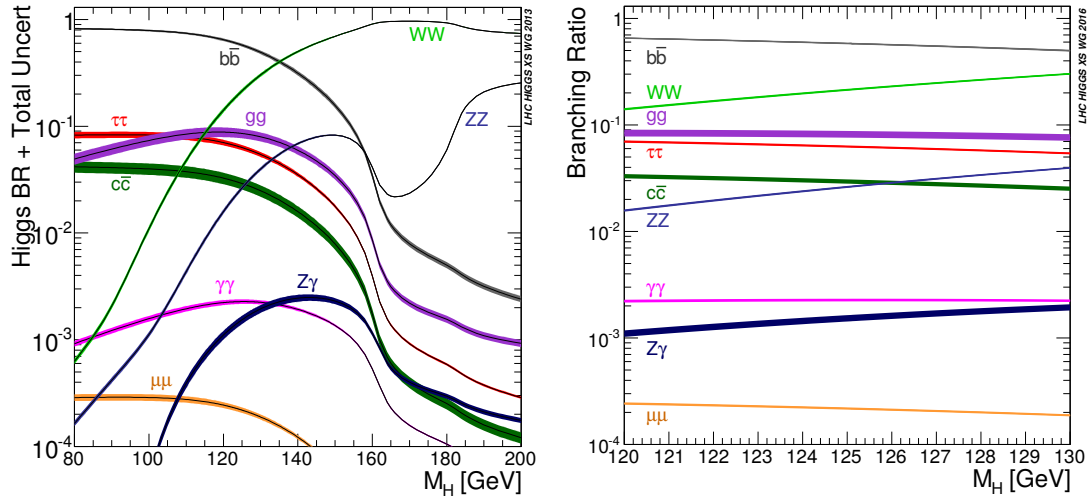
Figure 1.6.: Higgs boson decay branching ratios as a function of the Higgs boson mass m_H (left) in the range of $80\,\text{GeV} < m_H < 200\,\text{GeV}$ [23] and (right) in the range of $120\,\text{GeV} < m_H < 130\,\text{GeV}$ with latest values and uncertainties [6].

a pair of photons. The decay to a pair of tau leptons has a branching ratio of 6.29% [6]. The Higgs boson decays to electrons or muons are strongly suppressed compared to the decay to tau leptons, because of the much smaller Yukawa couplings, which scale linearly with the particle mass.

1.2.2. Discovery at the LHC

In July 2012 the ATLAS and CMS experiments at the LHC announced the discovery of a new particle with properties compatible with the SM Higgs boson [1, 2].

The search by the ATLAS collaboration is done in many Higgs boson decay channels using proton-proton collisions at center-of-mass energies of 7 and 8 TeV with integrated luminosities of 4.8 and $5.8\,\text{fb}^{-1}$ from 2011 and 2012 data taking, respectively. The decay modes to Z bosons and to a pair of photons provide a clean signature in the detectors.

The search for the $H \rightarrow ZZ$ decay proceeds through the leptonic Z boson decays leading to final states with four leptons. Figure 1.7 (left) shows the distribution of the invariant masses $m_{4\ell}$ of four light leptons ($\ell = e$ or μ) coming from the decay of two Z bosons. A signal of $H \rightarrow ZZ \rightarrow 4\ell$ is found at a significance maximising Higgs boson mass of about $m_H = 125.0\,\text{GeV}$ with a local significance of 3.6 standard deviations (σ) while 2.7σ are expected.

The $H \rightarrow \gamma\gamma$ decays are identified by two energetic photons in the detector. The distribution of the di-photon mass $m_{\gamma\gamma}$ is given in figure 1.7 (right). The highest local significance is observed at $m_H = 126.5\,\text{GeV}$ with 4.5σ where 2.5σ are expected.

In combination with all other searches for Higgs boson decay channels the largest observed local significance of 5.9σ (4.9σ expected) is found at $m_H = 126.5 \pm 0.4$ (stat.)
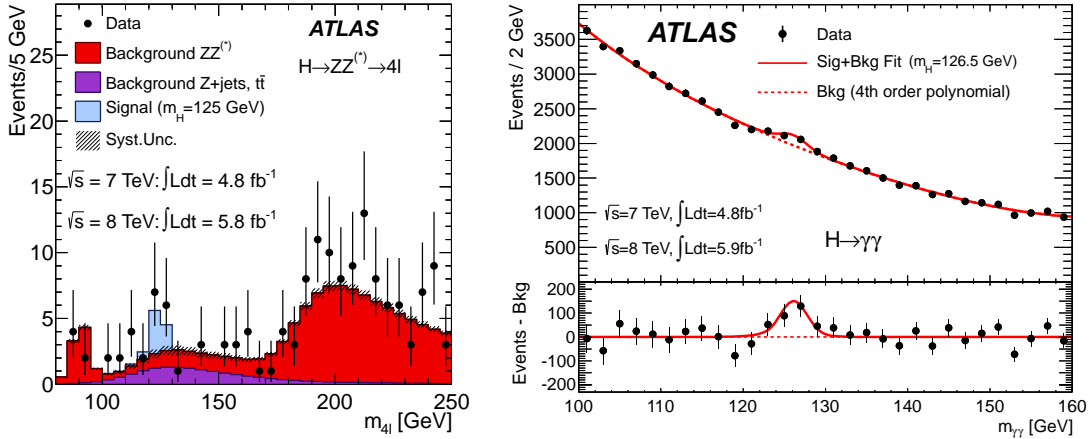
Figure 1.7.: Higgs boson mass peak in the ATLAS discovery paper in the distribution of (left) four-lepton invariant mass $m_{4\ell}$ in the search for $H \to ZZ^* \to 4\ell$ and (right) di-photon invariant mass $m_{\gamma\gamma}$ in the search for $H \to \gamma\gamma$ [1].

± 0.4 (syst.) GeV. This corresponds to a global significance of 5.1σ of the signal hypothesis in the mass range of $110\,\text{GeV} < m_H < 600\,\text{GeV}$.

Similarly, the CMS experiment found a new boson at a mass of $m_H = 125.3 \pm 0.4$ (stat.) ± 0.5 (syst.) GeV with a local significance of 5.0σ (5.9σ expected).

After its discovery the properties of this new particle have been investigated and found to be consistent with SM prediction. The quantum numbers of spin J and parity P are probed to be $J^P = 0^+$ as expected for a SM Higgs boson [24, 25]. The ATLAS and CMS measurements of the Higgs boson mass in the $H \to ZZ^* \to 4\ell$ and $H \to \gamma\gamma$ channels with full LHC Run 1 data were combined, leading to a value of $m_H = 125.09 \pm 0.21$ (stat.) ± 0.11 (syst.) GeV [26].

The different Higgs boson production and decay modes have been measured by the ATLAS and CMS experiments. A typical parameter of interest is the signal strength μ for a process $i \to H + x \to f$, defined as

$$\mu^{if} \equiv \mu^i \cdot \mu^f \equiv \frac{\sigma^i}{\sigma^i_{\text{SM}}} \cdot \frac{\mathcal{B}^f}{\mathcal{B}^f_{\text{SM}}} \tag{1.36}$$

which is the ratio of observed production cross section σ^i and branching ratio $\mathcal{B}^f$ over expected one by the SM. The production (decay) signal strength is denoted as $\mu^{i(f)}$.

The measurements of the signal strengths of the production and decay modes performed using the full LHC Run 1 data are shown in figure 1.8. In Run 1 combination, both the ggF and the VBF production as well as the decays $H \to \gamma\gamma, H \to ZZ, H \to WW$ and $H \to \tau\tau$ have been observed. Other production and decay modes have not been observed with a signal significance $> 5\sigma$ in Run 1, and are one of the goals of the Run 2 physics programme.

The $t\bar{t}H$ production cross section is in leading order proportional to λ_t^2 and hence it
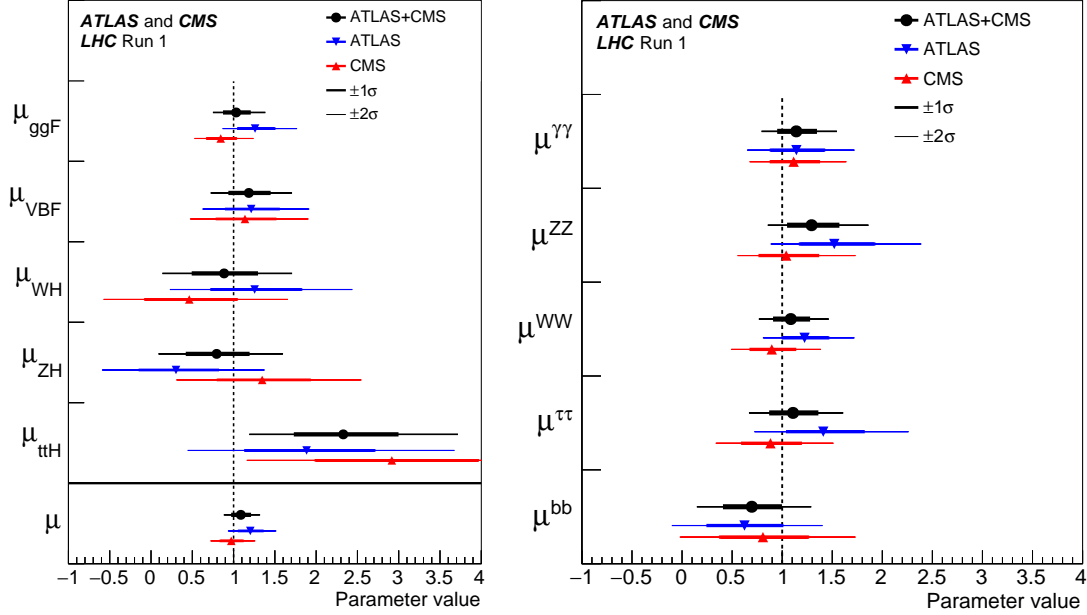
Figure 1.8.: Signal strengths of the major Higgs boson (left) production and (right) decay modes, measured in ATLAS, CMS and their combination in Run 1 [3].

can be used for a precise and direct measurement of the top quark Yukawa coupling. Because the top quark with a mass of $173.0 \pm 0.4\,\text{GeV}$ [27] is by far the heaviest SM fermion, its Yukawa coupling is the only one close to unity. It enters in many Higgs boson production and decay modes as indicated in the Feynman diagrams in figures 1.3 and 1.5, contributing mainly in ggF and $t\bar{t}H$ production and $H \to \gamma\gamma$ and $H \to gg$ decays. These production and decay modes provide a possibility to indirectly measure the top quark Yukawa coupling and to compare the result with the direct measurement in $t\bar{t}H$ production.

The observed signal strength of the $t\bar{t}H$ production in full Run 1 combination is $\mu_{t\bar{t}H} = 2.3^{+0.7}_{-0.6}$ with an observed (expected) significance of 4.4σ (2.0σ). With the increase of center-of-mass energy from 8 TeV (7 TeV) to 13 TeV at Run 2 of the LHC, the $t\bar{t}H$ production cross section increases from 133 fb (89 fb) to 507 fb. Together with the increase of luminosity from $20\,\text{fb}^{-1}$ at 8 TeV and $5\,\text{fb}^{-1}$ at 7 TeV to the amount of data recorded by the ATLAS experiment during 2015–2016 proton-proton collisions of $36.1\,\text{fb}^{-1}$ the expected number of $t\bar{t}H$ events is six times the amount in Run 1. This makes it possible to use elaborate techniques to discriminate the $t\bar{t}H$ signal from backgrounds in the search, presented in chapter 3 of this doctoral thesis. Final states with multiple leptons are examined, which mainly appear in Higgs boson decays to vector bosons and tau leptons.

1.3. Beyond the Standard Model

1.3.1. Unresolved questions in the Standard Model

Although the SM is a very successful theory describing particle physics and being confirmed by various experiments, it has several unsolved questions:

- Neutrino oscillations have been observed by various experiments and have their origin in a mixture of flavour and mass eigenstates. This requires masses for the neutrinos, which are not predicted by the SM (see section 1.1.3).

- Dark matter accounts for approximately 84% of the matter in the universe [28] and is predicted by different cosmological observations. Because it has no significant interaction with ordinary matter, it has not been observed directly, yet. Several new physics models provide particle candidates, the most prominent are supersymmetric models, where lightest stable particles are such candidates.

- The matter-antimatter asymmetry describes the observed excess of matter over antimatter in the universe. Although *CP*-violation is predicted by the quark flavour mixing with the CKM matrix, the SM does not predict sufficient large *CP*-violation to explain the asymmetry.

- The naturalness problem is known as the fact of many arbitrary constants in the SM. The fact of large differences e.g. the top quark has 10^5 times the mass of the up quark is considered to be unnatural.

- Grand Unified Theories (GUT) embed the three SM interactions of the $SU(3)_C \times SU(2)_L \times U(1)$ into one larger gauge symmetry group of e.g. $SU(5)$ or $SO(10)$. It can have one unified coupling constant at high scales at about 10^{16} GeV, combining strong, weak and electromagnetic forces. This can be achieved e.g. in the Minimal Supersymmetric Standard Model (MSSM) by adding a minimum number of additional supersymmetric partners to the SM particles.

- Gravity is not explained in the SM. The ultimate goal is a theory of everything (TOE), which fully consistently describes all forces of the GUT and the gravitational force. Quantum gravity aims for a theory of gravity according to the principles of quantum field theory.

Several new physics theories try to solve these problems and predict new particles or changed interaction strengths, which might be discovered by particle physics experiments. For instance, the study of flavour-changing neutral currents (FCNC) in proton-proton collisions can verify or exclude new physics models.

1.3.2. Flavour-changing neutral currents

Weak charged currents change the flavour of the interacting fermions as shown in section 1.1.2 for quarks. In contrast, flavour-changing neutral currents (FCNC) are not allowed at tree-level by the SM, neither in the electroweak (section 1.1.2) nor in the Higgs sector (section 1.1.3). However, higher order loop diagrams can introduce FCNC signatures, as for instance top quark decays to a Higgs boson and a lighter up-type quark ($t \rightarrow Hq$ with $q = u$ or c), via charged currents in the loop. This is illustrated in a Feynman diagram for this process in figure 1.9. The vertices of charged currents with a
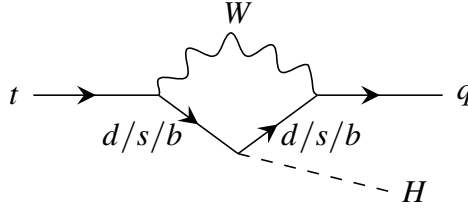
Figure 1.9.: Feynman diagram for the $t \rightarrow Hq$ decay in the SM with one loop.

W boson are proportional to the CKM matrix elements $\mathcal{V}$ (equation 1.18). Because there are two such vertices in the one loop diagram, the interaction terms are proportional to the product $\mathcal{V}_{tD}\mathcal{V}_{qD}^*$, where D can be any of the down-type quarks. Under the assumption of equal masses of the down-type quarks d, s and b the total interaction term becomes proportional to

$$\mathcal{V}_{td}\mathcal{V}_{qd}^* + \mathcal{V}_{ts}\mathcal{V}_{qs}^* + \mathcal{V}_{tb}\mathcal{V}_{qb}^* \qquad (1.37)$$

which is zero because of the CKM matrix unitarity. Since the masses of the down-type quarks are not equal, as given in figure 1.1, each term should in fact be multiplied by factors dependent on m_D^2/m_W^2 [29]. The theory of this suppression is known as GIM mechanism, named after Glashow, Iliopoulos and Maiani [30].

The branching ratio of the $t \rightarrow Hc$ decay in the SM is calculated to be $\mathcal{B} = 3 \times 10^{-15}$. The $t \rightarrow Hu$ decay is further suppressed by the ratio of CKM matrix elements $|\mathcal{V}_{ub}/\mathcal{V}_{cb}|^2 \approx 0.008$ [7, 29]. The smallness of this SM branching ratio makes it unobservable to any current and foreseen experiments. An observation would be a signature of new physics. Indeed, several models predict an enhancement of several orders of magnitude in FCNC top decay branching ratios, as illustrated in table 1.2. The largest branching ratio for the

Table 1.2.: Predicted branching ratios for FCNC $t \rightarrow Hq$ decays in the SM and several new physics models [7, 31].

	SM	2HDM	FP 2HDM	QS	MSSM	RPV	RS
$t \rightarrow Hc$	3×10^{-15}	2×10^{-3}	$\leq 10^{-5}$	4×10^{-5}	$\leq 10^{-5}$	$\leq 10^{-9}$	$\leq 10^{-4}$
$t \rightarrow Hu$	2×10^{-17}	6×10^{-6}	–	4×10^{-5}	$\leq 10^{-5}$	$\leq 10^{-9}$	–

$t \rightarrow Hc$ decay is expected for a generic model with two Higgs doublets (2HDM).

2HDMs have an extended scalar sector including two complex scalar doublets [32]. After the breaking of the electroweak symmetry, this leads to two predicted CP-even scalar Higgs bosons h and H, one CP-odd pseudo-scalar A and two charged Higgs bosons $H^\pm$. Six free parameters describe such models: four masses (m_h, m_H, m_A and $m_{H^\pm}$), the ratio of the two VEVs ($\tan\beta$) and the mixing angle of the two neutral CP-even Higgs bosons (α). Different types of 2HDMs are classified according to the coupling of the charged fermions to the Higgs doublets. In the Type-I and the Type-II models the up- and down-type quarks and the charged leptons couple only to one of the two doublets, while in a generic Type-III models all charged fermions couple to both doublets. Because of discrete symmetries in the Type-I and Type-II models only Type-III models can predict FCNC at tree-level.

In the latter the two Higgs doublets can be rotated, such that only one has a VEV and therefore generates the fermion masses like in the Yukawa Lagrangian in equation 1.29. The second Higgs doublet gives additional Yukawa Lagrangian terms with neutral flavour-changing couplings. For instance, the Lagrangian of the interaction between the up-type quarks and the second neutral Higgs field H_2^0 is

$$\mathcal{L}_{\text{FCNC},U} = -\frac{\tilde{\kappa}_{ab}^U}{\sqrt{2}} \bar{\tilde{U}}_L^a H_2^0 \tilde{U}_R^b + \text{h.c.} = -\frac{\kappa_{ab}^U}{\sqrt{2}} \bar{U}^a H_2^0 U^b \qquad (1.38)$$

where the matrix elements of $\kappa^U = V_L^U \tilde{\kappa}^U V_R^{U\dagger}$ are arbitrary. The Cheng-Sher ansatz [33] proposes, that the flavour-changing couplings are dependent on the fermion masses via $\kappa_{ab} \sim \frac{\sqrt{2}}{v}\sqrt{m_a m_b}$, allowing for large FCNC couplings for top quarks, but suppressing FCNC for light quarks to comply with existing experimental limits. This leads to an expected branching ratio of the $t \to Hc$ decay of $\mathcal{B}(t \to Hc) \approx 2 \times 10^{-3}$, consistent with the currently best observed 95% confidence level limit of $\mathcal{B}(t \to Hc) < 2.2 \times 10^{-3}$ in the ATLAS search with $H \to \gamma\gamma$ [8]. The $t \to Hu$ decay is further suppressed by the ratio of quark masses m_u/m_c and its branching ratio is $\mathcal{B}(t \to Hu) \approx 6 \times 10^{-5}$ [7, 34].

In flavour-preserving 2HDMs (FP 2HDM) the additional charged and neutral Higgs bosons can contribute in loops and significantly increase the branching ratios with respect to the SM expectation. The $t \to Hc$ decay branching ratio is expected to be $\mathcal{B}(t \to Hc) < 10^{-5}$ in these models [7, 35, 36].

Models with extra quark singlets (QS) can predict FCNC couplings at tree level, because of non-unitarity of the CKM matrix. Branching ratios of $\mathcal{B}(t \to Hq) < 4 \times 10^{-5}$ are expected [7].

In the minimal supersymmetric standard model (MSSM) [37] and non-minimal supersymmetric models with R parity violation (RPV) [38, 39] branching ratios are expected of up to $\mathcal{B} = 10^{-5}$ and 10^{-9}, respectively. Top FCNCs are predicted at one loop involving supersymmetric particles like the supersymmetric partners of the top quark and the gluon, the stop and the gluinos. The values for expected branching ratios are obtained for stop and gluino masses of 1 TeV.

In models with warped extra dimensions, so called Randall-Sundrum models (RS) [40, 41], e.g. composite Higgs boson models with only one Higgs doublet, branching ratios

of $\mathcal{B}(t \rightarrow Hc) < 10^{-4}$ are expected [42, 43].

Chapter 4 describes a search for flavour-changing $t \rightarrow Hq$ decays in multileptonic final states in proton-proton collisions, recorded by the ATLAS detector.

1.4. Conclusion

The SM is a very powerful theory which successfully describes the interactions and fundamental particles of particle physics. The search for $t\bar{t}H$ production is an important step towards validating this model. It has been shown, that the SM is not able to predict e.g. Dark Matter, neutrino masses or the matter-antimatter asymmetry. FCNC in top quark decays are an interesting portal, because they can appear in many different new physics models. The studies of such processes, presented in this doctoral thesis, are using proton-proton collision data from the ATLAS experiment at the LHC. The next chapter describes the detector and its performance of reconstructing the different SM particles.

2. The ATLAS detector at the LHC

The Large Hadron Collider (LHC) [44], located at the Swiss-French border near Geneva, and the associated detectors, such as the ATLAS [45] and the CMS [46], have been designed with the scientific goal to confirm the Standard Model of particle physics (SM) by precise cross-section and particle-property measurements and to search for new physics beyond the SM. One of the main achievements was the discovery of a new particle in July 2012 (during Run 1 of the LHC at a center-of-mass energy of $\sqrt{s} = 7$ and 8 TeV) with properties consistent of the predicted SM Higgs boson [1, 2].

The measurement of the Higgs boson couplings to the SM fermions is a particular interest of the currently ongoing Run 2 data-taking of proton-proton collisions at $\sqrt{s} = 13$ TeV. Due to the increase of $\sqrt{s}$ the $t\bar{t}H$ cross section is about four times as big as in Run 1 (see section 1.2.1). Because of the richness of the possible final state objects, a high-performance detector is needed, which can distinguish photons, electrons, muons, tau leptons and jets from quark hadronisation from each other.

As part of the ATLAS collaboration the present searches in this doctoral thesis have been done using proton-proton collision data recorded by the ATLAS detector. This chapter mainly contains the description of its set-up and performance of object reconstruction.

The LHC accelerator complex and physics programme is introduced in section 2.1. Section 2.2 describes the ATLAS detector and its sub-detectors. Because many different SM processes happen in proton-proton collisions, simulated events for signals and backgrounds are compared to the observed events in data to extract the signal significance. The generation of these events is described in section 2.3. Both in observed and simulated events the reconstruction of physics objects is an important ingredient to the analysis. Section 2.4 presents the performance of this reconstruction in Run 2 data. It includes the basic selection criteria of the physics objects, used in the searches for $t\bar{t}H$ (chapter 3) and flavour-changing $t \rightarrow Hq$ (chapter 4) production.

2.1. Large Hadron Collider

The LHC is a 27 kilometres long cyclotron that accelerates protons up to 99.9999991% of the light velocity. Two proton beams circulate in opposite directions and collide at the centre of the four experiments CMS, LHCb, ATLAS and ALICE. The design center-of-mass energy for proton-proton collisions is $\sqrt{s} = 14$ TeV and the current operation has

reached $\sqrt{s} = 13\,\text{TeV}$. Apart from protons the LHC is also able to collide heavy ions at a lower center-of-mass energy.

From 2010 to 2013 the first run of the LHC provided a total integrated luminosity of $L = 25\,\text{fb}^{-1}$ for proton-proton collisions with a center-of-mass energy up to 8 TeV in the experiments ATLAS and CMS.

After a break dedicated to several improvements of the detectors and the accelerator the first collisions at a center-of-mass energy of 13 TeV have been measured in May 2015. The goal for Run 2 is a total integrated luminosity of $150\,\text{fb}^{-1}$. This results in a significant increase in the available data samples for the measurement of particle physics phenomena.

2.1.1. Accelerator complex

The accelerator complex is sketched in figure 2.1. The protons are extracted by ionisation
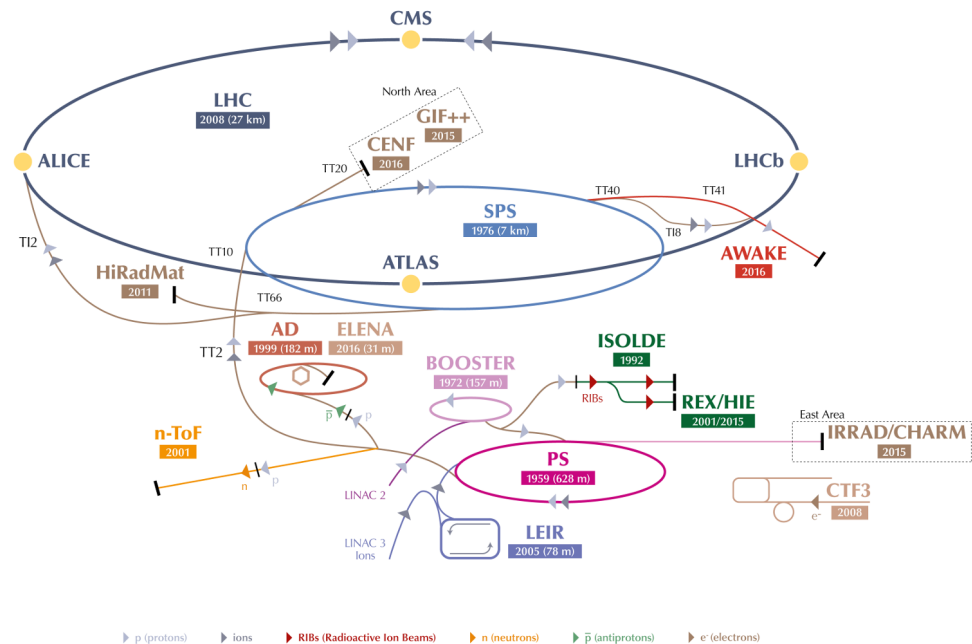
Figure 2.1.: CERN accelerator complex (© CERN [47]).

of hydrogen atoms from hydrogen gas. The linear accelerator LINAC 2 accelerates the protons to an energy of 50 MeV. The proton beam is then injected in the circular accelerator Proton Synchrotron Booster (BOOSTER) where an energy of 1.4 GeV is obtained. The protons are further sent to the Proton Synchrotron (PS) which is also able to accelerate ions coming from the LINAC 3 and LEIR (Low Energy Ion Ring) pre-accelerators. The protons leave the PS with an energy of 25 GeV and are accelerated to 450 GeV in the Super Proton Synchrotron (SPS). The beam of protons is finally injected in the LHC through two parallel rings in which the protons or ions circulate in opposite direction.

The circulation is maintained by a complex of 1,232 superconducting dipole magnets with lengths of 15 metres which bend the beams due to the Lorentz force with magnetic fields of up to 8.3 Tesla. 392 superconducting quadrupole magnets with lengths of five to seven metres focus the beams. The acceleration of the two beams to an energy of 6.5 TeV is obtained by 8 superconducting radio frequency (RF) cavities in each direction with oscillating electromagnetic fields at 400 MHz. The beam pipe is kept at a vacuum of 10^{-10} to 10^{-11} mbar and the whole system of magnets is cooled to 1.9 K ($-271.3\,°C$) to maintain superconductivity. A special insertion system of three quadrupole magnets is used in front of the four collision points to squeeze the particles together. This decreases the beam size by a factor of 12.5 from 0.2 millimetres down to 17 micrometres, which increases the probability of particle collisions.

One proton beam in the LHC main ring consists of up to 2,808 bunches with about 10^{11} protons each at the beginning of collisions. In Run 2 of the LHC the bunches are separated by 25 ns, which corresponds to a frequency of 40 MHz. The design and achieved parameters during the two runs of the LHC are given in table 2.1. The luminosity quan-

Table 2.1.: Parameters of the proton-proton collisions at the LHC [48–50]. *) The present searches do not use the 2017 data.

		Run 1			Run 2	
	design	2010/11	2012/13	2015	2016	2017*
beam energy [TeV]	7	3.5	4		6.5	
bunch spacing [ns]	25	50			25	
maximum number of bunches	2,808	1,380		2,244	2,200	2,556
protons per bunch [10^{11}]	1	1.3	1.5		1.15	
peak luminosity [$10^{33}\,cm^{-2}s^{-1}$]	10	3.5	7.7	5.1	14	21
integrated luminosity [fb^{-1}]	–	5.5	22.8	4.2	38.5	50.2
mean pile-up (ATLAS)	–	9.1	21	13.4	25.1	37.8

tifies the rate of collisions in an experiment. The instantaneous luminosity is defined as

$$\mathcal{L} = \frac{n_1 n_2 n_{\mathrm{b}} f_{\mathrm{rev}} F}{4\pi \sigma_x \sigma_y} \tag{2.1}$$

where n_1 and n_2 are the numbers of protons for the colliding bunches, n_{b} is the number of bunches in the beam, f_{rev} is the LHC beam revolution frequency, F is a geometric correction factor related to the crossing angle of the two bunches in the interaction point and σ_x and σ_y are the transverse beam dispersions assuming a Gaussian profile around the beam axis.

The integrated luminosity $L = \int \mathcal{L}\,dt$ quantifies the amount of collision data collected by an experiment. The number of events for a given physical process is $N = L\sigma\varepsilon$ where σ is the cross section and ε is the efficiency accounting for detector coverage, object reconstruction, selection and trigger efficiencies.

The peak instantaneous luminosity of the LHC has exceeded the design luminosity

by a factor of 2.1 in 2017. The total delivered integrated luminosity to the experiments ATLAS and CMS in Run 2 is 93 fb^{-1}. The analysis presented in this thesis uses the data from 2015 and 2016 with a delivered integrated luminosity of 43 fb^{-1}. In the ATLAS experiment a dataset with an integrated luminosity of $L = 36.1$ fb^{-1} passes the quality criteria chosen in the present analysis. The total integrated luminosity in dependence of the time in Run 2 until 2017 is shown in figure 2.2 (left).
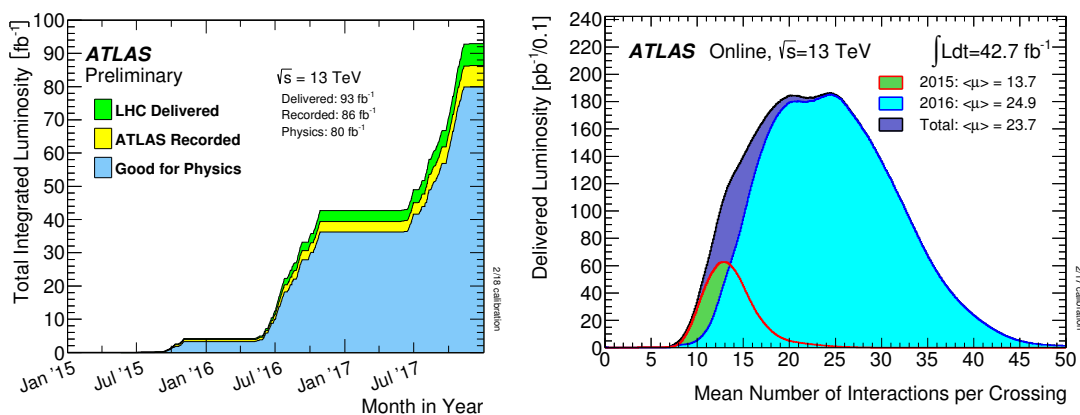
Figure 2.2.: Run 2 (left) total integrated luminosity (2015–2017) and (right) mean number of interactions per bunch crossing (2015–2016), measured by the ATLAS experiment [50].

In one bunch crossing several proton-proton pairs can interact simultaneously. This is quantified by the in-time pile-up

$$\mu = \frac{\mathcal{L}_\mathrm{b} \cdot \sigma_\mathrm{inel}}{f_\mathrm{rev}} \tag{2.2}$$

with the instantaneous per-bunch luminosity $\mathcal{L}_\mathrm{b}$, the inelastic proton-proton scatter cross section $\sigma_\mathrm{inel} = 80$ mb and $f_\mathrm{rev} = 11.245$ kHz at $\sqrt{s} = 13$ TeV. The distribution of the mean over all bunches $\langle \mu \rangle$ in 2015 and 2016 at the ATLAS experiment is shown in figure 2.2 (right). The mean pile-up, measured by the ATLAS experiment during data-taking at $\sqrt{s} = 13$ TeV in the years 2015–2016, is $\langle \mu \rangle = 23.7$. Out-of-time pile-up comes from interactions from bunch crossings prior or posterior to the analysed one.

2.1.2. Physics programme at the LHC

At the LHC particles collide in four different interaction points where the following experiments are located:

- The ATLAS (a toroidal LHC apparatus) [45] is a detector for studying a variety of particle physics phenomena in particle collisions at high energy. This includes precision measurements of the SM, search for exotic particles which could be dark matter candidates, extra dimensions, etc.

- The CMS (compact muon solenoid) [46] detector targets a similar physics programme as the ATLAS experiment. This allows to independently study the different phenomena and compare the results.

- The LHCb (LHC beauty) [51] detector studies CP violating phenomena in heavy flavour physics which indicate differences between matter and antimatter. In order to detect a maximum of beauty hadrons, it covers the small scattering angles and is situated on one side of the collision point only.

- The ALICE (a large ion collider experiment) [52] focuses on heavy ion collisions. It measures the dynamics and effects of strong interaction (QCD) of the quark-gluon plasma at high energy densities, which appear in heavy ion collisions.

- The TOTEM (total, elastic and diffractive cross-section measurement) [53] detectors measure protons from collisions at very small angles. It is the longest experiment at the LHC with a length of almost half a kilometre located in the forward and backward regions of the CMS detector.

- The LHCf (LHC forward) [54] experiment consists of two detectors at 140 metres in forward and backward direction of the interaction point of the ATLAS experiment measuring neutral particles at very small diffusion angles. This helps to constrain interaction models which describe high energy cosmic ray showers in the atmosphere of the earth.

2.2. ATLAS detector

With its length of 46 metres, its diameter of 25 metres and its weight of 7,000 tonnes the ATLAS is the largest particle detector at the LHC. It is located in a 100 metres deep underground cavern. A schematic overview of the ATLAS detector is shown in figure 2.3. It consists of several layers of detectors around the beams collision point. In the centre of the experiment bunches of protons collide and produce particles which go through these different detector layers. Each of these detectors is responsible for the measurement of a specific kind of particles. This is sketched in figure 2.4. Charged particles are bend by magnetic fields and their tracks are measured in the Inner Detector (ID). The Electromagnetic (EM) Calorimeter measures the EM showers of electrons and photons. Jets are showers of secondary particles, which are produced in hadronisation of quarks or gluons. They are reconstructed as many tracks in the ID and significant energy deposits in the EM and Hadronic Calorimeters. The muons are not stopped by the detectors and interact with the detectors as minimum ionising particles (MIPs). Their momenta are measured by the curvature of their tracks in magnetic fields using the ID and the muon spectrometer (MS). Because of the weak interaction with matter the neutrinos are not directly detectable. Their signature is a missing energy, which can be determined in the plane transverse to the beam axis because of the hermetic closure of the ATLAS detector.
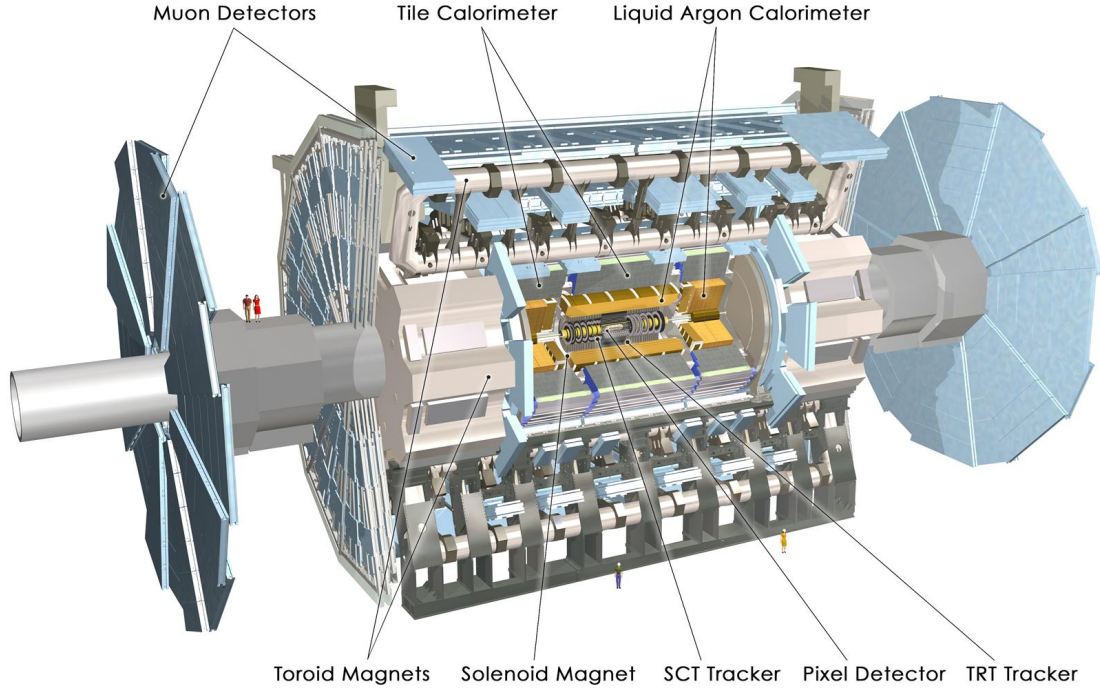
Figure 2.3.: ATLAS detector with the collision point in the centre and the different detectors around (© ATLAS Experiment, CERN).

The momenta of particles and energy deposits in the ATLAS detector are described by coordinates in a right-handed coordinate system with the origin at the interaction point in the centre. The *x* axis points to the centre of the LHC ring, the *y* axis points upwards and the *z* axis goes along the beam axis. The *x-y* plane is defined as the transverse plane. It is convenient to use the azimuthal angle ϕ in the transverse plane and the pseudorapidity η which is defined as

$$\eta = -\ln \tan \frac{\theta}{2} \tag{2.3}$$

with the polar angle θ between the positive *z*-axis and the particle direction. For massive objects like jets the rapidity

$$y = \frac{1}{2} \ln \frac{E+p_z}{E-p_z} \tag{2.4}$$

is used. Distances Δr between two particles in the (η, ϕ) plane are defined as

$$\Delta r = \sqrt{\Delta\phi^2 + \Delta\eta^2} \tag{2.5}$$

with the differences in pseudorapidity $\Delta\eta$ and in azimuthal angle $\Delta\phi$.

The transverse momentum p_{T} of a particle is defined by the projection of its momentum $\mathbf{p}$ on the transverse plane

$$p_{\mathrm{T}} = |\mathbf{p}| \sin \theta \tag{2.6}$$

using the polar angle θ.
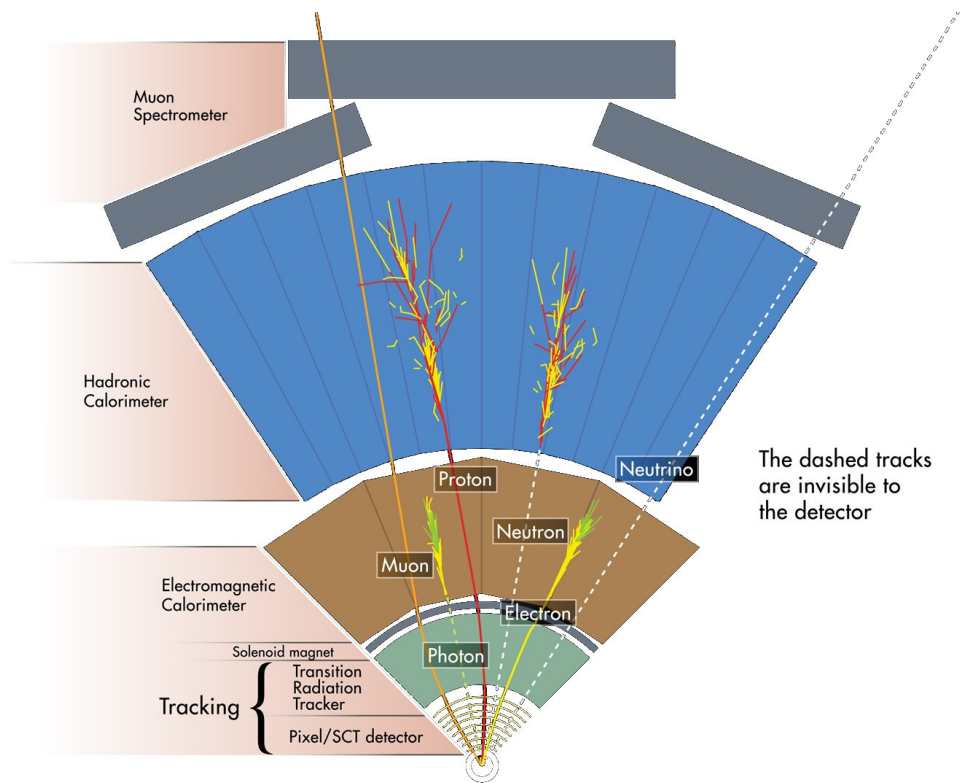
Figure 2.4.: Flow of different particles through the layers of the ATLAS detector (© ATLAS Experiment, CERN).

In the following subsections the different sub-detectors of the ATLAS detector are described.

2.2.1. Magnet system

Tracks of charged particles with a charge q are bend in a magnetic field $\mathbf{B}$ due to the Lorentz force $\mathbf{F} = q(\mathbf{v} \times \mathbf{B})$ where v is the velocity of the particle. The measurement of curved tracks allows to measure the momentum of charged particles. The ATLAS uses a system of superconducting magnet coils to provide strong magnetic fields mainly perpendicular to the particle trajectories. It consists of a central solenoid magnet inside the tile calorimeter with a magnetic field of 2 Tesla parallel to the beam axis, surrounded by toroid magnets as shown in figure 2.5 (left). The eight barrel and 16 end-cap toroids provide a magnetic field of 0.5 to 1 Tesla. Figure 2.5 (right) shows the barrel toroids during installation.

2.2.2. Inner detector

The inner detector consists of three sub-detectors, the pixel detector, the semiconductor tracker (SCT) and the transition radiation tracker (TRT) as shown in figure 2.6. Figure 2.7
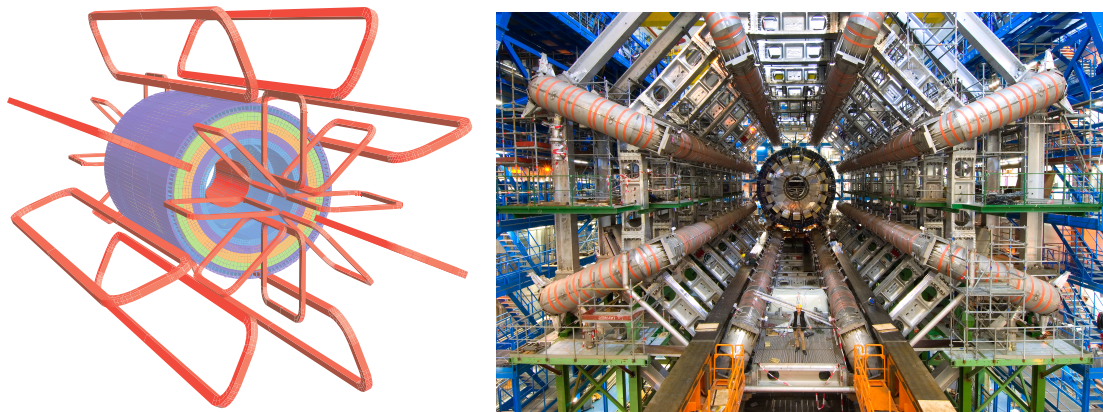
Figure 2.5.: ATLAS magnet system: (left) barrel and end-cap toroids in red and solenoid windings inside the tile calorimeter, modelled in four layers of different ferromagnetic properties [45] and (right) barrel toroids as seen during installation of the ATLAS (© CERN).
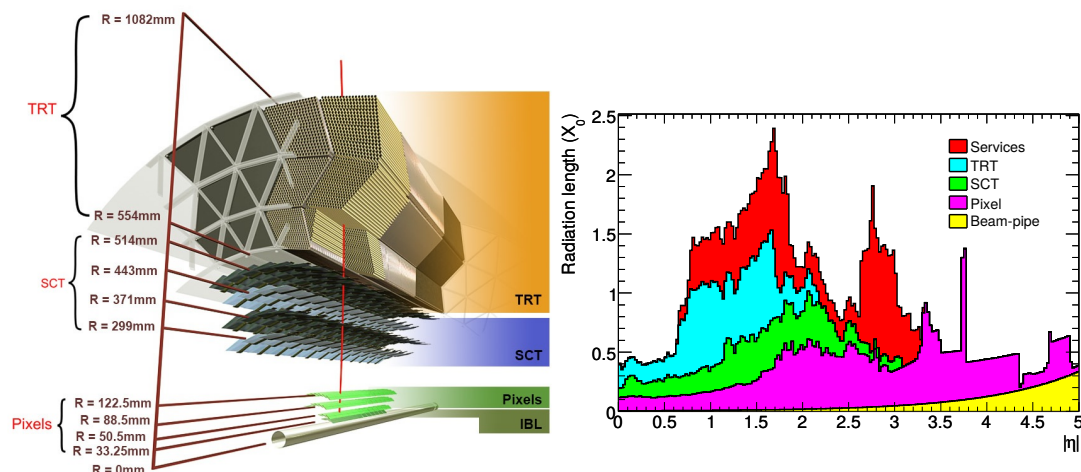
Figure 2.6.: ATLAS inner detector in the barrel region [55].

shows the detailed structure in a quarter view of the ATLAS in Run 1 of the LHC before addition of the insertable B-layer (IBL). It measures the charge, the direction and the momentum of charged particles with a pseudorapidity up to 2.5.

2.2.2.1. Pixel detector and insertable B-layer

The particles produced in the collision travel firstly through the pixel detectors. The innermost layer, the so called IBL, has been added to the pixel detector before start of Run 2 of the LHC. It is only 33.25 mm from the beam axis and consists of 224 modules with a total of six million pixels which are readout independently. The pixel detector consists of four cylindrical layers including the IBL in the barrel region and three disks in each of the two end-caps. The detailed parameters are given in table 2.2. The original
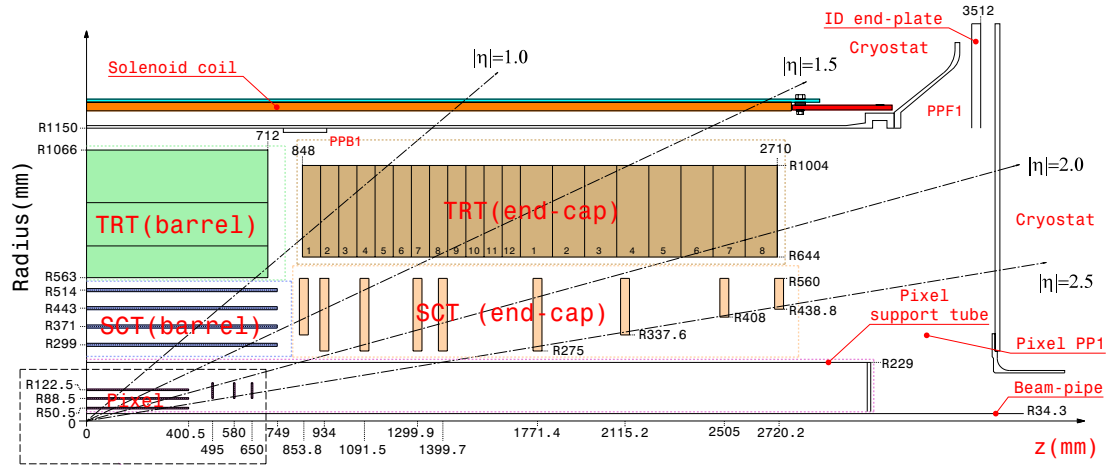
Figure 2.7.: ATLAS inner detector scheme [45].

Table 2.2.: Parameters of the ATLAS pixel detector. The pixel size and accuracy are given for $r \cdot \phi \times z$ and $r \cdot \phi \times r$ for the barrel layers and end-cap disks respectively.

	position [mm]	size [mm]	modules	pixels [10^6]	pixel size [µm^2]	accuracy [µm^2]
IBL	$r = 33.2$	$\|z\| < 332$	224	6.0	50×250	8×40
B-layer	$r = 50.5$	$\|z\| < 400.5$	286	13.2	50×400	14×115
layer 1	$r = 88.5$	$\|z\| < 400.5$	494	22.8	50×400	14×115
layer 2	$r = 122.5$	$\|z\| < 400.5$	676	31.2	50×400	14×115
disks	$\|z\| = 495, 580, 650$	$88.8 < r < 149.6$	6×48	13.2	50×400	14×115

pixel detector (without IBL) has in total 1,744 modules with about 80 million pixels. The accuracy of the track position measurement is given per module and reaches down to $\Delta(r \cdot \phi) = 8\,\mu\text{m}$ for the IBL.

2.2.2.2. Semiconductor tracker

The semiconductor tracker (SCT) consists of four cylindrical layers of silicon strips detectors in the barrel region at radii of 299–514 millimetres and two end-caps with nine planar disks each. It consists of 4,088 two-sided modules with 768 active microstrips on each silicon wafer spaced by 80 µm. Each strip is 12 centimetres long and is readout at both sides. This leads to an track position measurement accuracy of 17 µm vertical to the strips and 580 µm in the parallel direction. In total about 6.3 million channels are readout for the SCT. The detailed parameters are given in table 2.3.

Table 2.3.: Parameters of the ATLAS semiconductor tracker. The strip size and track position measurement accuracy are given for $r \cdot \phi \times z$ and $(r \cdot \phi \times r)$ for the barrel layers and end-cap disks respectively.

	position [mm]	size [mm]	modules	strips $[10^6]$	strip size $[\mu m^2]$	accuracy $[\mu m^2]$
layers	$r = 299 \ldots 514$	$|z| < 749$	2112	1.6	$80 \times 12,000$	17×580
disks	$|z| = 854 \ldots 2,720$	$275 < r < 560$	1976	1.5	$80 \times 12,000$	17×580

2.2.2.3. Transition radiation tracker

The TRT is the outermost part of the inner detector. Its purpose is the precise measurement of particle momenta at high radii and the identification of electrons. It consists of about 300,000 drift tubes (straws) of four millimetres diameter with a gold-plated tungsten wire in the centre and filled with a gas mixture of 70% Xenon, 27% carbon dioxide and 3% oxygen. The transition radiation material, surrounding the straws is polypropylene fibres. The amount of transition radiation is inverse proportional to the mass of the passing particle. This allows to distinguish e.g. electrons from pions. The track position measurement accuracy of the TRT is $130 \, \mu m$ in $r \cdot \phi$.

2.2.3. Calorimeters

The ATLAS calorimeter system identifies charged and neutral particles and measures their energies and positions. It consists of several calorimeters as shown in figure 2.8. When a particle passes through a calorimeter it looses its energy by interaction with
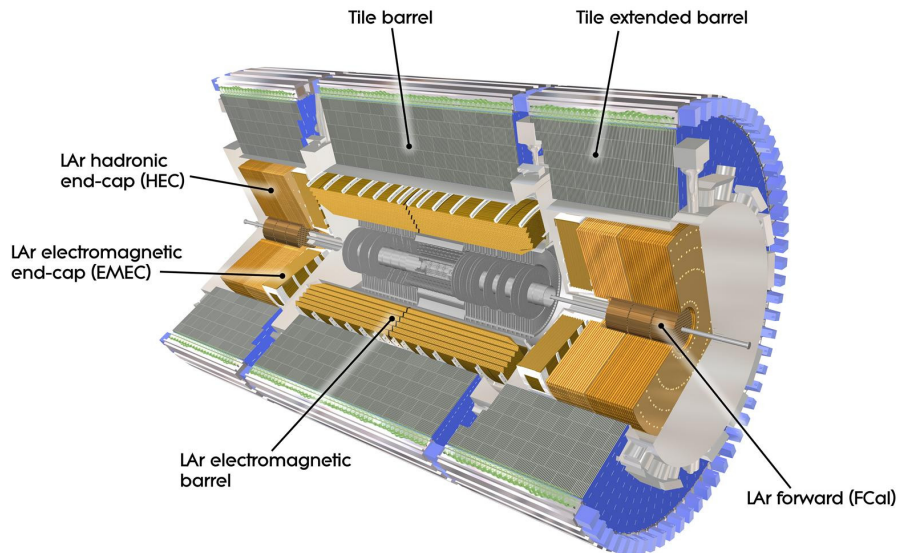

Figure 2.8.: ATLAS calorimeter system (© ATLAS Experiment, CERN).

the absorber material. Electrons and photons are measured in electromagnetic (EM)

calorimeters. The quark and gluons emerging from the primary collisions give rise to jets, composed predominantly of hadrons that are detected by both the EM and the hadronic calorimeters. Because of limited bandwidth not all proton-proton collisions can be recorded. An advanced trigger system uses coarse inputs from the calorimeters (and the muon spectrometer) to the first level of event selection (see section 2.2.5).

2.2.3.1. Liquid argon calorimeters

The Liquid Argon Calorimeter (LAr) plays a crucial role in the reconstruction of electrons, photons, jets and missing transverse energy. Particles interact with the absorber plates and create electromagnetic showers of electrons and photons. By ionisation of the liquid argon electrons are liberated and are collected by the read-out electrodes with a signal proportional to the energy of the primary particle.

The LAr Calorimeter is a sampling calorimeter with liquid argon as the active medium. It is radiation-resistant and has a stable response over time. In the electromagnetic barrel and end-caps (EMB and EMEC) it consists of accordion shaped lead absorbers and copper/kapton electrodes, which provides a full coverage of the azimuthal angle space. The barrel part covers a pseudorapidity range of $|\eta| < 1.475$ and the two end-cap components cover $1.375 < |\eta| < 3.2$.

The hadronic end-caps (HEC) use copper absorbers and copper/kapton electrodes and cover $1.5 < |\eta| < 3.2$. The forward calorimeter (FCAL) extends the pseudorapidity coverage to $3.1 < |\eta| < 4.9$. Its absorbers are made of copper in the electromagnetic section and tungsten in the hadronic section.

Photon and electron momenta are measured precisely due to a fine granularity and four separate layers, which is shown for a part of the EMB at $\eta = 0$ in figure 2.9. E.g. in the layer 1 (front layer) the strip cells have a granularity of $\Delta\eta \times \Delta\phi = 0.025/8 \times 0.1$ for $\eta < 1.4$. This allows to distinguish isolated photons from collimated multiple photons from neutral meson decays and is crucial in searches with final state photons like in the Higgs boson decay to a pair of photons ($H \rightarrow \gamma\gamma$). The typical energy resolution for photons and electrons in the EMB is about 1–2% [45].

The LAr Calorimeter has a total of 182,000 readout channels, collected in 1,600 front-end boards (FEBs), where the triangular ionisation signal pulses from the calorimeter cells are amplified, shaped at three different gains for a big dynamic range and sampled at 40 MHz. 200 readout driver boards (RODs) at the back-end receive the digital signals from the FEBs via optical links upon a level 1 trigger request. Additionally analog sums are made up of cell signals over the different layers in the layer sum boards (LSBs). They are combined in the tower builder boards (TBBs) with a course granularity of $\Delta\eta \times \Delta\phi = 0.1 \times 0.1$ and used as input to the level 1 trigger system.

Upgrades of the LHC and its experiments are foreseen for 2019–2020 and beyond to increase the statistics of proton-proton collisions. Chapter 5 describes the planned upgrades for the LAr Calorimeter readout.
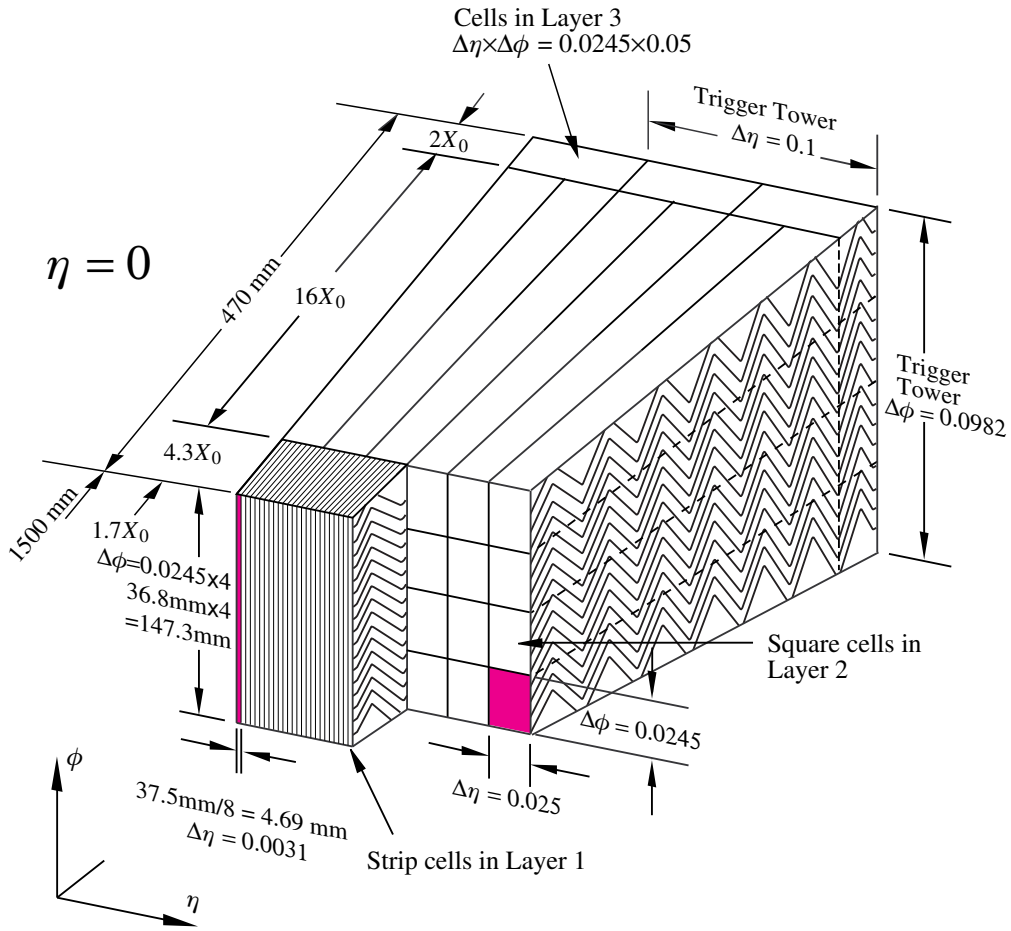
Figure 2.9.: LAr Calorimeter cells in the barrel region with their granularities $\Delta\eta \times \Delta\phi$ in three of four layers. The pre-sampler in front of the front layer (layer 1) is not shown [45].

2.2.3.2. Tile calorimeter

The tile calorimeter surrounds the electromagnetic calorimeter and measures the positions and energies of hadrons that are not fully stopped by the LAr Calorimeter. It uses steel as absorber and plastic scintillator as active medium. It covers a region of $|\eta| < 1.7$ by a barrel and two extended barrels. It has about 10,000 readout channels. Its energy resolution, measured in test beam data, ranges from less than 14% for pions with $p_T = 20\,\text{GeV}$ to less than 7% for pions with $p_T > 180\,\text{GeV}$ [56].

2.2.4. Muon spectrometer

Muons are the only detectable known SM particles that can traverse all the calorimeter absorbers. Their momenta and positions are measured in the Muon Spectrometer (MS) which is the outer-most layer of the detector. Its four different sub-detectors and bending

magnets are shown in figure 2.10. It uses the deflection of muon tracks by the super-
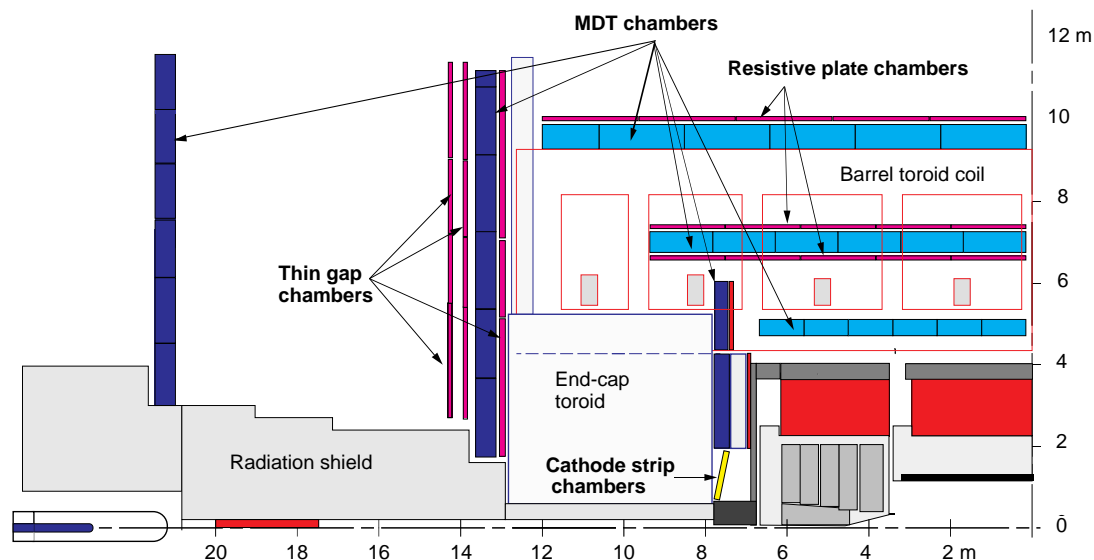
Figure 2.10.: Quarter of the ATLAS Muon Spectrometer in the *r-z* plane (derivative of [57]/CC BY 3.0).

conducting air-core toroid magnets. The large barrel toroids providing a bending power of 1.5 to 5.5 Tm bend muons with an $|\eta| < 1.4$. The end-cap magnets bend them for $1.6 < |\eta| < 2.7$ with 1 to 7.5 Tm. In the so called transition region of $1.4 < |\eta| < 1.6$ both magnets contribute to the bending.

The purpose of the Monitored Drift Tubes (MDTs) is the precise measurement of the track curvature and momentum of muons with a pseudorapidity of $|\eta| < 2.7$. It has a total of 354,000 readout channels. Because of its limited counting rate of 150 Hz/cm^2 and higher track multiplicities close to the beam axis, the inner-most layer of the end-caps uses Cathode Strip Chambers (CSCs) in the region of $2.0 < |\eta| < 2.7$. They have counting rates up to 1,000 Hz/cm^2 and a better time resolution than the MDTs. The CSC has 31,000 readout channels. The MDT (CSC) uses a gas mixture of 97% (80%) argon and 3% (20%) carbon dioxide. The obtained accuracies are 35 μm and 40 μm in the η direction for MDTs and CSCs, respectively. A total of 385,000 channels is readout from this sub-detectors for the track measurement.

Two more systems with a coarser granularity are used for a fast triggering of muon tracks up to $|\eta| < 2.4$. They provide additional information in the ϕ-plane, where the particle tracks are bend less. The Resistive Plate Chambers (RPCs) used in the barrel region up to $|\eta| < 1.05$ have a timing resolution of 1.5 ns, which is sufficient small to match tracks to the corresponding bunch crossing. They are filled with gas and consist of parallel electrode plates in a distance of 2 mm, providing an electric field of 4.9 kV/mm which leads to the amplification of the ionising track signals. The Thin Gap Chambers (TGCs) cover the η range of $1.05 < |\eta| < 2.7$ in the end-caps. They are multi-wire proportional chambers with copper wires oriented perpendicular to carbon strips. They

provide a timing resolution of 4 ns. The RPCs and TGCs are readout by 373,000 and 318,000 channels respectively.

The parameters of the MS are summarised in table 2.4.

Table 2.4.: Parameters of the ATLAS muon spectrometer (at Run 2).

	coverage in $|\eta|$	resolution in			number of	
		η-dir.	ϕ-dir.	t	chambers	channels
MDT	< 2.7	35 μm	–	–	1150	354,000
CSC	$[2.0, 2.7]$	40 μm	5 mm	7 ns	32	31,000
RPC	< 1.05	10 mm	10 mm	1.5 ns	606	373,000
TGC	$[1.05, 2.7]$	2–6 mm	3–7 mm	4 ns	3588	318,000

2.2.5. Trigger system

The high instantaneous luminosity of the LHC and the limited bandwidth and storage requires to quickly select and save only interesting collision events.

A two-step trigger system is used by the ATLAS data acquisition to collect up to 1,500 interesting collision events per second. The first level trigger (L1) selects events based on information from the calorimeters and the muon spectrometers with a limited bandwidth of 100 kHz and a fixed latency of 2.5 μs. The information from the calorimeters is reduced at this step by summing signals from adjacent cells, yielding a coarser granularity available for the L1 algorithms. Those algorithms search for particles with high transverse momenta, large missing transverse energy (E_T^{miss}) or large total transverse energy. The decision criteria include E_T or p_T thresholds and multiplicities of physics objects like electrons, muons, jets and hadronically decaying tau leptons (τ_{had}). The L1 is based on hardware: logical electronics perform the trigger decision with low latency.

The high level trigger (HLT) further decreases the event rate to about 600–1,500 Hz using inputs from the whole detector with full granularity. It uses multivariate analysis techniques and is implemented in a software framework running on a dedicated computer farm. Its latency is about 0.2 seconds. In Run 1 the HLT was split in second level (L2) trigger with a output event rate of 2–3 kHz and an event filter (EF) which made the final decision with a rate of 300–400 Hz, while for Run 2 the two levels were merged.

The HLT provides trigger streams which trigger on different event topologies designed to collect classes of physics processes. The present analysis uses triggers with one or two electrons or muons with different minimum transverse momenta.

2.3. Event simulation

The event simulation is an important ingredient to the measurement of the properties of physics processes in proton-proton collisions. The Monte Carlo (MC) simulation

uses theoretical and experimental predictions of probability density functions for physics quantities in the generation of events from random numbers. To compare the prediction of simulated events with observed data events, the detector response has to be modelled with high precision. The reconstruction of the physics objects like tracks, calorimeter clusters, etc. is done with the same reconstruction framework for both simulated and data samples. It uses the digitised information of the hits or energy deposits in the sub-detectors.

2.3.1. Event generation

The proton-proton collisions at the LHC involve physics processes at very different energy scales: the hard scattering involving the proton constituents, the parton showering and the hadronisation up to stable particles, which then travel through the detectors. This development is illustrated in figure 2.11.
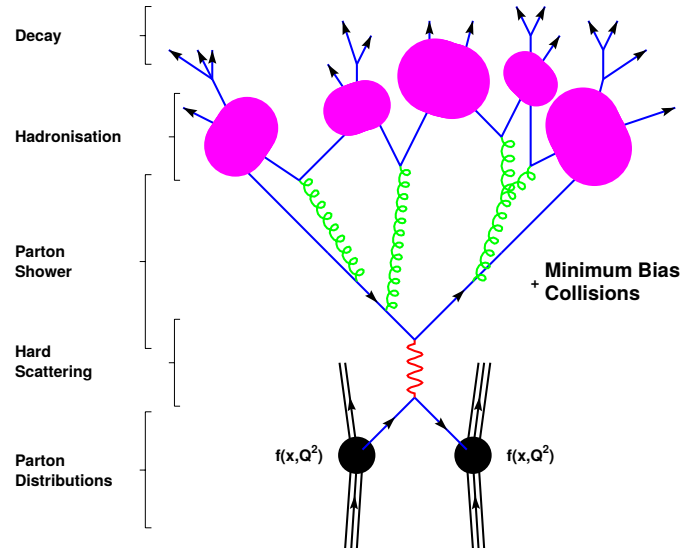
Figure 2.11.: Event generation of a proton-proton collision event (derivative of [58]/CC BY 4.0).

The event generators describe the following steps:

- The proton's constitution cannot be calculated by a perturbative QCD in the SM with sufficient precision. Therefore, the simulation of the momenta of the partons uses parton distribution functions (PDFs), which are measured in deep-inelastic scattering and hadron collider experiments. The PDFs used in the present analysis are NNPDF 2.3 LO [59], NNPDF 3.0 NLO [60], CTEQ6L1 [61, 62] and CT10 [63].

- The kinematic properties of the partons are then used in the matrix element (ME) calculation, which evaluates the cross section of the parton hard-scattering process

using a perturbative approach. The parton-level generators used in the present analysis are MadGraph5_aMC@NLO [64], Powheg-Box [65] and Sherpa [66–70].

- The involved partons can radiate gluons and photons via QED and QCD. The repetitive process of parton radiation and gluon decays to other gluons or pairs of quarks is the parton showering. Both initial state and final state radiation (ISR and FSR) change the event kinematics used in the ME calculation.

- Because of the colour confinement the partons form colourless hadrons at non-perturbative energy scales, which is called hadronisation. The simulation of the hadronisation and hadron decays relies on phenomenological models matched to data distributions of experimental measurements. The present analysis uses Pythia [71, 72] and Sherpa and Herwig++ [73] for the simulation of parton showering and hadronisation.

The detailed list of samples used in the present searches for $t\bar{t}H$ and flavour-changing $t \to Hq$ production is given in appendix A.

2.3.2. Detector simulation

After the event generation the interaction of the stable particles with the ATLAS detector material is simulated [74]. The full simulation uses the Geant 4 package [75] with implemented ATLAS detector geometry. Afterwards, the responses in the sub-detectors are digitised. Some physics studies use fast simulation, designed to reproduce the main features of the detector with sufficient precision in a considerably shorter computation time than for full simulation [76]. In this case the detector description is simplified and the electromagnetic showers in the calorimeters are pre-simulated, which allows to reduce the simulation time by a factor of more than ten.

The present search for $t\bar{t}H$ uses mainly full simulation samples, because high precision is necessary. Fast simulation samples are used for some templates of theoretical uncertainties, which are obtained comparing alternative samples with different event generators. Also the signal samples of the present search for new physics use the fast simulation.

2.4. Event reconstruction

This section introduces the algorithms to reconstruct interaction vertices, particle tracks and energy clusters in the calorimeters, which are used to identify physics objects as electrons, photons, muons, jets, hadronically decaying tau leptons and missing transverse momentum.

2.4.1. Tracks and vertices in the inner detector

Charged particle's trajectories close to the beam line are bent by the solenoid magnet and measured in the ID. Particles with $p_T > 400\,\text{MeV}$ and $|\eta| < 2.5$ are reconstructed using a pattern recognition algorithm applied to the hits in the pixel detectors and the first layer of the SCT. The hits are used with space and timing information to form track seeds, which are then extended using the whole SCT information. The track candidates are then fitted with global χ^2 [77] and Kalman-filter [78] techniques and quality cuts are applied to reject fakes. Then they are extrapolated into the TRT and re-fitted with the information of the whole ID. Unused track segments in the TRT are extrapolated back into the pixel detectors and the SCT for the improved measurement of secondary tracks from long-living particle decays or photon conversions.

The parameters used to describe the track helices are illustrated in figure 2.12 (left). The closest point of the track to the beam axis (z-axis) is parametrised by the transverse
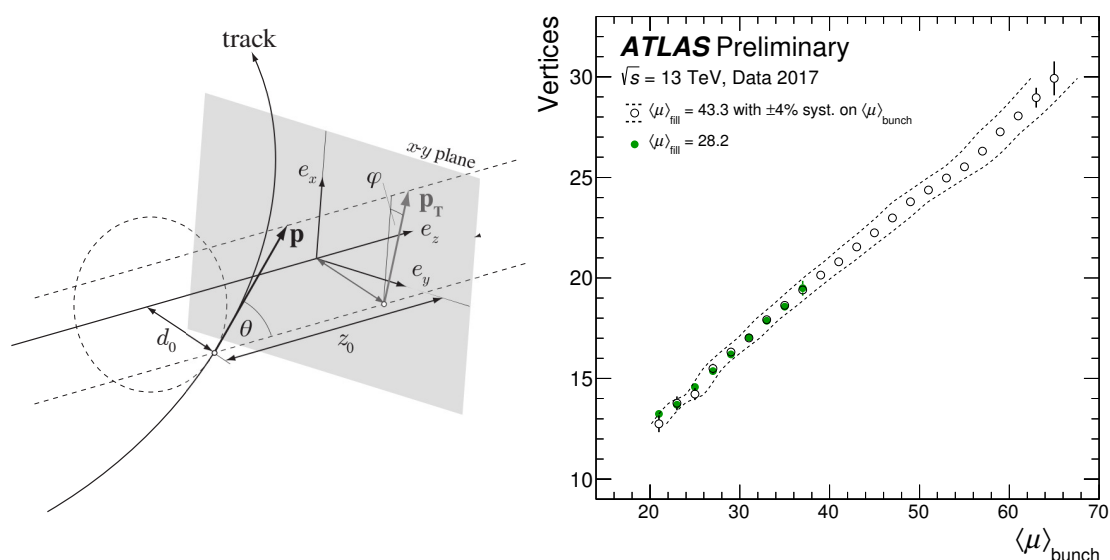
Figure 2.12.: (Left) parameters of the helix tracks in the inner detector [79] and (right) number of reconstructed primary vertices in dependency of the mean number of interactions per bunch crossing $\langle \mu \rangle$ from two high $\langle \mu \rangle$ fills in 2017 [80].

impact parameter (IP) d_0, which is the distance to the beam axis, and the longitudinal IP z_0, which is the distance of the transverse planes of the closest point and the primary vertex (PV) or the coordinate origin if the PV is not yet defined. The angles θ and ϕ are the polar and azimuthal angles respectively. The ratio of charge over momentum magnitude is also used in the algorithm.

Finally, primary and secondary vertices are calculated using the reconstructed tracks. Because of the pile-up there are usually several PVs in an event. Figure 2.12 (right) shows the number of reconstructed PVs as a function of $\langle \mu \rangle$ in two LHC fills with

$\langle\mu\rangle = 43.3$ and $\langle\mu\rangle = 28.2$. In the present analysis the actual PV is chosen by maximising the sum of squared p_T of the associated tracks with $p_T > 400$ MeV.

The IP resolution is shown in figure 2.13 for tracks with $|\eta| < 0.2$ as a function of the track p_T. Its improvement from 2012 (Run 1) to 2015 (Run 2) comes mainly from the
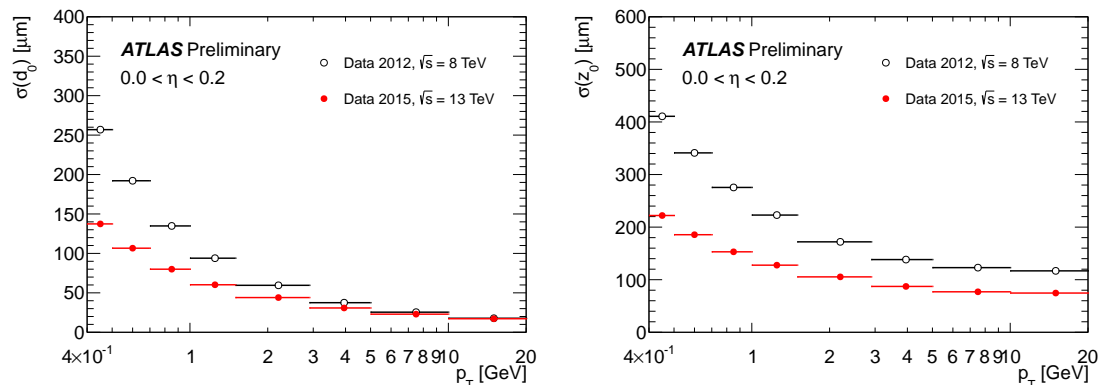
Figure 2.13.: (Left) transverse and (right) longitudinal IP resolution in the inner detector for tracks with $0.0 < |\eta| < 0.2$ in dependency on the track p_T, comparing data from 2012 and 2015 (including the IBL) [81].

additional information provided by the IBL. The transverse (longitudinal) IP resolution ranges from 150 (220) μm at low track p_T to 20 (80) μm at high p_T.

2.4.2. Electrons and photons

The energy deposits in the EM calorimeters are the key ingredient in the measurement of electrons and photons. Electrons leave curved tracks in the ID which distinguishes them from photons. This section concentrates on electrons [82], because photons are not considered in the present analysis. A schematic view of the electron path through the ATLAS sub-detectors is shown in figure 2.14.

2.4.2.1. Electron and photon reconstruction

The reconstruction of both the electrons and the photons in the calorimeter uses seeds from a clustering algorithm [83] in a sliding window with a size of 5×5 cells in units of $\Delta\eta \times \Delta\phi = 0.025 \times 0.0245$, corresponding to the cell size in the middle layer of the EMB. In the barrel the EM clusters are build around the seeds in towers of size 3×7 for electrons and converted photons and 3×5 for unconverted photons. The bigger size in ϕ for electrons and converted photons, which are actually produced pairs of electrons and positrons, is due to the electron track bending in ϕ direction by the magnetic field. In the end-caps all EM clusters are build with a size of 5×5. The size of the EM clusters is optimised to be large enough to contain most of the energy deposits and to reduce the noise from too large cell numbers. The efficiency of the clustering increases with the
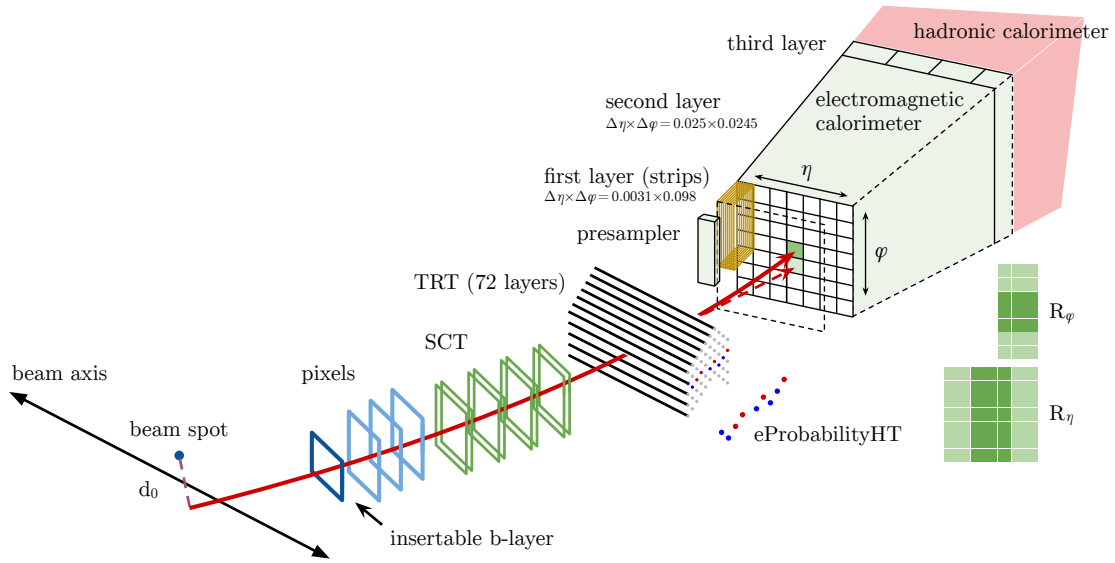
Figure 2.14.: Electron path through the sub-detectors [82].

particle's transverse energy (E_{T}) from about 95% at $E_{\mathrm{T}} = 7\,\mathrm{GeV}$ to more than 99% at $E_{\mathrm{T}} > 15\,\mathrm{GeV}$.

Tracks are seeded by pattern recognition from at least three hits in the pixel detectors or SCT. The standard tracking algorithm, assuming a pion hypothesis for the energy loss for the interaction with the detector material, is extended to allow bremsstrahlung with an energy loss of up to 30% at each point of interaction. If the χ^2 fit to pion hypothesis fails, the extended electron hypothesis is used.

A loose matching of EM clusters to the obtained tracks in the ID uses the distance Δr of the extrapolated track and the cluster centre in the middle layer of the EM calorimeter. If such a matching is found, the particles can be electrons or converted photons. An optimised Gaussian Sum Filter-based model for bremsstrahlung [84] is used to refit the electrons tracks and improve the precision on IPs. Finally, multivariate techniques are used on simulated electrons to calibrate the energy of the clusters [85].

The electron reconstruction efficiency is defined as the ratio of the number of reconstructed electrons over the number of EM clusters. It is measured in a sample of $Z \rightarrow ee$ decays for $E_{\mathrm{T}} > 15\,\mathrm{GeV}$ and $J/\psi \rightarrow ee$ decays for $7\,\mathrm{GeV} < E_{\mathrm{T}} < 20\,\mathrm{GeV}$ using a tag-and-probe method [82]. Figure 2.15 shows the electron reconstruction efficiency in $Z \rightarrow ee$ decays in proton-proton collision data from 2017. It ranges from 98% for low E_{T} to more than 99% for $E_{\mathrm{T}} > 80\,\mathrm{GeV}$. The crack region of the EM calorimeter with lower reconstruction efficiency is excluded in the present analysis. The difference of data to MC simulation is taken into account as a weight on simulated events.

Figure 2.15.: Electron reconstruction efficiency, measured in $Z \to ee$ decays of 2017 data, in dependency of (left) the transverse energy and (right) the pseudo-rapidity [86].

2.4.2.2. Electron identification

The electron identification uses a likelihood-based (LH) technique to distinguish signal-like electron candidates from jets or converted photons. It uses discriminant variables from the EM cluster and track measurement information. In Run 2 the addition of the IBL improves the discrimination of converted photons, which can have secondary indices close to the beam axis. Three LH operation points are given for the electron identification with increasing background rejection: loose, medium and tight.

The electron identification efficiency is measured with respect to reconstructed electrons in the same way as the reconstruction efficiency. Its measurement in 2017 data is shown in figure 2.16 for the three LH working points. The difference of the data versus the MC simulation is mainly due to mis-modelling of electron showers in the EM calorimeter by the GEANT 4 [75] simulation. In the analysis it is taken into account by re-weighting the simulated events by the ratios of data over MC.

2.4.2.3. Electron isolation

To further suppress backgrounds from jets or electrons from hadron decays, a loose isolation requirement with a flat isolation efficiency of 98% in electron transverse energy E_T and pseudorapidity is used for most of the electrons in the present analysis. Two isolation variables are used with a flat isolation efficiency of 99% both. Figure 2.17 shows their distributions for electrons from $Z \to ee$ decays at a tight identification working point.

The calorimetric isolation variable is the ratio $E_T^{cone0.2}/E_T$, where $E_T^{cone0.2}$ is the sum of all transverse energies of topological clusters in a cone of $\Delta r < 0.2$ around the electron cluster excluding the region of $\Delta\eta \times \Delta\phi = 0.125 \times 0.175$ around the electron. The
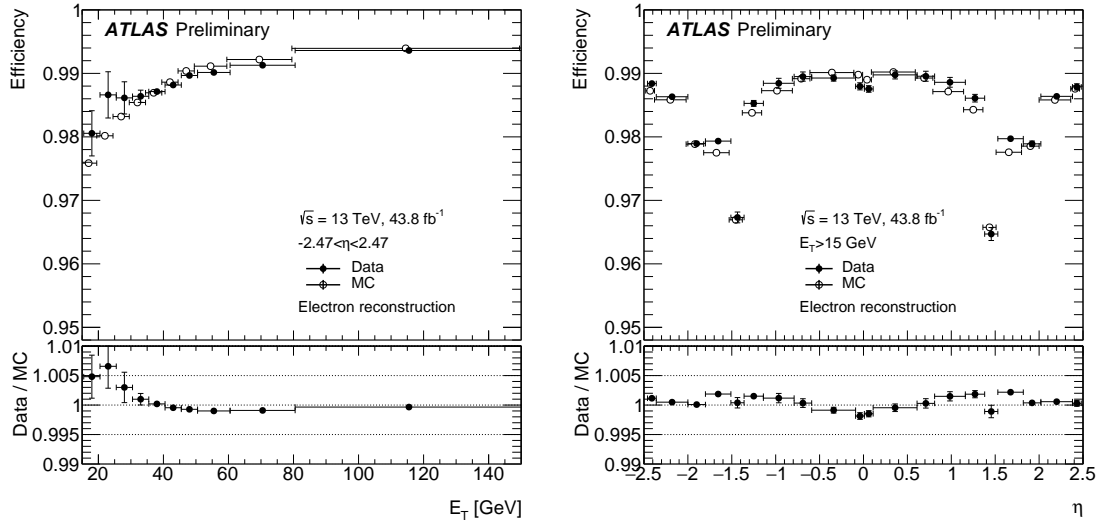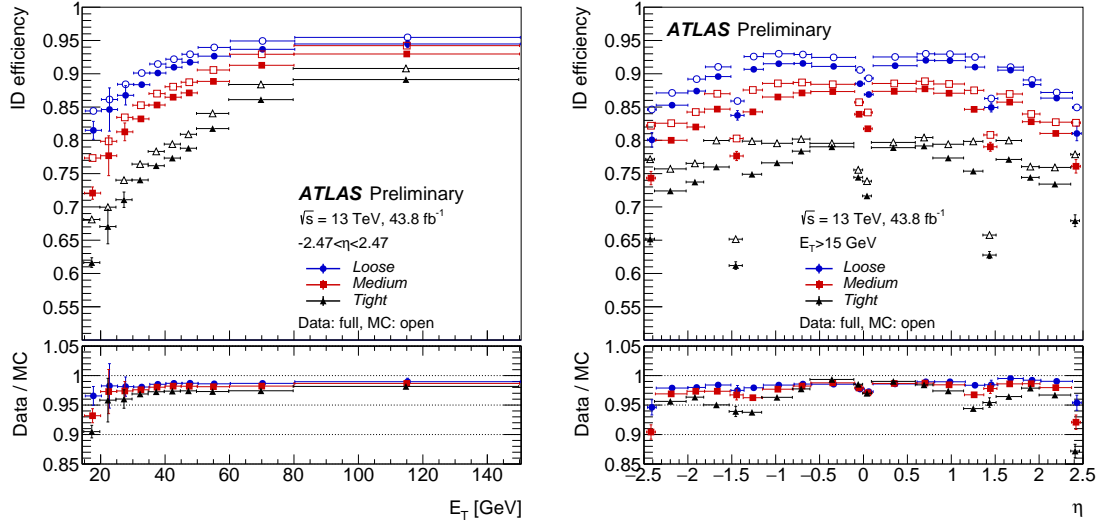
Figure 2.16.: Electron identification efficiency, measured in $Z \to ee$ decays of 2017 data, in dependency of (left) the transverse energy and (right) the pseudorapidity [86].

Figure 2.17.: Distributions of (left) the calorimetric and (right) the tracking isolation variable for electrons in $Z \to ee$ decays [82].

tracking isolation variable is the ratio $p_T^{\text{varcone0.2}}/E_T$, where $p_T^{\text{varcone0.2}}$ is the sum of all transverse momenta of good-quality tracks, excluding the electron track, in a variable cone size of $\Delta r < \min(0.2, 10\,\text{GeV}/E_T)$.

2.4.3. Muons

Muons are the only detectable SM particles which travel through the whole detector. Their reconstruction uses information from the ID, the MS and the calorimeters [87]. Because the present analysis uses only muons with $p_T > 10\,\text{GeV}$ and $|\eta| < 2.5$ [4], the following description excludes muons in the very forward region of $|\eta| > 2.5$.

2.4.3.1. Muon reconstruction and identification

The muon trajectories are bent by the magnetic fields of the solenoid and the toroid magnets. Their tracks in the ID and the MS are reconstructed independently and then combined in a global fit.

In the MS hit patterns of trajectories in each MDT and nearby RPCs and TGCs are used to build segments from a fit to a straight line. In the CSC a combinatorial search is used to build the segments. MS muon tracks are reconstructed by a combinatorial search, using at least two segments from different layers, except for the barrel-end-cap transition region, where one segment is sufficient. A global χ^2 fit of all hits in the segments associated to the track finds the best muon candidates.

These candidates from the MS are then used in a combined re-fit using the tracks found in the ID.

Because of the limited coverage of the MS at $|\eta| < 0.1$ the energy deposits in the calorimeters are used here, according to the muon's minimum-ionisation.

To reduce the number of fake muons from pion or kaon decays, the muon identification uses quality cuts on differences in MS and ID p_T measurements, normalised χ^2 of the combined track fit and several hit multiplicities in the ID sub-detectors. Muons are identified at four different working points: loose, medium, tight and high-p_T.

Like for electrons, the muon reconstruction and identification efficiency is obtained by a tag-and-probe method with $Z \to \mu\mu$ decays for muon's $p_T > 10\,\text{GeV}$ and $J/\psi \to \mu\mu$ decays for $5\,\text{GeV} < p_T < 15\,\text{GeV}$. Figure 2.18 shows its distribution in proton-proton collisions for $Z \to \mu\mu$ decays in proton-proton collisions of 2016 in dependency of p_T and η. The reconstruction efficiency is almost flat at 99% for $p_T > 10\,\text{GeV}$ and 0.1
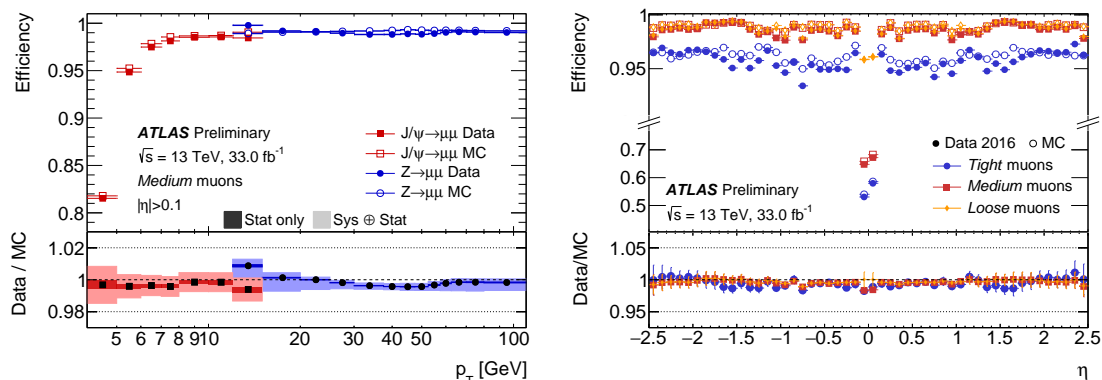
Figure 2.18.: Muon reconstruction efficiency measured in 2016 data (left) in dependency of transverse momentum for the medium identification working point with $|\eta| > 0.1$ and (right) in dependency of the pseudorapidity for different identification working points with $p_T > 10\,\text{GeV}$ from $Z \to \mu\mu$ decays [88].

$< |\eta| < 2.5$. In the of limited MS coverage ($|\eta| < 0.1$) the observed efficiency is about 96%. The differences of data to MC simulation are at 1% level and the ratio is taken into account in the present analysis as additional weights to the simulated events.

2.4.3.2. Muon isolation

Like in the case of electrons cuts on two isolation variables, the calorimetric and the tracking one, are used. Their distributions are shown in figure 2.19 for muons from $Z \to \mu\mu$ decays.
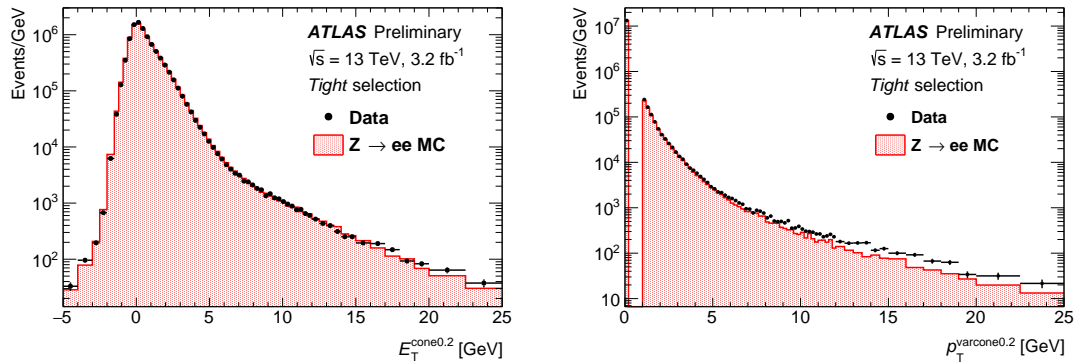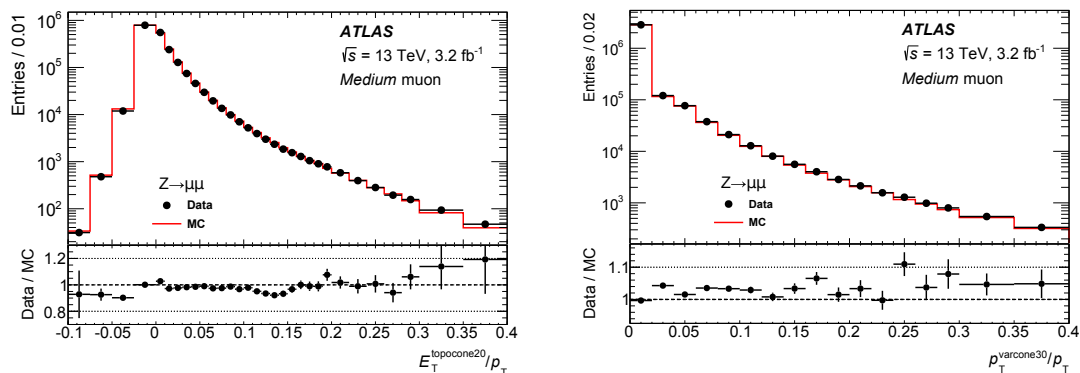

Figure 2.19.: Distributions of (left) the calorimetric and (right) the tracking isolation variable for muons in $Z \to \mu\mu$ decays [87].

The calorimetric isolation variable $E_{\mathrm{T}}^{\mathrm{topocone20}}/p_{\mathrm{T}}$ is the same as for electrons in a cone of $\Delta r < 0.2$ around the muon track, but excluding here the self-contribution of the muon ionisation in the calorimeter. Also the tracking isolation variable $p_{\mathrm{T}}^{\mathrm{varcone30}}/p_{\mathrm{T}}$ is defined the same as for electrons, but for muons a maximum variable cone size of 0.3 instead of 0.2 is used.

2.4.4. Jets

Quarks and gluons hadronise into jets of collimated hadrons, a phenomenon explained in QCD by the colour confinement. The signature of jets in the detector are energy clusters in the calorimeters, partially associated with tracks in the ID concentrated in common regions η and ϕ.

The kinematics of a jet can give hints on the kinematics at the origin of the jet. A dedicated algorithm searches for secondary vertices close to the beam axis corresponding to decays of long-living hadrons, mostly b-hadrons, that occur when the initial parton at the origin of a jet is a b-quark. This so called b-tagging algorithm is a key ingredient in the present analysis.

2.4.4.1. Jet reconstruction

Jets are reconstructed [89, 90] by the anti-k_t algorithm, where the geometrical distance of two particles scales with a negative power of the transverse momentum k_t [91, 92]. The present analysis uses the anti-k_t algorithm with a distance parameter of $R = 0.4$ and topological clusters [93] in the calorimeters with cell energies above the noise level as input.

2.4.4.2. Jet calibration

Figure 2.20 illustrates the several steps in the EM jet kinematics calibration [94] starting from the sum of energy deposits in the calorimeters. Firstly the jet direction of the
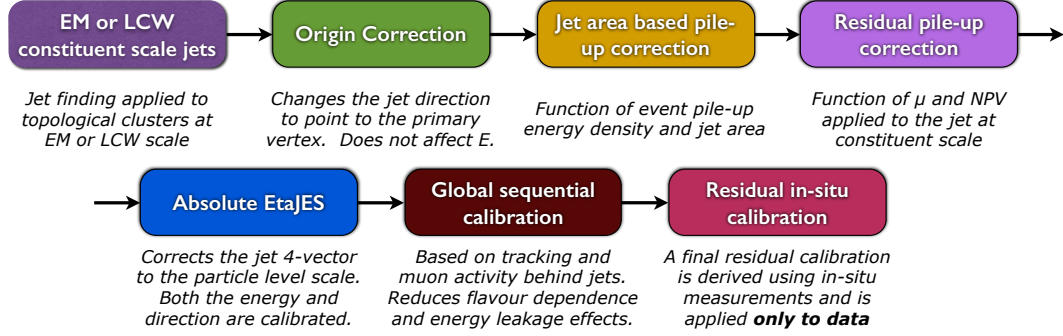
Figure 2.20.: Steps of jet calibration.

topological clusters corrected to point back PV instead of the detector centre.

Then an area based pile-up subtraction [95, 96] follows using a mean event pile-up density in η and ϕ. The remaining dependency on the jet p_T is corrected in dependency of the number of PVs N_{PV} for the residual in-time pile-up and $\langle\mu\rangle$ for the out-of-time pile-up. The corrected jet p_T due to pile-up can be expressed as

$$p_T^{corr} = p_T^{cluster} - \rho \cdot A - \alpha \cdot (N_{PV} - 1) - \beta \cdot \langle\mu\rangle \tag{2.7}$$

where $p_T^{cluster}$ is the jet p_T from the topological cluster, A is the calculated jet area, and α and β are the jet size dependent constants estimated from simulation, parametrised in p_T and $|\eta|$.

The absolute jet energy scale (JES) calibration corrects the jet p_T and direction to the truth jet kinematics using simulated isolated jets.

Jets initiated by quark and gluons differ in there response by up to 8%. The global sequential calibration reduces this effect. Moreover, the procedure corrects for high p_T jets which are not fully stopped by the calorimeters. Therefore the jet energy is corrected in five sequential stages based on energy deposits in the calorimeters, number of tracks associated to the jet, the size of the jet and the amount of activity in the MS behind the jet.

The final residual calibration uses in-situ techniques, based on the measurement of physics processes with jets and additional reference objects like photons, Z bosons or other jets. The ratio of the p_T of the probed jet p_T^{jet} and the p_T of the reference object p_T^{ref} is compared in data to MC simulation. The difference is applied as correction to the reconstructed jets in data with the ratio

$$\frac{\text{Response}_{data}}{\text{Response}_{MC}} = \frac{\left(p_T^{jet}/p_T^{ref}\right)_{data}}{\left(p_T^{jet}/p_T^{ref}\right)_{MC}}, \tag{2.8}$$

whose distribution is shown in figure 2.21 (left) for jets in the barrel region of $|\eta| < 0.8$ for 2016 data. Dijet events are used in the η-intercalibration of forward jets with $|\eta| >$
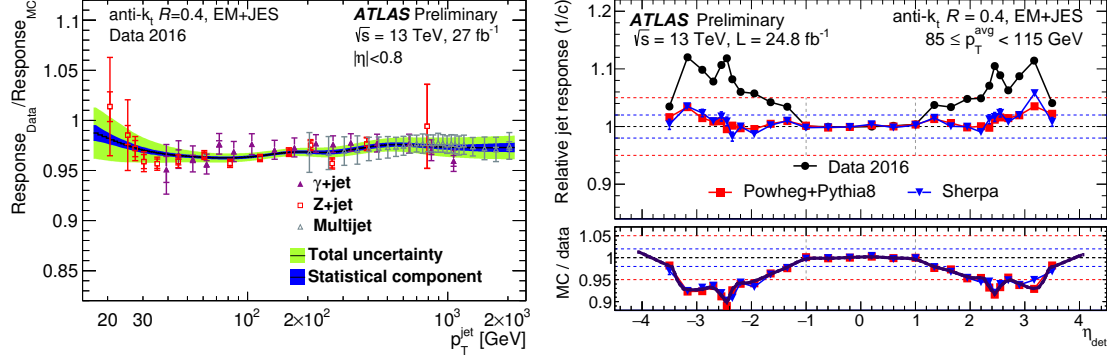
Figure 2.21.: Final residual in-situ jet energy calibration in 2016 data: (left) ratio of response in data to MC simulation in dependence of p_T and (right) relative jet response in dependence on η, measured with $L = 27\,\mathrm{fb}^{-1}$ and $24.8\,\mathrm{fb}^{-1}$ respectively [97].

0.8, to remove the residual dependence on η. The relative jet response to the one in the reference region of $|\eta| < 0.8$ is plotted in figure 2.21 (right) for 2016 data.

The total JES uncertainty combines all uncertainties on the JES calibration. Its dependency on p_T and η is shown in figure 2.22 for 2016 data. Because the present analysis
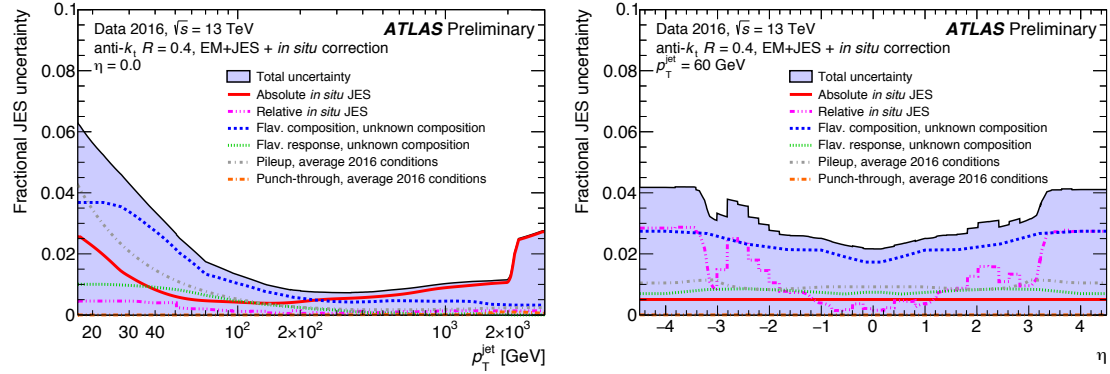
Figure 2.22.: Relative jet energy scale uncertainty in dependency of (left) p_T for jets at $\eta = 0$ and (right) η for jets at $p_\mathrm{T} = 60\,\mathrm{GeV}$ in 2016 data for unknown flavour composition [97].

considers final states with high jet multiplicities, the JES uncertainty has a major impact on the results. In the analysis the uncertainty on flavour composition has been decorrelated for processes with different quark to gluon fractions in the origin of jets.

2.4.4.3. Jet energy resolution

The precision of the jet energy is given by the jet energy resolution (JER), parametrised as a function of the noise effect N, the stochastic effect S due to the sampling of the calorimeters and the constant term C via

$$\frac{\sigma p_\mathrm{T}}{p_\mathrm{T}} = \frac{N}{p_\mathrm{T}} \oplus \frac{S}{\sqrt{p_\mathrm{T}}} \oplus C. \tag{2.9}$$

Like the JES it is measured using data with reference objects as vector bosons or other jets. It ranges from 20% at jet $p_\mathrm{T} = 25\,\mathrm{GeV}$ to less than 10% at $p_\mathrm{T} > 100\,\mathrm{GeV}$. The uncertainty on the JER is less than 2% for the selected jets with $p_\mathrm{T} > 25\,\mathrm{GeV}$ [94] and has a non-negligible impact on the result of the present analysis.

2.4.4.4. Identification of jets from b-hadrons

Jets originating from b-quarks can be identified by using the long life-time of the b-hadrons. Those have a high mass of about $m = 5\,\mathrm{GeV}$ and relatively long mean decay length of about $c\tau = 500\,\mathrm{\mu m}$ [27]. For instance, b-hadrons with $p_\mathrm{T} = 50\,\mathrm{GeV}$ fly about $\langle l_\mathrm{T} \rangle = \beta\gamma c\tau = \frac{p_\mathrm{T} \cdot c\tau}{mc} = 5\,\mathrm{mm}$ in transverse projection before they decay, a distance that is measurable given the resolution of the pixel detector. This feature is exploited by ana algorithm based on a boosted decision tree (BDT). In the present analysis the so called MV2c10 BDT algorithm is used, which has an improved performance compared to Run 1 taggers, mainly because of the addition of the IBL [98, 99]. It uses input variables from

- the likelihood-based IP3D algorithm exploiting the transverse and the longitudinal IP significance,

- the secondary vertex (SV) finding, which is fitting one inclusive SV inside the jet and

- the fit of the full b-hadron to c-hadron decay chain, reconstructing more than one displaced vertex.

The distribution of the MV2c10 BDT output for the signal of b-jets and the backgrounds of jets from c-hadrons (c-jets) and light-flavour jets from light (u, d or s) quarks or gluons is shown in figure 2.23 (left). The background rejection of c-jets and light-flavour jets is given in figure 2.23 (right) as a function of the b-jet tagging efficiency, varied by decreasing the cut value on the MV2c10 output. The rejection rate of c-jets is much smaller than for light jets, because c-hadrons have a similar $\langle l_\mathrm{T} \rangle$ as b-hadrons, which leads to a similar expected signature in the ID.

Four different working points are provided with fixed cuts on the MV2c10 output, which are summarised in table 2.5. The present analysis uses the working point with 70% b-tagging efficiency for the selection of b-tagged jets, which provides a light-flavour rejection rate of 381. Additionally some of the channels use the MV2c10 output for selected jets, binned in five bins, as input to the event BDTs separating signal from background. This is possible due to the so called pseudo-continuous b-tagging calibration,
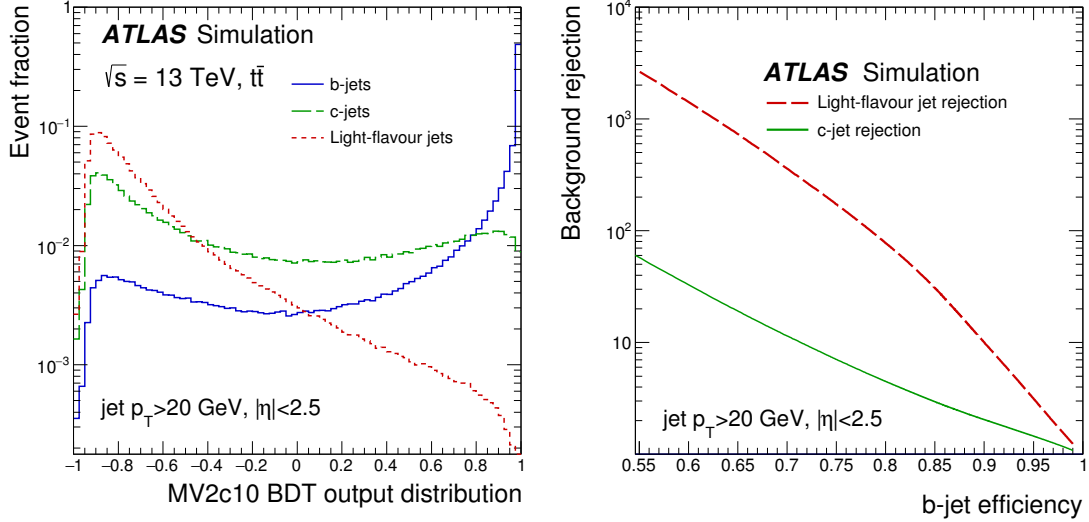
Figure 2.23.: (Left) MV2c10 BDT output distribution for *b*-jets (solid line), *c*-jets (dashed line) and light-flavour jets (dotted line) and (right) rejection of *c*-jets (solid line) and light-flavour jets (dashed line) in dependency of *b*-tagging efficiency in simulated $t\bar{t}$ events [99].

Table 2.5.: *b*-tagging efficiency and background rejection rates at different cuts on the MV2c10 BDT output in simulated $t\bar{t}$ events [100]. τ_{had} denotes hadronically decaying tau leptons, described in section 2.4.5.

cut on	efficiency for jets	background rejection rate of		
MV2c10	from *b*-hadrons	jets from *c*-hadrons	light-flavour jets	τ_{had}
> 0.9349	60%	34	1538	184
> 0.8244	70%	12	381	55
> 0.6459	77%	6	134	22
> 0.1758	85%	3.1	33	8.2

which provides scale factors to weight simulated events according to the ratio of observed over expected *b*-tagging efficiency. The likelihood-based measurement of the *b*-tagging efficiency and the scale factors are shown in figure 2.24 for the working point with 70% *b*-tagging efficiency.

2.4.5. Hadronically decaying tau leptons

The tau leptons (τ) are the heaviest leptons with a mass of $m = 1.78\,\text{GeV}$ and a mean decay length of $c\tau = 87\,\mu\text{m}$ [27]. A tau lepton with $p_{\text{T}} = 50\,\text{GeV}$ decays after a mean transverse flight length of $\langle l_{\text{T}} \rangle = 2.4\,\text{mm}$, which makes it difficult to be distinguished from tracks produced by hadrons originating from the primary interaction. 35 % of the tau leptons decay leptonically into light charged leptons (electrons or muons) and neu-
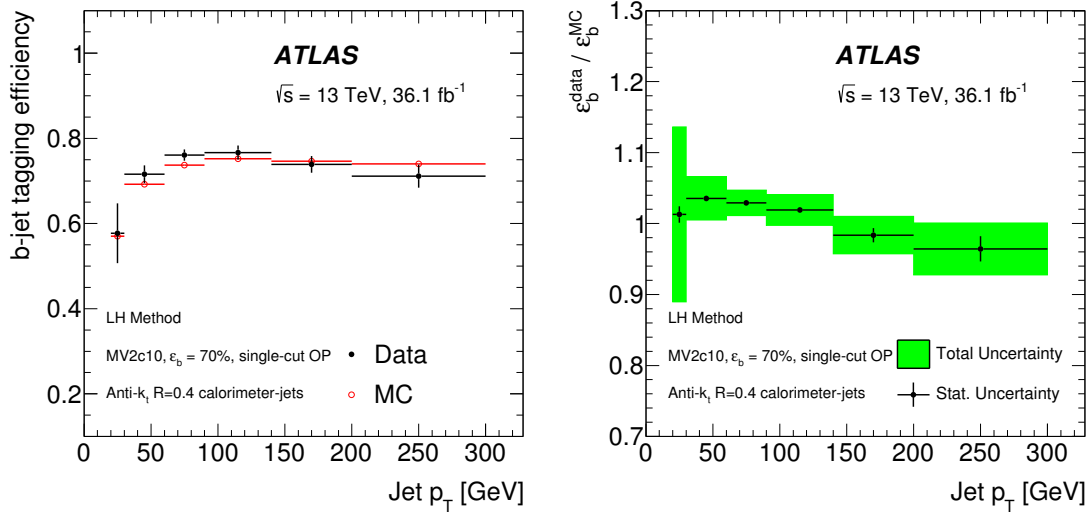
Figure 2.24.: (Left) *b*-tagging efficiency in dependency of jet p_T in data and simulation and (right) *b*-tagging scale factors for the working point with 70% *b*-tagging efficiency in combined 2015 and 2016 data [99].

trinos and are reconstructed as light leptons. 65 % of the tau leptons are hadronically decaying (τ_{had}) into mainly pions and a tau neutrino. Like the jet reconstruction, the reconstruction of τ_{had} uses cluster information from the calorimeters and tracks in the ID [101].

The τ_{had} decay products include exactly one (three) charged pions in 72% (22%) of all cases. Therefore, only candidates with one (three) charged associated tracks, called one-(three-)prong candidates, are considered in the present analysis. Figure 2.25 shows, that this selection has an efficiency of about 70% (65%) for one-(three-)prong candidates. The degradation of efficiency for high p_T three-prong candidates is explained by the
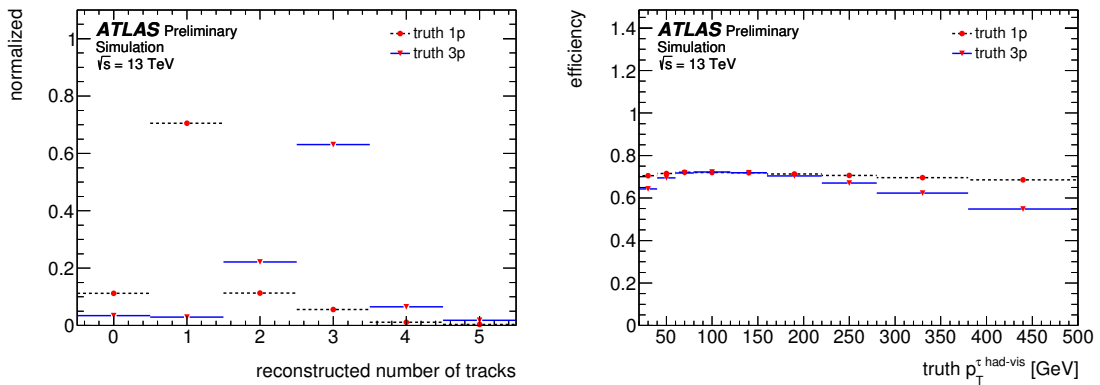
Figure 2.25.: (Left) number of reconstructed tracks and (right) efficiency for reconstructing one (three) tracks in dependency of p_T for simulated true one-prong (three-prong) τ_{had} candidates in dashed (solid) line [101].

possible merging of high p_T tracks such that only two of three tracks are reconstructed.

The main background of jets is reduced by a BDT using variables describing the narrower shower in the calorimeters and the SV from the tau lepton decay point. It is trained on simulated $Z \to \tau\tau$ events for signal and dijet events from data for background. Three working points of τ_{had} identification of loose, medium and tight are used in the present analysis with reconstruction and identification efficiencies of 60% (50%), 55% (40%) and 45% (30%) respectively for the one-(three-)prong candidates [102]. The efficiencies are measured in a tag-and-probe method in $Z \to \tau\tau$ events where the tag is a leptonically decaying tau lepton into a muon and neutrinos (τ_μ) and the probed object is a τ_{had}. Figure 2.26 shows the ratios of efficiencies observed in data over simulation, which are applied in the analysis as scale factors in the event weights on simulated events.
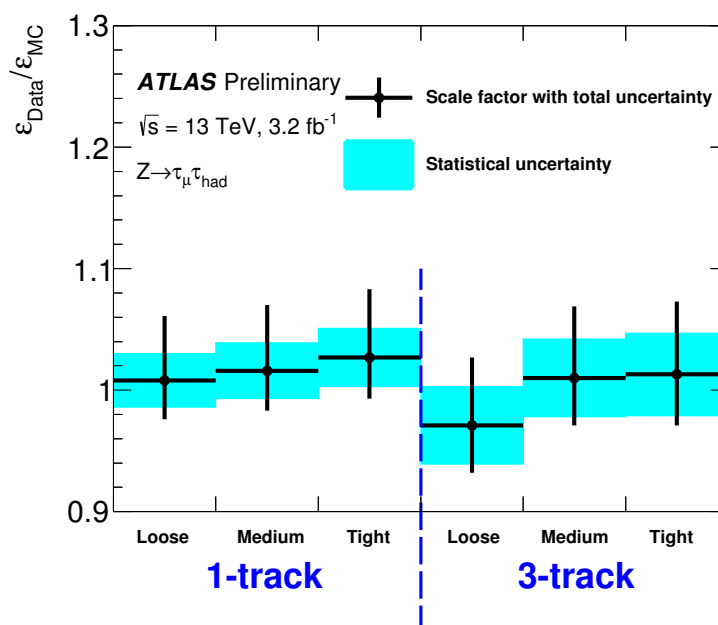
Figure 2.26.: Scale factors in one- and three-prong τ_{had} reconstruction and identification efficiencies in 2015 data $Z \to \tau_\mu\tau_{had}$ decays [102].

A second BDT is used to reject electrons which are reconstructed as one-prong τ_{had} candidates with an efficiency of 95%. Candidates overlapping with muons with low $p_T > 2\,\text{GeV}$ are removed. An important background to τ_{had} are jets from b-hadrons with a similar mean flight length and corresponding SV properties. τ_{had} candidates are removed if they are b-tagged at 70% b-tagging efficiency. The background of fakes from pile-up collisions is reduced by the requirement, that the τ_{had} candidates need to originate in the PV.

2.4.6. Missing transverse momentum

The missing transverse momentum ($\mathbf{E}_T^{miss}$) is the measurable signature of particles that are not directly detectable by the ATLAS detector. The missing transverse momentum is defined as

$$\mathbf{E}_T^{miss} = - \sum_{i \in \{\text{hard objects}\}} \mathbf{p}_T^i - \sum_{j \in \{\text{soft signals}\}} \mathbf{p}_T^j. \tag{2.10}$$

with the transverse momenta of selected hard objects i as leptons, jets and photons and soft signals j from unused tracks from the PV without associated reconstructed objects. The present analysis uses its absolute (E_T^{miss}) and its azimuthal angle ϕ^{miss} in the input for the multivariate analysis separating signal from background processes.

Figure 2.27 shows the resolution of x and y component of the $\mathbf{E}_T^{miss}$ in dependency of the scalar sum of transverse momenta of all objects, defined as

$$\Sigma E_T = - \sum_{i \in \{\text{hard objects}\}} \left| \mathbf{p}_T^i \right| - \sum_{j \in \{\text{soft signals}\}} \left| \mathbf{p}_T^j \right| \tag{2.11}$$

and the number of PVs N_{PV}, measured in $Z \to \mu\mu$ events with at least one jet in 3.2 fb^{-1} of 2015 data. The measurement of E_T^{miss} is dominated by uncertainties on the jet energies.
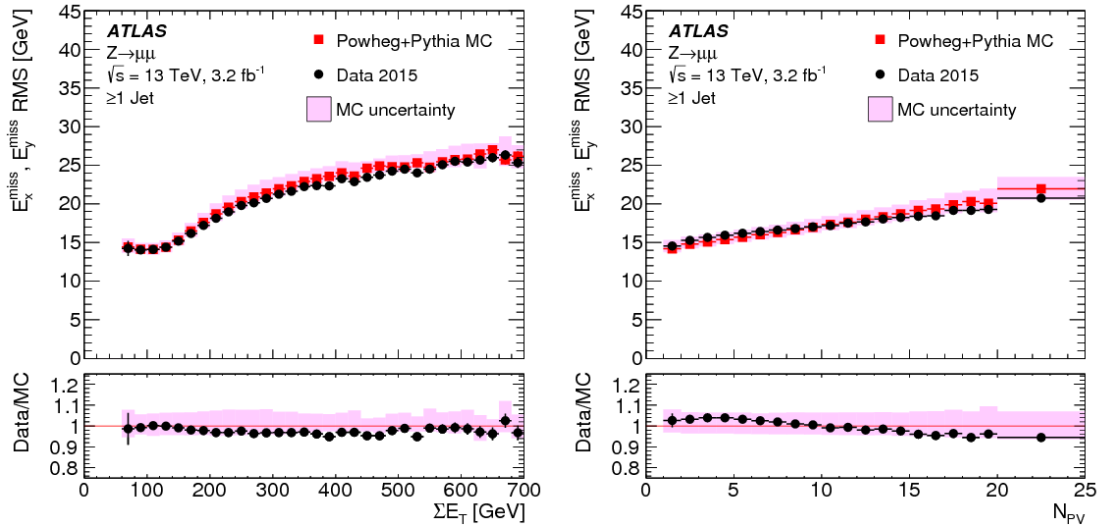
Figure 2.27.: The resolution of the E_T^{miss} in dependency of (left) the sum of the transverse momenta of all objects (ΣE_T) and (right) the number of PVs (N_{PV}) in $Z \to \mu\mu$ events with at least one jet in 2015 data [103].

As discussed in section 2.4.4, the JES uncertainty has a large contribution from pile-up subtraction, which explains the increase of E_T^{miss} uncertainty with N_{PV}.

2.4.7. Analysis framework

The collected data and simulated samples are distributed in several computing centres and analysed using a conceptual model described in figure 2.28 in Run 2 [104]. In xAOD
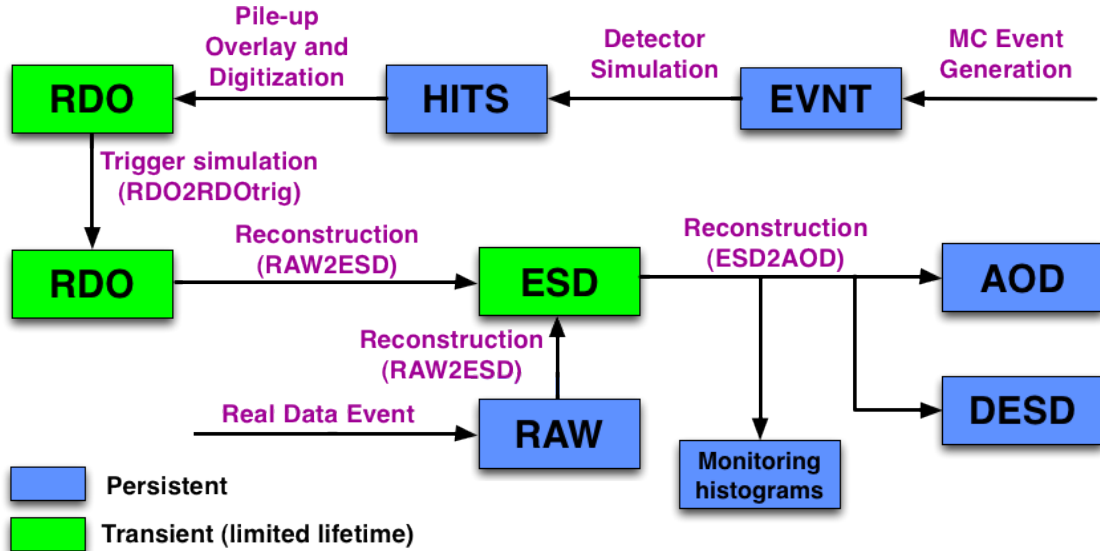
Figure 2.28.: Data flow for ATLAS analysises with the xAOD framework [104].

(AOD for Analysis Object Data) all information of an event like occurring particles or missing transverse energy are organised in classes.

Triggered events by the experiment or simulated events are firstly reconstructed using Athena leading to generic xAOD files. A derivation reduction framework is then used to build derived xAODs (DxAODs) for different purposes of interest with removing unnecessary information of the events. Because of the big physical size of the DxAOD datasets used in the present analysis the PanDA (Production ANd Distributed Analysis) framework [105] is used. A complete turnover includes about 500 tasks running in parallel on the grid. I have been responsible for the preparation of the inputs to the $t\bar{t}H \rightarrow$ multilepton analysis team, starting from the DxAODs.

2.5. Conclusion

The different experiments at the LHC have been very successful in collecting proton-proton collisions in the Run 1 and the ongoing Run 2 of the LHC. The well-performing LHC accelerator complex has accelerated proton beams to never before reached energies in experiments of 6.5 TeV per proton. The ATLAS is a multipurpose detector at one of the four interaction points of the LHC main ring. It has an excellent energy resolution for different reconstructed objects as photons, electrons, muons, jets, hadronically decaying tau leptons and missing transverse momentum. The searches described in the following two chapters use data recorded by the ATLAS detector in 2015–2016.

3. Search for the Higgs boson production with a top quark pair in multileptonic final states

The physics process of associated Higgs boson production with a pair of top quarks ($t\bar{t}H$) allows to directly access the top Yukawa coupling λ_t. The value of this coupling is predicted by the SM from top quark mass m_t and the vacuum expectation value (VEV) v of the Higgs field via the formula $\lambda_t = \frac{\sqrt{2}m_t}{v}$ (section 1.1.3). Any significant deviation from the SM value might be a hint for new physics.

The search for the $t\bar{t}H$ process can use events with multileptonic final states. Those are final states with at least two reconstructed leptons, namely light leptons ($\ell = e$ or μ) or hadronically decaying tau leptons (τ_{had}), in the detector. They are targeting Higgs boson decays of $H \rightarrow WW$, $H \rightarrow ZZ$ and $H \rightarrow \tau\tau$.

This chapter describes the $t\bar{t}H \rightarrow$ multilepton analysis of the ATLAS collaboration with a dataset of 2015–2016 proton-proton collisions with a center-of-mass energy of $\sqrt{s} = 13$ TeV and an integrated luminosity of $L = 36.1\,\mathrm{fb}^{-1}$ [4].

The $t\bar{t}H$ searches prior to Run 2 are summarised in section 3.1, followed by an introduction into searches for $t\bar{t}H$ in multilepton final states in section 3.2 at Run 2 with the ATLAS experiment. Section 3.3 gives an overview of the $t\bar{t}H$ signal properties and samples used in the presented analysis. Section 3.4 describes the basic event selection and the criteria for reconstructed objects. The event classification and signal regions are presented in section 3.5. The focus lies on the most significant channels with two or three ℓ without τ_{had}. Studies on an alternative event classification in the 3ℓ channel with similar performance as the default one are also presented. The $t\bar{t}H$ analysis has a variety of backgrounds of same order as signal contribution. Their estimates and suppression methods are elaborated in section 3.6. Section 3.7 develops the systematic uncertainties impacting the sensitivity of the analysis. The statistical model and the results are described in section 3.8. A special focus lies on the results with the alternative 3ℓ classification. The combination with other searches for $t\bar{t}H$ at the ATLAS experiment is described in 3.9. Finally, an outlook with extrapolation up to $3{,}000\,\mathrm{fb}^{-1}$ of proton-proton collisions at a high-luminosity LHC is discussed in section 3.10.

3.1. Previous searches for $t\bar{t}H$

Several experiments have searched for the associated Higgs boson production with a top quark pair. A first search for $t\bar{t}H$ targeting $H \to b\bar{b}$ decays has been performed by the CDF collaboration with data from proton-antiproton collisions at a center-of-mass energy of $\sqrt{s} = 1.96\,\mathrm{TeV}$ with an integrated luminosity of $L = 9.45\,\mathrm{fb}^{-1}$. For a Higgs boson mass of 125 GeV an observed (expected) upper limit at 95% confidence level (CL) of 20.5 (12.6) the SM expectation has been found [106].

Both the ATLAS and the CMS collaboration have explored the $t\bar{t}H$ production in proton-proton collisions at Run 1 of the LHC with $L = 25\,\mathrm{fb}^{-1}$ and $\sqrt{s} = 7$ and 8 TeV. They observed a signal strength $\mu_{t\bar{t}H}$, defined as the measured $t\bar{t}H$ yield divided by the prediction from the SM of $\mu_{t\bar{t}H} = 1.8 \pm 0.8$ and $\mu_{t\bar{t}H} = 2.8 \pm 1.0$, respectively [107, 108]. The combined measurement of Run 1 $t\bar{t}H$ searches at ATLAS and CMS is $\mu_{t\bar{t}H} = 2.3\,^{+0.7}_{-0.6}$ with an observed (expected) significance of 4.4 (2.0) standard deviations for the excess over the SM background hypothesis [3].

In the combined measurement of multileptonic final states the ATLAS collaboration found $\mu_{t\bar{t}H} = 2.1^{+1.4}_{-1.2}$ corresponding to 1.8σ (0.9σ) observed (expected) significance. Five channels have been examined categorised by the number of light leptons ($\ell = e$ or μ) and hadronically decaying tau leptons (τ_{had}). Their measured best-fit values of the signal strengths $\mu_{t\bar{t}H}$ and 95% CL upper limits on $\mu_{t\bar{t}H}$ are shown in figure 3.1. The
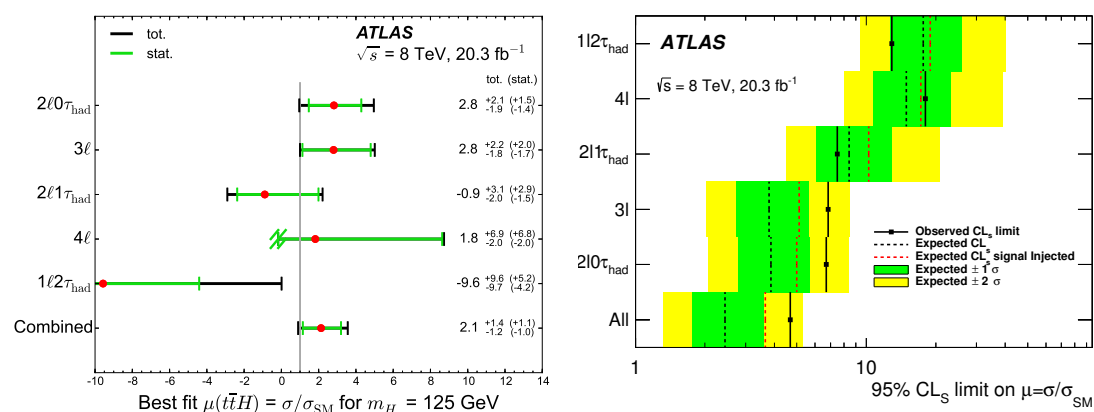
Figure 3.1.: Signal strength $\mu_{t\bar{t}H}$ (left) best-fit values and (right) 95 % CL upper limits in the combined and single channels of the $t\bar{t}H \to$ multilepton analysis by the ATLAS collaboration. In the 4ℓ channel the lower uncertainty is truncated because $\mu_{t\bar{t}H} < -0.17$ results in a negative expected total yield [109].

combined observed (expected) upper limit is $\mu_{t\bar{t}H} < 4.7$ (2.4) [109].

Other Higgs boson decays have been studied in dedicated $t\bar{t}H$ searches. Final states with one lepton or two opposite charged leptons coming from top quark decays are targeting the $H \to b\bar{b}$ decay and have been studied by the ATLAS [110] and the CMS collaboration [111]. Although the branching ratio of the $H \to \gamma\gamma$ decay is small its

signature in the detectors is clean and has been studied by both the ATLAS [112] and the CMS collaboration [108].

3.2. Run 2 $t\bar{t}H \to$ multilepton analysis with ATLAS

The ATLAS collaboration has published preliminary results of the $t\bar{t}H \to$ multilepton analysis in 2016 for the ICHEP conference with $L = 13.2\,\text{fb}^{-1}$ of proton-proton collision data at Run 2 of the LHC at a center-of-mass energy of $\sqrt{s} = 13\,\text{TeV}$. I have contributed in the validation of prompt background estimates and the extraction of the final results. Data to prediction comparison in different validation regions (VRs) is used to trust the proper modelling of prompt backgrounds by Monte Carlo (MC) simulation. In figure 3.2 some distributions are shown for $t\bar{t}Z$, WZ and $t\bar{t}W$ VRs. They show good
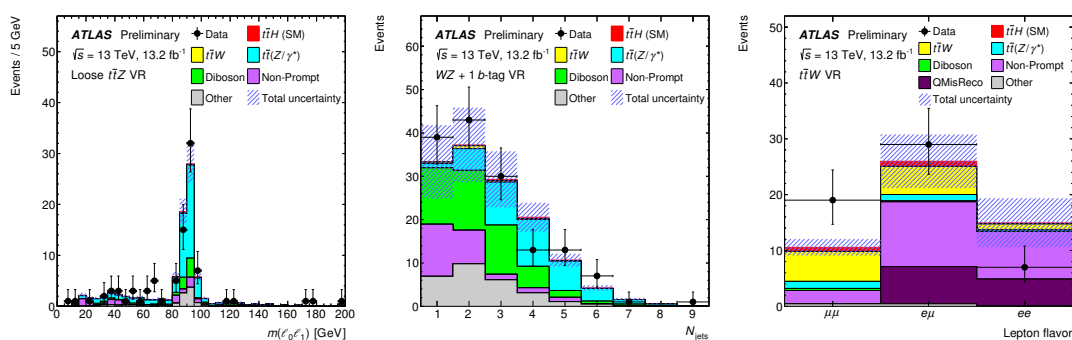
Figure 3.2.: Validation region distributions of (left) invariant mass of opposite-charge, same-flavour leptons for $t\bar{t}Z$ background, (middle) jet multiplicity for WZ background at $N_{b-\text{tags}} \geq 1$ and (right) lepton flavour in for the $t\bar{t}W$ background [113].

data-prediction agreement, but the poor statistical precision limits the validation power. Four categories have been combined in this analysis, summarised in table 3.1. The com-

Table 3.1.: Channels categorisation in ICHEP conference 2016 analysis.

	light leptons	had. tau leptons	total light lepton charge	jets	b-tags
2ℓSS	2	0	± 2	≥ 5	≥ 1
2ℓSS+$1\tau_{\text{had}}$	2	1	± 2	≥ 4	≥ 1
3ℓ	3	-	± 1	≥ 3 (or 4)	≥ 2 (or 1)
4ℓ	4	-	0	≥ 2	≥ 1

bined best-fit value of the signal strength was found to be $\mu_{t\bar{t}H} = 2.5\,^{+1.3}_{-1.1}$ with an observed (expected) upper limit at 95% CL of 4.9 (2.3) [113].

In 2015 and 2016 the ATLAS experiment collected a proton-proton collision data sample corresponding to an integrated luminosity of $L = 36.1\,\mathrm{fb}^{-1}$ at a center-of-mass energy of $\sqrt{s} = 13\,\mathrm{TeV}$. The analysis performed using this new data sample and the associated improvements are presented in the following.

Two kinds of backgrounds dominate the $t\bar{t}H \to$ multilepton analysis:

- The irreducible backgrounds are the SM processes with a similar topology and leptons originating in the hard scattering of the processes, so called prompt leptons.

- The reducible backgrounds have at least one fake, non-prompt or charge misreconstructed lepton. The channels with τ_{had} have big contributions of fake τ_{had} originating from light flavour jets and mis-identified electrons.

The estimate and suppression of this backgrounds will be discussed in section 3.6.

3.3. Signal topology

Due to its modest cross section of $\sigma_{t\bar{t}H} = 507\,\mathrm{fb}$ [6], the $t\bar{t}H$ production has much smaller yields than other Higgs production modes such as gluon-gluon fusion, vector boson fusion and associated production with a W or Z boson. In the $L = 36.1\,\mathrm{fb}^{-1}$ of proton-proton collisions $\sigma_{t\bar{t}H} \cdot L = 18{,}300$ signal events are expected, out of which about 5,600 events correspond to $H \to WW, H \to ZZ$ and $H \to \tau\tau$ decays. For $H \to WW, H \to ZZ$ and $H \to \tau\tau$ decays about 5,600 events are expected. Tree-level Feynman diagrams for the $t\bar{t}H$ production with these Higgs boson decays are shown in figure 3.3.
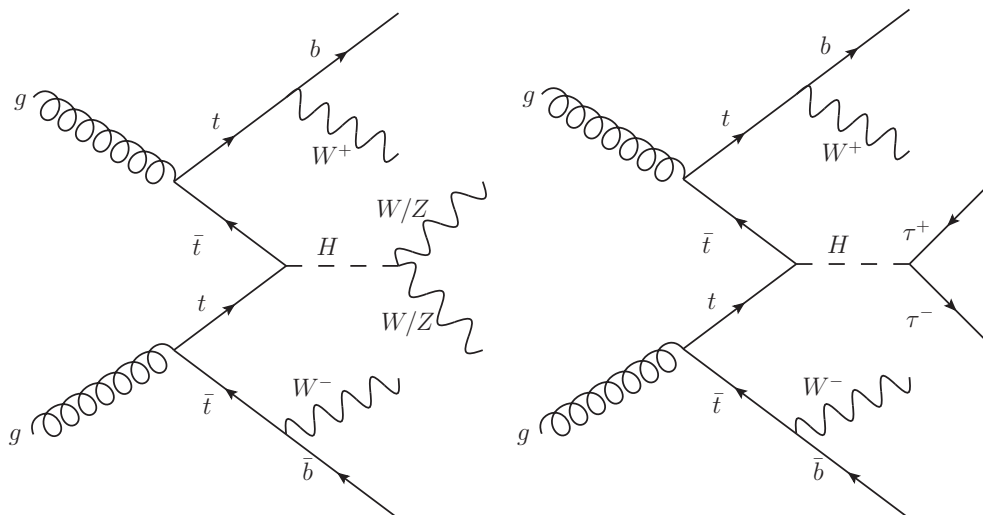
Figure 3.3.: Tree-level Feynman diagrams for $t\bar{t}H$ production with (left) $H \to WW/ZZ$ and (right) $H \to \tau\tau$ decay [4].

It should be noted that in about 58% of $t\bar{t}H$ events the Higgs boson decays into two bottom quarks because of its high branching ratio [6]. A dedicated analysis has been done for this signature with many b-tagged jets [114].

Due to detector coverage and various selection efficiencies for triggering, reconstruction and signal region event selection for background rejection, only about 1.6% of the $t\bar{t}H \rightarrow$ multilepton events can be selected in the signal regions of the $t\bar{t}H \rightarrow$ multilepton analysis, described in the following sections.

For the dominant decay of $H \rightarrow WW$ the further decay chain in the most significant channels with two same-charged or three light leptons is

$$t\bar{t}H \rightarrow 2W2b + H \rightarrow 4W + 2b \rightarrow 2\ell + E_\mathrm{T}^\mathrm{miss} + 6 \text{ jets (2 from } b) \text{ or}$$
$$\rightarrow 3\ell + E_\mathrm{T}^\mathrm{miss} + 4 \text{ jets (2 from } b) \quad (3.1)$$

where the W bosons are assumed to decay into a pair of quarks which hadronise or into a charged lepton and a neutrino. If the Higgs boson decays to tau leptons the dominant decay chain for the channels with two light leptons and one hadronically decaying tau lepton (τ_had) is

$$t\bar{t}H \rightarrow 2W2b + H \rightarrow 2W2b2\tau \rightarrow 2\ell + 1\tau_\mathrm{had} + E_\mathrm{T}^\mathrm{miss} + 4 \text{ jets (2 from } b) \quad (3.2)$$

with the τ_had coming from the Higgs boson decay and one light lepton from the leptonic decay of the second tau lepton and the other light lepton from the leptonic decay of a W boson from a top quark decay.

The nominal $t\bar{t}H$ signal samples are generated at next-to-leading-order (NLO) assuming a Higgs boson mass of 125 GeV and a top quark mass of 172.5 GeV with the MAD-GRAPH5_AMC@NLO parton-level generator, PYTHIA 8 parton shower. The event simulation at the ATLAS experiment is described in section 2.3. A parton shower uncertainty is estimated using an alternative sample given in appendix A. Uncertainties on the cross section are $^{+5.8}_{-9.2}$% from QCD factorisation and ±3.6% from PDFs and the strong coupling constant. Les Houches event weights [115, 116] are used to estimate the shape effect of renormalisation and factorisation scales. I have been responsible for the proper implementation of the samples and all systematic uncertainties in the extraction of the results.

3.4. Basic event selection and object reconstruction and identification

All $t\bar{t}H \rightarrow$ multilepton analysis channels use the same basic event and object selection. All events are required to have at least one reconstructed primary vertex (PV), based on the track and vertex reconstruction, described in section 2.4.1. The actual PV is chosen by maximising the sum of squared transverse momenta of the associated tracks with $p_\mathrm{T} > 400$ MeV.

A selected event has to be triggered by one of the lowest not pre-scaled HLT trigger items with one or two light leptons, summarised in table 3.2. Because of the increase

Table 3.2.: Lowest not pre-scaled triggers and their p_T thresholds, identification and isolation criteria in the $t\bar{t}H \rightarrow$ multilepton analysis. A '*' in the year column denotes, that the trigger item was used in both years. Unlike in 2015, the identification likelihood (LH) for electrons triggered in 2016 uses no d_0 information.

trigger	year	p_T thresholds [GeV]	identification (id.), isolation (iso.)
single-electron	2015	≥ 24	medium LH id.
	2016	≥ 26	tight LH id.
	*	≥ 60	medium LH id.
	*	≥ 120	loose LH id.
single-muon	2015	≥ 20	loose iso.
	2016	≥ 26	medium variable cone size iso.
	*	≥ 50	–
di-electron	2015	$\geq 12, \geq 12$	loose LH id.
	2016	$\geq 17, \geq 17$	very loose LH id.
di-muon	2015	$\geq 18, \geq 8$	–
	2016	$\geq 22, \geq 8$	–
electron-muon $[e, \mu]$	*	$\geq 17, \geq 14$	loose LH id. e

of instantaneous luminosity and mean pile-up (compare table 2.1) the trigger items have tighter selection in 2016 than in 2015 to maintain sufficient low output event rate at about 1 kHz. E.g. for the single-electron triggers the lowest lepton p_T is 24 GeV in 2015 and 26 GeV in 2016 data-taking. An event is rejected if no reconstructed light leptons are found, matching one of the above trigger items with a p_T greater than the trigger p_T threshold $+ 1$ GeV. E.g. an event from 2016 data, selected by the di-muon trigger is only accepted if there are two muons with $p_T > 23$ GeV and $p_T > 9$ GeV matched to the regions of interest (ROIs) of the trigger item or if the matching is satisfied for another trigger item.

Electron candidates (e) are classified using the information of energy clusters in the electromagnetic (EM) calorimeter and associated reconstructed tracks in the inner detector by applying a loose or tight likelihood identification. They are selected to be in the region of $|\eta_\text{cluster}| < 2.47$ with the additional requirement of being not in the crack region, $|\eta_\text{cluster}| \notin [1.37, 1.52]$. Only electron candidates with a transverse momentum of $p_T > 10$ GeV are chosen. For the IPs along the beam (z_0) and transverse to the beam (d_0) the requirements are $|z_0 \sin \theta| < 0.5$ mm with the polar angle θ and d_0 significance $|d_0|/\sigma_{d_0} < 5$ where σ_{d_0} is the estimated uncertainty on d_0. If two electron candidates have a distance of $\Delta r < 0.1$, the one with lower p_T is rejected [4].

Muon (μ) candidates are reconstructed using tracks from the ID, signatures in the MS and energy deposits in the calorimeters. Loosely identified muon candidates are chosen with a pseudorapidity of $|\eta| < 2.5$ and a transverse momentum of $p_T > 10$ GeV. Similar

cuts on the impact parameters and isolation variables like for electrons are applied to reduce the contribution of fake muons: $|z_0 \sin\theta| < 0.5$ mm, and $|d_0|/\sigma_{d_0} < 3$. Most of the muon candidates are required to pass a loose isolation requirement with a flat isolation efficiency of 99% for both calorimetric and tracking isolation variable cuts.

Hadronically decaying tau leptons (τ_{had}) are reconstructed from energy clusters in the hadronic and electromagnetic calorimeters. All τ_{had} candidates are required to have $p_T > 25$ GeV and $|\eta| < 2.5$, excluding the crack region of the EM calorimeter, and exactly one or three associated charged tracks. To reject jet backgrounds a boosted decision tree (BDT) with inputs from the calorimeter and tracking is used. τ_{had} candidates are rejected if they overlap with any selected electron or muon in a cone of $\Delta r < 0.2$.

Jets are reconstructed applying an anti-k_t algorithm with $R = 0.4$ using energy deposits in the calorimeters. They are selected with $p_T > 25$ GeV and $|\eta| < 2.5$. The number of pile-up jets is reduced by the requirement, that jets with $p_T < 60$ GeV and $|\eta| < 2.4$ have a high sum of track's $|p_T|$ coming from the PV. This requirement, called the Jet Vertex Tagger (JVT), has a selection efficiency of 92% for jets from hard scattering of the actual event. Jets are classified as b-tagged using a multivariate analysis technique at a working point of 70% b-tagging efficiency (see section 2.4.4.4 for details).

The leptons are classified using isolation requirements and other properties. This is summarised in table 3.3. The BDTs used to suppress backgrounds of non-prompt leptons and charge misassignment are described in section 3.6.

Table 3.3.: Loose (L), loose and isolated (L†), loose, isolated and passing the non-prompt BDT (L*), tight (T) and very tight (T*) lepton classification [4].

		e					μ	
	L	L†	L*	T	T*	L	L†	L*/T/T*
Isolation	No		Yes			No		Yes
Non-prompt lepton BDT		No		Yes			No	Yes
Identification		Loose		Tight			Loose	
Charge misassignment veto BDT		No		Yes			No	
Transverse impact parameter significance, $|d_0|/\sigma_{d_0}$		< 5					< 3	
Longitudinal impact parameter, $|z_0 \sin\theta|$					< 0.5 mm			

3.5. Event classification and signal regions

The events are categorised in seven orthogonal channels by multiplicities of light leptons ($\ell = e, \mu$) and hadronically decaying tau leptons (τ_{had}). The leptonically decaying tau leptons (τ_{lep}) are not distinguishable from light leptons in the reconstruction. The seven channels, summarised in figure 3.4, are

- two same-charge light leptons and no τ_{had} (2ℓSS);

- three light leptons and no τ_{had} (3ℓ);

75
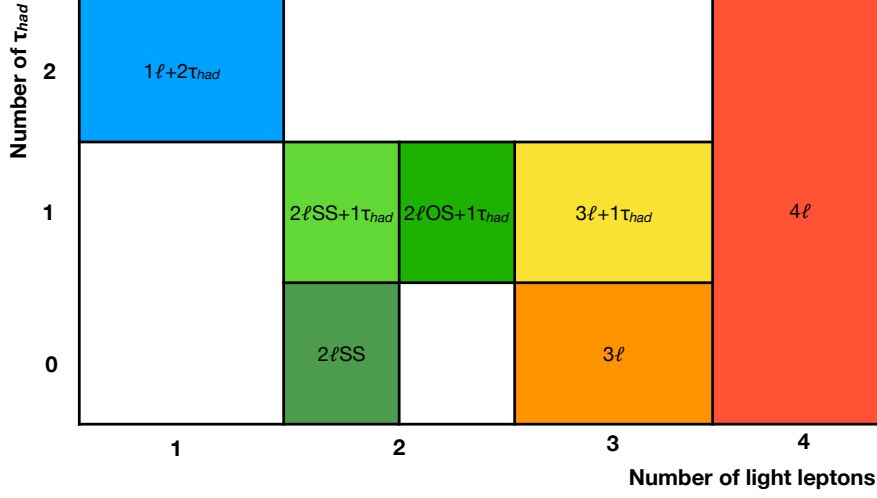
Figure 3.4.: The classification of the seven analysis channels by τ_{had} and light lepton multiplicities [4].

- four light leptons (4ℓ);

- one light lepton and two opposite-charge τ_{had} ($1\ell+2\tau_{\text{had}}$);

- two same-charge light leptons and one τ_{had} ($2\ell\text{SS}+1\tau_{\text{had}}$);

- two opposite-charge light leptons and one τ_{had} ($2\ell\text{OS}+1\tau_{\text{had}}$);

- three light leptons and one τ_{had} ($3\ell+1\tau_{\text{had}}$).

All channels require at least one b-tagged jet, since the top quarks from the $t\bar{t}H$ signal decay into W bosons and bottom quarks. In all channels, at least one lepton from Higgs decays and one lepton from top decays are involved. To suppress backgrounds with low jet multiplicities the basic cut on the number of jets is $N_{\text{jets}} \geq 2$. On top of that, the $2\ell\text{SS}$ and $2\ell\text{SS}+1\tau_{\text{had}}$ ($2\ell\text{OS}+1\tau_{\text{had}}$ and $1\ell+2\tau_{\text{had}}$) channels require at least 4 (3) jets. The detailed event selection for all channels is described in table 3.4.

In total eight signal regions (SRs) are defined with one SR per channel, apart from the 4ℓ channel, where a Z-enriched and a Z-depleted SR are defined. Additionally, the 3ℓ channel defines four control regions (CRs) for the major backgrounds. In the statistical analysis the observed and predicted distributions of selected discriminants or single event counts are compared with each other. The expected pre-fit yields, distributions and uncertainties correspond to the SM expectation with a $t\bar{t}H$ signal strength of $\mu_{t\bar{t}H} = 1$. In the fit procedure the observed signal strength and adjustments of the systematic uncertainties is obtained from a maximum-likelihood fit. The expected post-fit values include these adjustments, which usually improve the agreement of observation and expectation.

This thesis dissertation concentrates on the two channels of the $t\bar{t}H \to$ multilepton analysis with highest sensitivity: the $2\ell\text{SS}$ and the 3ℓ channel. The event selection in

76

Table 3.4.: Event selection in the seven single channels [4].

Channel	Selection criteria
Common	$N_{\text{jets}} \geq 2$ and $N_{b\text{-jets}} \geq 1$
$2\ell\text{SS}$	Two very tight light leptons with $p_{\text{T}} > 20$ GeV
	Same-charge light leptons
	Zero medium τ_{had} candidates
	$N_{\text{jets}} \geq 4$ and $N_{b\text{-jets}} < 3$
3ℓ	Three light leptons with $p_{\text{T}} > 10$ GeV; sum of light-lepton charges ± 1
	Two same-charge leptons must be very tight and have $p_{\text{T}} > 15$ GeV
	The opposite-charge lepton must be loose, isolated and pass the non-prompt BDT
	Zero medium τ_{had} candidates
	$m(\ell^+\ell^-) > 12$ GeV and $|m(\ell^+\ell^-) - 91.2 \text{ GeV}| > 10$ GeV for all SFOC pairs
	$|m(3\ell) - 91.2 \text{ GeV}| > 10$ GeV
4ℓ	Four light leptons; sum of light-lepton charges 0
	Third and fourth leading leptons must be tight
	$m(\ell^+\ell^-) > 12$ GeV and $|m(\ell^+\ell^-) - 91.2 \text{ GeV}| > 10$ GeV for all SFOC pairs
	$|m(4\ell) - 125 \text{ GeV}| > 5$ GeV
	Split 2 categories: Z-depleted (0 SFOC pairs) and Z-enriched (2 or 4 SFOC pairs)
$1\ell + 2\tau_{\text{had}}$	One tight light lepton with $p_{\text{T}} > 27$ GeV
	Two medium τ_{had} candidates of opposite charge, at least one being tight
	$N_{\text{jets}} \geq 3$
$2\ell\text{SS} + 1\tau_{\text{had}}$	Two very tight light leptons with $p_{\text{T}} > 15$ GeV
	Same-charge light leptons
	One medium τ_{had} candidate, with charge opposite to that of the light leptons
	$N_{\text{jets}} \geq 4$
	$|m(ee) - 91.2 \text{ GeV}| > 10$ GeV for ee events
$2\ell\text{OS} + 1\tau_{\text{had}}$	Two loose and isolated light leptons with $p_{\text{T}} > 25, 15$ GeV
	One medium τ_{had} candidate
	Opposite-charge light leptons
	One medium τ_{had} candidate
	$m(\ell^+\ell^-) > 12$ GeV and $|m(\ell^+\ell^-) - 91.2 \text{ GeV}| > 10$ GeV for the SFOC pair
	$N_{\text{jets}} \geq 3$
$3\ell + 1\tau_{\text{had}}$	3ℓ selection, except:
	One medium τ_{had} candidate, with charge opposite to the total charge of the light leptons
	The two same-charge light leptons must be tight and have $p_{\text{T}} > 10$ GeV
	The opposite-charge light lepton must be loose and isolated

these channels is described in detail in the following. Details for the other channels can be found in [4].

3.5.1. 2ℓSS channel

Events with exactly two reconstructed loose light leptons with same electric charge and zero τ_{had} candidates are selected in the 2ℓSS channel. To suppress the non-prompt light lepton background from b-hadron decays in $t\bar{t}$, single-top and tW production or photon conversions, the leptons are required to have a $p_{\text{T}} > 20$ GeV and to fulfil the very tight selection. This includes cuts on the non-prompt light lepton BDT and on the charge misassignment veto BDT, which will be described in section 3.6. The events in the signal region are required to have at least 4 jets including exactly one or two b-tagged jets.

The dominant backgrounds are $t\bar{t}V$ production and non-prompt light leptons. Two independent BDTs are trained using TMVA [117] to discriminate the $t\bar{t}H$ signal against these backgrounds. The input variables to the BDTs are lepton properties like transverse momenta of the leptons, jet and b-tagged jet multiplicities, angular distances between the leptons and closest jets and the missing transverse momentum (E_T^{miss}). The final BDT output is the linear combination of the two BDTs with a maximised signal significance. Its pre-fit distribution is shown in figure 3.5 (left) and data agrees well with the prediction.
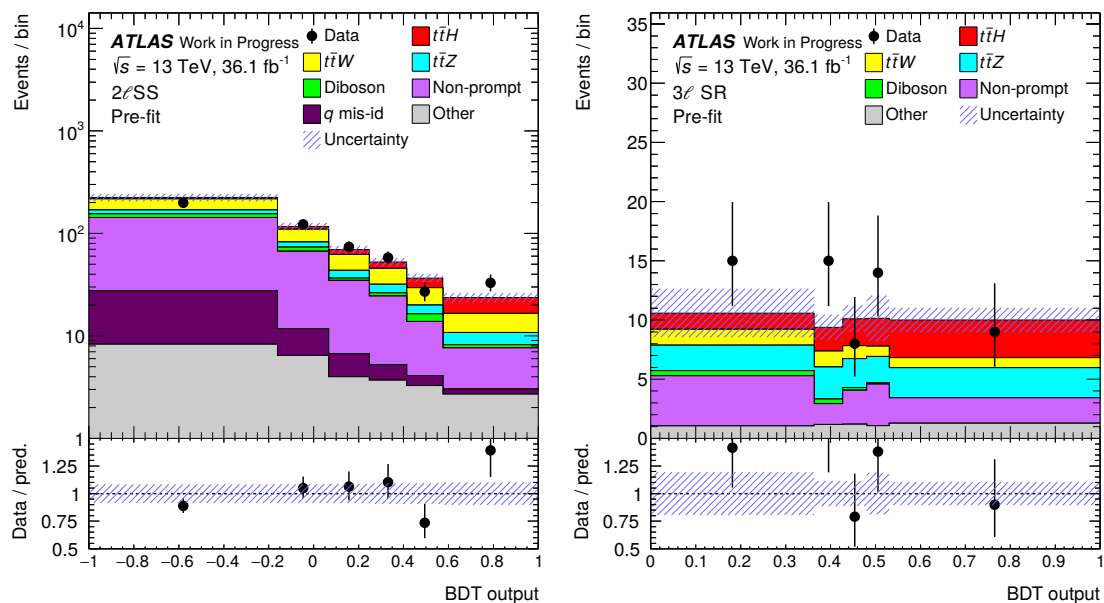
Figure 3.5.: Pre-fit distribution of discriminants in (left) 2ℓSS and (right) 3ℓ SR. The observed data events are compared to the pre-fit yields of total background and signal at expected $\mu_{t\bar{t}H} = 1$. The blue shaded area indicates the total systematic uncertainty on the expectation.

3.5.2. 3ℓ channel

The 3ℓ channel selects events with exactly three reconstructed light leptons and zero medium τ_{had} candidates. The sum of light-lepton charges is required to be ± 1 as expected in the signal process. The lepton with opposite charge is denoted as lepton 0 (ℓ_0), the lepton with the smaller angular distance to ℓ_0 is called lepton 1 (ℓ_1) and the remaining one (ℓ_2). The same-charge leptons (ℓ_1 and ℓ_2) are chosen to be very tight and to have $p_T > 15$ GeV. The opposite-charge lepton (ℓ_0) is loose, isolated and passes the non-prompt light-lepton BDT. The $t\bar{t}Z$ background is reduced by a Z-veto, removing events with same-flavour opposite-charge (SFOC) lepton pairs with an invariant mass inside a window of 10 GeV around the Z boson mass: $|m(\ell^+\ell^-) - 91.2$ GeV$| > 10$ GeV. Low

mass resonances are suppressed by the requiring a minimum of $m(\ell^+\ell^-) > 12\,\text{GeV}$ for all SFOC lepton pairs. Potential background from $Z \rightarrow \ell\ell\gamma^* \rightarrow \ell\ell\ell'(\ell')$ where one lepton has very low momentum and is not reconstructed, is removed by applying the Z-veto on the three lepton invariant mass: $|m(3\ell) - 91.2\,\text{GeV}| > 10\,\text{GeV}$.

A five-dimensional BDT using the XGBoost library [118] discriminates different target categories against all other events. These target categories are the $t\bar{t}H$ signal and the four background processes of $t\bar{t}W$, $t\bar{t}Z$, $t\bar{t}$ and diboson production. The most important input variables to the BDT are the jet and b-tagged jet multiplicities, the transverse momenta of the leptons and angular distances of leptons to closest jets or b-tagged jets.

3.5.2.1. Standard event classification

In the standard 3ℓ analysis, presented in [4], the five binned BDTs are used in the classification procedure with a probability density estimation method (PDE-Foam) [119] to build orthogonal regions enhanced in the different target categories for the signal and different background processes. The region targeting the $t\bar{t}H$ signal is the signal region (SR) and uses five bins of the $t\bar{t}H$ discriminant, which maximise the signal significance. Its pre-fit distribution is shown in figure 3.21 (right) and good agreement of data with prediction is observed. The four other regions are used as single event-count control regions (CRs). In the classification process, the Z-veto is removed and then applied to the $t\bar{t}H$ SR and the $t\bar{t}W$ and $t\bar{t}$ CRs to suppress backgrounds with Z bosons. The data-driven background estimate for $t\bar{t}$ is used in the classification, while simulated samples are used in the BDT training.

3.5.2.2. Alternative event classification

Here I present my studies for an alternative categorisation of the 3ℓ channel with similar performance as the standard event classification. It uses three of the five BDTs. Two orthogonal regions are defined including or excluding possible Z-boson candidates.

The first region is the so called Z-depleted SR for $t\bar{t}H$. In this region events are vetoed which have an opposite sign, same flavour lepton pair with an invariant mass of $|m(\ell^+\ell^-) - 91.2\,\text{GeV}| \leq 10\,\text{GeV}$. It has a signal over background ratio of about 9.1%. In the extraction of results (fit) the shape of the $t\bar{t}H$ event BDT weight against all other backgrounds is used with an automatic binning applied with a total of seven bins, optimising the significance.

The second region is the so called Z-enriched CR for $t\bar{t}Z$ and diboson (VV) backgrounds where events are selected which have at least one pair of leptons fulfilling the requirement of $|m(\ell^+\ell^-) - 91.2\,\text{GeV}| \leq 10\,\text{GeV}$. It has an overall $t\bar{t}H$ signal over background ratio of about 1.3 %. Here the shape of the difference of $t\bar{t}Z$ and VV BDT is used in the fit according to the formula ($t\bar{t}Z$ BDT $-$ VV BDT) with in total three bins.

In figure 3.6 the pre-fit distribution of the discriminants are shown. A good agreement of the observed events with the prediction is observed. In the Z-depleted SR the signal is flatly distributed over the BDT bins with enhanced signal over background ratio at the
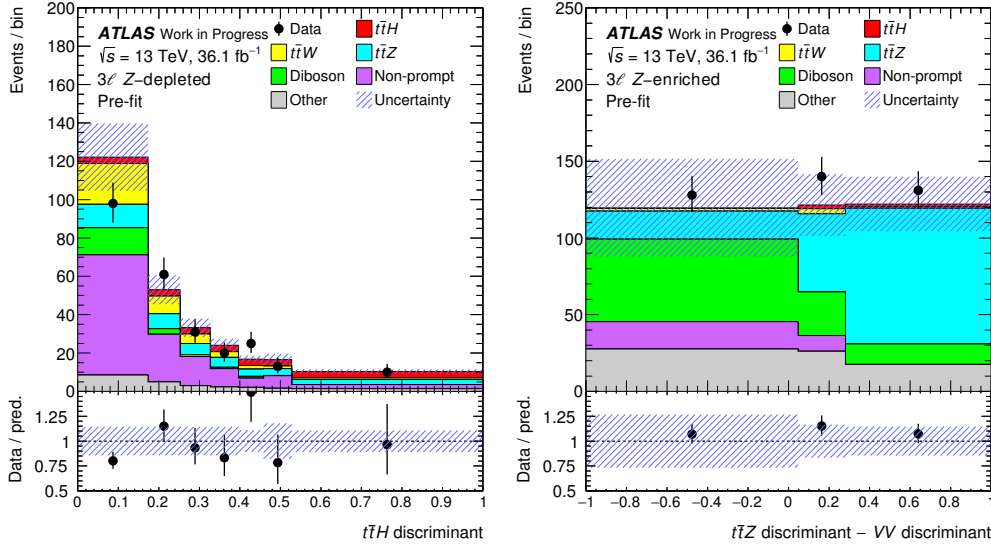
Figure 3.6.: Pre-fit distribution of discriminants in (left) Z-depleted signal region: $t\bar{t}H$ discriminant and (right) Z-enriched control region: $(t\bar{t}Z$ discriminant $-$ VV discriminant$)$. The blue shaded area indicates the total systematic, MC and data-driven statistical uncertainties.

rightmost bins. The BDT difference used in the Z-enriched CR separates well the $t\bar{t}Z$ background on the right from the VV background on the left. Table 3.5 summarises the expected (pre-fit) yields in these two regions including full systematic uncertainties.

Table 3.5.: Pre- and post-fit yields in alternative 3ℓ fit with Z-depleted signal and Z-enriched control region and fixed $t\bar{t}V$ normalisation. The uncertainties include statistical and systematic uncertainties as well as the observed uncertainties on $\mu_{t\bar{t}H}$ in the post-fit yields for the $t\bar{t}H$ contribution.

Category	Non-prompt	$t\bar{t}W$	$t\bar{t}Z$	Diboson	Other	Total Bkgd.	$t\bar{t}H$	Data
			Pre-fit yields					
3ℓ Z-dep.	126 ± 31	43 ± 6	41 ± 5	20 ± 11	24 ± 5	253 ± 33	23 ± 3	258
3ℓ Z-enr.	28 ± 8	6.0 ± 0.9	158 ± 24	96 ± 53	71 ± 25	359 ± 64	4.7 ± 0.5	399
			Post-fit yields					
3ℓ Z-dep.	103 ± 16	42 ± 6	43 ± 4	22 ± 7	25 ± 5	234 ± 17	32 ± 16	258
3ℓ Z-enr.	25 ± 6	6.0 ± 0.8	166 ± 19	108 ± 30	80 ± 25	385 ± 24	6.4 ± 3.3	399

3.6. Backgrounds

In the following the backgrounds in the 2ℓSS and 3ℓ channels are described. The details for the other channels can be found in [4].

3.6.1. Irreducible backgrounds with prompt leptons

The main irreducible background sources are associated W or Z boson production with a top quark pair ($t\bar{t}W$, $t\bar{t}Z$) and diboson production (VV). Those processes have similar final states as the $t\bar{t}H$ signal. Their estimates rely on Monte Carlo (MC) simulation and are validated in 3ℓ control regions (CRs), defined by the standard classification, described in section 3.5.2. In figure 3.7 the pre-fit distribution of the jet multiplicity is shown for both $t\bar{t}Z$ and $t\bar{t}W$ CR. The distributions of observed and expected events agree well.
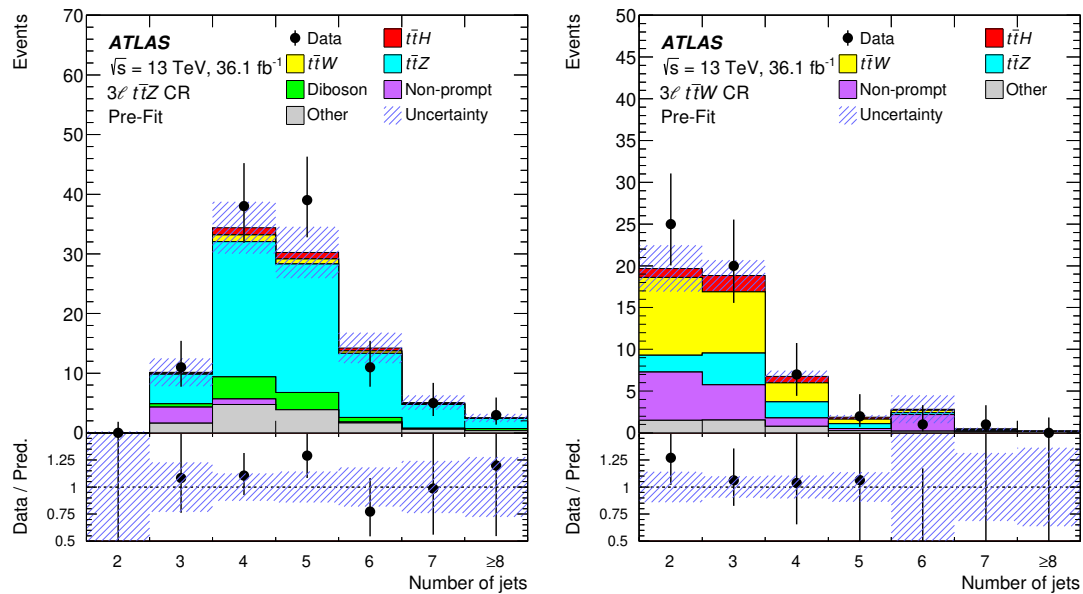
Figure 3.7.: Pre-fit distribution of the jet multiplicity in the (left) $t\bar{t}Z$ and (right) $t\bar{t}W$ CR. The blue shaded area indicates the total systematic and statistical uncertainties [4].

Further rare backgrounds of $t\bar{t}WW$, tH, tZ, four-top, triboson and WtZ production are estimated from MC simulation, too.

To account for differences in data and MC simulation each selected MC event gets a weight applied, which is a product of following weights:

- pile-up re-weighting accounts for the difference of the pile-up (average number of simultaneous interactions per bunch crossing) distribution (see figure 2.2);

- *b*-tagging weight accounts for the difference of *b*-tagging efficiency and light- and *c*-quark rejection for the selected jets in the event (see figure 2.24);

- lepton scale-factors account for differences in trigger, identification, reconstruction and isolation efficiency (see figures 2.15–2.17 for electrons, figures 2.18 and 2.19 for muons and figures 2.25 and 2.26);

- JVT (jet-vertex-tagger) weight accounts for the differences in the JVT efficiency which is an algorithm to supress pile-up jets (see section 3.4).

3.6.2. Charge mismeasurement in the 2ℓSS channel

The events in $t\bar{t}$ with two true opposite sign leptons among which one is an electron of misassigned charge enter mainly in the 2ℓSS SR. Their origin are hard bremsstrahlung with a high-p_{T} photon, which decays asymmetrically in an electron-positron pair ($e^{\pm} \to e^{\pm}\gamma^{*} \to e^{\pm}e^{+}e^{-}$) or wrongly measured track curvatures for high-p_{T} electrons. The contribution of muons with misassigned charge is negligible for the p_{T} range which is used in this analysis.

The probability of charge misassignment $\epsilon_{\mathrm{mis\text{-}id}}$ is measured as a function of the electron's p_{T} and $|\eta|$ using a sample of Z boson decays to two electrons. Its distribution is shown in figure 3.8 (left) and it ranges from 5×10^{-5} for electrons at low $p_{\mathrm{T}} < 90\,\mathrm{GeV}$ and low $|\eta| < 0.6$ to 10^{-2} at high $p_{\mathrm{T}} > 130\,\mathrm{GeV}$ and high $|\eta| > 2$. These probabilities
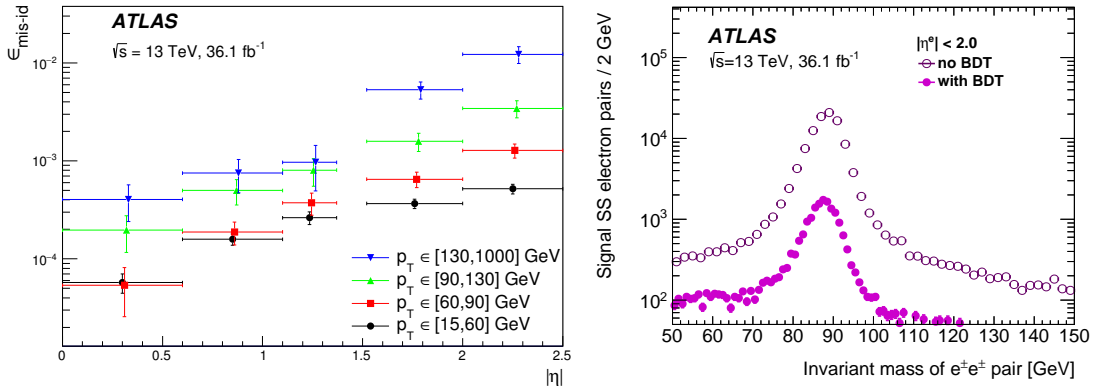
Figure 3.8.: (Left) electron charge misassignment rates for different ranges of p_{T} in dependency of $|\eta|$ [4] and (right) distribution of invariant mass of same-charge electron pairs with and without charge misassignment BDT cut applied [120].

are used to define the event weights $\omega_{\mathrm{mis\text{-}id}}$:

$$\omega_{\mathrm{mis\text{-}id}} = \epsilon_{\mathrm{mis\text{-}id},1}(1 - \epsilon_{\mathrm{mis\text{-}id},2}) + \epsilon_{\mathrm{mis\text{-}id},2}(1 - \epsilon_{\mathrm{mis\text{-}id},1}) \tag{3.3}$$

with $\epsilon_{\text{mis-id},k}$ the chosen charge misassignment probability in the corresponding p_T-$|\eta|$ bin for lepton k. Those weights are applied on the data events selected in the 2ℓSS SR, but reverting the same-charge requirement. The resulting yield constitutes the estimate of the background contribution originating from charge mismeasured electrons.

The systematic uncertainty on $\omega_{\text{mis-id}}$ includes the statistical uncertainty of the sample of $Z \rightarrow ee$ events, the comparison between the measured rates and rates when using truth matching in the $Z \rightarrow ee$ MC sample and the variations of the yield when the width of the selection of invariant masses for the Z boson peak is varied. The resulting relative systematic uncertainty is of about 30%.

To reduce the background of charge misassigned electrons a BDT discriminant is build using the electron cluster-related variables and the track parameters as input. At the chosen BDT cut with a 95% efficiency for electrons with correct charge, a rejection factor for electrons with wrong charge of 17 is obtained. This is demonstrated in figure 3.8 (right), where the distribution of the invariant mass of same-charge electrons is shown before and after the BDT cut application in a signal region with two same-charge electrons of a search for supersymmetry [120].

In the 2ℓSS channel the electrons with misassigned charge contribute with 33 ± 11 events, corresponding to 7% of the total background.

3.6.3. Non-prompt light leptons in 2ℓSS and 3ℓ channels

The reducible backgrounds have at least one fake, non-prompt or charge misreconstructed lepton. Non-prompt light leptons originate mainly from b-hadron decays in $t\bar{t}$, single-top and tW production or photon conversions. They are the dominant background source in the 2ℓSS, 2ℓSS+1τ_{had} and 3ℓ SRs.

To reject non-prompt leptons from b-hadron decays, dedicated lepton BDT discriminants for both electrons and muons have been developed achieving a rejection factor of 20 with high prompt lepton efficiencies. This so called 'non-prompt lepton BDT' uses sensitive input variables such as the angular distance between leptons and jets, b-tagging algorithm output, lepton isolation, number of tracks in the jet and ratio between lepton p_T and jet p_T. The efficiencies for prompt leptons are measured in data using Z boson decays events. They are shown in figure 3.9. The difference of data to MC prediction are at most 10% at low p_T (see ratio plots) and are taken into account in the lepton scale-factors applied in the MC event weights for the irreducible backgrounds, described in section 3.6.1.

The so called matrix method [121, 122] is used to obtain a fully data-driven estimate of the fake-lepton background in the 2ℓSS and the 3ℓ channel. The method uses probabilities for loose leptons to be prompt ε_r or non-prompt ε_f in event weights $\omega_{\text{non-prompt}}$. The background estimate is obtained by applying those weights on a selection of data events with loose same-sign leptons instead of tight ones in the signal regions. The loose leptons are defined according to table 3.3, denoted as L, removing isolation and other tight requirements.

The probabilities ε_r and ε_f are measured in the 2ℓ control regions (CRs), which have
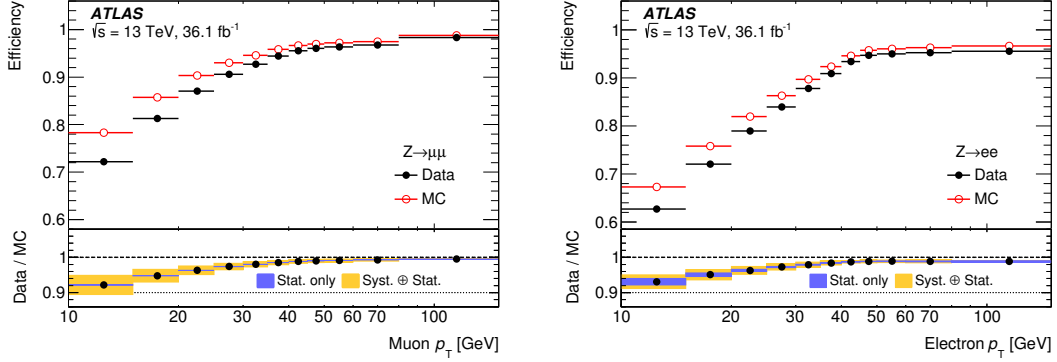
Figure 3.9.: The efficiencies for prompt leptons in dependency of the lepton p_T in data and MC simulation for (left) muons and (right) electrons [4].

a close selection to the 2ℓSS SR. The CRs are defined at lower jet multiplicities of $2 \leq N_{jets} \leq 3$ and are therefore orthogonal to the SR. The events in the CRs are required to have one tight and one loose lepton with $p_T > 20\,(15)\,\text{GeV}$ for 2ℓSS (3ℓ) estimate. As in the signal regions, events with τ_{had} are vetoed.

Using this CRs, the efficiencies needed for the matrix method are calculated as follows:

- The efficiency for loose prompt leptons to be tight ε_r is estimated from oppositely charged opposite-flavour events, which are dominated by $t\bar{t}$ decays. A tag-and-probe method is used, where the tagged light lepton is a tight (T) lepton which is trigger matched to one of the single-lepton triggers (see table 3.2). The probability is defined as

$$\varepsilon_r = \frac{N_{data}^T - N_{non\text{-}prompt}^T}{N_{data}^L - N_{non\text{-}prompt}^L} \tag{3.4}$$

  with number of events in data with tight (loose) probe lepton $N_{data}^{T(L)}$. The number of non-prompt background events $N_{non\text{-}prompt}^{T(L)}$ with tight (loose) probe lepton is a small contribution mostly coming from $t\bar{t}$ and single-top and therefore estimated from MC simulation. A conservative uncertainty of 30% has been assigned to this number. It is measured as a function of the lepton p_T and its distribution is shown in figure 3.10 (left). It shows an increasing dependency on the lepton p_T because the non-prompt leptons are softer in p_T than the prompt leptons.

- The efficiency for loose non-prompt leptons to be tight ε_f is done in a same-charge opposite-flavour CR for electrons and in a same-charge di-muon CR for muons. In the electron case this takes advantage of the very low probability of a tight, trigger matched muon to be non-prompt and additionally reduces the charge misassignment contribution compared to di-electron events. In the muon case opposite-flavour events are not suitable because in case of both leptons to be tight, the probability of non-prompt leptons becomes too small. Therefore di-muon events are used in a tag-and-probe approach. In case of two trigger matched tight muons, the
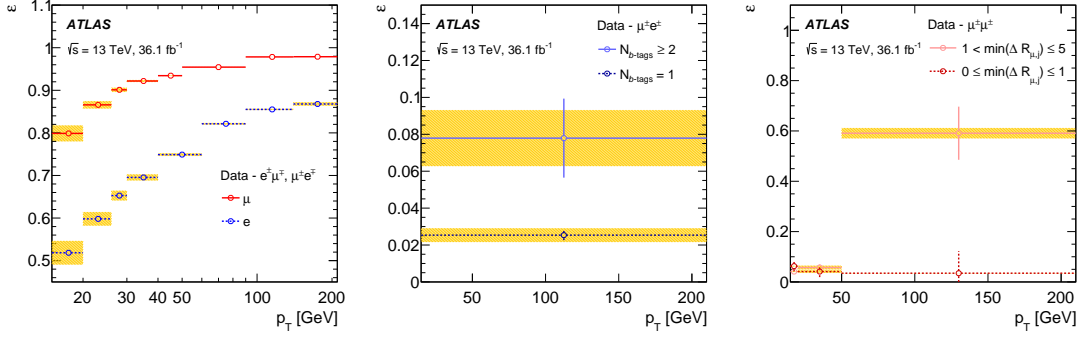
84

Figure 3.10.: Efficiencies to be tight for loose (left) prompt leptons, (middle) non-prompt electrons and (right) non-prompt muons. The error bars indicate the statistical and the yellow bands indicate the total systematic uncertainties [4].

low-p_{T} muon is chosen as the non-prompt lepton. The efficiency is defined as

$$\varepsilon_{\mathrm{f}} = \frac{N_{\mathrm{data}}^{\mathrm{T}} - N_{q\ \mathrm{mis\text{-}id}}^{\mathrm{T}} - N_{\mathrm{prompt\ (MC)}}^{\mathrm{T}}}{N_{\mathrm{data}}^{\mathrm{L}} - N_{q\ \mathrm{mis\text{-}id}}^{\mathrm{L}} - N_{\mathrm{prompt\ (MC)}}^{\mathrm{L}}} \tag{3.5}$$

with number of events in data with tight (loose) probe lepton $N_{\mathrm{data}}^{\mathrm{T(L)}}$. In the electron case the charge misassignment contribution $N_{q\ \mathrm{mis\text{-}id}}^{\mathrm{T(L)}}$ needs to be subtracted. Its contribution is estimated using the method described in section 3.6.2. The subtraction of prompt backgrounds $N_{\mathrm{prompt\ (MC)}}^{\mathrm{T(L)}}$ is non-negligible for both electron and muon case and their contribution is predicted from MC simulation. Systematic uncertainties are assigned amongst others to the $t\bar{t}W$ and diboson subtraction which are later correlated with the cross-section uncertainties on these background processes. Additionally to binning in p_{T} the ε_{f} are binned in the number of b-tagged jets for electrons to account for different non-prompt lepton composition at $N_{b-\mathrm{tags}} = 1$ and $N_{b-\mathrm{tags}} \geq 2$. In the case of muons an additional binning in angular distance to the closest jet $\Delta R_{\mu,j}$ reduces the dependency on the effect of nearby jets. The chosen binning is the best compromise between proper non-prompt modelling and limited statistics in the control regions. The measured non-prompt efficiencies are shown in figure 3.10 (middle) for electrons and (right) for muons.

In the matrix method the data events with loose lepton selection get an event weight $\omega_{\mathrm{non\text{-}prompt}}$ assigned according to different categories. These categories are

- both leptons tight (TT),

- leading lepton (in p_{T}) tight and second lepton loose but not tight, denoted as (T$\bar{\mathrm{T}}$),

- subleading lepton (in p_{T}) tight and other (first) lepton loose but not tight ($\bar{\mathrm{T}}$T) and

- both leptons loose but not tight ($\bar{\mathrm{T}}\bar{\mathrm{T}}$).

This is mapped to the categories of both leptons prompt (rr), leading lepton prompt and subleading lepton non-prompt (rf), leading lepton non-prompt and subleading lepton prompt (fr) and both leptons non-prompt (ff) via a 4×4 matrix

$$
\begin{pmatrix} N^{\mathrm{TT}} \\ N^{\mathrm{T\bar{T}}} \\ N^{\mathrm{\bar{T}T}} \\ N^{\mathrm{\bar{T}\bar{T}}} \end{pmatrix} = \begin{pmatrix} \varepsilon_{\mathrm{r},1}\varepsilon_{\mathrm{r},2} & \varepsilon_{\mathrm{r},1}\varepsilon_{\mathrm{f},2} & \varepsilon_{\mathrm{f},1}\varepsilon_{\mathrm{r},2} & \varepsilon_{\mathrm{f},1}\varepsilon_{\mathrm{f},2} \\ \varepsilon_{\mathrm{r},1}\bar{\varepsilon}_{\mathrm{r},2} & \varepsilon_{\mathrm{r},1}\bar{\varepsilon}_{\mathrm{f},2} & \varepsilon_{\mathrm{f},1}\bar{\varepsilon}_{\mathrm{r},2} & \varepsilon_{\mathrm{f},1}\bar{\varepsilon}_{\mathrm{f},2} \\ \bar{\varepsilon}_{\mathrm{r},1}\varepsilon_{\mathrm{r},2} & \bar{\varepsilon}_{\mathrm{r},1}\varepsilon_{\mathrm{f},2} & \bar{\varepsilon}_{\mathrm{f},1}\varepsilon_{\mathrm{r},2} & \bar{\varepsilon}_{\mathrm{f},1}\varepsilon_{\mathrm{f},2} \\ \bar{\varepsilon}_{\mathrm{r},1}\bar{\varepsilon}_{\mathrm{r},2} & \bar{\varepsilon}_{\mathrm{r},1}\bar{\varepsilon}_{\mathrm{f},2} & \bar{\varepsilon}_{\mathrm{f},1}\bar{\varepsilon}_{\mathrm{r},2} & \bar{\varepsilon}_{\mathrm{f},1}\bar{\varepsilon}_{\mathrm{f},2} \end{pmatrix} \begin{pmatrix} N^{\mathrm{rr}} \\ N^{\mathrm{rf}} \\ N^{\mathrm{fr}} \\ N^{\mathrm{ff}} \end{pmatrix} \tag{3.6}
$$

with the prompt and non-prompt efficiencies $\varepsilon_{\mathrm{r},k}$ and $\varepsilon_{\mathrm{f},k}$ for leading ($k = 1$) and subleading ($k = 2$) lepton. The complementary efficiencies $\bar{\varepsilon}_{r(f)}$ are the probabilities for loose prompt (non-prompt) leptons to be not tight. They are related to the prompt (non-prompt) efficiencies by $\bar{\varepsilon}_{r(f)} = 1 - \varepsilon_{r(f)}$. To obtain the number of events with two tight leptons among which least one is non-prompt $N_{\mathrm{TT}}^{\mathrm{f}}$ the matrix needs to be inverted:

$$
\begin{pmatrix} N^{\mathrm{rr}} \\ N^{\mathrm{rf}} \\ N^{\mathrm{fr}} \\ N^{\mathrm{ff}} \end{pmatrix} = \begin{pmatrix} \varepsilon_{\mathrm{r},1}\varepsilon_{\mathrm{r},2} & \varepsilon_{\mathrm{r},1}\varepsilon_{\mathrm{f},2} & \varepsilon_{\mathrm{f},1}\varepsilon_{\mathrm{r},2} & \varepsilon_{\mathrm{f},1}\varepsilon_{\mathrm{f},2} \\ \varepsilon_{\mathrm{r},1}\bar{\varepsilon}_{\mathrm{r},2} & \varepsilon_{\mathrm{r},1}\bar{\varepsilon}_{\mathrm{f},2} & \varepsilon_{\mathrm{f},1}\bar{\varepsilon}_{\mathrm{r},2} & \varepsilon_{\mathrm{f},1}\bar{\varepsilon}_{\mathrm{f},2} \\ \bar{\varepsilon}_{\mathrm{r},1}\varepsilon_{\mathrm{r},2} & \bar{\varepsilon}_{\mathrm{r},1}\varepsilon_{\mathrm{f},2} & \bar{\varepsilon}_{\mathrm{f},1}\varepsilon_{\mathrm{r},2} & \bar{\varepsilon}_{\mathrm{f},1}\varepsilon_{\mathrm{f},2} \\ \bar{\varepsilon}_{\mathrm{r},1}\bar{\varepsilon}_{\mathrm{r},2} & \bar{\varepsilon}_{\mathrm{r},1}\bar{\varepsilon}_{\mathrm{f},2} & \bar{\varepsilon}_{\mathrm{f},1}\bar{\varepsilon}_{\mathrm{r},2} & \bar{\varepsilon}_{\mathrm{f},1}\bar{\varepsilon}_{\mathrm{f},2} \end{pmatrix}^{-1} \begin{pmatrix} N^{\mathrm{TT}} \\ N^{\mathrm{T\bar{T}}} \\ N^{\mathrm{\bar{T}T}} \\ N^{\mathrm{\bar{T}\bar{T}}} \end{pmatrix} \tag{3.7}
$$

and plugged into the formula

$$
N_{\mathrm{TT}}^{\mathrm{f}} = N_{\mathrm{TT}}^{\mathrm{rf}} + N_{\mathrm{TT}}^{\mathrm{fr}} + N_{\mathrm{TT}}^{\mathrm{ff}} = \varepsilon_{\mathrm{r},1}\varepsilon_{\mathrm{f},2}N^{\mathrm{rf}} + \varepsilon_{\mathrm{r},2}\varepsilon_{\mathrm{f},1}N^{\mathrm{fr}} + \varepsilon_{\mathrm{f},1}\varepsilon_{\mathrm{f},2}N^{\mathrm{ff}}. \tag{3.8}
$$

This leads to rather complicated expressions for the event weights. The weights are then applied to all events with loose instead of tight leptons in the 2ℓSS and 3ℓ signal and control regions. The estimate for 3ℓ is only treating the two same-charge leptons of the final state. Simulation shows, that the opposite-charge lepton is in 97% prompt and hence it is assumed to be always prompt.

Because the non-prompt electron origin is substantially more likely to come from photon conversions in the SRs than in the non-prompt efficiency CRs, this contribution is treated with a dedicated extrapolation factor estimated from simulation. A conservative uncertainty of 40% is assigned to this γ-conversion fraction.

To validate the matrix-method a closure test is done on simulated $t\bar{t}$ events, comparing the results from matrix-method with the prediction from simulation. The difference has been found to be less than 20% and is treated as systematic uncertainty.

The estimate of the non-prompt lepton background is validated in 2ℓSS validation regions, which are shown in figure 3.11. Good modelling is observed for both muons and electrons.

The estimated total yield of non-prompt lepton background is 233 ± 39 (126 ± 31) which corresponds to 48% (49%) of the total background in the 2ℓSS (3ℓ Z-depleted) SR.
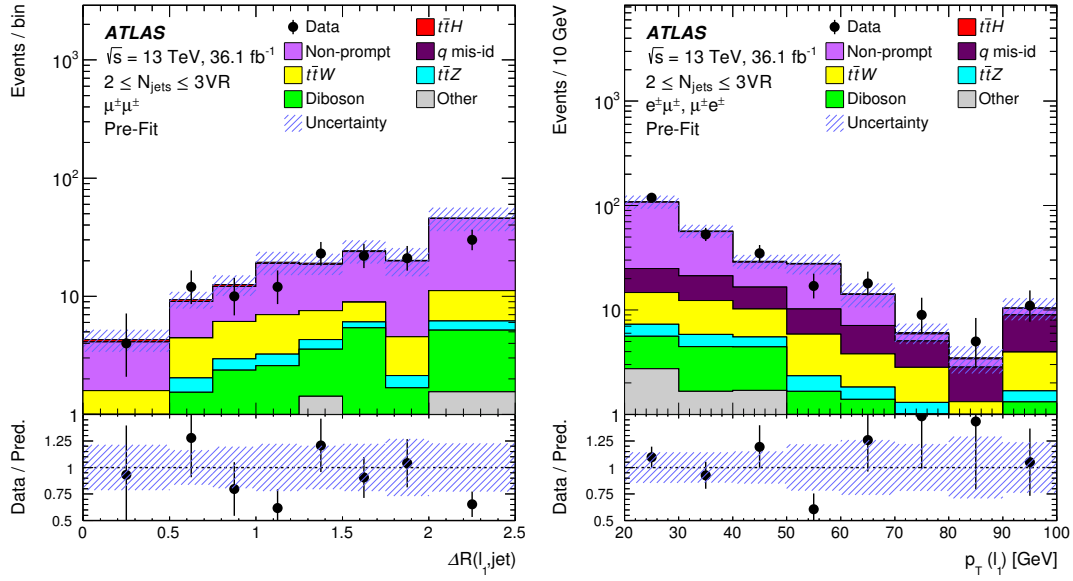
Figure 3.11.: Validation of matrix method estimate of non-prompt lepton background in 2ℓSS validation regions with low jet multiplicity $2 \leq N_{\text{jets}} \leq 3$ for (left) muons and (right) electrons [4].

3.6.4. Background composition in signal and control regions

Figure 3.12 shows the background composition for the alternative event classification in the 3ℓ channel. The background composition for all $t\bar{t}H \rightarrow$ multilepton channels is
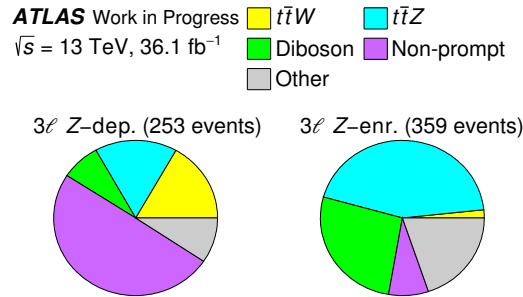
Figure 3.12.: Pre-fit background composition in the (left) 3ℓ Z-depleted SR and (right) 3ℓ Z-enriched CR of the alternative 3ℓ event classification.

shown in figure 3.13.

The SRs of the two most significant channels 2ℓSS and 3ℓ are dominated by the contribution of non-prompt light lepton background, while in 4ℓ this background plays a minor role. In the regions with τ_{had} the background of fake τ_{had} dominates.

Figure 3.13.: Pre-fit background composition in signal and control regions [4].

3.7. Systematic uncertainties

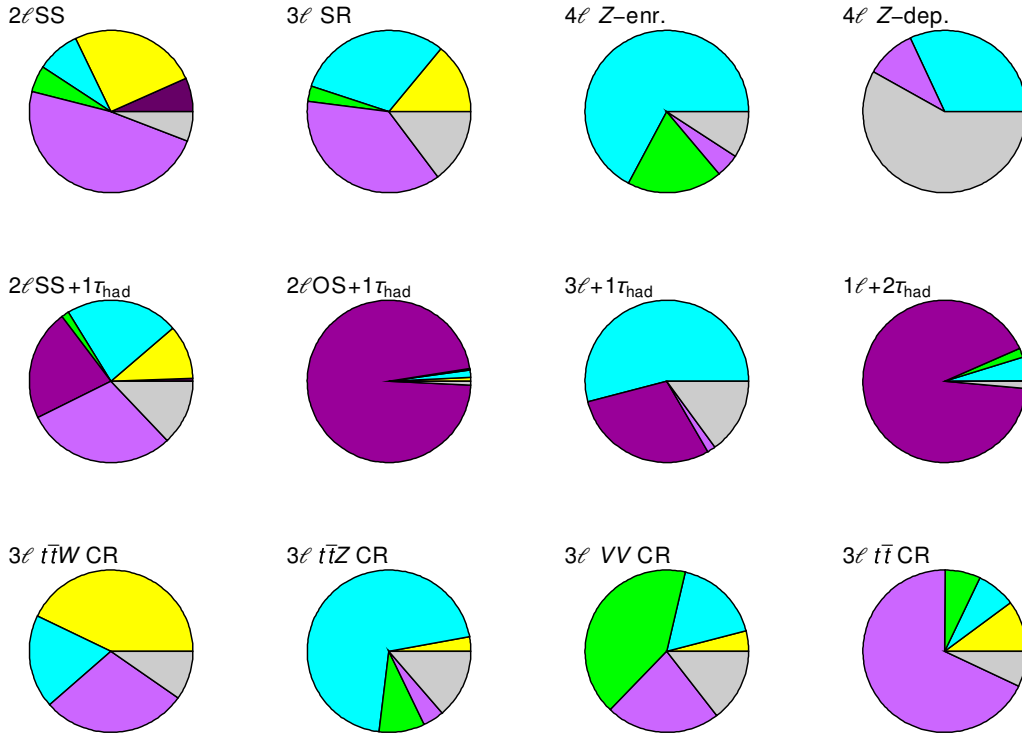In table 3.6 all sources of systematic uncertainties are summarised. Three groups of systematic uncertainties are considered. They are included in the fit of data events to expectation in discriminant distributions through the so-called nuisance parameters (NPs) allowing for changes in the normalisation and the shape of these discriminant distributions. The NPs can therefore be of type normalisation-only (N), shape-only (S) or combined shape and normalisation (SN). The normalisation of an uncertainty has an impact on the total event yield of a signal or background sample. An uncertainty which is affecting the shape of a discriminating distribution is taken into account by the corresponding variation of input histograms in the fit.

The experimental systematic uncertainties include an normalisation-only uncertainty related to the integrated luminosity the full 2015 and 2016 dataset of $\pm 2.1\,\%$. This uncertainty is estimated from a calibration using the *x-y* beam-separation scans performed in August 2015 and May 2016 with the method described in [123]. The pile-up reweighting uncertainty accounts for possible differences in the pile-up profile between data and

Table 3.6.: Sources of systematic uncertainties with numbers and types of NPs. The different types N, S and SN stand for normalisation-only, shape-only and combined shape and normalisation NPs respectively [4].

Systematic uncertainty	Type	Components
Luminosity	N	1
Pileup reweighting	SN	1
Physics Objects		
Electron	SN	6
Muon	SN	15
τ_{had}	SN	10
Jet energy scale and resolution	SN	28
Jet vertex fraction	SN	1
Jet flavor tagging	SN	126
$E_{\text{T}}^{\text{miss}}$	SN	3
Total (Experimental)	–	191
Data-driven non-prompt/fake leptons and charge misassignment		
Control region statistics	SN	38
Light-lepton efficiencies	SN	22
Non-prompt light-lepton estimates: non-closure	N	5
γ-conversion fraction	N	5
Fake τ_{had} estimates	N/SN	12
Electron charge misassignment	SN	1
Total (Data-driven reducible background)	–	83
$t\bar{t}H$ **modeling**		
Cross section	N	2
Renormalization and factorization scales	S	3
Parton shower and hadronization model	SN	1
Higgs boson branching fraction	N	4
Shower tune	SN	1
$t\bar{t}W$ **modeling**		
Cross section	N	2
Renormalization and factorization scales	S	3
Matrix-element MC event generator	SN	1
Shower tune	SN	1
$t\bar{t}Z$ **modeling**		
Cross section	N	2
Renormalization and factorization scales	S	3
Matrix-element MC event generator	SN	1
Shower tune	SN	1
Other background modeling		
Cross section	N	15
Shower tune	SN	1
Total (Signal and background modeling)	–	41
Total (Overall)	–	315

MC. The systematic uncertainties on physics objects are related to the reconstruction and the identification of the leptons and jets as well as missing transverse energy $E_{\text{T}}^{\text{miss}}$, and are treated as uncorrelated NPs. The light-lepton reconstruction, identification, isolation and trigger efficiency uncertainties are negligible. The τ_{had} identification efficiency uncertainty is $\pm 6\,\%$. The total uncertainty on the energy scale and resolution of a recon-

structed jet is 1–5.5 % depending on the jet p_{T}. The uncertainties on jet flavour tagging (b-tagging) efficiencies are 2 % for b-jets, 10 % for c-jets and τ_{had} and 30 % for light jets.

The uncertainties on the data-driven reducible background originate from the estimates of the non-prompt light-leptons, the electron charge misassignment and the fake τ_{had}. The statistical uncertainties related to the CRs where the weights are applied to estimate the background (e.g. non-prompt lepton background in 2ℓSS or 3ℓ) are treated as one-per-bin NPs with no correlation. For instance, in 2ℓSS there are 6 NPs for the non-prompt lepton and 6 NPs for the electron charge misassignment estimate contributing to the total number of 38 NPs.

For both signal and irreducible background estimates various modelling uncertainties are treated to account for simulation differences using different generators or MC simulation options. The major uncertainties are coming from the cross section scale and acceptance in the $t\bar{t}H$, $t\bar{t}W$ and $t\bar{t}Z$ processes. In figure 3.14 systematics distributions of the shape and normalisation uncertainties $t\bar{t}H$ parton shower and hadronisation model and $t\bar{t}Z$ event generator are shown. They have an overall impact (normalisation) of 4% on the $t\bar{t}H$ sample with $H \to WW$ and 8.5% on the $t\bar{t}Z$ sample respectively. As the solid lines are almost flat for the $t\bar{t}H$ parton shower no shape dependence is observed here after smoothing. The smoothing is a procedure which is used to decrease the fluctuations in shape systematics due to low statistics. Studies on this smoothing are presented in appendix B. For the $t\bar{t}Z$ generator uncertainty both normalisation and shape have a non-negligible impact.
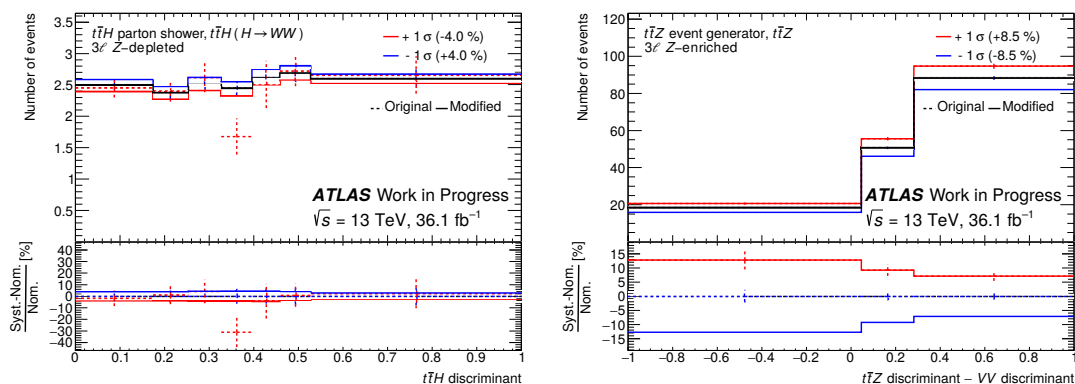

Figure 3.14.: Distribution of (left) the $t\bar{t}H$ parton shower and hadronisation model systematic on $t\bar{t}H$ sample with the H boson decaying to WW in the 3ℓ Z-depleted SR and (right) the $t\bar{t}Z$ event generator uncertainty on the $t\bar{t}Z$ sample in the 3ℓ Z-enriched CR. The black line indicates the nominal shape of the concerned sample and the red (blue) the 1σ up-(down-)variation of the systematic. The dotted lines show the distributions before the application of the smoothing procedure.

3.8. Statistical model and results

A maximum-likelihood fit with the $t\bar{t}H$ signal strength $\mu_{t\bar{t}H}$ as parameter of interest is performed in all SRs and CRs simultaneously. I have implemented the statistical analysis and have extracted the results included in the ATLAS publication [4]. Techniques of computing time optimisation (pruning and smoothing) are applied (see appendix B for further studies).

The analysis has been done in a 'blinded' way. This means that all configuration and optimisation has been fixed before looking at the actual data events. To study the signal sensitivity and the fit properties a so called Asimov dataset is created, which is the sum of predicted background and signal contributions at $\mu_{t\bar{t}H} = 1$. The associated statistical uncertainty corresponds to the expected precision of the available data sample. This is used for the results of expected signal significance and uncertainties on $\mu_{t\bar{t}H}$.

3.8.1. Signal extraction in the 3ℓ channel

This section describes the results of the signal extraction using the 3ℓ Z-depleted SR and 3ℓ Z-enriched CR as described in section 3.5.2.2. The pre-fit distributions of the corresponding BDTs have been shown in figure 3.6. The default fit assumes fixed normalisation on $t\bar{t}W$ and $t\bar{t}Z$ backgrounds from MC simulation.

The fit can be performed using the normalisation of $t\bar{t}Z$ and $t\bar{t}W$ as parameters in the fit as normalisation factors $\mu_{t\bar{t}Z}$ and $\mu_{t\bar{t}W}$, respectively. Results for floating $t\bar{t}Z$ normalisation or floating both $t\bar{t}W$ and $t\bar{t}Z$ normalisation are shown as well. In the free floating case the corresponding cross-section uncertainties (QCD scale and PDF) for $t\bar{t}W$ or $t\bar{t}Z$ are removed from the fit.

The correlations amongst fit parameters are shown in figure 3.15 for fixed $t\bar{t}V$ normalisation. No strong correlations with the signal strength $\mu_{t\bar{t}H}$ are observed in the fit with fixed $t\bar{t}V$ normalisation. The highest correlation (32.3%) is observed for the non-prompt light-lepton non-closure uncertainty, which is the dominant uncertainty on the non-prompt estimate in 3ℓ (18%). The high correlation of diboson uncertainties for cross section and shower tune come from the fact, that they are of similar size (50% and 26%, respectively) and impacting mainly the same bins of the Z-enriched CR. In the case of free floating $t\bar{t}Z$ and $t\bar{t}W$ normalisation higher correlations are expected. For instance, the non-prompt light-lepton non-closure uncertainty and the $t\bar{t}W$ normalisation factor have a correlation of 60%. This originates in the fact, that both the $t\bar{t}W$ and the non-prompt light lepton background are dominating the same first bins of the $t\bar{t}H$ discriminant in the Z-depleted SR.

The fit results are summarised in table 3.7. In the case of fixed $t\bar{t}V$ normalisation, the error on the signal strength $\mu_{t\bar{t}H}$ in the Asimov fit is $^{+0.77}_{-0.70}$. The expected results use the NP pulls for the background predictions, which are observed in the fit to data. Due to a small excess of data over the SM expectation in the Z-enriched CR, the post-fit background yields are increased slightly. No significant change of the significance is observed whether the 3ℓ Z-enriched CR is included in the fit or not.

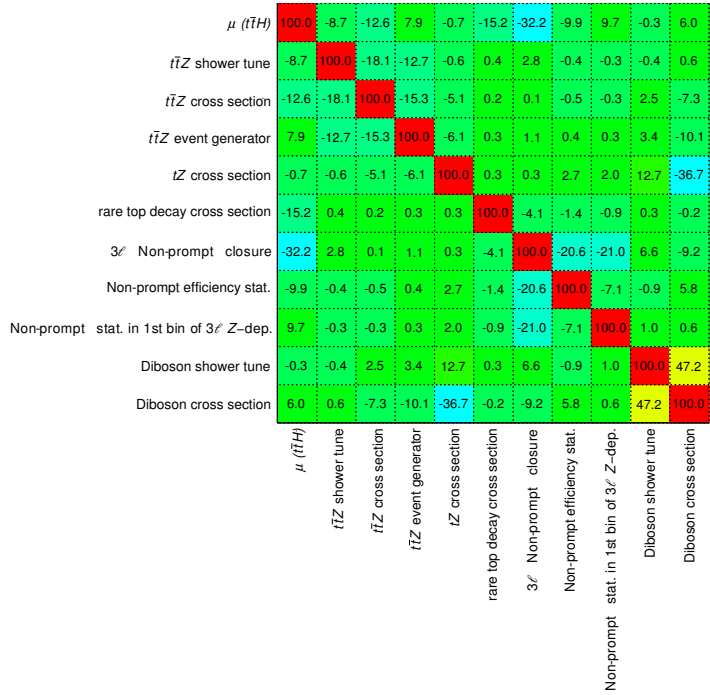|	$\mu\,(t\bar{t}H)$	$t\bar{t}Z$ shower tune	$t\bar{t}Z$ cross section	$t\bar{t}Z$ event generator	tZ cross section	rare top decay cross section	3ℓ Non-prompt closure	Non-prompt efficiency stat.	Non-prompt stat. in 1st bin of 3ℓ Z-dep.	Diboson shower tune	Diboson cross section
$\mu\,(t\bar{t}H)$	100.0	-8.7	-12.6	7.9	-0.7	-15.2	-32.2	-9.9	9.7	-0.3	6.0
$t\bar{t}Z$ shower tune	-8.7	100.0	-18.1	-12.7	-0.6	0.4	2.8	-0.4	-0.3	-0.4	0.6
$t\bar{t}Z$ cross section	-12.6	-18.1	100.0	-15.3	-5.1	0.2	0.1	-0.5	-0.3	2.5	-7.3
$t\bar{t}Z$ event generator	7.9	-12.7	-15.3	100.0	-6.1	0.3	1.1	0.4	0.3	3.4	-10.1
tZ cross section	-0.7	-0.6	-5.1	-6.1	100.0	0.3	0.3	2.7	2.0	12.7	-36.7
rare top decay cross section	-15.2	0.4	0.2	0.3	0.3	100.0	-4.1	-1.4	-0.9	0.3	-0.2
3ℓ Non-prompt closure	-32.2	2.8	0.1	1.1	0.3	-4.1	100.0	-20.6	-21.0	6.6	-9.2
Non-prompt efficiency stat.	-9.9	-0.4	-0.5	0.4	2.7	-1.4	-20.6	100.0	-7.1	-0.9	5.8
Non-prompt stat. in 1st bin of 3ℓ Z-dep.	9.7	-0.3	-0.3	0.3	2.0	-0.9	-21.0	-7.1	100.0	1.0	0.6
Diboson shower tune	-0.3	-0.4	2.5	3.4	12.7	0.3	6.6	-0.9	1.0	100.0	47.2
Diboson cross section	6.0	0.6	-7.3	-10.1	-36.7	-0.2	-9.2	5.8	0.6	47.2	100.0

Figure 3.15.: Correlation of NPs and signal strength $\mu_{t\bar{t}H}$ with fixed $t\bar{t}V$ normalisation. Only correlations of more than 15% are shown.

The fit procedure prepared using the Asimov simulation is applied on data. The observed $t\bar{t}H$ signal strength is

$$\mu_{t\bar{t}H} = 1.37\,^{+0.56}_{-0.52}\,(\text{stat.})\,^{+0.52}_{-0.45}\,(\text{syst.}) = 1.37\,^{+0.76}_{-0.69} \tag{3.9}$$

which is compatible with the SM expectation of $\mu_{t\bar{t}H} = 1$. The observed (expected) significance of this excess over background-only expectation is 2.06 (1.53) standard deviations. The post-fit distributions for this fit are shown in figure 3.16. The post-fit yields are given in table 3.5. The fit without Z-enriched CR gives the same central value for $\mu_{t\bar{t}H}$ with only slightly worse errors.

In the case of free floating $t\bar{t}Z$ normalisation, a $t\bar{t}Z$ signal strength of $\mu_{t\bar{t}Z} = 1.11\,^{+0.22}_{-0.19}$ has been observed. The expected significance decreases by about 6% and the observed $\mu_{t\bar{t}H}$ is compatible with both the SM expectation of $\mu_{t\bar{t}H} = 1$ and the observed $\mu_{t\bar{t}H}$ in the fixed normalisation case. The fit with both free floating $t\bar{t}Z$ and $t\bar{t}W$ normalisation gives similar results and uncertainties for $\mu_{t\bar{t}H}$ and $\mu_{t\bar{t}Z}$. The determination of the $t\bar{t}W$ signal strength is not favoured by this 3ℓ analysis, because no dedicated $t\bar{t}W$ CR is included in this set-up. Here a value of $\mu_{t\bar{t}W} = 0.19\,^{+0.84}_{-0.95}$ is found, compatible with the SM expectation of $\mu_{t\bar{t}W} = 1$. This is mainly determined by the first bin of the Z-depleted CR. In combination with 2ℓSS channel some sensitivity on this normalisation factor might be

Table 3.7.: Observed and expected best-fit values of the signal strength $\mu_{t\bar{t}H}$ and significances in the 3ℓ channel for fixed $t\bar{t}V$, floating $t\bar{t}Z$ and floating both $t\bar{t}Z$ and $t\bar{t}W$ normalisation. The first row represents the fit without Z-enriched CR and with fixed $t\bar{t}V$ normalisation for the alternative classification.

	Channel	Best-fit $\mu_{t\bar{t}H}$		Significance	
		Observed	Expected	Observed	Expected
alternative	3ℓ Z-dep. only	$1.37\,^{+0.78}_{-0.70}$	$1.00\,^{+0.77}_{-0.70}$	2.03σ	1.51σ
	3ℓ Z-dep. & Z-enr.	$1.37\,^{+0.76}_{-0.69}$	$1.00\,^{+0.77}_{-0.70}$	2.06σ	1.53σ
	floating $t\bar{t}Z$ $(\mu_{t\bar{t}Z} = 1.11\,^{+0.22}_{-0.19})$	$1.28\,^{+0.78}_{-0.73}$	$1.00\,^{+0.79}_{-0.73}$	1.81σ	1.44σ
	floating $t\bar{t}Z$ & $t\bar{t}W$ $(\mu_{t\bar{t}Z} = 1.14\,^{+0.22}_{-0.20},$ $\mu_{t\bar{t}W} = 0.19\,^{+0.84}_{-0.95})$	$1.57\,^{+0.90}_{-0.79}$	$1.00\,^{+0.83}_{-0.76}$	2.04σ	1.36σ
standard	standard 3ℓ	$1.76\,^{+0.86}_{-0.76}$	$1.00\,^{+0.77}_{-0.70}$	2.38σ	1.48σ
	floating $t\bar{t}Z$ & $t\bar{t}W$ $(\mu_{t\bar{t}Z} = 1.17\,^{+0.27}_{-0.23},$ $\mu_{t\bar{t}W} = 1.10\,^{+0.50}_{-0.47})$	$1.42\,^{+0.95}_{-0.88}$	$1.00\,^{+0.88}_{-0.79}$	1.64σ	1.25σ

recovered. Nevertheless, the observed (expected) signal significance over background-only hypothesis is 2.04σ (1.36σ) in this case.

The systematic uncertainties are classified as a function of their impact on the uncertainty on the signal strength $\Delta\mu_{t\bar{t}H}$ in the so-called 'ranking'. The ranking plots for the three fits with fixed $t\bar{t}V$ normalisation, free floating $t\bar{t}Z$ and both free floating $t\bar{t}Z$ and $t\bar{t}W$ normalisation are presented in figures 3.17.

The systematic uncertainties with largest impact in the fit with fixed $t\bar{t}V$ normalisation are $t\bar{t}H$ and $t\bar{t}Z$ cross-section uncertainty as well as the non-prompt light lepton non-closure uncertainty. There is a slight negative pull of the NP for this non-closure uncertainty which is driven by the slight deficit in data in the first bins of the $t\bar{t}H$ discriminant, as visible in figure 3.6. In the fits with free floating $t\bar{t}V$ normalisations, the normalisation factors have the largest impact on the uncertainty on $\mu_{t\bar{t}H}$.

In figure 3.18 the likelihood scans on the test statistics for the signal strength $\mu_{t\bar{t}H}$ are drawn for the fit with fixed and floating $t\bar{t}V$ normalisation. They show smooth behaviour and no weird features. In the case of floating $t\bar{t}V$ normalisation the parabola is wider, because the sensitivity is smaller than in the case of fixed $t\bar{t}V$ normalisation.

The analysis presented in [4] does not include this result of alternative event classification in 3ℓ, but the standard event classification, explained in section 3.5.2. The observed signal strength using this classification is

$$\mu_{t\bar{t}H} = 1.76\,^{+0.61}_{-0.57}\,(\text{stat.})\,^{+0.60}_{-0.50}\,(\text{syst.}) = 1.76\,^{+0.86}_{-0.76} \tag{3.10}$$
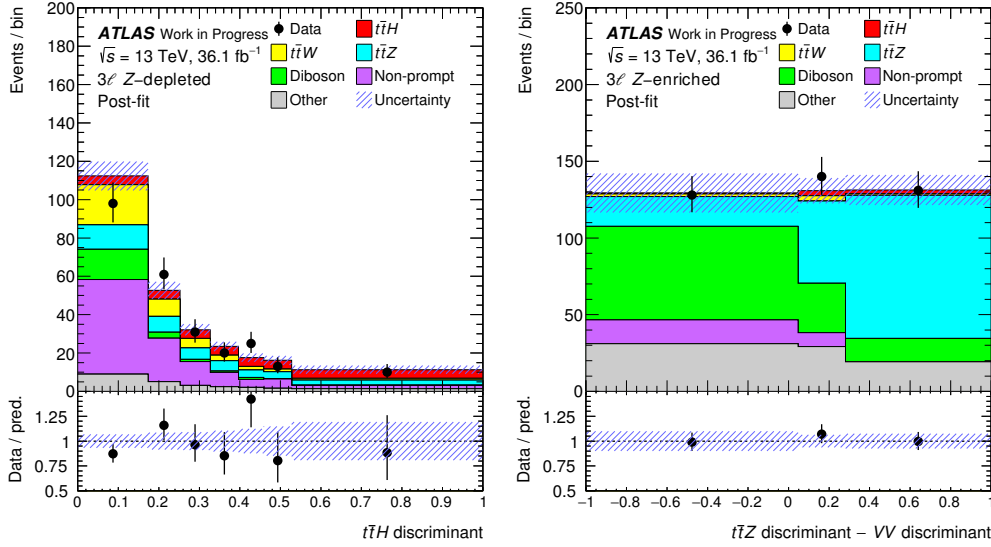
Figure 3.16.: Post-fit distribution of discriminants in (left) Z-depleted signal region: $t\bar{t}H$ discriminant and (right) Z-enriched control region: ($t\bar{t}Z$ discriminant$-$ VV discriminant) for the fit with $t\bar{t}V$ normalisations from SM expectation. The blue shaded area indicates the total systematic, MC and data-driven statistical uncertainties including the observed uncertainty on the signal strength $\mu_{t\bar{t}H}$.

with an observed (expected) signal significance of 2.38σ (1.48σ). While the standard classification aims for the simultaneous separation of the $t\bar{t}H$ signal and the four background processes of $t\bar{t}W$, $t\bar{t}Z$, diboson and $t\bar{t}$ from each other with high purity in each of the five regions, the alternative classification has only two regions and uses the discriminants as separators. In the case of floating both $t\bar{t}Z$ and $t\bar{t}W$ normalisation the alternative classification performs slightly better in $t\bar{t}H$ signal significance (see table 3.7), but the measured $t\bar{t}W$ best-fit signal strength is not very trustful, although compatible with the SM expectation of one. Because the standard classification includes a dedicated $t\bar{t}W$ control region, the measured $\mu_{t\bar{t}W}$ is more reasonable in this case.

The two classifications have similar performance. An advantage of the alternative classification is, that it includes the full phase-space of the 3ℓ pre-selection, which is useful in case of re-interpretation for new physics searches, done outside of the ATLAS collaboration.

3.8.2. Properties of the seven channels used in the $t\bar{t}H \rightarrow$ multilepton analysis

The seven analysis channels target different Higgs boson decays. This is shown in figure 3.19 (left). The light lepton channels with no τ_{had} (2ℓSS, 3ℓ and 4ℓ) target mainly
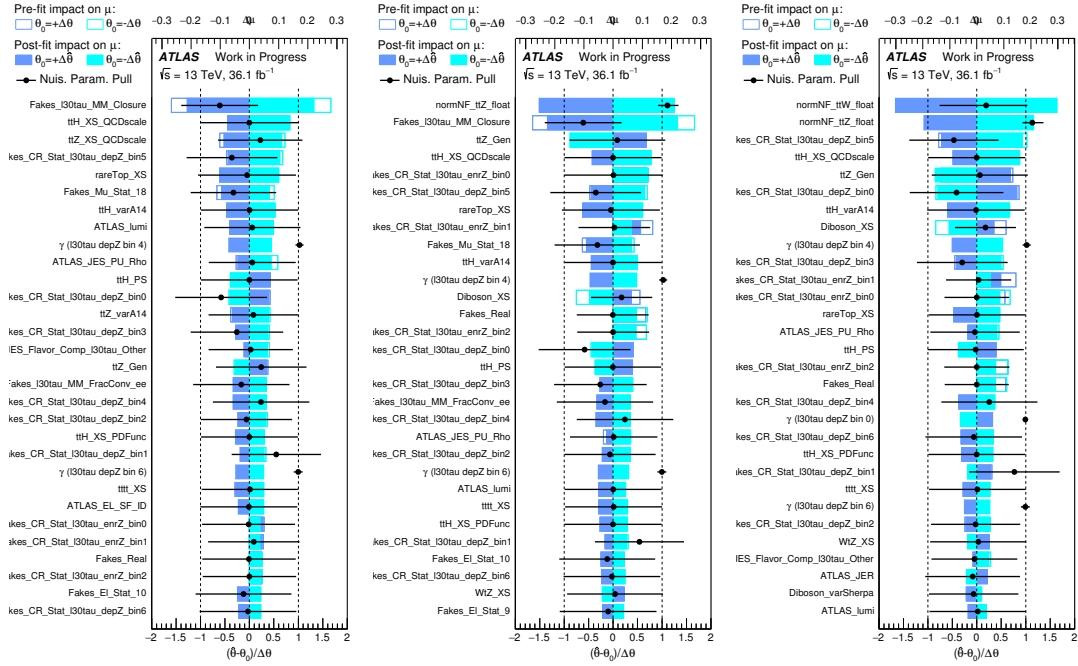
Figure 3.17.: Ranking of nuisance parameters with highest impact on the error on the signal strength $\Delta\mu_{t\bar{t}H}$ (left) for fixed $t\bar{t}V$, (middle) for floating $t\bar{t}Z$ and (right) for floating both $t\bar{t}Z$ and $t\bar{t}W$ normalisation.

the $H \rightarrow WW$ and $H \rightarrow \tau\tau$ decays with leptonically decaying tau leptons. The other channels are more sensitive to the $H \rightarrow \tau\tau$ decays, where at least one tau lepton decays hadronically. The ratios of signal S over total background B and $S/\sqrt{B}$ are shown in figure 3.19 (right). The latter is an indicator of how significant a certain region is
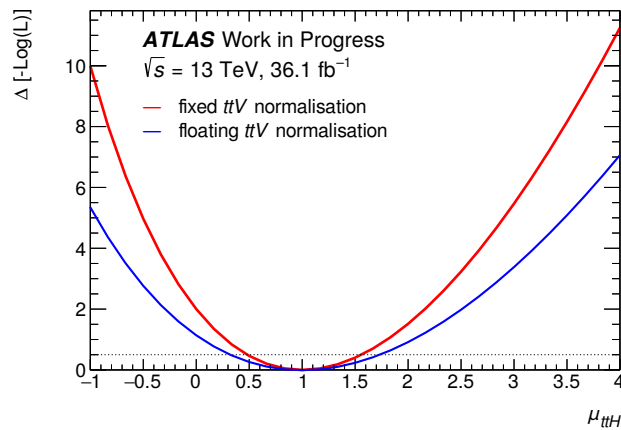
Figure 3.18.: Likelihood scan of $\mu_{t\bar{t}H}$ with (red) fixed $t\bar{t}V$ normalisation and (blue) both floating $t\bar{t}Z$ and $t\bar{t}W$ normalisation.
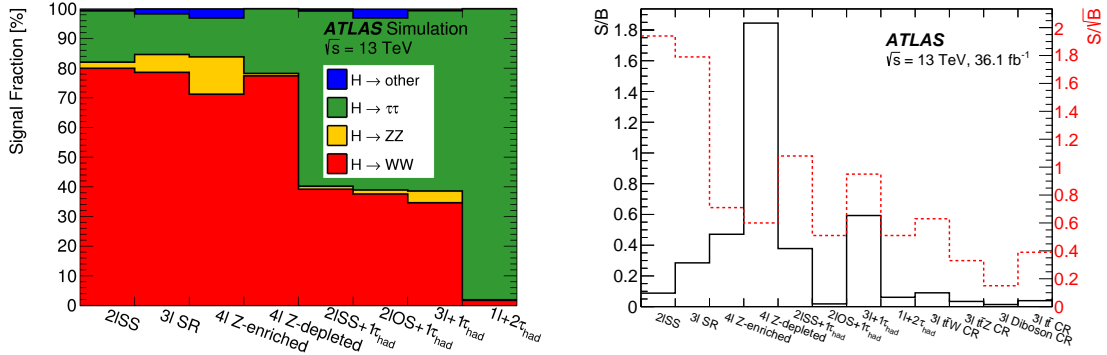
Figure 3.19.: (Left) Fraction of Higgs boson decays in the $t\bar{t}H$ signal in the signal regions and (right) S/B and $S/\sqrt{B}$ for all signal and control regions with signal S and total background B. All values are estimated from SM pre-fit expectation [4].

to measure $\mu_{t\bar{t}H}$. The 2ℓSS and 3ℓ SRs are the most significant channels. The 4ℓ and $3\ell+1\tau_{\mathrm{had}}$ SRs, in particular the 4ℓ Z-depleted SR, have the highest purity of signal with a ratio of up to $S/B = 1.85$, but their significance is much lower because of the statistical limitation of these SRs.

The acceptance times efficiency $A \times \epsilon$ is the fraction of total $t\bar{t}H$ signal which is expected in a certain region. It is given in table 3.8 for all SRs. These numbers al-

Table 3.8.: Acceptance times efficiency $A \times \epsilon$ of the $t\bar{t}H$ signal for the eight SRs from SM pre-fit signal expectation. The number in brackets includes the signal contribution in the 3ℓ CRs.

	2ℓSS	3ℓ SR	4ℓ Z-enr.	4ℓ-dep.	2ℓSS+$1\tau_{\mathrm{had}}$	2ℓOS+$1\tau_{\mathrm{had}}$	$3\ell+1\tau_{\mathrm{had}}$	$1\ell+2\tau_{\mathrm{had}}$
$A \times \epsilon$ [10^{-4}]	23	6.1 (11)	0.58	0.11	1.7	7.8	0.83	2.3

low to estimate the number of signal events expected in the analysis. For instance, in the 4ℓ Z-depleted SR an $A \times \epsilon = 0.11$ is expected which corresponds to a yield of $S = {A\times\epsilon}/{\sigma_{t\bar{t}H}^{\mathrm{SM}}\cdot L} = 0.20$ signal events with $t\bar{t}H$ cross section $\sigma_{t\bar{t}H}^{\mathrm{SM}} = 507$ fb and total integrated luminosity of $L = 36.1\,\mathrm{fb}^{-1}$.

3.8.3. Results of combination with all analysis channels

A global fit has been performed in order to extract the signal strength from all channels by properly taking into account the NPs for all uncertainties and their correlations. All channels use same fit configuration with same systematic uncertainties on MC predicted backgrounds and signal and additionally systematic and statistical uncertainties related to the respective data-driven background estimates.

The seven channels included in the analysis are summarised in table 3.9. In five of the channels, the BDT discriminant shape in the SR is included in the fit. The four CRs, the

Table 3.9.: The seven analysis channels with their basic region characteristics. In the 4ℓ region the two entries correspond to Z-enriched and Z-depleted SRs, respectively [4].

	2ℓSS	3ℓ	4ℓ	1ℓ+2τ_{had}	2ℓSS+1τ_{had}	2ℓOS+1τ_{had}	3ℓ+1τ_{had}
BDT trained against	Fakes and $t\bar{t}V$	$t\bar{t}$, $t\bar{t}W$, $t\bar{t}Z$, VV	$t\bar{t}Z$ / -	$t\bar{t}$	all	$t\bar{t}$	-
Discriminant	2×1D BDT	5D BDT	Event count	BDT	BDT	BDT	Event count
Number of bins	6	5	1 / 1	2	2	10	1
Control regions	-	4	-	-	-	-	-

3ℓ+1τ_{had} and the two 4ℓ SRs with low statistics enter the fit as one bin each. The total number of bins included in the fit is 32.

The predicted yields for backgrounds and signal at SM prediction of $\mu_{t\bar{t}H} = 1$ are given in table 3.10 (top) in comparison with observed data events. In the combined fit

Table 3.10.: (Top) pre- and (bottom) post-fit yields in all regions. The post-fit yields and uncertainties include the prediction at $\mu_{t\bar{t}H} = 1.6\,^{+0.5}_{-0.4}$ [4].

Category	Non-prompt	Fake τ_{had}	q mis-id	$t\bar{t}W$	$t\bar{t}Z$	Diboson	Other	Total Bkgd.	$t\bar{t}H$	Observed
					Pre-fit yields					
2ℓSS	233 ± 39	–	33 ± 11	123 ± 18	41.4 ± 5.6	25 ± 15	28.4 ± 5.9	484 ± 38	42.6 ± 4.2	514
3ℓ SR	14.5 ± 4.3	–	–	5.5 ± 1.2	12.0 ± 1.8	1.2 ± 1.2	5.8 ± 1.4	39.1 ± 5.2	11.2 ± 1.6	61
3ℓ $t\bar{t}W$ CR	13.3 ± 4.3	–	–	19.9 ± 3.1	8.7 ± 1.1	< 0.2	4.53 ± 0.92	46.5 ± 5.4	4.18 ± 0.46	56
3ℓ $t\bar{t}Z$ CR	3.9 ± 2.5	–	–	2.71 ± 0.56	66 ± 11	8.4 ± 5.3	12.9 ± 4.2	93 ± 13	3.17 ± 0.41	107
3ℓ VV CR	27.7 ± 8.7	–	–	4.9 ± 1.0	21.3 ± 3.4	51 ± 30	17.9 ± 6.1	123 ± 32	1.67 ± 0.25	109
3ℓ $t\bar{t}$ CR	70 ± 17	–	–	10.5 ± 1.5	7.9 ± 1.1	7.2 ± 4.8	7.3 ± 1.9	103 ± 17	4.00 ± 0.49	85
4ℓ Z-enr.	0.11 ± 0.07	–	–	< 0.01	1.52 ± 0.23	0.43 ± 0.23	0.21 ± 0.09	2.26 ± 0.34	1.06 ± 0.14	2
4ℓ Z-dep.	0.01 ± 0.01	–	–	< 0.01	0.04 ± 0.02	< 0.01	0.06 ± 0.03	0.11 ± 0.03	0.20 ± 0.03	0
1ℓ+2τ_{had}	–	65 ± 21	–	0.09 ± 0.09	3.3 ± 1.0	1.3 ± 1.0	0.98 ± 0.35	71 ± 21	4.3 ± 1.0	67
2ℓSS+1τ_{had}	2.4 ± 1.4	1.80 ± 0.30	0.05 ± 0.02	0.88 ± 0.24	1.83 ± 0.37	0.12 ± 0.18	1.06 ± 0.24	8.2 ± 1.6	3.09 ± 0.46	18
2ℓOS+1τ_{had}	–	756 ± 80	–	6.5 ± 1.3	11.4 ± 1.9	2.0 ± 1.3	5.8 ± 1.5	782 ± 81	14.2 ± 2.0	807
3ℓ+1τ_{had}	–	0.75 ± 0.15	–	0.04 ± 0.04	1.38 ± 0.24	0.002 ± 0.002	0.38 ± 0.10	2.55 ± 0.32	1.51 ± 0.23	5
					Post-fit yields					
2ℓSS	211 ± 26	–	28.3 ± 9.4	127 ± 18	42.9 ± 5.4	20.0 ± 6.3	28.5 ± 5.7	459 ± 24	67 ± 18	514
3ℓ SR	13.2 ± 3.1	–	–	5.8 ± 1.2	12.9 ± 1.6	1.2 ± 1.1	5.9 ± 1.3	39.0 ± 4.0	17.7 ± 4.9	61
3ℓ $t\bar{t}W$ CR	11.7 ± 3.0	–	–	20.4 ± 3.0	8.9 ± 1.0	< 0.2	4.54 ± 0.88	45.6 ± 4.0	6.6 ± 1.9	56
3ℓ $t\bar{t}Z$ CR	3.5 ± 2.1	–	–	2.82 ± 0.56	70.4 ± 8.6	7.1 ± 3.0	13.6 ± 4.2	97.4 ± 8.6	5.1 ± 1.4	107
3ℓ VV CR	22.4 ± 5.7	–	–	5.05 ± 0.94	22.0 ± 3.0	39 ± 11	18.1 ± 5.9	106.8 ± 9.4	2.61 ± 0.82	109
3ℓ $t\bar{t}$ CR	56.0 ± 8.1	–	–	10.7 ± 1.4	8.1 ± 1.0	5.9 ± 2.7	7.1 ± 1.8	87.8 ± 7.9	6.3 ± 1.8	85
4ℓ Z-enr.	0.10 ± 0.07	–	–	< 0.01	1.60 ± 0.22	0.37 ± 0.15	0.22 ± 0.10	2.29 ± 0.28	1.65 ± 0.47	2
4ℓ Z-dep.	0.01 ± 0.01	–	–	< 0.01	0.04 ± 0.02	< 0.01	0.07 ± 0.03	0.11 ± 0.03	0.32 ± 0.09	0
1ℓ+2τ_{had}	–	58.0 ± 6.8	–	0.11 ± 0.11	3.31 ± 0.90	0.98 ± 0.75	0.98 ± 0.33	63.4 ± 6.7	6.5 ± 2.0	67
2ℓSS+1τ_{had}	1.86 ± 0.91	1.86 ± 0.27	0.05 ± 0.02	0.97 ± 0.26	1.96 ± 0.37	0.15 ± 0.20	1.09 ± 0.24	7.9 ± 1.2	5.1 ± 1.3	18
2ℓOS+1τ_{had}	–	756 ± 28	–	6.6 ± 1.3	11.5 ± 1.7	1.64 ± 0.92	6.1 ± 1.5	782 ± 27	21.7 ± 5.9	807
3ℓ+1τ_{had}	–	0.75 ± 0.14	–	0.04 ± 0.04	1.42 ± 0.22	0.002 ± 0.002	0.40 ± 0.10	2.61 ± 0.30	2.41 ± 0.68	5

to data the observed signal strength is

$$\mu_{t\bar{t}H} = 1.56\,^{+0.30}_{-0.29}\,(\text{stat.})\,^{+0.39}_{-0.30}\,(\text{syst.}) = 1.56\,^{+0.49}_{-0.42}. \tag{3.11}$$

This measurement corresponds to an observed (expected) signal significance of 4.1 (2.8) standard deviations versus the background-only hypothesis. The post-fit yields are given in table 3.10 and illustrated in figure 3.20. The agreement of data yield with post-fit prediction of backgrounds and signal at the observed $\mu_{t\bar{t}H}$ is very good. Figure 3.21 shows the post-fit distribution of the discriminants in the signal regions of the most-significant channels of 2ℓSS and 3ℓ.

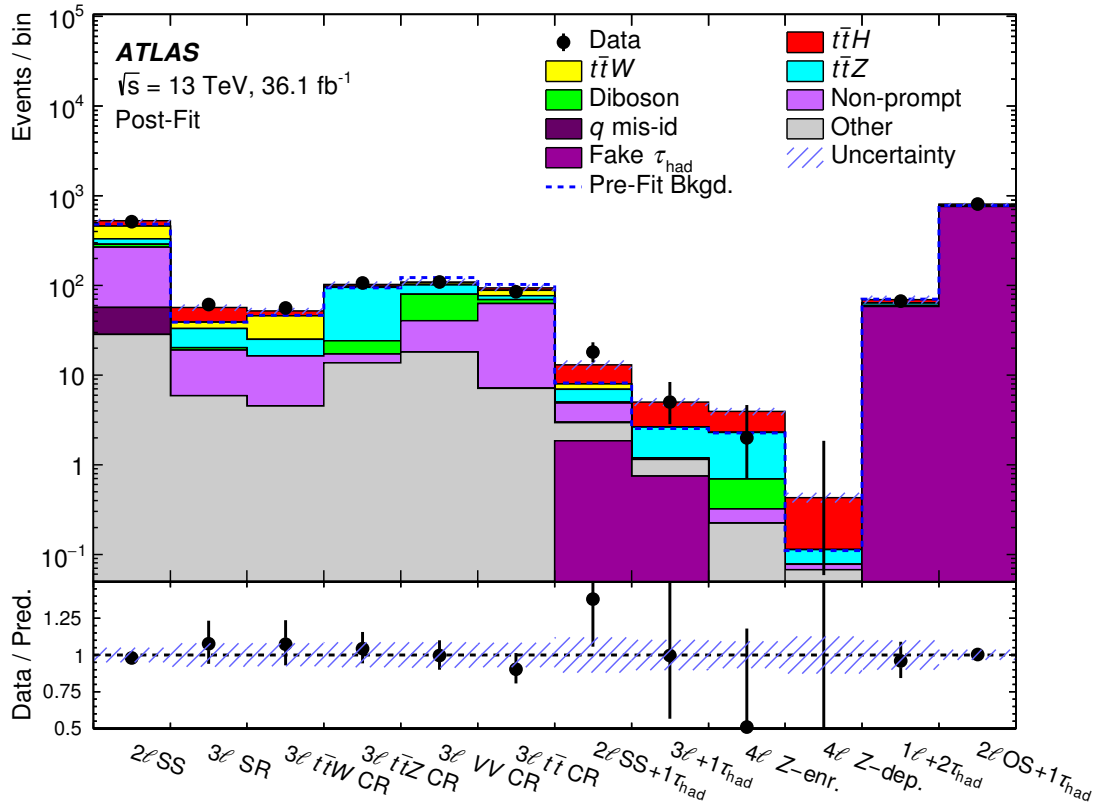The systematic uncertainties and their impact on the errors on the $\mu_{t\bar{t}H}$ uncertainty are

Figure 3.20.: Comparison of data event yields in all regions to the post-fit yields of total background and signal at observed $\mu_{t\bar{t}H} = 1.6\,^{+0.5}_{-0.4}$. The blue shaded area indicates the total systematics including the uncertainty on $\mu_{t\bar{t}H}$ [4].

listed in table 3.11. Figure 3.22 shows the impact, pulls and constraints of the fifteen most important NPs.

The analysis sensitivity is dominated by the theoretical prediction of the $t\bar{t}H$ cross section, namely the QCD factorization and renormalisation scale variations with $^{+5.8\%}_{-9.2\%}$ and the PDFs and the strong coupling with $\pm 3.6\%$ [6]. Its impact on the error on $\mu_{t\bar{t}H}$ ($\Delta\mu_{t\bar{t}H}$) is $^{+0.20}_{-0.09}$.

Several NPs related to jet energy scale (JES) are high ranked in their impact on $\Delta\mu_{t\bar{t}H}$. In particular, the NPs for JES pile-up subtraction and the flavour composition in 2ℓSS are highly ranked, because in the selection of the most significant 2ℓSS channel four jets are required with each having a JES uncertainty of up to $\sim 5\%$ at $p_T = 25$ GeV. This is shown in figure 2.22 (left) of section 2.4.4, where pile-up subtraction and flavour composition are the dominant JES uncertainties at low jet p_T. Together with jet energy resolution (JER) the JES uncertainties have an impact of $^{+0.18}_{-0.15}$ on $\Delta\mu_{t\bar{t}H}$.

The third most important uncertainties are the ones related to the non-prompt light lepton estimates with an impact of $^{+0.15}_{-0.13}$ on $\Delta\mu_{t\bar{t}H}$. The NPs of this category with highest impact are the 3ℓ non-prompt closure and the non-prompt statistics in the 4th bin of 3ℓ
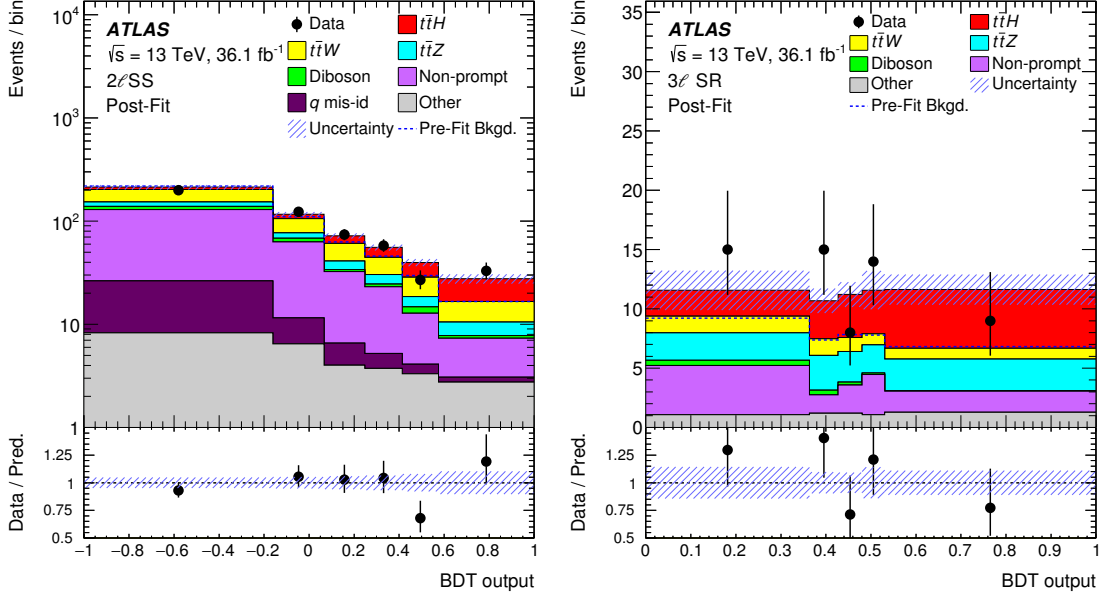
Figure 3.21.: Post-fit distribution of discriminants in (left) 2ℓSS and (right) 3ℓ SR. The observed data events are compared to the post-fit yields of total background and signal at observed $\mu_{t\bar{t}H} = 1.6\,^{+0.5}_{-0.4}$. The blue shaded area indicates the total systematics including the uncertainty on $\mu_{t\bar{t}H}$ [4].

Table 3.11.: Impact of systematic uncertainties on errors on $\mu_{t\bar{t}H}$ [4].

Uncertainty Source	$\Delta\mu$	
$t\bar{t}H$ modeling (cross section)	+0.20	−0.09
Jet energy scale and resolution	+0.18	−0.15
Non-prompt light-lepton estimates	+0.15	−0.13
Jet flavor tagging and τ_{had} identification	+0.11	−0.09
$t\bar{t}W$ modeling	+0.10	−0.09
$t\bar{t}Z$ modeling	+0.08	−0.07
Other background modeling	+0.08	−0.07
Luminosity	+0.08	−0.06
$t\bar{t}H$ modeling (acceptance)	+0.08	−0.04
Fake τ_{had} estimates	+0.07	−0.07
Other experimental uncertainties	+0.05	−0.04
Simulation sample size	+0.04	−0.04
Charge misassignment	+0.01	−0.01
Total systematic uncertainty	+0.39	−0.30

SR. The NP on 3ℓ non-prompt closure shows a -0.6σ pull from the nominal, which originates from a small deficit of about 22 events in pre-fit in the 3ℓ $t\bar{t}$ CR (compare pre-fit expectation with observed events in table 3.10). The statistics of the CRs where the weights are applied to estimate the non-prompt light leptons have a major contribution
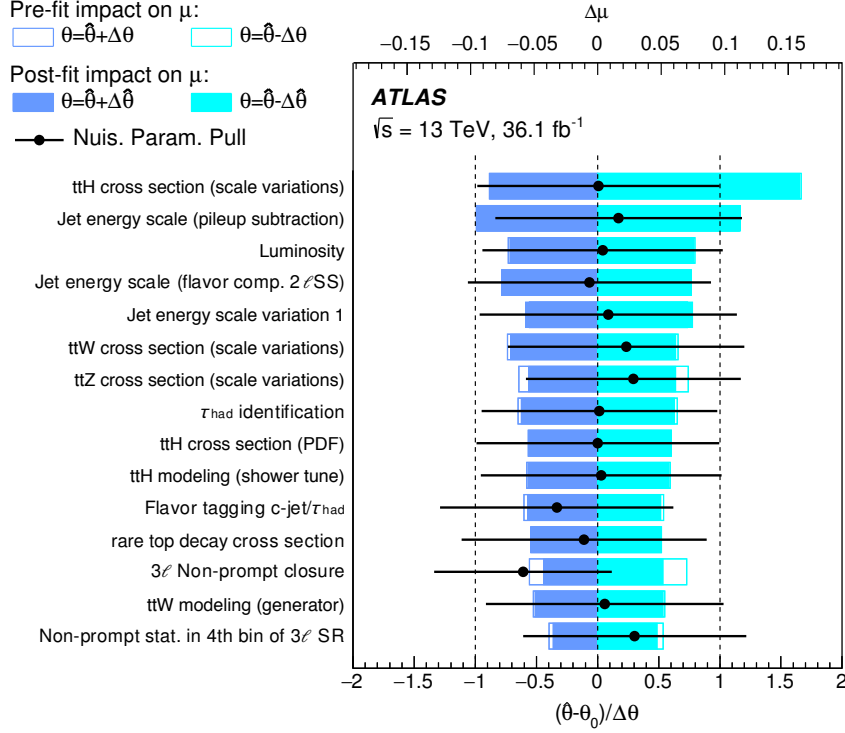
Figure 3.22.: Ranking of the NPs with largest impact on errors on $\mu_{t\bar{t}H}$ [4].

to the uncertainties on the non-prompt light lepton estimates.

Table 3.12 summarises the observed and expected best-fit signal strength and significance for the seven analysis channels and the combination. This measurement of the

Table 3.12.: Observed and expected best-fit values of $\mu_{t\bar{t}H}$ and observed and expected signal significance for the seven single channels and their combination in the $t\bar{t}H \rightarrow$ multilepton analysis [4].

Channel	Best-fit μ		Significance	
	Observed	Expected	Observed	Expected
$2\ell\mathrm{OS}+1\tau_{\mathrm{had}}$	$1.7\ ^{+1.6}_{-1.5}$ (stat.) $^{+1.4}_{-1.1}$ (syst.)	$1.0\ ^{+1.5}_{-1.4}$ (stat.) $^{+1.2}_{-1.1}$ (syst.)	0.9σ	0.5σ
$1\ell+2\tau_{\mathrm{had}}$	$-0.6\ ^{+1.1}_{-0.8}$ (stat.) $^{+1.1}_{-1.3}$ (syst.)	$1.0\ ^{+1.1}_{-0.9}$ (stat.) $^{+1.2}_{-1.1}$ (syst.)	$-$	0.6σ
4ℓ	$-0.5\ ^{+1.3}_{-0.8}$ (stat.) $^{+0.2}_{-0.3}$ (syst.)	$1.0\ ^{+1.7}_{-1.2}$ (stat.) $^{+0.4}_{-0.2}$ (syst.)	$-$	0.8σ
$3\ell+1\tau_{\mathrm{had}}$	$1.6\ ^{+1.7}_{-1.3}$ (stat.) $^{+0.6}_{-0.2}$ (syst.)	$1.0\ ^{+1.5}_{-1.1}$ (stat.) $^{+0.4}_{-0.2}$ (syst.)	1.3σ	0.9σ
$2\ell\mathrm{SS}+1\tau_{\mathrm{had}}$	$3.5\ ^{+1.5}_{-1.2}$ (stat.) $^{+0.9}_{-0.5}$ (syst.)	$1.0\ ^{+1.1}_{-0.8}$ (stat.) $^{+0.5}_{-0.3}$ (syst.)	3.4σ	1.1σ
3ℓ	$1.8\ ^{+0.6}_{-0.6}$ (stat.) $^{+0.6}_{-0.5}$ (syst.)	$1.0\ ^{+0.6}_{-0.5}$ (stat.) $^{+0.5}_{-0.4}$ (syst.)	2.4σ	1.5σ
$2\ell\mathrm{SS}$	$1.5\ ^{+0.4}_{-0.4}$ (stat.) $^{+0.5}_{-0.4}$ (syst.)	$1.0\ ^{+0.4}_{-0.4}$ (stat.) $^{+0.4}_{-0.4}$ (syst.)	2.7σ	1.9σ
Combined	$1.6\ ^{+0.3}_{-0.3}$ (stat.) $^{+0.4}_{-0.3}$ (syst.)	$1.0\ ^{+0.3}_{-0.3}$ (stat.) $^{+0.3}_{-0.3}$ (syst.)	4.1σ	2.8σ

$t\bar{t}H$ production in multileptonic final states has been firstly published in a public note in October 2017 and in April 2018 in Physical Review D [4].

In March 2018 the CMS collaboration has published its own search for $t\bar{t}H$ production in multileptonic final states [124] using 35.9 fb^{-1} of proton-proton collisions from 2016. Apart from the 2ℓOS channel which has the lowest signal significance, the categorisation of the other six channels is done in a similar way as by the ATLAS collaboration. The analysis has observed a signal strength of

$$\mu_{t\bar{t}H} = 1.23\,^{+0.45}_{-0.43} = 1.23\,^{+0.26}_{-0.25}\,(\text{stat.})\,^{+0.37}_{-0.35}\,(\text{syst.}) \tag{3.12}$$

and has a similar performance as the presented search with an observed (expected) signal significance of 3.2 (2.8) standard deviations.

3.9. Combination with $t\bar{t}H$ searches in other Higgs boson decays

The results of this analysis have been combined with other searches for $t\bar{t}H$ production with proton-proton collision data of 36 fb^{-1} at a center-of-mass energy of $\sqrt{s} = 13$ TeV. These searches target different Higgs boson decays. The search with the Higgs boson decaying to $b\bar{b}$ in lepton+jets and di-leptonic $t\bar{t}$ final states observed a value of $\mu_{t\bar{t}H} = 0.8^{+0.6}_{-0.6}$ [114]; the di-photon decay channel found $\mu_{t\bar{t}H} = 0.6^{+0.7}_{-0.6}$ [125] and the search with $H \rightarrow ZZ \rightarrow 4\ell$ in the mass window of the Higgs boson mass ± 5 GeV observed a 68% CL upper limit on $\mu_{t\bar{t}H}$ of 1.9 [126]. The results are summarised in figure 3.23 (left) for the input channels and their combination. The search for $t\bar{t}H$ production in
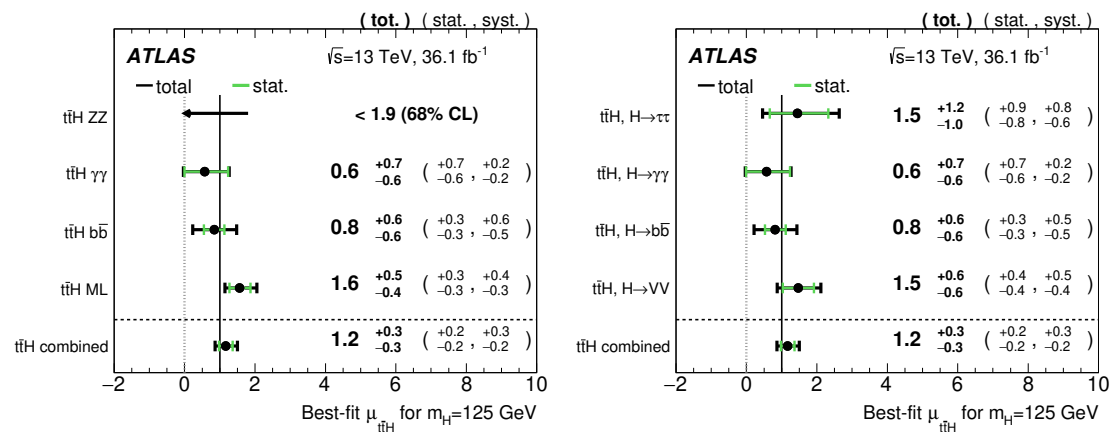
Figure 3.23.: Best-fit $\mu_{t\bar{t}H}$ (left) in single $t\bar{t}H$ searches and combination and (right) in Higgs boson decay modes. Because of zero events observation the upper limit at 68% CL is given for the search with $H \rightarrow ZZ \rightarrow 4\ell$ [4].

multilepton final states has a major impact on the combination results. The combined best-fit value is $\mu_{t\bar{t}H} = 1.2 \pm 0.3$. The observed (expected) statistical significance of this excess over the background-only hypothesis is 4.2 (3.8) standard deviations [4].

The CMS collaboration has reported the observation of the $t\bar{t}H$ production in combination of Run 1 and Run 2 data with an observed (expected) significance of 5.2 (4.2) standard deviations [127]. The ATLAS collaboration followed with an updated combination including up to 79.8 fb^{-1} of proton-proton collisions from 2015–2017 in the searches for $t\bar{t}H$ production with $H \rightarrow \gamma\gamma$ and $H \rightarrow ZZ \rightarrow 4\ell$ [5]. Figure 3.24 (left) shows the observed signal strength in the single searches in collision data with $\sqrt{s} = 13$ TeV and in their combination. A value of 1.3 ± 0.3 times the SM expectation is observed in
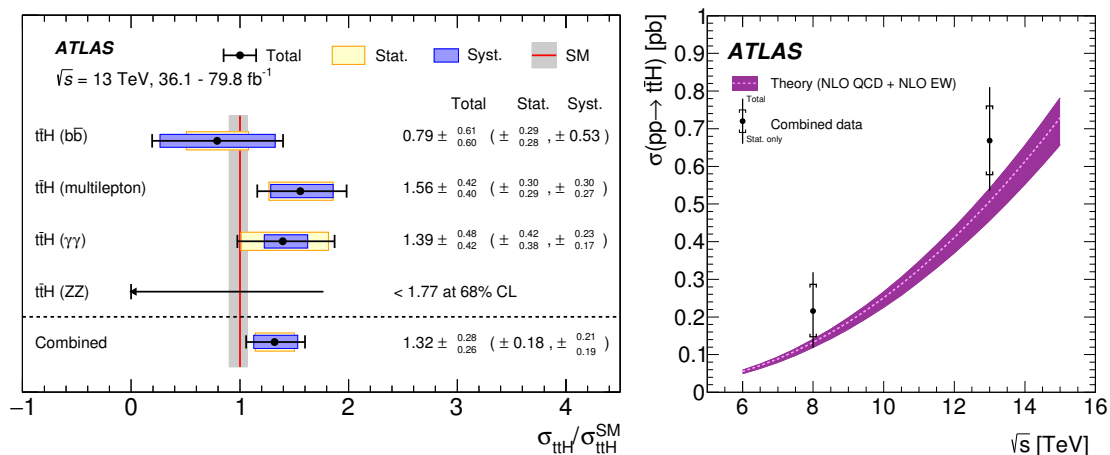
Figure 3.24.: (Left) best-fit $\sigma_{t\bar{t}H}/\sigma_{t\bar{t}H}^{SM}$ in single $t\bar{t}H$ searches and combination and (right) $t\bar{t}H$ cross section measurement and prediction as function of the center-of-mass energy using up to 79.8 fb^{-1} of proton-proton collision data [5].

combination with an observed statistical significance of 5.8 standard deviations, while 4.9 are expected. Combining with searches done at $\sqrt{s} = 7$ and 8 TeV the observed (expected) signal significance of the excess is 6.3 (5.1) standard deviations, which clearly states observation of the $t\bar{t}H$ production and hence the Yukawa coupling between the Higgs boson and the top quark pair.

The measured cross section as a function of center-of-mass energy is presented and compared to the SM expectation in figure 3.24 (right). At $\sqrt{s} = 13$ TeV a cross section of $670 \pm 90\,(\text{stat.})\,^{+110}_{-100}\,(\text{syst.})$ fb is measured, which agrees well with the SM expectation of $507\,^{+35}_{-50}$ fb [6].

3.10. Outlook

The analysis presented here includes only a part of the Run 2 luminosity. In particular, the presented $t\bar{t}H \rightarrow$ multilepton analysis (seven channels) has a sensitivity of

$$\mu_{t\bar{t}H} = 1.00\,^{+0.43}_{-0.39} = 1.00\,^{+0.29}_{-0.28}\,(\text{stat.})\,^{+0.32}_{-0.27}\,(\text{syst.}) \tag{3.13}$$

for a dataset corresponding to $36.1\,\mathrm{fb}^{-1}$ of proton-proton collisions. A significance of 2.8σ is therefore expected.

For the expected luminosity of Run 2 ($150\,\mathrm{fb}^{-1}$), a conservative extrapolation predicts a sensitivity of

$$\mu_{t\bar{t}H} = 1.00\,^{+0.30}_{-0.26} = 1.00\,^{+0.14}_{-0.14}\,(\text{stat.})\,^{+0.26}_{-0.23}\,(\text{syst.}) \tag{3.14}$$

which corresponds to an expected significance of 4.1σ. This extrapolation scales all the yields and systematic uncertainties by the ratio of luminosities. It is expected, that some of the systematic uncertainties decrease, because of their statistical origin (e.g. the non-prompt lepton estimates and uncertainties on the non-prompt lepton efficiencies are expected to improve significantly).

Assuming a HL-LHC with same parameters as the LHC, but with $L = 3,000\,\mathrm{fb}^{-1}$, the current $t\bar{t}H \to$ multilepton analysis can be naively extrapolated to

$$\mu_{t\bar{t}H} = 1.00\,^{+0.20}_{-0.17} = 1.00\,^{+0.03}_{-0.03}\,(\text{stat.})\,^{+0.20}_{-0.17}\,(\text{syst.}) \tag{3.15}$$

with a signal significance of 6.3σ. Nevertheless the conditions are not the same at the HL-LHC, e.g. the pile-up is expected to increase from currently ~ 30 to up to 200 interactions per bunch crossing. This is taken into account in the extrapolation studies by the ATLAS collaboration for the $t\bar{t}H$ production in $H \to \gamma\gamma$ decays, which predict $\mu_{t\bar{t}H} = 1.00\,^{+0.13}_{-0.12}\,(\text{stat.})\,^{+0.18}_{-0.12}\,(\text{syst.})$ with a significance of 8.2σ, dominated by theoretical cross section uncertainties [128]. In combination with other Higgs boson decay channels (here excluding $H \to b\bar{b}$) a relative uncertainty on the $t\bar{t}H$ cross-section measurement of about 10% is expected [129].

3.11. Conclusion

The $t\bar{t}H$ production has been observed in proton-proton collisions with $\sqrt{s} = 7$, 8 and 13 TeV by the ATLAS collaboration with a signal significance of 6.3 standard deviations (5.1 expected). This measurement constitutes a direct observation of the top quark Yukawa coupling to the Higgs boson. The $t\bar{t}H \to$ multilepton analysis, presented in more detail in this doctoral thesis, is the most-significant analysis channel. This result has been only possible due to the excellent performance of the LHC and the ATLAS detector and the intensive work on the background estimates and suppression.

My study on an alternative classification in the 3ℓ channel has been presented in this chapter, and has a similar performance as the one used in the publication.

All results have been found compatible with the SM expectation with a Higgs boson with a mass of about 125 GeV. Nevertheless new physics can contribute in a different phase-space. The next chapter presents the search for flavour-changing top quark decays to a Higgs boson and a lighter up-type quark, which are strongly suppressed in the SM but may be enhanced in certain new physics models.

4. Search for flavour-changing neutral currents in top quark decays in multileptonic final states

Flavour-changing neutral currents (FCNC) in top quark decays are strongly suppressed in the SM. Nevertheless, many new physics models predict an enhancement of the branching ratios of top decays with FCNC, mainly through virtual contributions related to new heavy particles. This chapter presents a search for FCNC in top quark decays to a Higgs boson and a lighter up-type quark ($t \rightarrow Hq$, $q = u$ or c). Such decays can be of top quarks searched for using the abundant production of top quark pairs at the LHC. The second top quark in the event is assumed to undergo a SM decay to a W boson and a b quark. The analysis on final states with two or three light leptons ($t \rightarrow Hq \rightarrow$ multi-lepton) is sensitive to $H \rightarrow WW$, $H \rightarrow ZZ$ and $H \rightarrow \tau_{\mathrm{lep}}\tau_{\mathrm{lep}}$ decays. The final states are very similar to the ones in the $t\bar{t}H \rightarrow$ multilepton analysis, presented in chapter 3 and therefore a similar analysis strategy is chosen. It uses the same dataset of $36.1\,\mathrm{fb}^{-1}$ of proton-proton collisions, collected by the ATLAS experiment. The signal regions are chosen similarly to the ones used in the $t\bar{t}H \rightarrow$ multilepton analysis. This allows to take advantage of the existing developments, e.g. the non-prompt lepton rejection and matrix method estimate [9].

Section 4.1 gives an overview about previous searches, focusing on results from the ATLAS and CMS experiments. The analysis strategy of the new search for $t \rightarrow Hq \rightarrow$ multilepton is presented in section 4.2. The non-prompt lepton estimate using the matrix method is modified and an additional systematic uncertainty is added to properly treat the signal contamination in the control region of fake rate measurement. This is described in detail in section 4.3 before the results are given in section 4.4. Finally, section 4.5 gives an outlook on FCNC searches for $t \rightarrow Hq$ with projections with high integrated luminosities of up to $3000\,\mathrm{fb}^{-1}$ corresponding to the planned goal for a high-luminosity LHC (HL-LHC).

4.1. Previous searches for FCNC in top quark decays

Several hadron or electron collision experiments have done searches for FCNC in top quark decays. The most stringent limits have been set by the ATLAS and CMS experiments with proton-proton collision data from Run 1 and partial Run 2 of the LHC.

Figure 4.1 shows the latest limits at 95% confidence level (CL) on branching ratios of different top quark decays with FCNC by May 2018. The expected theory predictions
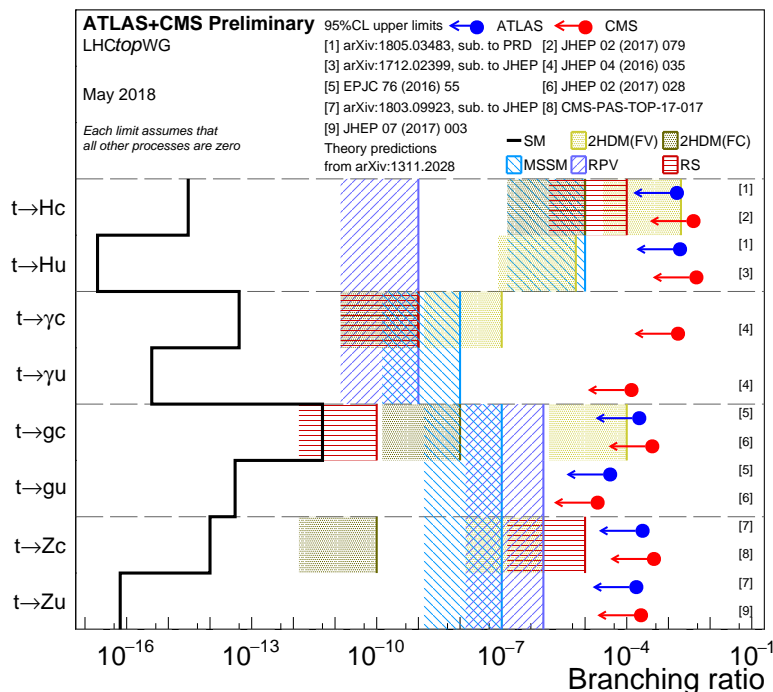
Figure 4.1.: Best observed 95% confidence level upper limits on the branching ratios of different top decays in ATLAS (blue) and CMS (red). The SM prediction is shown (black line) as well as predicted ranges by different new physics models predicting FCNC in top quark decays [130].

are shown as well for different models, discussed in section 1.3.2. The flavour violating 2HDM models have the highest predicted branching ratios for $t \to Hc$ and $t \to gc$, because the branching ratio in these models is usually assumed to scale with $\sqrt{m_q m_t / m_W^2}$. This explains also the enhancement in decays involving the charm-quark ($q = c$) versus the ones involving the lighter up-quark ($q = u$).

The current best observed and expected limits on $\mathcal{B}(t \to Hq)$ by the ATLAS and CMS experiments from Run 1 and Run 2 proton-proton collision data are summarised in table 4.1. Until May 2018 only two searches for $t \to Hq$ have been published using $36\,\text{fb}^{-1}$ of Run 2 proton-proton collision data with $\sqrt{s} = 13\,\text{TeV}$. In an analysis searching for $H \to \gamma\gamma$ decays, the ATLAS experiment excluded $\mathcal{B}(t \to Hc) > 0.22\%$ at 95% CL with an expectation of $\mathcal{B}(t \to Hc) > 0.16\%$. Observed (expected) limits of 0.47% (0.44%) have been reported in the search for $H \to b\bar{b}$ decays by the CMS experiment.

The best to date upper limits in the channels with multileptonic final states are 0.79% and 0.78% (while 0.54% and 0.57% are expected) for the $t \to Hc$ and $t \to Hu$ branching ratios, respectively. The presented analysis aims for improving these limits significantly.

Table 4.1.: Observed and expected 95% CL upper limits on the branching ratios of $t \rightarrow Hq$ by the ATLAS (CMS) experiment. *) In Run 1 the ATLAS $t \rightarrow Hq \rightarrow$ multilepton analysis included the channel of $2\ell SS+1\tau_{\text{had}}$.

Channel	Limit on $\mathcal{B}(t \rightarrow Hu)$ [%]		limit on $\mathcal{B}(t \rightarrow Hc)$ [%]	
	Observed	Expected	Observed	Expected
Run 1, $\sqrt{s} = 8\,\text{TeV}$, $20\,\text{fb}^{-1}$				
$H \rightarrow WW, ZZ, \tau\tau$ [109, 131]	0.78* (0.86)	0.57* (0.82)	0.79* (0.93)	0.54* (0.89)
$H \rightarrow \gamma\gamma$ [131, 132]	0.79 (0.42)	0.51 (0.60)	0.79 (0.47)	0.51 (0.67)
$H \rightarrow b\bar{b}$ [131, 133]	0.61 (1.92)	0.64 (0.84)	0.56 (1.16)	0.42 (0.89)
Combined [131, 133]	0.45 (0.55)	0.29 (0.40)	0.46 (0.40)	0.25 (0.43)
Run 2, $\sqrt{s} = 13\,\text{TeV}$, $36\,\text{fb}^{-1}$				
$H \rightarrow \gamma\gamma$ [8]	0.24 (–)	0.17 (–)	0.22 (–)	0.16 (–)
$H \rightarrow b\bar{b}$ [134]	– (0.47)	– (0.34)	– (0.47)	– (0.44)

4.2. Signal, backgrounds and event selection

The search for $t \rightarrow Hq \rightarrow$ multilepton in pairs of top quarks ($t\bar{t}$) follows closely the analysis strategy of the $t\bar{t}H \rightarrow$ multilepton analysis, described in chapter 3. It considers final states with exactly two or three light leptons ($\ell = e$ or μ). Hadronically decaying tau leptons (τ_{had}) are vetoed for orthogonality with the search for $t \rightarrow Hq$ with $H \rightarrow \tau_{\text{had}}\tau_{\text{had}}$. The signal decay chain for these processes with the dominant $H \rightarrow WW$ decay is given by

$$t\bar{t} \rightarrow Wb + Hq \rightarrow 3W + bq \rightarrow 2\ell + E_T^{\text{miss}} + 4 \text{ jets (1 from } b\text{) or}$$
$$\rightarrow 3\ell + E_T^{\text{miss}} + 2 \text{ jets (1 from } b\text{)} \tag{4.1}$$

where the jets result from the quark's hadronisation and the missing transverse energy (E_T^{miss}) is due to the neutrinos coming from the leptonic W boson decays. The final states are similar to the ones expected in $t\bar{t}H \rightarrow$ multilepton, namely

$$t\bar{t}H \rightarrow 2W2b + H \rightarrow 4W + 2b \rightarrow 2\ell + E_T^{\text{miss}} + 6 \text{ jets (2 from } b\text{) or}$$
$$\rightarrow 3\ell + E_T^{\text{miss}} + 4 \text{ jets (2 from } b\text{)} \tag{4.2}$$

which have one more light and one more jet from a b-quark expected. This analysis uses the same object and signal region event selection as the $t\bar{t}H \rightarrow$ multilepton analysis which are described in sections 3.4 and 3.5.

To suppress the dominant background of 2ℓOS events from $t\bar{t}$, at least two leptons are required to have the same electric charge like in the $t\bar{t}H \rightarrow$ multilepton analysis. The signal region definition of the 2ℓSS channel is given in section 3.5.1. For the 3ℓ channel, this analysis uses the Z-depleted signal region from the alternative 3ℓ event classification, described in section 3.5.2.2.

The signal of $pp \rightarrow (t \rightarrow Hq)(\bar{t} \rightarrow \bar{b}W^-) + $ h.c. is generated with the next-to-leading

order (NLO) generator MADGRAPH5_aMC@NLO [64]. The top quark decays are simulated using MADSPIN [135] and the Higgs boson decays, parton showering, hadronisation and underlying events are generated with PYTHIA 8 [72]. The $t\bar{t}$ production cross section at $\sqrt{s} = 13$ TeV is $\sigma_{t\bar{t}} = 832^{+40}_{-46}$ pb as calculated with the Top++2.0 program to next-to-next-to-leading order in perturbative QCD, including soft-gluon re-summation to next-to-next-to-leading-log order [136] and uncertainties from cross-section scale and acceptance following the PDF4LHC prescription [59, 60, 137–139]. Depending on the branching ratio ($\mathcal{B}$) of the $t \rightarrow Hq$ decay, the signal cross section is

$$\sigma_{t\rightarrow Hq} = 2 \cdot \mathcal{B} \cdot (1 - \mathcal{B}) \cdot \sigma_{t\bar{t}} \xrightarrow{\mathcal{B} \ll 1} 2 \cdot \mathcal{B} \cdot \sigma_{t\bar{t}}. \tag{4.3}$$

where the factor 2 comes from the fact that both the top and the anti-top can decay via FCNC. Systematic uncertainties on the signal process include shape effects of renormalisation and factorisation scale uncertainties, parton shower, event generator and initial and final state radiation (ISR, FSR) uncertainties. Due to limited computation time, no dedicated alternative signal samples have been simulated. I have implemented a model using existing alternative samples for $t\bar{t}$ (given in appendix A) for the estimate of parton shower, event generator and ISR/FSR uncertainties. In this model, 2ℓOS events are selected with the same selection as in 2ℓSS SR but with lower jet multiplicity of $N_{\text{jets}} \geq 2$. For the 3ℓ channel the shape estimate with $t\bar{t}$ samples is not possible because only two prompt leptons are expected. Therefore the normalisation impact is extrapolated from the estimate in 2ℓSS without any shape dependence.

The dominant Higgs boson decays in the selected events of the two SRs are shown in figure 4.2 (left). In both the 2ℓSS and the 3ℓ SR the $H \rightarrow WW$ decay is dominant,
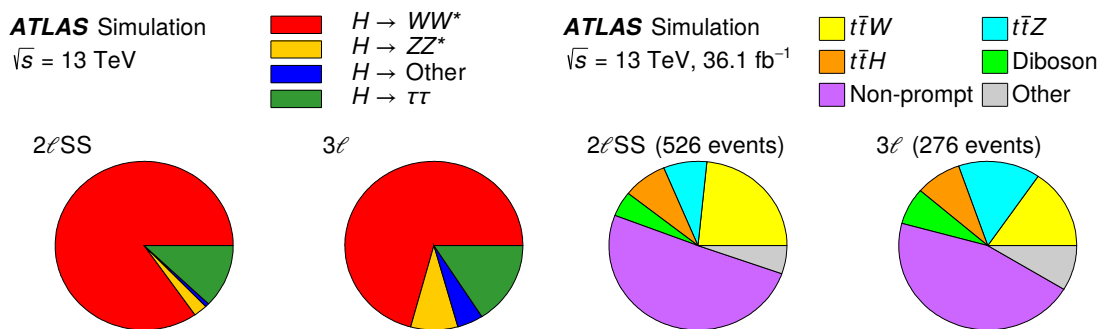
Figure 4.2.: Contribution of (left) different Higgs boson decays in the $t \rightarrow Hq$ signal and (right) different backgrounds in the 2ℓSS and 3ℓ SRs [9].

followed by decays to tau leptons which decay leptonically into muons or electrons.

Similar to the $t\bar{t}H \rightarrow$ multilepton analysis, the backgrounds are dominated by two types:

- The irreducible backgrounds, described in section 3.6.1, are dominated by the associated vector boson production with top quark pairs ($t\bar{t}V$), followed by diboson

and $t\bar{t}H$ production. The main decay chain for $t\bar{t}V$ is

$$t\bar{t}V \rightarrow 2W2b + V \rightarrow 2\ell + E_{\mathrm{T}}^{\mathrm{miss}} + 4 \text{ jets } (2 \text{ from } b) \text{ or}$$
$$\rightarrow 3\ell + E_{\mathrm{T}}^{\mathrm{miss}} + 2\text{–}4 \text{ jets } (2 \text{ from } b) \qquad (4.4)$$

where $t\bar{t}Z$ is mainly populating the 3ℓ channel when the Z boson decays to a pair of leptons. Because the results of the searches for $t\bar{t}H$ production are consistent with the SM expectation, here its contribution is fixed to that prediction. The irreducible background is estimated using MC simulation, as described in section 2.3 using the samples, summarised in appendix A.

- The reducible backgrounds are the background of non-prompt light leptons and electrons with charge misassignment. Their data-driven estimate and suppression by dedicated BDTs is described in sections 3.6.3 and 3.6.2, respectively. Because the $t \rightarrow Hq$ signal predicts lower multiplicities of jets and b-tagged jets, it has a non-negligible contribution to the control region (CR) used to estimate the probability to be non-prompt ε_{f}. For $\mathcal{B} \neq 0$ this leads to different yields and shapes of the non-prompt background, which is taken into account and described in detail in section 4.3.

Figure 4.2 (right) shows the relative contribution of the different backgrounds in the two SRs at $\mathcal{B} = 0$. In this chapter, the non-prompt contribution in the 2ℓSS SR includes both the electron charge misassignment and non-prompt light leptons from mainly b-hadron decays or photon conversion. In the 2ℓSS and 3ℓ SR the contribution from SM background predicts 526 and 276 events, respectively. Because these regions are the same as in the $t\bar{t}H \rightarrow$ multilepton analysis the pre-fit contributions are the same as in figures 3.13 and 3.12, with the $t\bar{t}H$ production considered here as an additional background.

Multivariate techniques are used to discriminate the $t \rightarrow Hq$ signal against the major backgrounds of $t\bar{t}V$ and against non-prompt leptons. Therefore two BDTs are trained using TMVA [117] of the $t \rightarrow Hu$ or $t \rightarrow Hc$ signal against the two kinds of background. The input variables to the BDTs are summarised in table 4.2. The distributions of the variables with best separation of signal versus backgrounds are shown in figure 4.3 and 4.4 for 2ℓSS and 3ℓ SRs, respectively. The observed data shows a good agreement with the expected background prediction in each variable.

The number of b-tagged jets is a strongly discriminating variable of the $t \rightarrow Hq$ signal from both the non-prompt lepton and the $t\bar{t}V$ background, because in these backgrounds two jets from b-quarks are expected from the decay of the pair of top quarks while only one is expected in the signal as illustrated in equation 4.1. The signal of $t \rightarrow Hc$ has slightly higher probability of two b-tagged jets compared to $t \rightarrow Hu$, because of the lower b-tagging rejection rate for jets from c-quarks than from light jets as described in section 2.4.4.4 (table 2.5).

The non-prompt leptons have lower p_{T} and are less isolated than prompt signal leptons in the 2ℓSS channel. Thus, the $p_{\mathrm{T}}(\ell_1)$ and the angular distance to the closest jet

Table 4.2.: Input variables to the BDTs (marked with ×) of $t \to Hq$ vs. backgrounds in 2ℓSS and 3ℓ channels [9].

Variable	2ℓSS	3ℓ
p_T of higher-p_T lepton	×	
p_T of lower-p_T lepton	×	
p_T of lepton ℓ_0		×
p_T of lepton ℓ_1		×
p_T of lepton ℓ_2		×
Dilepton invariant masses (all combinations)	×	×
Trilepton invariant mass		×
Best Z candidate invariant mass		×
Maximum lepton $|\eta|$	×	
Lepton flavor	×	
Number of jets	×	×
Number of b-tagged jets	×	×
p_T of highest-p_T jet		×
p_T of second highest-p_T jet		×
p_T of highest-p_T b-tagged jet		×
$\Delta R(\ell_0, \ell_1)$		×
$\Delta R(\ell_0, \ell_2)$		×
$\Delta R(\text{higher-}p_T \text{ lepton, closest jet})$	×	
$\Delta R(\text{lower-}p_T \text{ lepton, closest jet})$	×	
$\Delta R(\ell_1, \text{closest jet})$		×
Smallest $\Delta R(\ell_0, b\text{-tagged jet})$		×
E_T^{miss}	×	
m_{eff}	×	×

$\Delta R(\ell_1, \text{jet})$ of the lower-p_T lepton (ℓ_1) are discriminant variables against this background. In the 3ℓ channel several invariant masses and the angular distance of the opposite sign leptons with smaller angular distance $\Delta R(\ell_0, \ell_1)$ are powerful variables in the non-prompt lepton background discrimination.

The quantity of $m_{\text{eff}} \equiv E_T^{\text{miss}} + H_T$ with the scalar p_T sum of all leptons and jets H_T and E_T^{miss} can discriminate against the $t\bar{t}V$ background

In the 2ℓSS channel the predicted signal shapes of the input variables are sufficiently similar for $t \to Hu$ and $t \to Hc$, such that the BDTs are trained with a combined signal sample.

Finally the BDTs are combined linearly to build limit optimising discriminants of $t \to Hu$ or $t \to Hc$ against all backgrounds. The number of bins in the two regions is optimised to six and four for 2ℓSS and 3ℓ SR, respectively. It has been found, that flat signal distribution in both regions performs best.
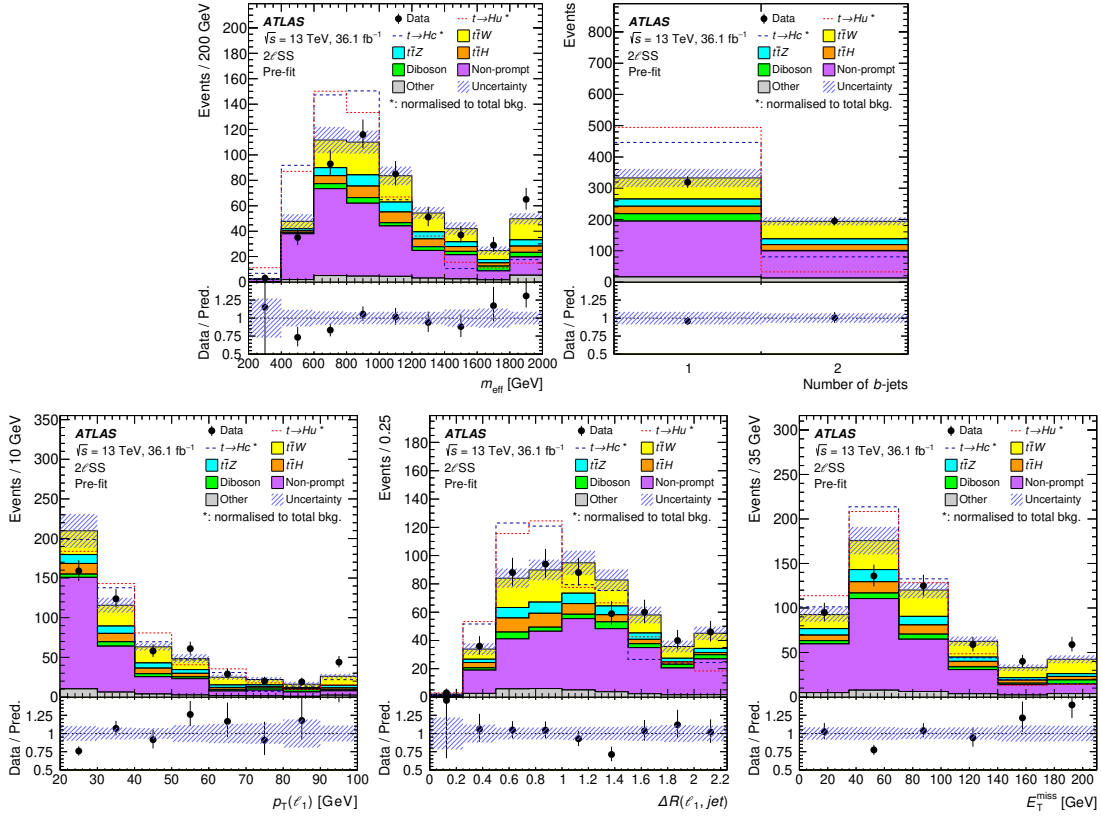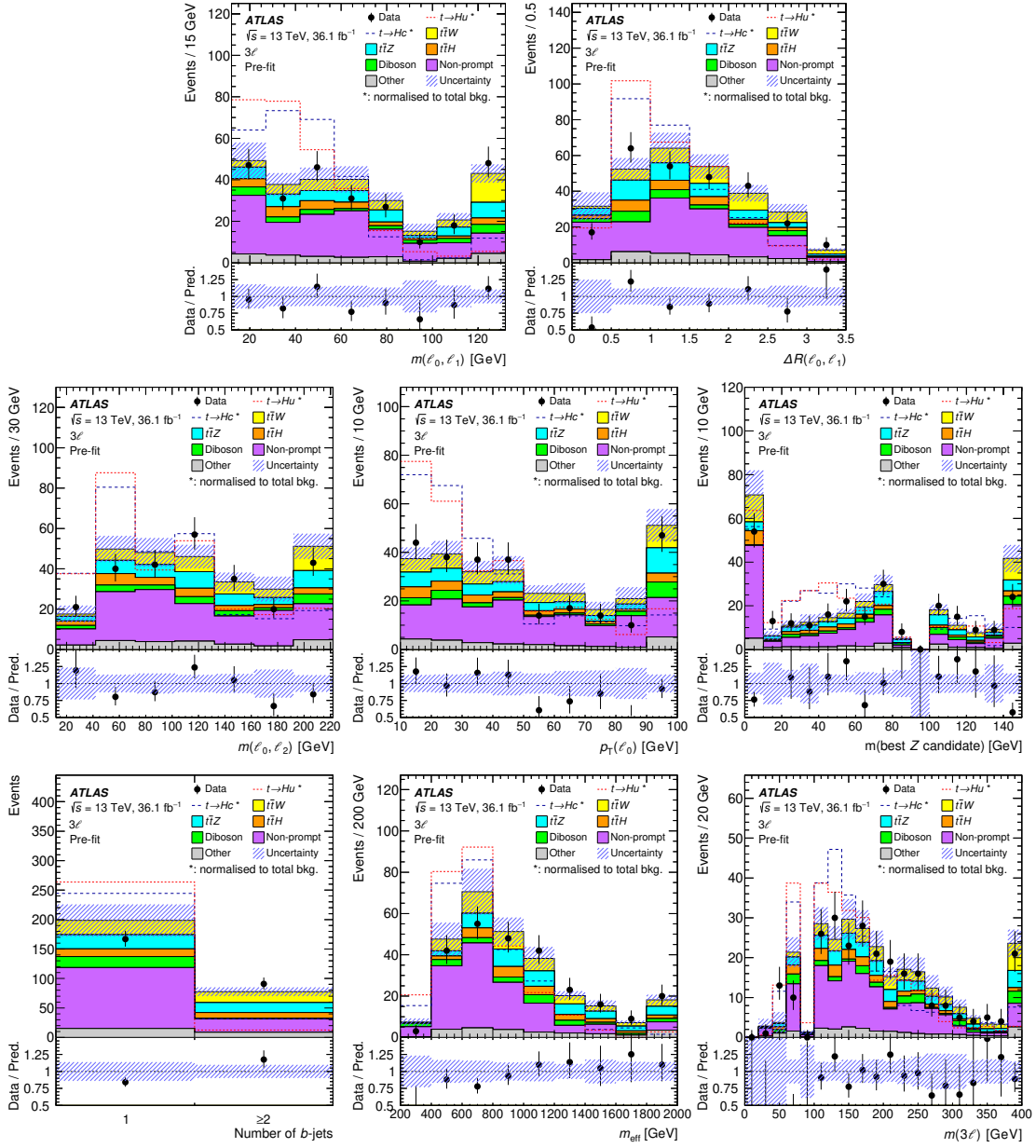
Figure 4.3.: Pre-fit distributions at $\mathcal{B}(t \to Hq) = 0$ for the five input variables to the 2ℓSS BDTs with highest separation of signal versus background. The distribution of the signal of $t \to Hu$ and $t \to Hc$ is shown normalised to the total background in red and blue, respectively [9].

4.3. Signal contamination in the non-prompt light lepton estimate

The non-prompt light leptons from b-hadron decays and photon conversion are a major background in this analysis. Their estimate uses the matrix-method, described in section 3.6.3. However, the signal contamination of the CRs used for the background estimates needs to be taken into account. Indeed, in the 2ℓ final state, the $t \to Hq$ signal peaks at four jets where one is coming from a b-quark, which leads to a non-negligible contribution in the 2ℓSS CR of two or three jets, used in the numerator of the non-prompt probability ε_f in equation 3.5. Assuming $\mathcal{B} = 0.2\%$, corresponding to the current best upper limit, the signal contamination in these control regions is about 30% of the total background from prompt leptons or electrons with misassigned charge. This yields to a reduction in the non-prompt lepton estimate of about 40% in the 2ℓSS and 30% in the 3ℓ SR. In the following I describe the treatment of this signal contamination, that I have developed.

Figure 4.4.: Pre-fit distributions at $\mathcal{B}(t \to Hq) = 0$ for the eight input variables to the 3ℓ BDTs with highest separation of signal versus background. The distribution of the signal of $t \to Hu$ and $t \to Hc$ is shown normalised to the total background in red and blue, respectively [9].

Not only the normalisation but also the shape differs for different $\mathcal{B}$. To correlate the contamination with $\mathcal{B}$, the procedure has been repeated for $\mathcal{B} = 0$ and 0.2%. This results in the bin-dependent yields of $N_{\text{non-prompt}}^{\text{orig.}}$ and $N_{\text{non-prompt}}^{\mathcal{B}=0.2\%}$, respectively. For any non-prompt lepton estimate $N_{\text{non-prompt}}(\mathcal{B})$ in each bin of the SRs the dependency of the

branching ratio is then given by a linear extrapolation

$$N_{\text{non-prompt}}(\mathcal{B}) = N_{\text{non-prompt}}^{\text{orig.}} - \frac{\mathcal{B} \cdot \left(N_{\text{non-prompt}}^{\text{orig.}} - N_{\text{non-prompt}}^{\mathcal{B}=0.2\%}\right)}{0.2\%}. \tag{4.5}$$

This extrapolation has been validated by additional working points between $\mathcal{B} = 0$ and 0.3%. The signal for $t \to Hc$ differs from $t \to Hu$ e.g. in the distribution of number of b-tagged jets, which is used in the binning of the non-prompt lepton efficiency measurement. Therefore, different estimates have been used for the two signals.

Figure 4.5 shows the estimated $t \to Hu$ discriminant distributions of the non-prompt lepton estimate in 2ℓSS and 3ℓ SR at different branching ratios.
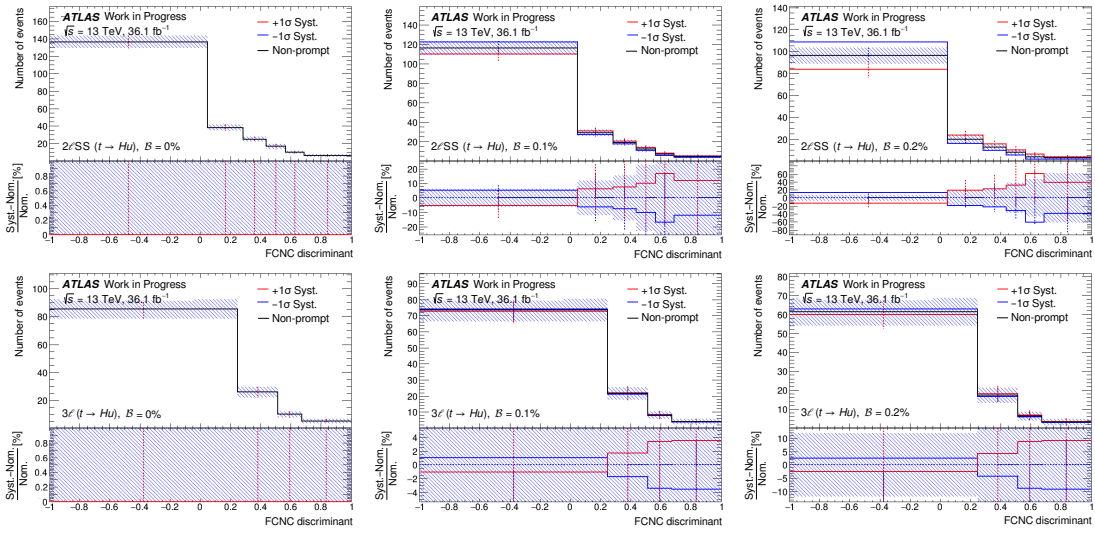
Figure 4.5.: $t \to Hu$ discriminant distribution of non-prompt lepton estimate for (top) 2ℓSS and (bottom) 3ℓ at $\mathcal{B} = 0$, 0.1% and 0.2% from left to right. The shape uncertainty with its 1σ up- and down-variations (red and blue line) are mainly smaller than the statistical uncertainty from the per-bin control regions (blue hashed area).

The difference in shape of the two estimates at $\mathcal{B} = 0$ and 0.2% is added as a shape-only systematic uncertainty on the non-prompt lepton estimate. Because it affects $N_{\text{non-prompt}}^{\mathcal{B}=0.2\%}$ in the subtrahend in equation 4.5 this uncertainty scales with the branching ratio. At $\mathcal{B} = 0.2\%$ it yields up to about 60% (10%) in the rightmost bins of the discriminant with the most signal in the 2ℓSS (3ℓ) SR. Only for $\mathcal{B} > 0.2\%$ and in the rightmost bins of the 2ℓSS SR it contributes more than the statistical uncertainty from the per-bin control regions where the matrix method weights are applied.

4.4. Results

The extraction of the $t \to Hu$ and $t \to Hc$ branching ratios uses a binned maximum-likelihood fit like in the $t\bar{t}H \to$ multilepton analysis. The likelihood function $\mathcal{L}(\mathcal{B}, \boldsymbol{\theta})$ is a product of per-bin Poisson probability terms related to the expected and observed event yields. The terms for Gaussian constraints of the nuisance parameters $\boldsymbol{\theta}$ are additional factors in $\mathcal{L}(\mathcal{B}, \boldsymbol{\theta})$. The test statistic is the negative profile likelihood ratio

$$-2 \ln \Lambda_\mathcal{B} = -2 \ln \frac{\mathcal{L}(\mathcal{B}, \hat{\hat{\boldsymbol{\theta}}})}{\mathcal{L}(\hat{\mathcal{B}}, \hat{\boldsymbol{\theta}})} \qquad (4.6)$$

where $\hat{\mathcal{B}}$ and $\hat{\boldsymbol{\theta}}$ are the best-fit values of branching ratio and nuisance parameter pulls maximising the likelihood $\mathcal{L}$ and $\hat{\hat{\boldsymbol{\theta}}}$ are the nuisance parameter pulls maximising the likelihood for a given $\mathcal{B}$. The parameter of interest (POI) is $\hat{\mathcal{B}}$.

The results for $t \to Hc$ and $t \to Hu$ are obtained independently assuming the other signal to have zero yield. Limits on the branching ratios at 95% confidence level (CL) are obtained using the $\mathrm{CL_S}$ method [140].

Apart from the signal contamination studies, described in the previous section, my main contribution to this $t \to Hq \to$ multilepton analysis has been the extraction and validation of all results, which are presented in the following.

The expected and observed yields in the 2ℓSS and 3ℓ SRs are presented in table 4.3. The observed and the pre-fit SM background yields for the 2ℓSS and 3ℓ SR are consistent

Table 4.3.: Expected and observed yields in the SRs for (top) $t \to Hu$ and (bottom) $t \to Hc$ fit. The non-prompt leptons include the contribution from charge misassigned electrons. While their pre-fit estimate assumes no $t \to Hq$ signal, their post-fit yields include the subtraction due to signal contamination in the non-prompt efficiency CRs. The pre-fit $t \to Hq$ yields are given for $\mathcal{B} = 0.2\%$ [9].

Category		Non-prompt leptons	$t\bar{t}V$	$t\bar{t}H$	Diboson	Other prompt SM	Total SM	FCNC	Data
					$t \to Hu$				
2ℓSS	Pre-fit	266 ± 40	165 ± 19	43 ± 4	25 ± 15	28 ± 6	526 ± 39	61 ± 13	514
	Post-fit	240 ± 37	167 ± 18	43 ± 4	24 ± 14	28 ± 6	502 ± 33	13 ± 21	
3ℓ	Pre-fit	126 ± 31	84 ± 8	23 ± 3	20 ± 11	24 ± 5	276 ± 33	32 ± 6	258
	Post-fit	104 ± 20	84 ± 8	23 ± 3	19 ± 10	24 ± 5	254 ± 18	7 ± 11	
					$t \to Hc$				
2ℓSS	Pre-fit	266 ± 40	165 ± 19	43 ± 4	25 ± 15	28 ± 6	526 ± 39	62 ± 13	514
	Post-fit	264 ± 41	165 ± 18	42 ± 4	20 ± 11	28 ± 6	520 ± 36	−3 ± 25	
3ℓ	Pre-fit	126 ± 31	84 ± 8	23 ± 3	20 ± 11	24 ± 5	276 ± 33	30 ± 6	258
	Post-fit	116 ± 21	84 ± 8	23 ± 3	15 ± 8	23 ± 5	262 ± 19	−1 ± 12	

with the yields in the $t\bar{t}H \to$ multilepton analysis in tables 3.10 and 3.5, respectively.

The observed branching ratios combining $2\ell\text{SS}$ and 3ℓ channel are

$$\mathcal{B}(t \to Hu) = 0.04\,^{+0.06}_{-0.06}\,(\text{stat.})\,^{+0.05}_{-0.04}\,(\text{syst.})\,\% = 0.04\,^{+0.08}_{-0.07}\,\% \qquad (4.7)$$

for the $t \to Hu$ and

$$\mathcal{B}(t \to Hc) = -0.01\,^{+0.06}_{-0.06}\,(\text{stat.})\,^{+0.05}_{-0.05}\,(\text{syst.})\,\% = -0.01\,^{+0.08}_{-0.08}\,\% \qquad (4.8)$$

for the $t \to Hc$ signal. They are compatible with the hypothesis of no signal. The best-fit branching ratios of the single channel fits for $2\ell\text{SS}$ and 3ℓ and combination are shown in figure 4.6 (left) and are compatible with each other and with zero. The behaviour of the
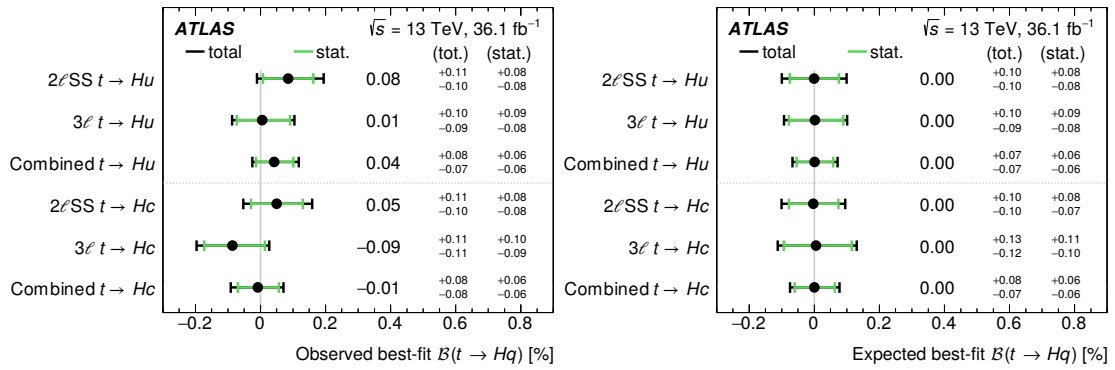
Figure 4.6.: (Left) observed and (right) expected best-fit $t \to Hq$ branching ratio in single channel and combination fits [9].

fits has been validated in fits to Asimov data with observed NP pulls θ and branching ratio. Similar uncertainties are observed as shown in figure 4.6 (right).

The post-fit yields for background and $t \to Hq$ signal, given in table 4.3, agree well with the observed number of events of 514 in $2\ell\text{SS}$ and 258 in 3ℓ SR. The distribution of the $t \to Hu$ and $t \to Hc$ discriminants in the SRs is shown in figure 4.7. The contribution of $t \to Hc$ is not visible in the stack of the histograms, because of the observed $\mathcal{B}(t \to Hc) < 0$. For both $t \to Hu$ and $t \to Hc$ the signal, normalised to the observed limit on $\mathcal{B}$, is shown, too. Its distribution is flat in dependency of the discriminant, because the binning with this configuration has shown optimal expected limits.

Upper limits on the branching ratios at 95% CL are calculated and presented in figure 4.8. The combined fits expect for both $t \to Hu$ and $t \to Hc$ upper limits on $\mathcal{B}$ of 0.15%. Similar expected upper limits have been published in the search for $t \to Hq$ with $H \to \gamma\gamma$ analysis (compare table 4.1). The observed upper limits are 0.19% and 0.16% for $t \to Hu$ and $t \to Hc$, respectively.

The distribution of the test statistics in function of $\mathcal{B}$ is shown in figure 4.9. It shows a well behaviour around the root, where the likelihood $\mathcal{L}$ is maximised.
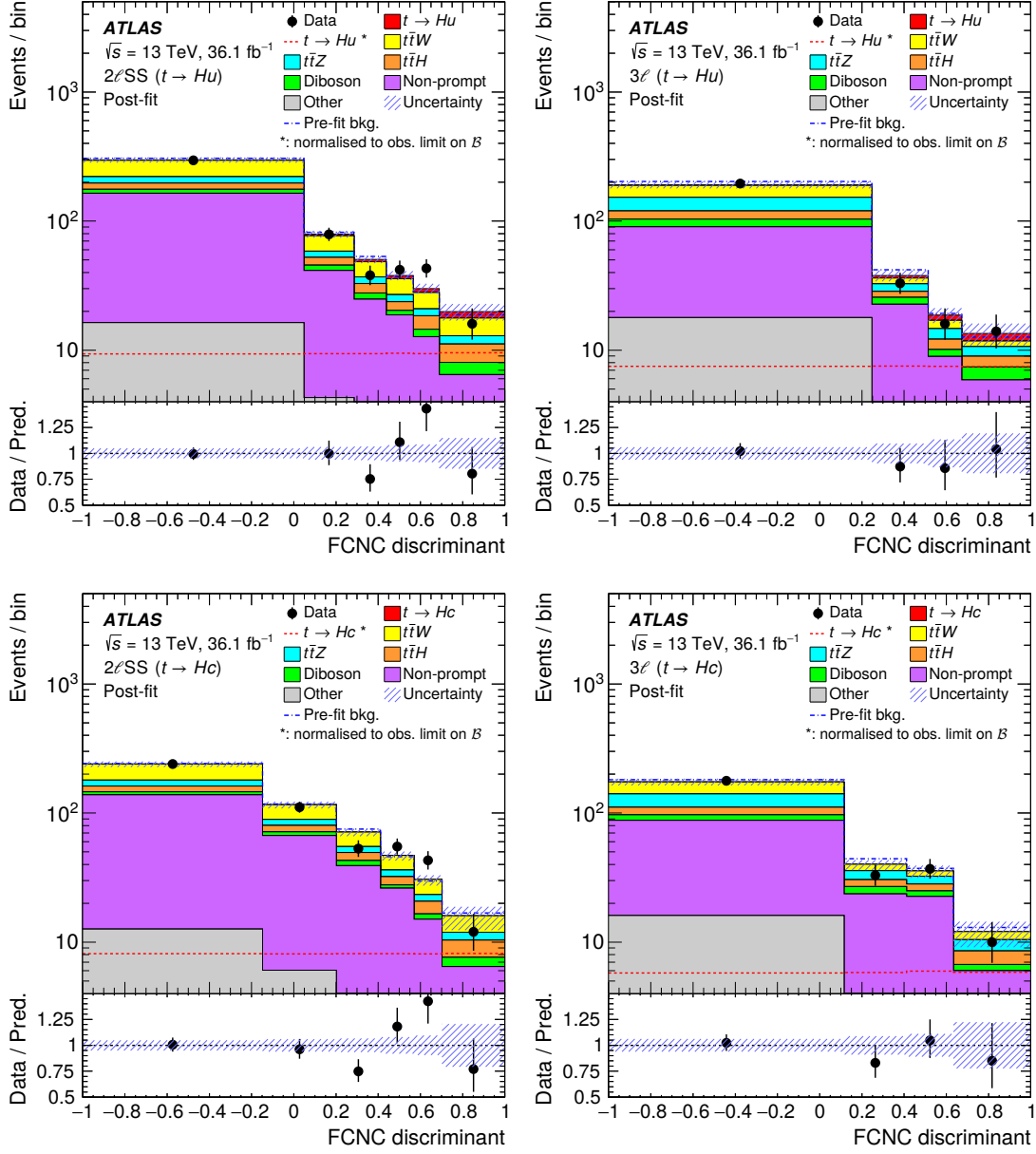
Figure 4.7.: Post-fit distributions for FCNC discriminants for measured (top) $t \rightarrow Hu$ and (bottom) $t \rightarrow Hc$ signal in (left) 2ℓSS and (right) 3ℓ SR [9].

4.4.1. Systematic uncertainties

The major impact on the uncertainty on $\mathcal{B}$ comes from the statistics, related to the amount of events in each bin. The largest impact from systematic uncertainties originates from the per-bin CRs for the matrix method weight application, the non-prompt lepton efficiencies and the diboson production cross section. The NPs with largest impact on $\mathcal{B}$ are shown in figure 4.10. The NPs with the biggest pulls are related to per-bin CR statis-
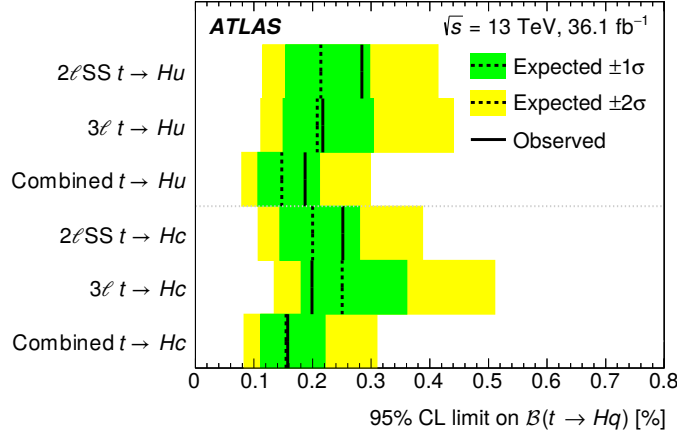
Figure 4.8.: 95% CL upper limits on $t \rightarrow Hq$ branching ratio in single channel and combination fits [9].
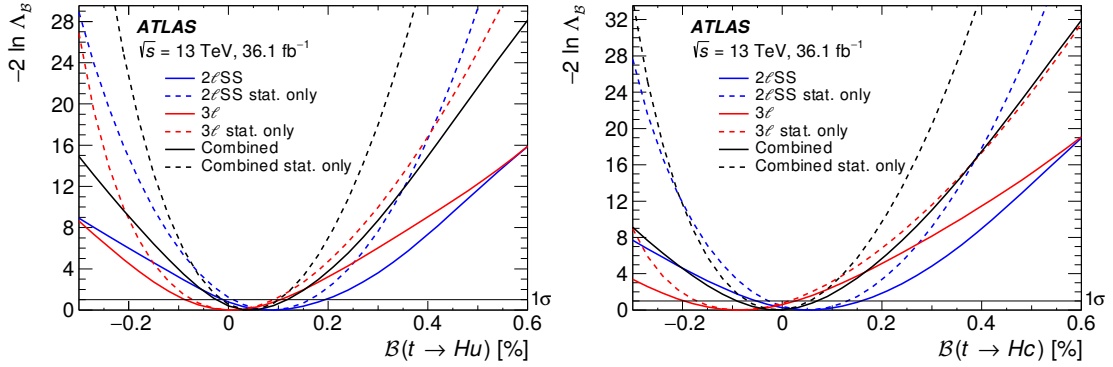
Figure 4.9.: Profile likelihood ratio for (left) $t \rightarrow Hu$ and (right) $t \rightarrow Hc$ in single channels and combination [9].

tics for the non-prompt lepton estimate, where the matrix method weights are applied. This is expected in particular for the 3rd and the 5th bin of the 2ℓSS SR, because of the small deficit and excess, respectively, which is visible in the discriminant distributions in figure 4.7.

The systematic uncertainties on the signal are dominated by the choice of parton shower algorithm and yield to a relative $\mathcal{B}$ uncertainty of $\frac{\Delta\mathcal{B}}{\mathcal{B}} = 8\%$. The uncertainty on the non-prompt lepton estimate from signal contribution in the non-prompt lepton efficiency CR scales with $\mathcal{B}$ and its impact is $\Delta\mathcal{B} = 0.02\%$ for a true $\mathcal{B} = 0.2\%$. The remaining background uncertainties contribute to the $\mathcal{B}$ uncertainty with $\Delta\mathcal{B} = 0.04\%$.

The impact of the signal contamination in the non-prompt lepton efficiency CRs is tested by decorrelating the branching ratio used in the non-prompt lepton estimate $N_{\text{non-prompt}}(\mathcal{B}_{\text{non-prompt}})$ in equation 4.5 from the one for the $t \rightarrow Hq$ signal ($\mathcal{B}_{\text{signal}}$). No difference in the best-fit values, uncertainties and upper limits on $\mathcal{B}_{\text{signal}}$ has been found. In the case of $t \rightarrow Hu$ and $t \rightarrow Hc$ fit they are measured to be $\mathcal{B}_{\text{non-prompt}}(t \rightarrow Hu) =$
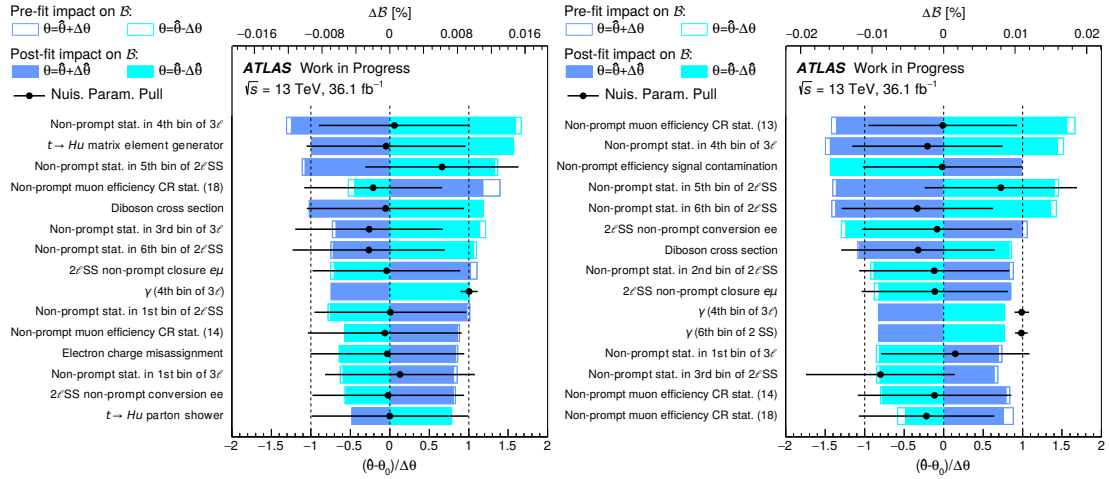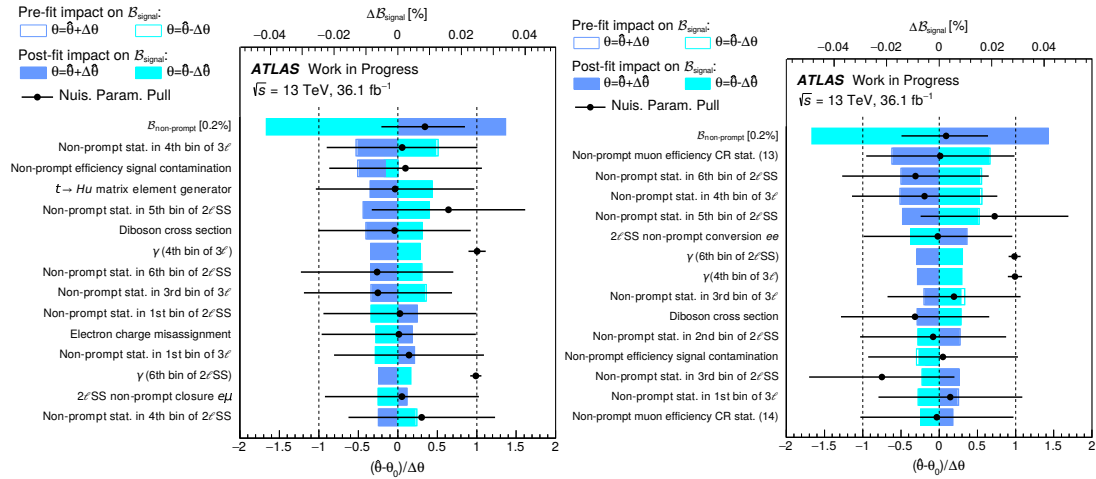
Figure 4.10.: Ranking of the 15 most impacting NPs on $\mathcal{B}(t \to Hq)$ in (left) $t \to Hu$ and (right) $t \to Hc$ fit.

$0.07\,^{+0.10}_{-0.11}\,\%$ and $\mathcal{B}_{\text{non-prompt}}(t \to Hc) = 0.02\,^{+0.11}_{-0.12}\,\%$, respectively. The ranking of the 15 most-impacting NPs on $\mathcal{B}$ is shown in figure 4.11 and can be compared with the nominal fit in figure 4.10. In the decorrelated model the uncertainty with the major impact on $\mathcal{B}_{\text{signal}}$ is the uncertainty on the free parameter of $\mathcal{B}_{\text{non-prompt}}$ with $\Delta\mathcal{B}_{\text{signal}} \approx 0.04\text{–}0.05\%$. Other NPs follow with similar ranking as in the nominal case and $\Delta\mathcal{B} < 0.015\%$.

An iterative signal injection test is performed where iteratively $\mathcal{B}^{n+1}_{\text{non-prompt}}$ is fixed to the $\mathcal{B}^{n}_{\text{signal}}$ observed in the previous iteration. It reaches a plateau at $\mathcal{B}_{\text{signal}}(t \to Hu) = 0.03\,^{+0.06}_{-0.06}\,\%$ and $\mathcal{B}_{\text{signal}}(t \to Hc) = -0.02\,^{+0.06}_{-0.07}\,\%$, compatible with the observed results given in equations 4.7 and 4.8.

Figure 4.11.: Ranking of the 15 most impacting NPs on $\mathcal{B}_{\text{signal}}(t \to Hq)$ in (left) $t \to Hu$ and (right) $t \to Hc$ fit in the case of decorrelated $\mathcal{B}$ for signal and non-prompt lepton estimate.

Another possibility is to derive matrix method weights by injecting the observed $\mathcal{B}$. This test has been done for $t \to Hu$ and the same $\mathcal{B}$ are observed as in the nominal fit. All these tests give confidence that the treatment of the signal contamination in the CRs for the non-prompt lepton estimate does not induce any bias on the final results.

4.4.2. Simultaneous fit of $t \to Hu$ and $t \to Hc$ signals

To check the correlation of the $t \to Hu$ and the $t \to Hc$ signal an additional fit configuration has been developed, where for both signals one POI is assigned. Here both signals have contamination in the non-prompt lepton efficiency CR, which is taken into account properly. The SRs use the $t \to Hu$ discriminants with a binning, such that the signal is flat if $\mathcal{B}(t \to Hu) = \mathcal{B}(t \to Hc)$. The observed best-fit branching ratios are $\mathcal{B}(t \to Hu) = -0.02^{+0.26}_{-0.25}\%$ and $\mathcal{B}(t \to Hc) = 0.02^{+0.29}_{-0.29}\%$. The post-fit discriminant distributions are shown in figure 4.12. No signal is visible, because the two signal com-
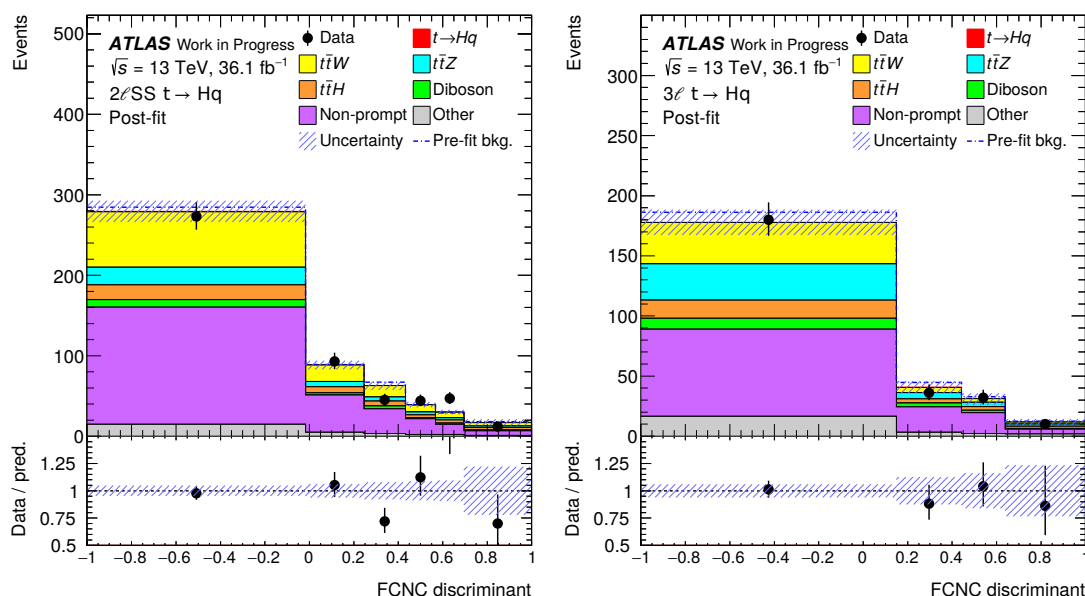
Figure 4.12.: Post-fit distributions for FCNC discriminants for simultaneous fit of $t \to Hu$ and $t \to Hc$ signal in (left) 2ℓSS and (right) 3ℓ SR.

ponents have similar discriminant distribution and their contributions cancel each other due to $\mathcal{B}(t \to Hu) \approx -\mathcal{B}(t \to Hc)$.

The two POIs are strongly correlated with each other, which can be observed in the contour lines of the test statistic in figure 4.13. The major axis of the ellipse lies on the function of $\mathcal{B}(t \to Hu) + \mathcal{B}(t \to Hc) = 0$. This is due to the fact, that firstly, no signal is observed and secondly, this analysis is not optimised to distinguish $t \to Hu$ from $t \to Hc$ signal.
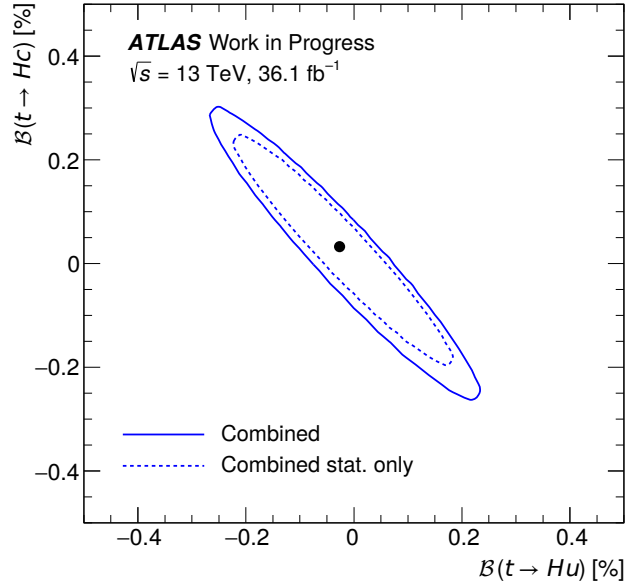
Figure 4.13.: Best-fit branching ratios (black dot) and 1σ contour lines of the test statistic $-2\ln\Lambda_{\mathcal{B}}$ (blue) for fit with all systematics (solid line) and only statistical (dashed line) when fitting both $t \to Hc$ and $t \to Hu$ simultaneously.

4.5. Outlook

The described $t \to Hq \to$ multilepton uses $36.1\,\text{fb}^{-1}$ of proton-proton collisions, which leads to an expected upper limit on $\mathcal{B}$ of 0.15% for both $t \to Hu$ or $t \to Hc$. This improves the expected upper limits from Run 1 $t \to Hq \to$ multilepton analysis with $20\,\text{fb}^{-1}$ at $8\,\text{TeV}$ by a factor of more than five.

The extrapolation to the expected Run 2 integrated luminosity of $150\,\text{fb}^{-1}$ is done by scaling all yields with the luminosity. This leads to an expected upper limit of about 0.10%, assuming the same systematic uncertainties as in the current analysis. At this point already the systematic uncertainties dominate the result and the improvement with higher luminosity is marginal. Assuming a HL-LHC with $L = 3{,}000\,\text{fb}^{-1}$ would only improve the expected limit to about 0.07% with current systematic uncertainties, not accounting for effects of harsher pile-up conditions.

On the other hand several improvements can be included in an analysis with the full Run 2 data:

- Additional channels can be added, e.g. the channel of $2\ell\text{SS}+1\tau_{\text{had}}$ has not been included in this round, while it was in the corresponding Run 1 analysis [109]. This channel aims for $H \to \tau\tau$ decays with one tau lepton decaying hadronically and the other one leptonically.

- Due to the need for a robust estimate of non-prompt leptons, the analysis does not effectively use the region of $2\ell\text{SS}$ with two or three jets for the estimate of the signal branching ratio, while about 60% of the $t \to Hq$ signal lies in this region.

There is a big room for gain if a development using other side-bands, e.g. events with two *b*-tagged jets, is successful.

- Both 2ℓSS and 3ℓ SR have been chosen to be very close to the regions used in the $t\bar{t}H \to$ multilepton analysis. This significantly has helped in validating the analysis and reusing elements of the $t\bar{t}H \to$ multilepton analysis, such as background estimates and suppression, fit set-up, etc. Nevertheless, an optimisation of the event selection in the SRs can improve the sensitivity. E.g. the *b*-tagged jets multiplicity and the *b*-tagging efficiency working point can be object of optimisation, although it was tested, that excluding the events with more than one *b*-tagged jet does not change the result significantly.

An analysis with different detector upgrade scenarios has been published in the search for $t \to Hq$ with $H \to b\bar{b}$ by the ATLAS collaboration. The expected limits on the $\mathcal{B}(t \to Hq)$ are 0.01–0.02 % for a HL-LHC with $L = 3{,}000\,\text{fb}^{-1}$ and $\sqrt{s} = 14\,\text{TeV}$ [141]. If no signal is found, in combination with searches in other Higgs boson decays this could allow to constrain the allowed phase space for new physics, in particular the flavour-violating 2HDM model as it predicts $\mathcal{B}(t \to Hc) < 0.15\,\%$ (compare figure 4.1, [31]).

4.6. Conclusion

A search for the flavour-changing top quark decay to the Higgs boson and an up-type quark in multileptonic final states has been performed using proton-proton collision data from 2015–2016, recorded by the ATLAS detector. Two channels with two leptons with same electric charge or with three leptons have been examined and optimised separately for the best expected limits. The signal contamination in the control regions for the non-prompt lepton estimate has been investigated and is properly treated in the fit. The observed best-fit values are consistent with the SM expectation of negligible signal with branching ratios $\mathcal{B}(t \to Hq) < 3 \times 10^{-15}$. Observed (expected) upper limits at 95 % CL are 0.19 % (0.15 %) and 0.16 % (0.15 %) for $t \to Hu$ and $t \to Hc$ decays, respectively. They are the best experimental limits on this flavour-changing top quark decays to date and compatible with the previously observed upper limits in the search with $H \to \gamma\gamma$ by the ATLAS collaboration.

The presented search in multileptonic final states is dominated by statistical uncertainties. Therefore, the sensitivity will improve by using the full Run 2 data.

Both the searches for $t\bar{t}H$ (chapter 3) and for flavour-changing top decays (this chapter) will improve a lot by additional data beyond Run 2. To achieve this, the LHC and its experiments will be upgraded in a long shut-down in 2019–2020. The next chapter describes the current status of this upgrade for the ATLAS Liquid Argon Calorimeter.

5. Phase 1 upgrade of the ATLAS Liquid Argon Calorimeter

The upgrade of the LHC, scheduled for 2019-2020, plans to increase the instantaneous luminosity to more than two times the nominal value. The purpose and overview of this upgrade plan for the LHC and the ATLAS experiment is presented in section 5.1. To cope with the increase of ATLAS trigger rates, the trigger signals from the ATLAS Liquid Argon Calorimeter will be rearranged in 34,000 so-called super cells to get a 5 to 10 times finer granularity. This will improve the background rejection performance through more precise energy measurements and the use of shower shape information to discriminate electrons, photons and hadronically decaying tau leptons from jets. The new system will process the super cell signal at 40 MHz and with 12 bit precision. The data will be transmitted at 5.12 Gb/s to the back-end system using a custom serialiser and optical transmitter. The Phase 1 upgrade of the LAr Calorimeter readout electronics is described in section 5.2. To verify the full functionality, a demonstrator set-up has been installed on the ATLAS detector and operated during the LHC Run 2. Its set-up and performance in calibration and proton-proton collisions is discussed in section 5.3. I have contributed to these measurements in calibration and in early collision data-taking.

5.1. LHC at high luminosity

For many searches for new physics or rare SM processes statistical uncertainties have a huge impact. With increasing integrated luminosity L, which is proportional to the data taking time t, they decrease only by $1/\sqrt{L} \propto 1/\sqrt{t}$. Increasing the instantaneous luminosity $\mathcal{L}$ is the only way to beat this limitation. To reach that both the LHC accelerator system and the detectors pass through an ambitious upgrade plan.

Detector upgrades are necessary to cope with the high radiation as the present detectors are qualified only up to an $L = 1{,}000 \, \text{fb}^{-1}$. With increasing instantaneous luminosity the physics performance of the detectors should be kept similar. Therefore, e.g. the trigger selectivity needs to be improved to avoid bandwidth saturation. This can be reached by adding new information as timing or higher granularity in the inputs to the trigger and reconstruction. Additionally the detector coverage, in particular at high pseudorapidity, can be increased where possible. At last, some parts of the electronics are already older than 15 years and cannot be manufactured and maintained in the future.

The plan for the LHC and the high-luminosity LHC (HL-LHC) is shown in figure 5.1. The currently on-going Run 2 of proton-proton collision data-taking will be followed by
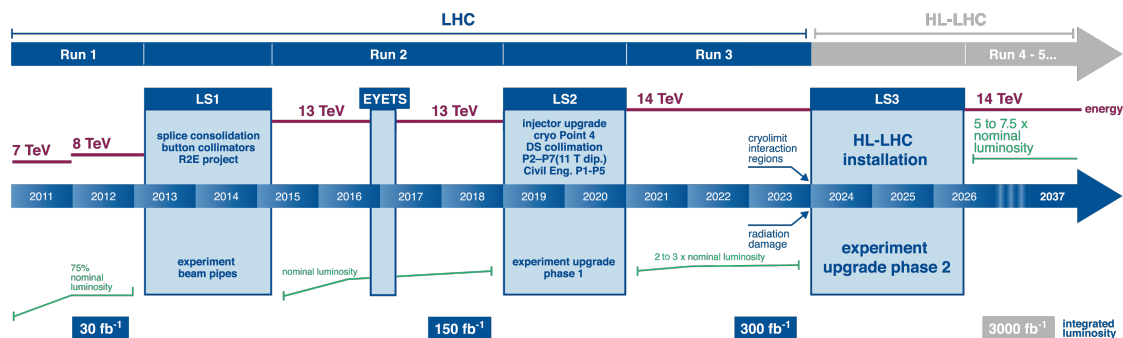

Figure 5.1.: LHC data taking periods (Runs), long shut-downs (LS) and high-luminosity LHC (HL-LHC) forecast with the center-of-mass energy of the collisions in red and luminosity in green (derivative of [142]/CC BY 4.0).

the long shut-down 2 (LS2) during 2019/2020, in which the Phase 1 upgrade system will be installed. The Phase 2 upgrade is foreseen for 2024–2026 during LS3.

With the Phase 1 upgrade of the experiments at the LHC an instantaneous luminosity of up to three times the design value ($\mathcal{L} = 3 \times 10^{34} \, \text{cm}^{-2}\text{s}^{-1}$) with the mean number of interactions per bunch crossing $\langle \mu \rangle = 80$ will be reached. The Phase 2 upgrade prepares for the HL-LHC with instantaneous luminosity of about $\mathcal{L} = 7.5 \times 10^{34} \, \text{cm}^{-2}\text{s}^{-1}$ and $\langle \mu \rangle = 200$. The ultimate goal is to collect proton-proton collision data with an integrated luminosity of about $3{,}000 \, \text{fb}^{-1}$ during 10 years of data-taking.

Figure 5.2 shows extrapolations for Higgs boson and top FCNC studies at HL-LHC conditions. The high integrated luminosity allows to precisely measure even rare Higgs boson decays as $H \rightarrow \mu\mu$. Also the $t\bar{t}H$ production in multileptonic final states is expected to be measured with less than 20% relative uncertainty on the signal strength as discussed in section 3.10 with an own extrapolation. The precise measurement of the Higgs boson couplings to fermions will allow to improve the limits on new physics, which is entering e.g. in loops of gluon-gluon fusion or $H \rightarrow \gamma\gamma$ decays.

The 95% CL limits on FCNC top decays are mainly statistically limited and in the case of no signal observation in particular the $t \rightarrow Hc$ and $t \rightarrow \gamma c$ limits can be improved by one order of magnitude using the full expected HL-LHC dataset. The own extrapolation of the FCNC decay of $t \rightarrow Hc$ in multileptonic final states expects an upper limit on the branching ratio of 7×10^{-4} at full expected HL-LHC luminosity, improving the current expected limits at $L = 36.1 \, \text{fb}^{-1}$ by a factor of two (see section 4.5).

5.1.1. Phase 1 ATLAS detector upgrade

The Phase 1 upgrades of the ATLAS detector mainly aim at improving the trigger selectivity to cope with increasing luminosity [146].
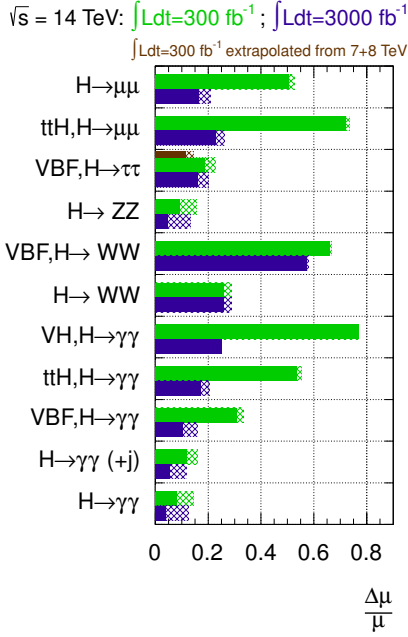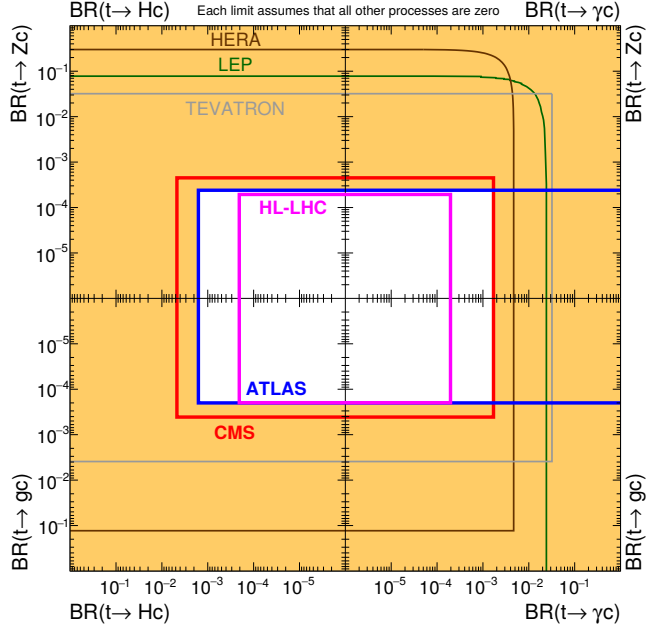
Figure 5.2.: (Left) ATLAS projection of relative uncertainty on the signal strength for different Higgs boson production and decay modes for $L = 300$ and $3{,}000\,\mathrm{fb}^{-1}$ [143]. (Right) observed 95% CL limits on branching ratios of different top quark decays involving FCNC [130]. The projection to HL-LHC is added in pink following the references [141, 144] for $t \to Hc$ and $t \to Zc$ and [145] for $t \to \gamma c$. No extrapolation studies for $t \to gc$ have been published so far.

The EM total L1 trigger rate at the ATLAS has a limited 20 kHz of the 100 kHz global bandwidth. Figure 5.3 shows the measurement of L1 trigger rates for different objects as a function of the instantaneous luminosity. The light lepton trigger rates increase linearly and the forward-jet and missing transverse energy trigger rates increase exponentially with luminosity and number of interactions per bunch crossing. As increasing the energy thresholds to maintain the limited bandwidth cuts out interesting physics, the Phase 1 upgrade plans to improve the L1 trigger inputs by a higher granularity in the LAr calorimeter readout. Therefore the LAr trigger readout electronics are going to be upgraded during LS2 [148]. The details of this upgrade are described in section 5.2.

It is planned to replace the small wheels in the muon spectrometer (MS) by new ones (NSW) to reconstruct muon tracks with higher precision and to improve the inputs to the L1 trigger [149]. In particular, the L1 trigger input fake rate from low energy particles has been measured to be about 90% in an analysis done on 2012 proton-proton collision data. This will be significantly improved by the NSW for $1.3 < |\eta| < 2.5$. Additionally the modules of the inner barrel in the barrel to end-cap transition region of $1 < |\eta| < 1.3$ will be replaced by a new triplet of Resistive Plate Chambers (RPCs) to reduce the fake
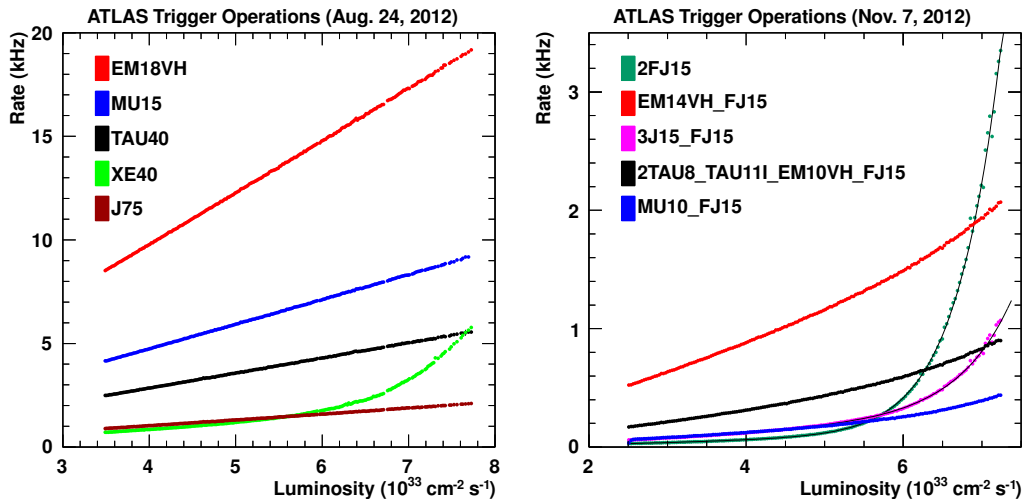
Figure 5.3.: L1 trigger rates as a function of instantaneous luminosity for (left) electron or photon (EM18VH), muon (MU15), hadronically decaying tau lepton (TAU40), jet (J75) and missing transverse energy (XE40) and (right) different forward jet triggers from proton-proton collisions in 2012 [147].

trigger rate in this region, too [150].

The proposed Fast Tracker (FTK) is an hardware based global track reconstruction for events selected by the L1 trigger [151]. It uses information from the SCT and the pixel detectors, including the IBL. More than 1,000 FPGAs will perform the pattern recognition and the track fitting. The output will serve as input to the high-level trigger (HLT).

The Trigger and Data Acquisition (TDAQ) system will be updated to cope with the changes to the detector and to maintain the low trigger thresholds at the high instantaneous luminosity of Run 3 [152].

5.1.2. Phase 2 ATLAS detector upgrade

Several upgrades of the ATLAS detector are necessary to sustain the harsh radiation conditions at the HL-LHC [143].

It is planned to replace the inner tracker by an all-silicon tracker and to upgrade the trigger to use track information at low-level.

For the calorimeters and muon spectrometers the readout systems are upgraded and the new trigger system will use their information at high rates and granularity. The program foresees e.g. the replacement of the current LAr main readout electronics, which is described in section 5.4. The MS upgrade foresees the addition of a new layer of RPCs in the innermost barrel layer.

An extrapolation of the Phase 1 L1 trigger rates to HL-LHC luminosity without increasing trigger thresholds would lead to trigger rates of more than 500 kHz exceeding the bandwidth for input to the HLT. Therefore the low-level trigger will be split into

two: L0, which uses e.g. the super cells from the LAr calorimeter and has an output rate of 1 MHz within a latency of 6 µs and L1, which uses tracking information and full LAr calorimeter granularity to reduce the rate further to about 200 kHz at an additional latency of 14 µs.

5.2. Phase 1 LAr Calorimeter readout electronics upgrade

The current L1 trigger system uses trigger towers with a pseudorapidity $\times$ polar angle size of $\Delta\eta \times \Delta\phi = 0.1 \times 0.1$ in the EMB as input from the LAr Calorimeter. The Phase 1 upgrade of the LAr Calorimeter readout electronics foresees an increase of granularity by a factor of 5 to 10, resulting in the so-called super cells, which are refined sums of LAr Calorimeter cells as sketched in figure 5.4. Longitudinal shower information is
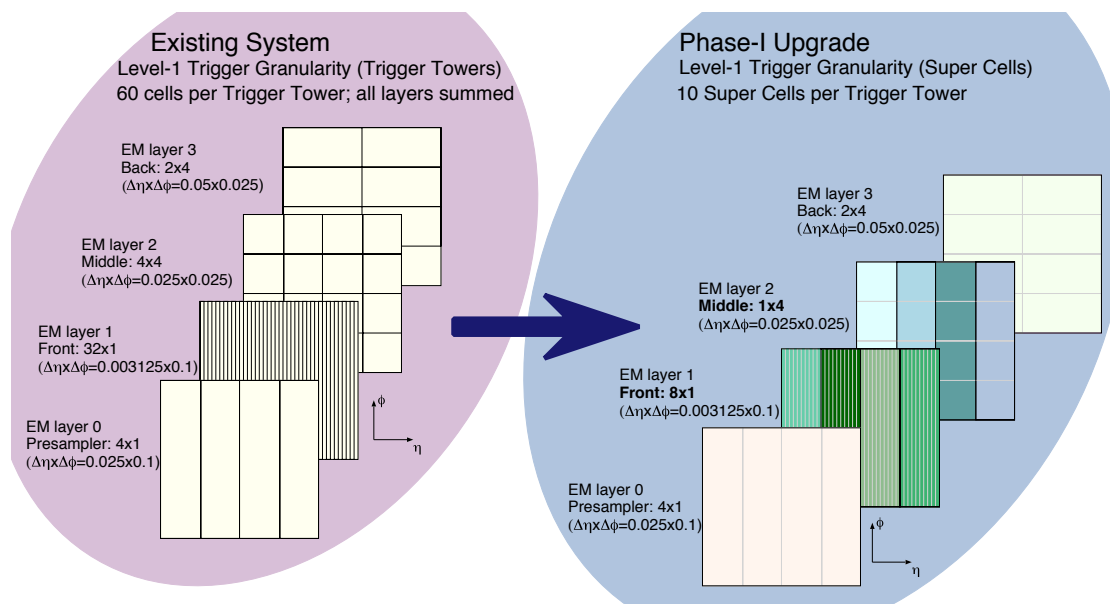
Figure 5.4.: L1 trigger granularity in the EMB (left) in existing system and (right) after the Phase 1 upgrade to super cells [148].

added by separating the four layers in the new readout format. This is illustrated for a simulated shower of an electron in figure 5.5. New discriminant variables can improve to distinguish interesting physics objects as electrons and hadronically decaying tau leptons from jets at the L1 trigger level.

A schematic diagram of the Phase 1 LAr Calorimeter readout electronics upgrade is shown in figure 5.6 with the new components indicated by red outlines and arrows. To perform the analog sums to the super cell signals the current LSBs will be replaced. New Base-planes are needed to keep the compatibility with the existing set-up and to route the new super cell signals, which brings about ten times more signal lines. The LAr
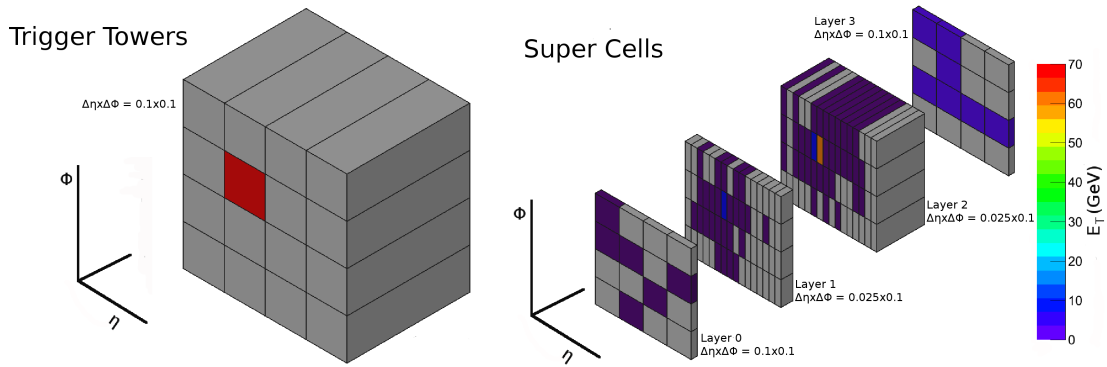
Figure 5.5.: Shower of a simulated electron with a transverse energy of 70 GeV (left) in current L1 trigger towers and (right) in super cells after Phase 1 upgrade [148].
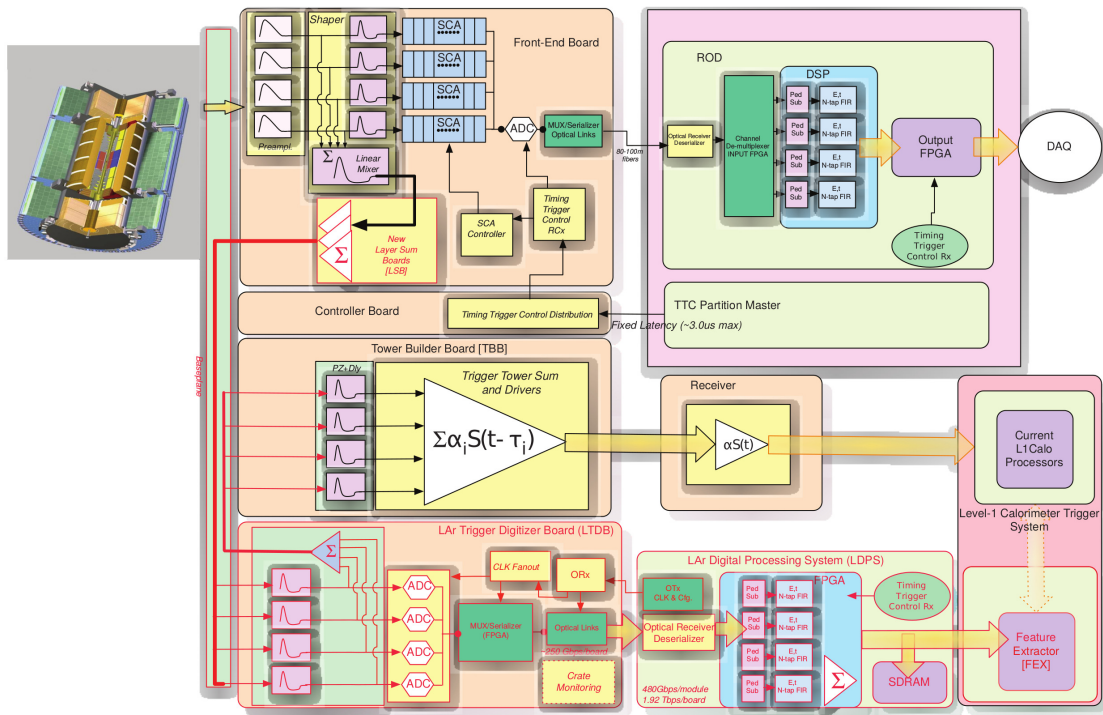

Figure 5.6.: Phase 1 LAr Calorimeter readout electronics upgrade with new components shown by red outlines and arrows [148].

Trigger Digitizer Boards (LTDBs) receive, digitize and send the super cell signals to the off-detector back-end system, the so-called LAr Digital Processing System (LDPS). It calculates the transverse energy of each super cell and various sums of super cells at fixed latency and sends the results continuously at 40 MHz to the L1Calo feature extractors. The old analog trigger path using the trigger towers from the TBBs will remain for backup while commissioning in Run 3. It is planned to be removed at Phase 2 upgrade.

5.2.1. Front-end electronics upgrade

5.2.1.1. Base-plane, FEBs and LSBs

The connectivity, cross-talk and noise performance has been verified for the standard base-planes for EMB and EMEC with prototypes and the production has started. The development of the special base-planes for EMEC, HEC and FCAL is progressing. The procurement of common parts such as ground springs and alignment pins is ongoing. The FEBs will remain unchanged until Phase 2, but the LSBs will be replaced to comply with super cell signal summing. Their production is ongoing.

5.2.1.2. LTDB

There are a total of 124 LTDBs reading 34 thousand super cells to be installed. Each LTDB reads up to 320 super cells. It digitizes analog signals with 12 bits at 40 MHz using custom analog-to-digital converters (ADCs). The digital signals are transmitted using 40 optical links at 5.12 Gb/s with custom application-specific integrated circuits (ASICs). It has 5 GigaBit Transceiver (GBT) serializer-de-serializer links for trigger, timing and control (TTC) signals. Its power distribution board (PDB) has to comply with the total power consumption of around 125 W. The whole system is on the detector and thus, all components need to be radiation-tolerant. It has full compatibility with the Phase-2 upgrade. The final design has been fixed and prototypes are being produced.

5.2.1.3. LTDB custom ADCs

Each LTDB requires 80 custom ADCs that continuously process the sampling and digitization of four super cell signals at 40 MHz. The power dissipation is less than 50 mW per channel and the latency must be less than 200 ns. The dynamic range is 11.7 bits per sample. The Nevis13 ADC fulfils all requirements. Its layout is based on a 130 nm IBM CMOS 8RF of 3.6 mm × 3.6 mm with 72 quad-flat no-leads (QFN) pins. It uses four multiplying digital-to-analog converters (MDACs) for the most significant bits and one successive approximation ADC (SAR) for the lower eight bits. It is tested for radiation up to 10 Mrad which corresponds to 100 times more than currently expected at HL-LHC.

5.2.1.4. LTDB optical links

Two kinds ASICs for optical links on the LTDB are developed. The serializer (LOCx2) is based on a 250 nm silicon-on-sapphire technology with a die of 6.0 mm × 3.7 mm and 100 QFN pins. Its output is at 5.12 Gb/s at a latency of less than 75 ns. It has about 1 W of power consumption. The laser driver (LOCld) uses the same technology as the LOCx2 on a die of 2.1 mm × 1.1 mm and 40 QFN pins. It is a dual-channel vertical-cavity surface-emitting laser (VCSEL) driver. Both ASICs have been tested on radiation-tolerance. Only few change in the output eye diagrams has been observed after about 200 kHz. The wafers are produced and tests on the LTDB prototypes are ongoing.

5.2.2. Back-end electronics upgrade

5.2.2.1. LDPS

The LDPS receives the digital 12 bit data from the front-end system. It calculates the transverse energy of each super cell and various sums of super cells at fixed latency and transmits the results at 40 MHz to the L1Calo feature extractors. Additionally it buffers the calculated results for a readout upon L1 trigger decision for debugging and monitoring. Because the back-end LDPS is off-detector, there is no need to be radiation-tolerant as the front-end system. Its main component are about 30 LAr Digital Processing Blades (LDPBs) which read the outputs of 124 LTDBs. Each LDPB consists of one LAr carrier board (LArC) with four advanced mezzanine cards (AMCs) and a rear transition module (RTM). It is a custom advanced telecommunications computing architecture (ATCA) board and uses a Xilinx Virtex7 FPGA. It carries four AMCs and drives the communication to the FELIX system [153] and the data acquisition for the data monitoring. The AMCs have 48 input fibres at 5.12 Gb/s and the same amount of output fibres at 11.2 Gb/s. They are called LATOME, acronym for LAr trigger processing mezzanine.

5.2.2.2. LATOME

The LATOME receives super cell data from the LTDBs at 5.12 Gb/s on up to 48 optical links. It is responsible for the computation of transverse energies of super cells and sums of super cells using optimal filtering algorithm (OF) [11] at fixed latency. It assigns bunch crossings by timing measurement. Finally it sends the data at 11.2 Gb/s on up to 48 optical links to the L1 trigger. Furthermore it monitors the data and sends report to the DAQ system upon request. In figure 5.7 a picture of the LATOME board prototype is shown. Its heart is an Intel Arria10 FPGA. First prototypes have been successfully tested and integrated. The validated features include the optical links up to 11.2 Gb/s,
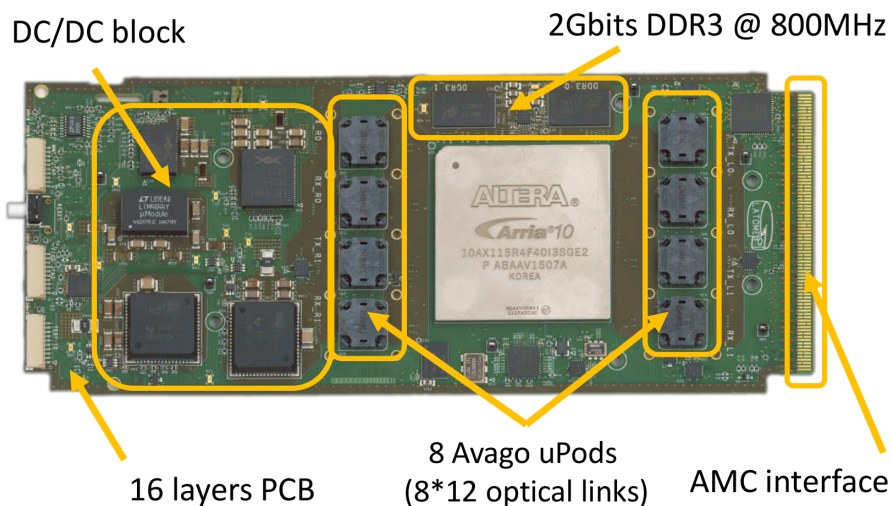

Figure 5.7.: Picture of the LATOME board.

1 Gb Ethernet and GBT. The system test is ongoing to check all functionalities and the communication of the LDPB with other systems.

The firmware of the LATOME is build in a modular way and consists of following parts. The input stage treats the reception of the ADC data at 40 MHz and aligns the input fibres to the same time reference (TTC). The configurable remapping matches the input channels to the detector geometry. The user code computes the transverse energy at the correct bunch crossing time using OF. The output summing calculates sums of super cell transverse energies for various L1Calo feature extractors and sends the data to L1 trigger system at 40 MHz. It has a latency of less than 375 ns and buffers ADC data and energies for at least 2.5 μs, which allows to monitor at the L1 trigger rate of 100 kHz. All LATOME firmware blocks have been developed and are under test. The overall system test on the hardware is ongoing.

5.3. LAr demonstrator

The LAr demonstrator is a pre-prototype of the calorimeter readout of the L1 processors. It has been installed in 2014 during LS1 at the ATLAS experiment. It covers 3.1% of the EMB and is located at $\eta \times \phi \in [0, 1.4] \times [1.77, 2.16]$. Before its installation no disturbance to the current system has been verified. It validates the energy reconstruction and bunch-crossing identification development. The system is successfully calibrated and data from proton-proton (and heavy-ion) collisions is taken during the Run 2. Two LTDB prototypes provide the analog summing of calorimeter cell signals to super cells at the rate of 40 MHz. The AMC pre-prototypes are the so-called ABBAs (ATCA board for a baseline of liquid argon acquisition). In early 2018 the two LTDBs and the LDPS have been replaced by the final prototypes. This includes two LATOME boards, which are then tested in 2018 proton-proton collisions.

5.3.1. LTDB pre-prototypes

The two LTDBs handle each up to 320 super cell signals in two slices of ϕ (140 super cells in the EMB for one slice of ϕ with $0 < \eta < 1.4$). The super cell signals are digitised with a commercial, not radiation-tolerant 12 bit ADC (TI ADS5272). On one 4.8 Gb/s optical link eight super cell signals are multiplexed. Two prototypes with different technology have been developed by several institutes. The first one uses an analog mezzanine and a digital main board and the second one uses a digital mezzanine together with an analog main board. Both versions are successfully operated during Run 2.

5.3.2. ABBA – LDPS pre-prototypes

The ABBA is the pre-prototype for the LDPS and a picture with its components is shown in figure 5.8. One ABBA receives the digital signals of up to 320 super cells from one LTDB on up to 48 optical links at 4.8 Gb/s. It stores the ADC super cell data in circular
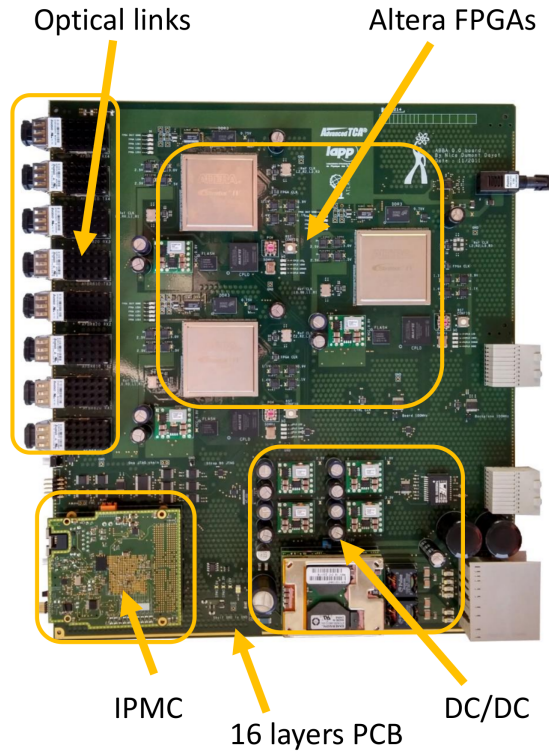
Figure 5.8.: Picture of the ABBA with its optical links and three FPGAs.

buffers and sends it using the IP-based protocol IPbus over user datagram protocol (UDP) on a 10 Gb Ethernet upon a L1 trigger accept in the so-called 'monitoring mode'. It contains three Intel (former Altera) Stratix4 FPGAs.

In end of 2017 three ABBA boards were installed in the ATLAS counting room. The online software is operational and read out in parallel with the ATLAS default readout since October 2015. It has been integrated in the automated ATLAS data acquisition since November 2016 with still separate data-flow. In early 2018 the ABBAs have been replaced by the new prototypes of LATOME boards.

5.3.3. Performance in calibration

In the calibration of the demonstrator electronic pulses are sent by the same calibration board as the one used for the LAr Calorimeter calibration. The size of the calibration pulse is given by the DAC value, which can be set as a value between 0 and $\max(\text{DAC}) = 2^{16} - 1 = 65{,}535$. Additionally the pulse can be delayed by up to one clock cycle of $\Delta t_{\text{TTC}} = 1/40.08 \, \text{MHz} = 24.95 \, \text{ns}$ in steps of $\Delta t_{\text{delay}} = \Delta t_{\text{TTC}}/239$.

Its response in the demonstrator is measured by the LDPS in ADC. The full pulse shape in a super cell can be measured by scanning the delay, e.g. in steps of $10\Delta t_{\text{delay}}$. In the presented calibration studies 40 samples have been measured which corresponds to a total scanned time of up to $1{,}000 \, \text{ns}$.

The distribution of measured ADC as a function of time is shown in figure 5.9 (left) for four super cells in different layers of the EMB for calibration pulses with DAC = 1000 to each constituent LAr Calorimeter cell. All pulses start with a pedestal which is used
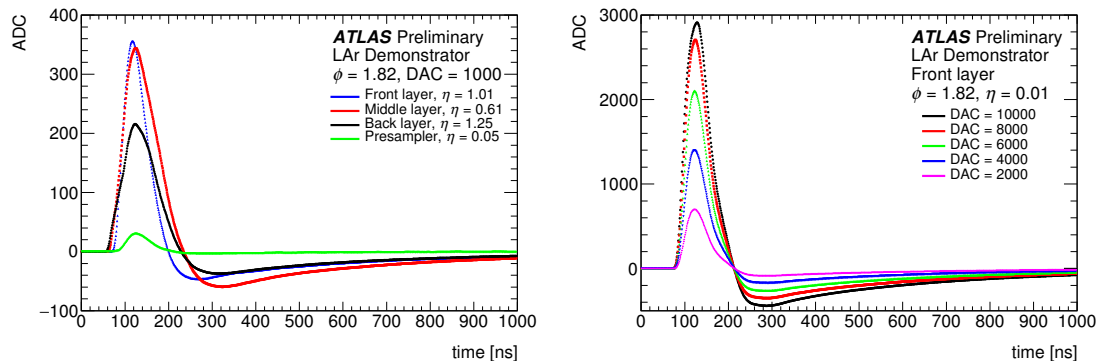

Figure 5.9.: Pulse shapes in calibration for (left) four representative super cells in different layers at calibration pulses with DAC = 1,000 and (right) one super cell in the front layer at different DAC values [10].

for noise measurement. Although its value is usually at an ADC of about 1000, for simplicity here the ADC usually refers to the measured value with subtracted pedestal. Because the over time integrated pulse shapes are zero by construction they start with a peak from which the pulse height can be measured, followed by a long lasting undershoot. Depending on the detector and electronics properties the shapes differ for different super cells.

The response to different DAC values of injected calibration pulse for a super cell in the front layer is shown in figure 5.9 (right) and shows a good linearity up to DAC = 8,000. Beyond that analog saturation already before the LTDBs of the demonstrator is observed as expected.

Figure 5.10 (left) shows the measured pulse heights in ADC for 140 super cells at $\phi = 1.82$ and $0 < \eta < 1.4$ in the four layers of the EMB for injected calibration pulses with DAC = 1,000. The corresponding equivalent transverse energies E_T for LAr calorimeter cells can be calculated from the relation of

$$E_\text{T}^\text{cell}(\text{DAC}, \eta, l) = \frac{\text{DAC}}{\max(\text{DAC})} \cdot \frac{5\,\text{V}}{R(\eta, l) \cdot c(\eta, l)} \cdot \sin 2 \arctan\left(e^{-\eta}\right) \quad (5.1)$$

where $R(\eta, l)$ and $c(\eta, l)$ are the layer (l) and η dependent resister and current to target energy (E) conversion constants, respectively, and the last factor is due to the conversion from total to transverse energy. For the super cell transverse energies the constituent LAr calorimeter cells are summed:

$$E_\text{T}(\text{DAC}, \eta, l) = \sum_{\text{constituent cells}} E_\text{T}^\text{cell}(\text{DAC}, \eta^\text{cell}, l). \quad (5.2)$$

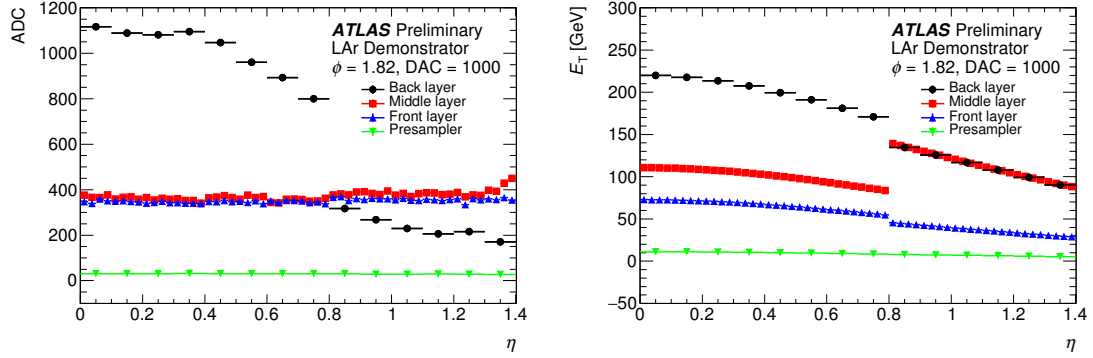The prediction of the transverse energies for the 140 super cells from above is shown in

Figure 5.10.: For each super cell in the EMB at $\phi = 1.82$ and $0 < \eta < 1.4$ (left) measured pulse heights (ADC) in calibration and (right) predicted equivalent transverse energy for an injected calibration pulse with DAC $= 1{,}000$ [10].

figure 5.10 (right).

From the pulse height measurements and the predicted transverse energies each super cell is calibrated with calibration constants

$$k(\eta, l) = \frac{E_{\mathrm{T}}(1{,}000, \eta, l)}{\mathrm{ADC}(1{,}000, \eta, l)} \tag{5.3}$$

which can be used e.g. in pulse measurements of collision data to roughly estimate the super cell energy via $E_{\mathrm{T}}(\eta, l) = k(\eta, l) \cdot \mathrm{ADC}(\eta, l)$.

The noise level, shown in figure 5.11 for the same 140 super cells as above, is the root mean square (RMS), measured in calibration with the pedestal data points of the first 50 ns of super cell pulse shapes. It is given both in ADC and in equivalent transverse en-
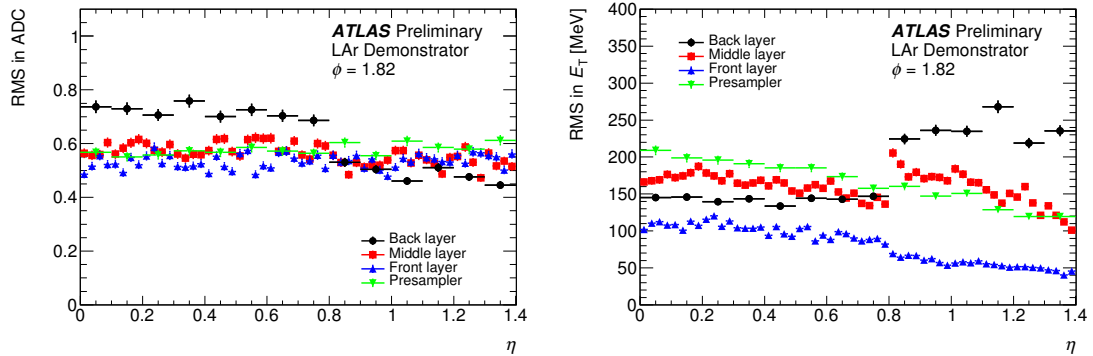
Figure 5.11.: Noise level for each super cell in the EMB at $\phi = 1.82$ and $0 < \eta < 1.4$ in (left) ADC and (right) equivalent transverse energy [10].

ergy, using the calibration constants $k(\eta, l)$. Consistently with test bench measurements it is well below 1 ADC and less than 300 MeV, respectively. At $\eta = 0.8$ the change of absorber thickness, electrodes and calibration resistors leads to an expected jump of

noise.

Figure 5.12 shows the linearity and saturation, as in figure 5.9 (right), for four super cells in front and middle layer at low and high η. Good linearity is observed up to
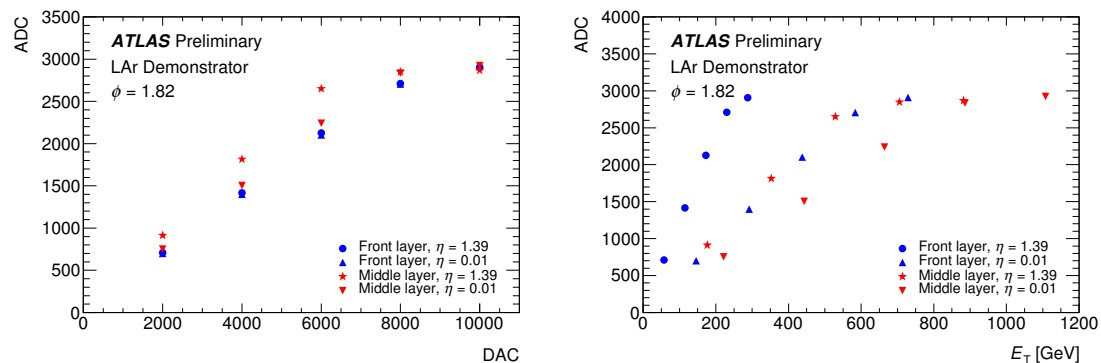

Figure 5.12.: Pulse heights for super cells in front and middle layer at low and high η (ADC) versus (left) DAC value of injected calibration pulse and (right) equivalent transverse energy [10].

DAC = 8,000 and DAC = 6,000 for the super cells in front and middle layer, respectively. This supports the use of calibration constants at the range of transverse energies up to few hundred GeV for the super cells as first rough estimate of their transverse energies.

5.3.4. Performance in hadron collisions

Since 2015 data is taken with proton-proton and heavy-ion collisions. Therefore a dedicated topological L1 trigger item is required, which selects EM clusters in the LAr demonstrator region. The L1 trigger type T_{L1} is an 8 bit number with each bit addressing an event property as summarised in table 5.1. Events in the demonstrator are triggered

Table 5.1.: Properties of the bits i for the L1 trigger type $T_{L1} = \sum_i 2^i$.

bit i	0	1	2	3	4	5	6	7
property	Random	Zero-bias	Calori-meter	Muon	LAr de-monstrator	FTK	CTP NIMDIR, ALFA	Physics

if $T_{L1} > 0x90 = 2^4 + 2^7$, which corresponds to the bits 4 and 7 for the LAr demonstrator and physics, respectively. Figure 5.13 shows the distribution of T_{L1} in events from 2015 proton-proton collision data. Both the demonstrator and the ATLAS main readout show a similar distribution of the triggered events with the most common trigger types 0x94 (bits 2, 4 and 7) and 0x9c (bits 2, 3, 4 and 7). The good coverage of the demonstrator region by reconstructed electrons and jets in the ATLAS main readout is shown in figure 5.14 for one proton-proton collision data-taking run in October 2016. Partially the
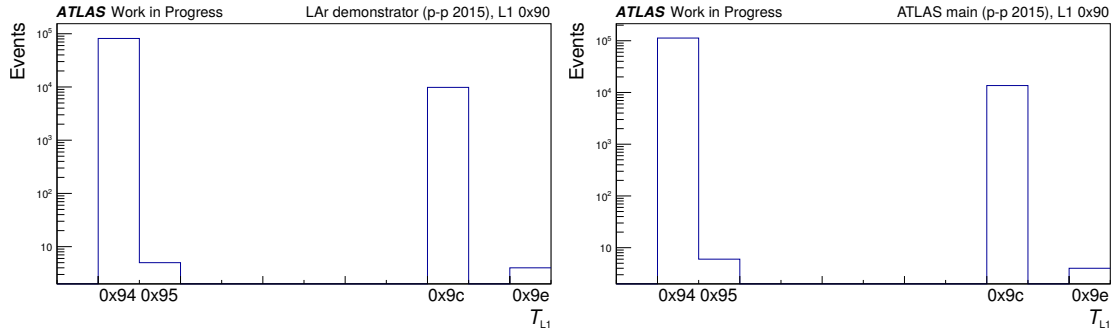
Figure 5.13.: Distribution of L1 trigger type T_{L1} in 2015 proton-proton collision events with $T_{L1} > 0x90$ in (left) demonstrator and (right) ATLAS main readout.
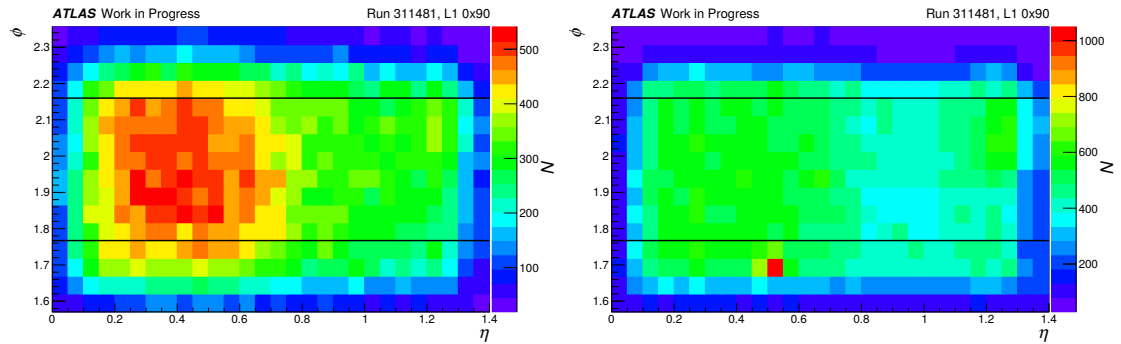

Figure 5.14.: Distribution in η and ϕ of (left) electrons and (right) jets in events with L1 trigger type $T_{L1} > 0x90$ in ATLAS main readout in a run from October 2016. The region of the demonstrator marked with black lines is well covered. The spot in the jets distribution at $(\eta \times \phi \approx 0.5 \times 1.7)$ is a relict which is cleaned by data quality assessment in physics analyses.

region was not well covered in former runs which has been fixed by the ATLAS L1Topo team.

The collected demonstrator data can then be analysed and compared with the events read out by the ATLAS main readout. Until end of 2016, the data taking of the demonstrator had not been integrated in the automated ATLAS data acquisition. Therefore the matching of events from both readout streams has been a challenge. The developed matching algorithm uses the L1 trigger type, the bunch crossing identification number (BCID) and the L1 identification number (L1ID). The L1ID is a 32 bit number with 24 bit for the event counter (EVID), delivered by the L1 trigger and 8 bit for the event counter reset counter (ECRC). The latter has not been identical in events from ATLAS main and demonstrator readout and therefore has not be used in the matching. Although the combination of these identifiers is not absolutely unique, it is sufficient to the matching. E.g. in 126,000 ATLAS events there are eight pairs of events with the same identifiers.

In a first step the transverse energy of a super cell in the demonstrator readout can be approximated multiplying the pulse heights by the calibration constants in equation 5.3. An

example for an event from 2015 proton-proton collision data is shown in figure 5.15. The
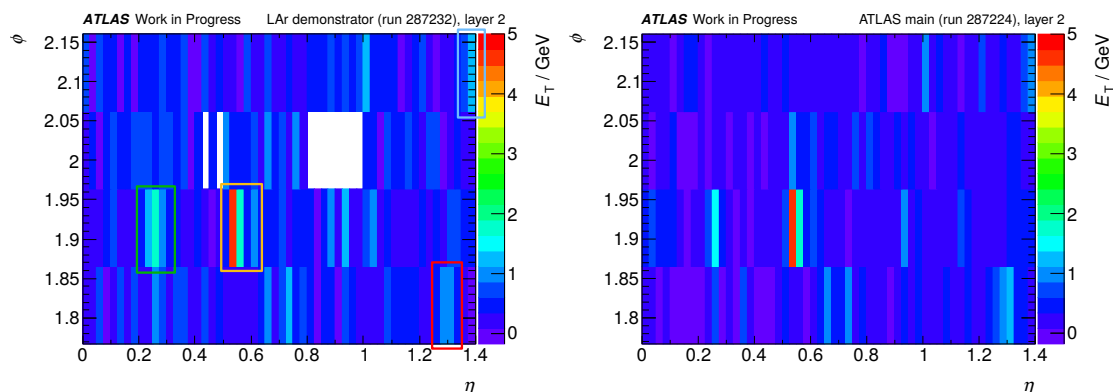

Figure 5.15.: Distribution of transverse energies for one event from 2015 proton-proton collisions in (left) super cells of the demonstrator and (right) summed constituent LAr cell transverse energies of the ATLAS main readout in the middle layer. The colourful boxes label the regions where electrons and photons are reconstructed in the ATLAS main readout.

signature in both the super cells of the demonstrator readout and the summed constituent LAr cell transverse energies of the ATLAS main readout is shown. Good agreement is observed between the two different readouts. Furthermore distinct particle showers in the demonstrator readout can be matched to reconstructed objects from the ATLAS main readout. The reconstructed electrons and photons in this event are marked with colourful boxes and their properties are summarised in table 5.2. Their $\eta \times \phi$ positions nicely

Table 5.2.: Properties of the reconstructed electrons ($e^{\pm}$) and photons (γ) in the event from figure 5.15 in the ATLAS main readout, selected in the demonstrator region.

particle	p_{T} [GeV]	η	ϕ	marker colour in figure 5.15
e^-	11.0	0.55	1.95	yellow
e^-	5.6	1.39	2.14	light blue
e^+	6.7	1.32	1.82	red
e^-	3.2	0.68	1.79	–
γ	6.3	0.27	1.89	green
γ	4.8	1.32	1.82	red

match with the showers of transverse energies observed in the super cells of the demonstrator readout. The white areas in figure 5.15 appear due to data quality assessment for super cells with data corruption.

The ADC pulses are measured in the detector at equidistant samples with about 25 ns difference. In the current readout of the LTDB in 'monitoring mode' in most of the collision data-taking 50 samples had been read in parallel, which is possible due to the

circular buffers in the ABBA boards. This has been only possible at low trigger rates. E.g. the trigger rate of the L1 trigger with $T_{L1} > 0x90$ has been about 1 Hz. In the planned readout of digitised super cell information at a rate of 40 MHz as input to the L1 trigger only up to five samples can be evaluated per pulse. The optimal filtering (OF) is used to estimate both the transverse energy from the pulse amplitude A and the timing t via

$$A = \sum_i a_i S_i$$
$$t = \frac{1}{A} \sum_i b_i S_i \tag{5.4}$$

from the measured samples S_i ($i = 0, \ldots, 4$) using OF coefficients a_i and b_i obtained in calibration [11].

While the above described performance studies have been done by myself, validating the basic functionality of the demonstrator system, the following plots using the advanced OF have been published by the LAr Calorimeter group using calibration coefficients and proton-proton collision data from 2017.

Figure 5.16 shows the comparison of measured normalised and averaged pulse shapes in two super cells (one in front and one in middle layer) in demonstrator collision data from August 2017. It has been checked, that the applied quality cuts do not bias the pulse
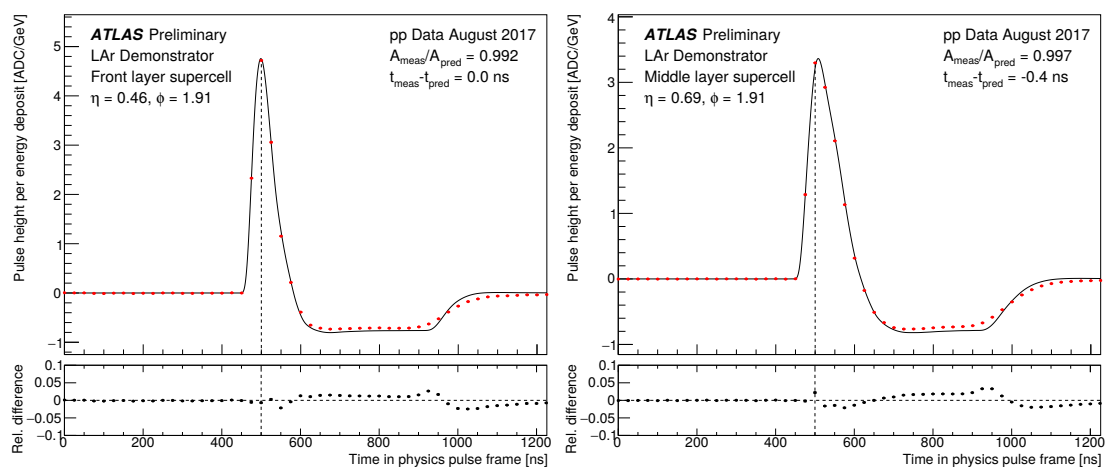

Figure 5.16.: Normalised and averaged pulse shapes for two super cells in (left) front and (right) middle layer. The measured samples of the pulses in proton-proton collision data from August 2017 are shown in red. The predicted pulses in black are estimated using the response transformation method on the OF coefficients. The estimates of A_{meas} and t_{meas} use five samples around the peak sample (dashed line) [10].

shapes. The averaging uses 133 and 282 events in the front and middle layer, respectively. The normalisation is obtained from the transverse energies, measured in the matched

events by the ATLAS main readout. A good agreement is observed between the pulse shapes from collision data and prediction. The difference in shape at about 500 ns after the pulse peak is expected and originates from the modelling of the electrode positions in the LAr calorimeter.

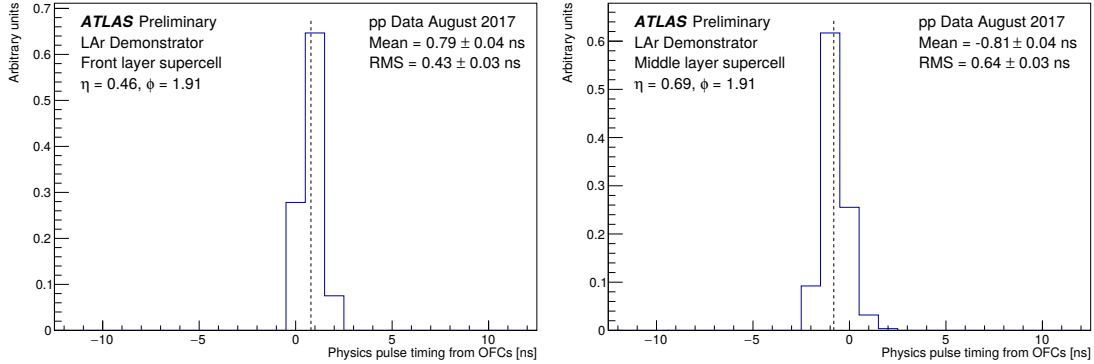The timing distribution of the two super cells is given in figure 5.17. An excellent tim-

Figure 5.17.: Timing distribution for two super cells in (left) front and (right) middle layer. The dashed vertical lines mark the means of the distribution which are slightly shifted from the prediction due to the preliminary calibration [10].

ing resolution with the root mean square (RMS) < 1 ns is observed. It is much smaller than the time between two bunch crossings of about 25 ns and hence pulses can be easily matched to a given bunch crossing. Further this helps to discriminate signal pulses against e.g. backgrounds from out-of-time pile-up. The difference of the mean from the prediction is already small and can be further improved by using more up-to-date calibration.

The difference in transverse energy measurement by the demonstrator and the ATLAS main readout in the two super cells of above is shown in figure 5.18. A good linearity between the two readouts is observed and the width of the distributions is 107 MeV and 143 MeV in the front and back layer super cell, respectively. This is consistent with the expected noise level shown in figure 5.11. The means of the distributions are slightly shifted by less than 10 MeV because of an outdated calibration.

Finally, figure 5.19 shows an event display of a particle shower in comparison of demonstrator and ATLAS main readout in the whole demonstrator region. The shower in both readouts look compatible with each other. Compared to figure 5.19 all four layers are shown here and the super cell energy estimate uses the more advanced technique of OF.
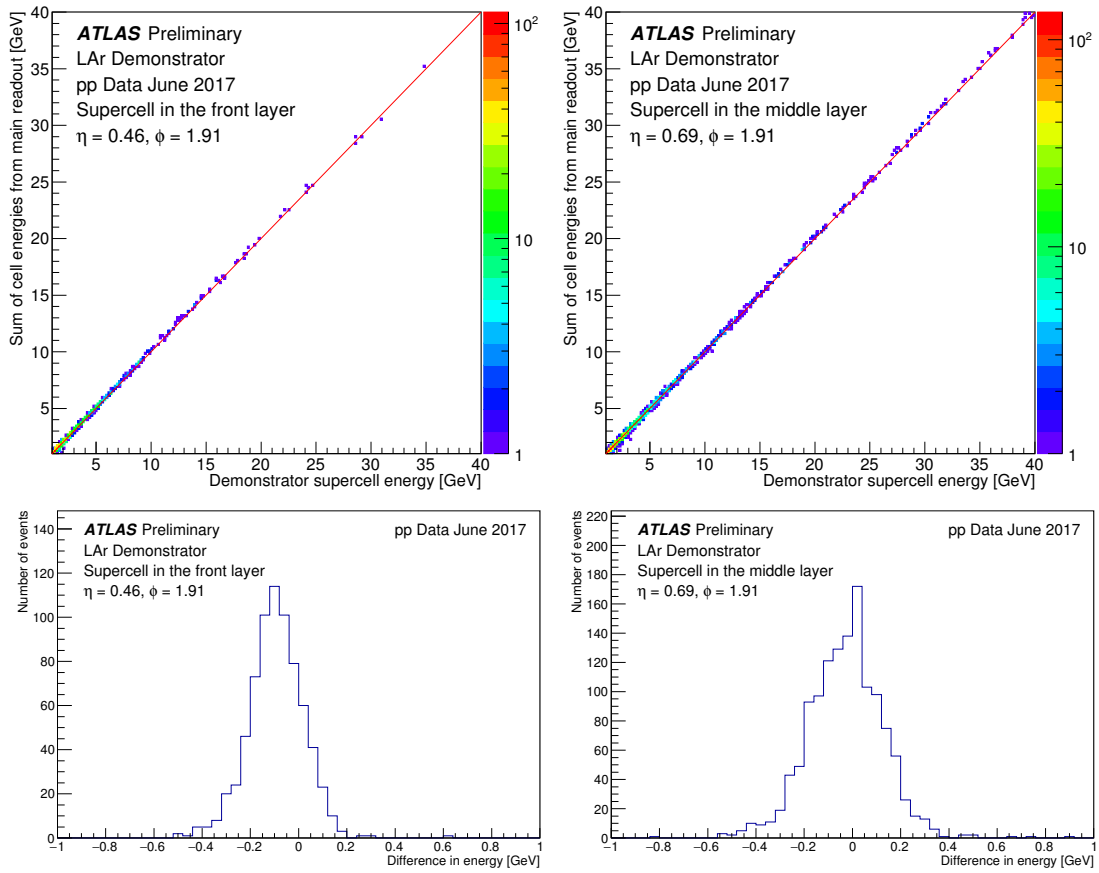
Figure 5.18.: Transverse energy (E_T) measurement for two super cells in (left) front and (right) middle layer. Each entry in the histograms corresponds to one event. In the top plots the super cell's transverse energy E_T^{SC} in the demonstrator is compared with the sum of constituent cells $\sum_{i \in SC} E_T^i$ in the main readout and in the bottom plots the distribution of their difference $E_T^{SC} - \sum_{i \in SC} E_T^i$ for $E_T^{SC} > 2\,\mathrm{GeV}$ are shown [10].
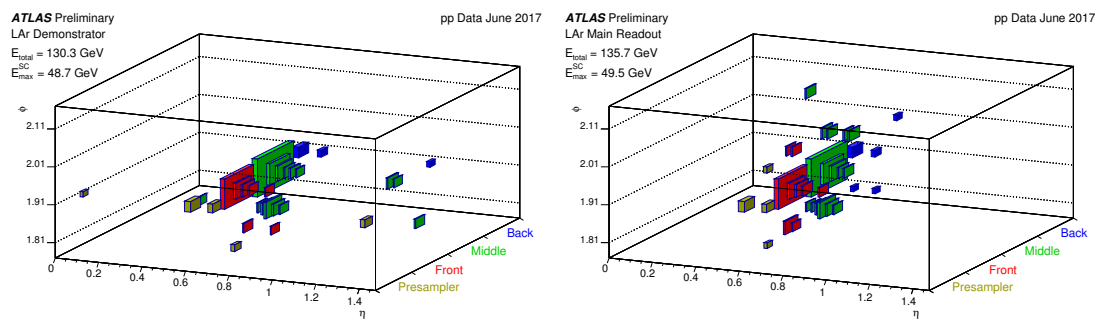

Figure 5.19.: Event display of a particle shower as seen by (left) the demonstrator and (right) the ATLAS main readout [10].

5.4. Phase 2 LAr Calorimeter readout electronics upgrade

The Phase 2 upgrade foresees the replacement of the main readout electronics of the LAr Calorimeter. Some parts of the current front-end boards are not radiation-tolerant beyond Run 3 and need to be replaced to survive the full HL-LHC run.

Figure 5.20 sketches the planned upgrade of the readout electronics. The new readout
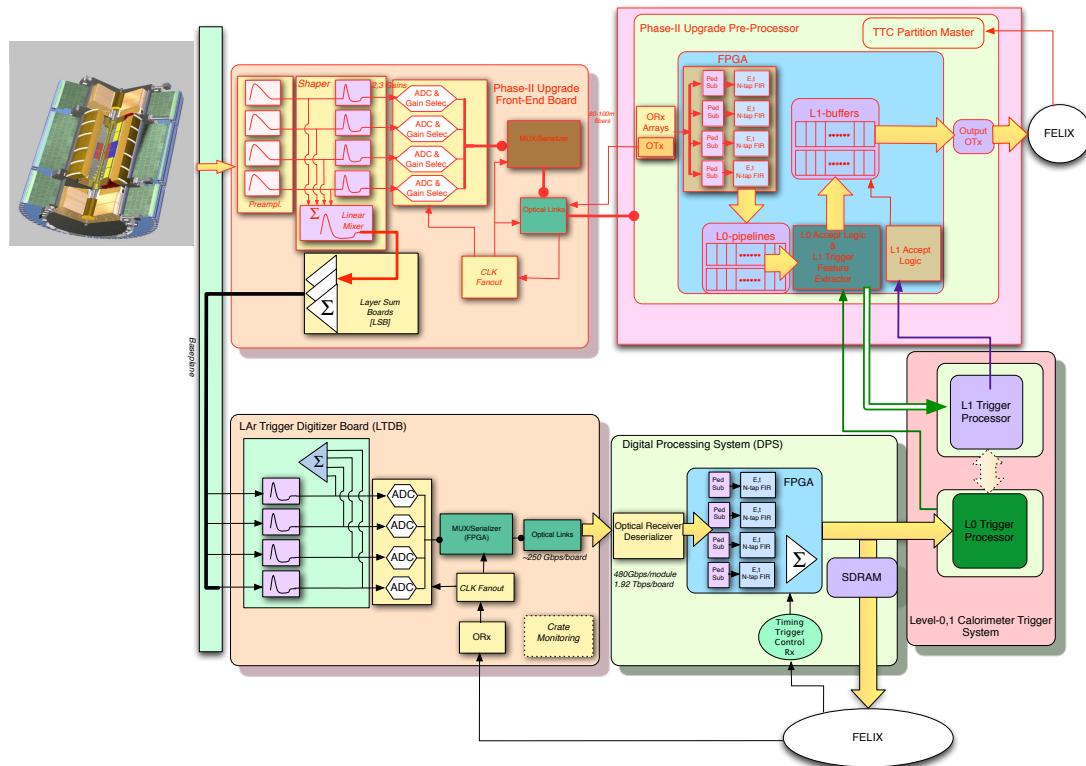

Figure 5.20.: Phase 2 LAr Calorimeter readout electronics upgrade with new components shown by red outlines and arrows [143].

electronics will digitise the transverse energies and timing information of all calorimeter cells in full granularity at 40 MHz. The amplified, shaped and sampled signals from the upgraded front-end boards will be transmitted via optical links to the upgraded back-end readout driver system (ROD). There the physics information of the cell signal pulses is calculated using OF in FPGAs.

The upgraded low-level trigger systems will be able to use both the calorimeter cell and the super cell information with high flexibility. The currently used analog trigger path with trigger towers will be decommissioned during LS3.

5.5. Conclusion

To comply with the challenging requirements of radiation and high background from pile-up collisions in the environment of up to 3 (7.5) times luminosity in the LHC (HL-LHC) future the ATLAS LAr calorimeter will be upgraded in two steps.

After the Phase 1 upgrade during the LS2 in 2019–2020 the trigger path will be digitized at the front-end level with increased granularity. New LTDB (front-end) and LDPS (back-end) systems have been developed. The digitization and readout of this system will be done at 40 MHz. Specific radiation tolerant ADCs and optical links have been designed and tested for the LTDBs. The production has been started in 2018.

To test the performance in the environment of hadron collisions, a demonstrator system has been installed and successfully run since 2015 for data-taking from proton-proton and heavy-ion collisions. This gives valuable data to study the filtering algorithm development for super cell energy measurement. Good agreement of the particle showers between demonstrator and main readout has been observed. The timing of the super cells shows an excellent performance with an RMS of about 1 ns, which allows to identify corresponding bunch crossings. In February 2018 the LTDB and LDPS have been replaced by the final prototypes to test the full pre-production readout chain with proton-proton collision data in 2018.

The Phase 1 upgrade is a stepping stone towards the full readout upgrade in Phase 2 which will allow the low-level trigger system to use calorimeter cell information with the full granularity with 40 MHz at each bunch crossing.

Conclusion

The Standard Model of particle physics (SM) is a very successful theory describing the fundamental particles and their interaction. The experiments at the LHC have so far confirmed its predictions with unprecedented precision. After the Higgs boson has been discovered and the QCD and electroweak interaction have been measured precisely in Run 1, the focus of Run 2 with increased center-of-mass energy and luminosity lies on the investigation of the Higgs boson couplings and on searches for new physics. In Run 1 the top quark Yukawa coupling (λ_t) could be measured with a precision of 15% only due to its contribution in top quark loops of the Higgs boson production with high cross section (gluon-gluon fusion) and of the Higgs boson decay to a pair of photons. Because it contributes at tree-level in the associated Higgs boson production with a pair of top quarks ($t\bar{t}H$), the search for this production mode is carried out by both the ATLAS and the CMS collaborations.

The presented search in multileptonic final states in $36.1\,\mathrm{fb}^{-1}$ of proton-proton collisions at $\sqrt{s} = 13\,\mathrm{TeV}$, recorded by the ATLAS detector, uses advanced techniques for the background estimates and discrimination. I have been mainly responsible for the preparation of input samples and the implementation of the statistical analysis for the result extraction. The $t\bar{t}H$ production has been found at a value of $1.6 \pm 0.3\,(\mathrm{stat.}) \pm 0.3\,(\mathrm{syst.})$ times the SM expectation in good agreement with the SM. The statistical significance of this excess is 4.1 standard deviations, while 2.8 are expected. Unlike in the search for $t\bar{t}H$ with $H \to b\bar{b}$ which is dominated by systematic uncertainties and the searches with $H \to \gamma\gamma$ or $H \to ZZ \to 4\ell$ which are statistically dominated, the statistical and systematic uncertainties are of same size in the $t\bar{t}H \to$ multilepton result. The major systematic uncertainties are those related to the $t\bar{t}H$ signal cross section, to the jet energy scale and resolution, because final states with many jets are investigated, and to the data-driven estimate of non-prompt light lepton background, which dominates the background in the most significant 2ℓSS and 3ℓ channels. The impact and correlation of these uncertainties and the behaviour of the fit with respect to configuration changes has been studied extensively.

The channel with three light leptons (3ℓ) is the second most significant channel. I have presented my studies of an alternative signal and control region definition which has similar performance as the one used in the published article. While the standard classification simultaneously optimises for the signal and different background categories with high purities, the alternative classification benefits from the high statistics in the most significant bins of the signal region. Both classifications have an expected signal significance

of about 1.5 standard deviations.

The search for the $t\bar{t}H$ production in multileptonic final states has been pre-published in October 2017 and published in April 2018 [4] including the combination with searches in other Higgs boson decay channels with $36.1\,\mathrm{fb}^{-1}$ of Run 2 data, collected by the ATLAS detector. In April 2018 the CMS collaboration reported the observation of the $t\bar{t}H$ production in combination of Run 1 and Run 2 searches with an observed (expected) significance of 5.2 (4.2) standard deviations [127]. In the meanwhile, searches with $H \to \gamma\gamma$ and $H \to ZZ \to 4\ell$, where the statistical uncertainty is dominant, have been repeated by the ATLAS collaboration using $79.8\,\mathrm{fb}^{-1}$ of proton-proton collisions from 2015–2017 [5]. The measured $t\bar{t}H$ production cross section at $\sqrt{s} = 13\,\mathrm{TeV}$ is $670 \pm 90\,(\text{stat.})\,^{+110}_{-100}\,(\text{syst.})\,\mathrm{fb}$, compatible with the SM expectation of $507\,^{+35}_{-50}\,\mathrm{fb}$ [6]. The Run 1 and Run 2 combined observed (expected) significance is 6.3 (5.1) standard deviations. Because the cross section scales at tree-level with λ_t^2, this discovery establishes the first direct measurement of the coupling between the top quark and the Higgs boson with a precision of 10%.

Although, the $t\bar{t}H$ production has been found at the expected event yields, new physics may hide in a different phase space. It can enhance the flavour-changing neutral currents (FCNC) in top quark decays by many orders of magnitude. E.g. the branching ratio of the $t \to Hc$ decay can increase from 3×10^{-15} in the SM up to 2×10^{-3} in generic models with two Higgs doublets. Because the presented search for $t \to Hq$ ($q = u$ or c) decay in multileptonic final states uses the same basic selection for the 2ℓSS and the 3ℓ channels as the $t\bar{t}H \to$ multilepton analysis, many developments, e.g. the estimate of backgrounds, could be reused. I have developed a robust model for the treatment of the signal contamination in the control regions for the estimate of the dominant background of non-prompt light leptons. Like in the $t\bar{t}H \to$ multilepton analysis my work on the fit and implementation of systematic uncertainties has been essential in the extraction of the results. No enhancement of the $t \to Hq$ decay branching ratios has been observed and upper limits at 95% confidence level are observed (expected) at $\mathcal{B}(t \to Hc) < 1.6\,(1.5) \times 10^{-3}$ and $\mathcal{B}(t \to Hu) < 1.9\,(1.5) \times 10^{-3}$ [9]. The combination with searches in other Higgs boson decays and additional data will further improve these limits.

Upgrades of the LHC and its experiments are planned for 2019–2020 (Phase 1) after the full Run 2 data-taking. A demonstrator for the ATLAS Liquid Argon Calorimeter readout upgrade has been operated on the ATLAS detector since 2015. I have presented my early performance studies of calibration and of the first data in proton-proton collisions. An upgraded version of this demonstrator with the final prototype has been installed in the beginning of 2018 and its parts are tested for a successful installation on the full detector. The Phase 2 upgrade prepares for the high-luminosity LHC, which aims for a total integrated luminosity of $3{,}000\,\mathrm{fb}^{-1}$ at a center-of-mass energy of $14\,\mathrm{TeV}$. This will allow to improve the precision of the Higgs boson coupling measurements. Until now, new physics has been hiding, but the future searches may reveal it. My preliminary extrapolations of both the presented $t\bar{t}H \to$ multilepton and the $t \to Hq \to$ multilepton analysis expect an improvement of factor two in cross-section uncertainty and limits on the branching ratios, respectively.

Bibliography

[1] ATLAS Collaboration, *Observation of a new particle in the search for the Standard Model Higgs boson with the ATLAS detector at the LHC*, Phys. Lett. B **716** (2012) 1, arXiv: 1207.7214 [hep-ex].

[2] CMS Collaboration, *Observation of a new boson at a mass of 125 GeV with the CMS experiment at the LHC*, Phys. Lett. B **716** (2012) 30, arXiv: 1207.7235 [hep-ex].

[3] ATLAS and CMS Collaborations, *Measurements of the Higgs boson production and decay rates and constraints on its couplings from a combined ATLAS and CMS analysis of the LHC pp collision data at $\sqrt{s} = 7$ and 8 TeV*, JHEP **08** (2016) 045, arXiv: 1606.02266 [hep-ex].

[4] ATLAS Collaboration, *Evidence for the associated production of the Higgs boson and a top quark pair with the ATLAS detector*, Phys. Rev. D **97** (2018) 072003, arXiv: 1712.08891 [hep-ex].

[5] ATLAS Collaboration, *Observation of Higgs boson production in association with a top quark pair at the LHC with the ATLAS detector*, Phys. Lett. B **784** (2018) 173, arXiv: 1806.00425 [hep-ex].

[6] LHC Higgs Cross Section Working Group, *Handbook of LHC Higgs Cross Sections: 4. Deciphering the Nature of the Higgs Sector*, vol. 2, CERN Yellow Rep.: M. CERN, 2017, arXiv: 1610.07922 [hep-ph].

[7] J. A. Aguilar-Saavedra, *Top flavor-changing neutral interactions: Theoretical expectations and experimental detection*, Acta Phys. Polon. B **35** (2004) 2695, arXiv: hep-ph/0409342.

[8] ATLAS Collaboration, *Search for top quark decays $t \rightarrow qH$, with $H \rightarrow \gamma\gamma$, in $\sqrt{s} = 13$ TeV pp collisions using the ATLAS detector*, JHEP **10** (2017) 129, arXiv: 1707.01404 [hep-ex].

[9] ATLAS Collaboration, *Search for flavor-changing neutral currents in top quark decays $t \rightarrow Hc$ and $t \rightarrow Hu$ in multilepton final states in proton-proton collisions at $\sqrt{s} = 13$ TeV with the ATLAS detector*, Phys. Rev. D **98** (2018) 032002, arXiv: 1805.03483 [hep-ex].

[10] ATLAS Liquid Argon Calorimeter Group, *Public Liquid-Argon Calorimeter Plots on Upgrade*, 2018 (accessed June 15, 2018), URL: https://twiki.cern.ch/twiki/bin/view/AtlasPublic/LArCaloPublicResultsUpgrade.

[11] W. E. Cleland and E. G. Stern, *Signal processing considerations for liquid ionization calorimeters in a high rate environment*, Nucl. Instrum. Meth. Phys. A **338** (1994) 467.

[12] S. L. Glashow, *Partial-symmetries of weak interactions*, Nucl. Phys. **22** (1961) 579.

[13] A. Salam, *Elementary particle theory, Relativistic groups and analyticity*, Proceedings of the Eighth Nobel Symposium, Almquist & Wiksell, 1968 367.

[14] S. Weinberg, *A Model of Leptons*, Phys. Rev. Lett. **19** (1967) 1264.

[15] Cush et al., *Standard Model of Elementary Particles*, via Wikimedia Commons, 2018, URL: https://commons.wikimedia.org/wiki/File:Standard_Model_of_Elementary_Particles.svg.

[16] C. S. Wu et al., *Experimental Test of Parity Conservation in Beta Decay*, Phys. Rev. **105** (1957) 1413.

[17] J. H. Christenson et al., *Evidence for the 2π Decay of the K_2^0 Meson*, Phys. Rev. Lett. **13** (1964) 138.

[18] F. Englert and R. Brout, *Broken Symmetry and the Mass of Gauge Vector Mesons*, Phys. Rev. Lett. **13** (1964) 321.

[19] P. W. Higgs, *Broken Symmetries and the Masses of Gauge Bosons*, Phys. Rev. Lett. **13** (1964) 508.

[20] G. S. Guralnik, C. R. Hagen and T. W. B. Kibble, *Global Conservation Laws and Massless Particles*, Phys. Rev. Lett. **13** (1964) 585.

[21] P. W. Higgs, *Spontaneous Symmetry Breakdown without Massless Bosons*, Phys. Rev. **145** (1966) 1156.

[22] T. W. B. Kibble, *Symmetry Breaking in Non-Abelian Gauge Theories*, Phys. Rev. **155** (1967) 1554.

[23] LHC Higgs Cross Section Working Group, *LHC Higgs Cross Section WG Picture Gallery*, 2016 (accessed June 15, 2018), URL: https://twiki.cern.ch/twiki/bin/view/LHCPhysics/LHCHXSWGCrossSectionsFigures.

[24] ATLAS Collaboration, *Evidence for the spin-0 nature of the Higgs boson using ATLAS data*, Phys. Lett. B **726** (2013) 120, arXiv: 1307.1432 [hep-ex].

[25] CMS Collaboration, *Study of the Mass and Spin-Parity of the Higgs Boson Candidate Via Its Decays to Z Boson Pairs*, Phys. Rev. Lett. **110** (2013) 081803, arXiv: 1212.6639 [hep-ex].

[26] ATLAS and CMS Collaborations, *Combined Measurement of the Higgs Boson Mass in pp Collisions at $\sqrt{s} = 7$ and 8 TeV with the ATLAS and CMS Experiments*, Phys. Rev. Lett. **114** (2015) 191803, arXiv: 1503.07589 [hep-ex].

[27] Particle Data Group, *Review of Particle Physics*, Phys. Rev. D **98** (2018) 030001, URL: http://pdg.lbl.gov/2018.

[28] Planck Collaboration, *Planck 2013 results. I. Overview of products and scientific results*, Astron. Astrophys. **571** (2014) A1, arXiv: 1303.5062 [astro-ph.CO].

[29] G. Eilam, J. L. Hewett and A. Soni, *Rare decays of the top quark in the standard and two-Higgs-doublet models*, Phys. Rev. D **44** (1991) 1473, Erratum: Phys. Rev. D **59** (1998) 039901.

[30] S. L. Glashow, J. Iliopoulos and L. Maiani, *Weak Interactions with Lepton-Hadron Symmetry*, Phys. Rev. D **2** (1970) 1285.

[31] Top Quark Working Group, *Working Group Report: Top Quark*, (2013), arXiv: 1311.2028 [hep-ph].

[32] G. C. Branco et al., *Theory and phenomenology of two-Higgs-doublet models*, Phys. Rept. **516** (2012) 1, arXiv: 1106.0034 [hep-ph].

[33] T. P. Cheng and M. Sher, *Mass-matrix ansatz and flavor nonconservation in models with multiple Higgs doublets*, Phys. Rev. D **35** (1987) 3484.

[34] D. Atwood, L. Reina and A. Soni, *Phenomenology of two Higgs doublet models with flavor changing neutral currents*, Phys. Rev. D **55** (1997) 3156, arXiv: hep-ph/9609279.

[35] S. Bejar, J. Guasch and J. Sola, *Loop induced flavor changing neutral decays of the top quark in a general two Higgs doublet model*, Nucl. Phys. B **600** (2001) 21, arXiv: hep-ph/0011091.

[36] S. Bejar, *Flavor changing neutral decay effects in models with two Higgs boson doublets: Applications to LHC Physics*, PhD thesis (2006), arXiv: hep-ph/0606138.

[37] J. J. Cao et al., *SUSY-induced FCNC top-quark processes at the large hadron collider*, Phys. Rev. D **75** (2007) 075021, arXiv: hep-ph/0702264.

[38] J. M. Yang, B.-L. Young and X. Zhang, *Flavor changing top quark decays in r parity violating SUSY*, Phys. Rev. D **58** (1998) 055001, arXiv: hep-ph/9705341.

[39] G. Eilam et al., *Top quark rare decay $t \rightarrow ch$ in R-parity violating SUSY*, Phys. Lett. B **510** (2001) 227, arXiv: hep-ph/0102037.

[40] L Randall and R. Sundrum, *A Large mass hierarchy from a small extra dimension*, Phys. Rev. Lett. **83** (1999) 3370, arXiv: hep-ph/9905221.

[41] L. Randall and R. Sundrum, *An Alternative to compactification*, Phys. Rev. Lett. **83** (1999) 4690, arXiv: hep-th/9906064.

[42] K. Agashe, G. Perez and A. Soni, *Collider Signals of Top Quark Flavor Violation from a Warped Extra Dimension*, Phys. Rev. D **75** (2007) 015002, arXiv: hep-ph/0606293.

[43] K. Agashe and R. Contino, *Composite Higgs-Mediated FCNC*, Phys. Rev. D **80** (2009) 075016, arXiv: 0906.1542 [hep-ph].

[44] L. Evans and P. Bryant, *LHC Machine*, JINST **3** (2008) S08001.

[45] ATLAS Collaboration, *The ATLAS Experiment at the CERN Large Hadron Collider*, JINST **3** (2008) S08003.

[46] CMS Collaboration, *The CMS experiment at the CERN LHC*, JINST **3** (2008) S08004.

[47] E. Mobs, *The CERN accelerator complex. Complexe des accélérateurs du CERN*, (2016), General Photo, URL: https://cds.cern.ch/record/2197559.

[48] O. S. Brüning et al., *LHC Design Report*, CERN Yellow Rep.: M. CERN, 2004, URL: https://cds.cern.ch/record/782076.

[49] R. Bruce et al., *LHC Run 2: Results and challenges*, (2016) MOAM5P50. 7 p, URL: https://cds.cern.ch/record/2201447.

[50] ATLAS Collaboration, *ALTAS Experiment – Luminosity Public Results Run 2*, 2018, URL: https://twiki.cern.ch/twiki/bin/view/AtlasPublic/LuminosityPublicResultsRun2 (visited on 25/04/2018).

[51] LHCb Collaboration, *The LHCb Detector at the LHC*, JINST **3** (2008) S08005.

[52] ALICE Collaboration, *The ALICE experiment at the CERN LHC*, JINST **3** (2008) S08002.

[53] TOTEM Collaboration, *The TOTEM Experiment at the CERN Large Hadron Collider*, Journal of Instrumentation **3** (2008) S08007.

[54] LHCf Collaboration, *The LHCf detector at the CERN Large Hadron Collider*, Journal of Instrumentation **3** (2008) S08006.

[55] ATLAS Collaboration, *Track Reconstruction Performance of the ATLAS Inner Detector at $\sqrt{s} = 13$ TeV*, ATL-PHYS-PUB-2015-018, 2015, URL: https://cds.cern.ch/record/2037683.

[56] T. Davidek, M. Volpi and T. Zenis, *Response of the ATLAS Tile Calorimeter to Hadrons in Stand-Alone Testbeam Data*, ATL-TILECAL-PUB-2009-004, 2009, URL: https://cds.cern.ch/record/1161351.

[57] ATLAS Collaboration, *Commissioning of the ATLAS Muon Spectrometer with Cosmic Rays*, Eur. Phys. J. C **70** (2010) 875, arXiv: 1006.4384 [physics.ins-det].

[58] M. Dobbs and J. B. Hansen, *The HepMC C++ Monte Carlo Event Record for High Energy Physics*, Comput. Phys. Commun. **134** (2001) 41, URL: https://cds.cern.ch/record/684090.

[59] NNPDF Collaboration, *Parton distributions with LHC data*, Nucl. Phys. B **867** (2013) 244, arXiv: 1207.1303 [hep-ph].

[60] NNPDF Collaboration, *Parton distributions for the LHC Run II*, JHEP **04** (2015) 040, arXiv: 1410.8849 [hep-ph].

[61] J. Pumplin et al., *New generation of parton distributions with uncertainties from global QCD analysis*, JHEP **07** (2002) 012, arXiv: `hep-ph/0201195`.

[62] P. M. Nadolsky et al., *Implications of CTEQ global analysis for collider observables*, Phys. Rev. D **78** (2008) 013004, arXiv: `0802.0007 [hep-ph]`.

[63] H.-L. Lai et al., *New parton distributions for collider physics*, Phys. Rev. D **82** (2010) 074024, arXiv: `1007.2241 [hep-ph]`.

[64] J. Alwall et al., *The automated computation of tree-level and next-to-leading order differential cross sections, and their matching to parton shower simulations*, JHEP **07** (2014) 079, arXiv: `1405.0301 [hep-ph]`.

[65] R. Frederix, E. Re and P. Torrielli, *Single-top t-channel hadroproduction in the four-flavour scheme with POWHEG and aMC@NLO*, JHEP **09** (2012) 130, arXiv: `1207.5391 [hep-ph]`.

[66] T. Gleisberg et al., *Event generation with SHERPA 1.1*, JHEP **02** (2009) 007, arXiv: `0811.4622 [hep-ph]`.

[67] F. Cascioli, P. Maierhofer and S. Pozzorini, *Scattering Amplitudes with Open Loops*, Phys. Rev. Lett. **108** (2012) 111601, arXiv: `1111.5206 [hep-ph]`.

[68] T. Gleisberg and S. Hoeche, *Comix, a new matrix element generator*, JHEP **12** (2008) 039, arXiv: `0808.3674 [hep-ph]`.

[69] S. Schumann and F. Krauss, *A Parton shower algorithm based on Catani-Seymour dipole factorisation*, JHEP **03** (2008) 038, arXiv: `0709.1027 [hep-ph]`.

[70] S. Hoeche et al., *QCD matrix elements + parton showers: The NLO case*, JHEP **04** (2013) 027, arXiv: `1207.5030 [hep-ph]`.

[71] T. Sjostrand, S. Mrenna and P. Z. Skands, *PYTHIA 6.4 Physics and Manual*, JHEP **05** (2006) 026, arXiv: `hep-ph/0603175`.

[72] T. Sjostrand, S. Mrenna and P. Z. Skands, *A Brief Introduction to PYTHIA 8.1*, Comput. Phys. Commun. **178** (2008) 852, arXiv: `0710.3820 [hep-ph]`.

[73] M. Bahr et al., *Herwig++ Physics and Manual*, Eur. Phys. J. C **58** (2008) 639, arXiv: `0803.0883 [hep-ph]`.

[74] ATLAS Collaboration, *The ATLAS Simulation Infrastructure*, Eur. Phys. J. C **70** (2010) 823, arXiv: `1005.4568 [physics.ins-det]`.

[75] GEANT4 Collaboration, *GEANT4: A Simulation toolkit*, Nucl. Instrum. Meth. Phys. A **506** (2003) 250.

[76] A. Basalaev and Z. Marshall, *The Fast Simulation Chain for ATLAS*, J. Phys.: Conf. Ser. **898** (2017) 042016.

[77] T. G. Cornelissen et al., *The global χ^2 track fitter in ATLAS*, J. Phys.: Conf. Ser. **119** (2008) 032013.

[78] R. Fruhwirth, *Application of Kalman filtering to track and vertex fitting*, Nucl. Instrum. Meth. Phys. A **262** (1987) 444.

[79] T. Cornelissen et al., *Concepts, Design and Implementation of the ATLAS New Tracking (NEWT)*, ATL-SOFT-PUB-2007-003, 2007, URL: https://cds.cern.ch/record/1020106.

[80] ATLAS Collaboration, *Vertexing performance in high <μ> 2017 data*, IDTR-2017-008, 2017, URL: https://atlas.web.cern.ch/Atlas/GROUPS/PHYSICS/PLOTS/IDTR-2017-008.

[81] ATLAS Collaboration, *Impact Parameter Resolution*, IDTR-2015-007, 2017, URL: https://atlas.web.cern.ch/Atlas/GROUPS/PHYSICS/PLOTS/IDTR-2015-007.

[82] ATLAS Collaboration, *Electron efficiency measurements with the ATLAS detector using the 2015 LHC proton–proton collision data*, ATLAS-CONF-2016-024, 2016, URL: https://cds.cern.ch/record/2157687.

[83] W. Lampl et al., *Calorimeter Clustering Algorithms: Description and Performance*, ATL-LARG-PUB-2008-002, 2008, URL: https://cds.cern.ch/record/1099735.

[84] ATLAS Collaboration, *Improved electron reconstruction in ATLAS using the Gaussian Sum Filter-based model for bremsstrahlung*, ATLAS-CONF-2012-047, 2012, URL: https://cds.cern.ch/record/1449796.

[85] ATLAS Collaboration, *Electron and photon energy calibration with the ATLAS detector using LHC Run 1 data*, Eur. Phys. J. C **74** (2014) 3071, arXiv: 1407.5063 [hep-ex].

[86] ATLAS Collaboration, *Electron efficiency measurements in 2017 data and electron identification discriminating variables from 2016 data*, EGAM-2018-002, 2018, URL: https://atlas.web.cern.ch/Atlas/GROUPS/PHYSICS/PLOTS/EGAM-2018-002.

[87] ATLAS Collaboration, *Muon reconstruction performance of the ATLAS detector in proton–proton collision data at $\sqrt{s} = 13$ TeV*, Eur. Phys. J. C **76** (2016) 292, arXiv: 1603.05598 [hep-ex].

[88] ATLAS Collaboration, *ATLAS Muon Combined Performance with 2017 and 2016 dataset*, MUON-2017-002, 2017, URL: https://atlas.web.cern.ch/Atlas/GROUPS/PHYSICS/PLOTS/MUON-2017-002.

[89] ATLAS Collaboration, *Jet energy measurement with the ATLAS detector in proton–proton collisions at $\sqrt{s} = 7$ TeV*, Eur. Phys. J. C **73** (2013) 2304, arXiv: 1112.6426 [hep-ex].

[90] ATLAS Collaboration, *Properties of jets and inputs to jet reconstruction and calibration with the ATLAS detector using proton–proton collisions at $\sqrt{s} = 13$ TeV*, ATL-PHYS-PUB-2015-036, 2015, URL: https://cds.cern.ch/record/2044564.

[91] M. Cacciari, G. P. Salam and G. Soyez, *The Anti-k(t) jet clustering algorithm*, JHEP **04** (2008) 063, arXiv: 0802.1189 [hep-ph].

[92] M. Cacciari, G. P. Salam and G. Soyez, *FastJet User Manual*, Eur. Phys. J. C **72** (2012) 1896, arXiv: 1111.6097 [hep-ph], URL: http://fastjet.fr.

[93] ATLAS Collaboration, *Topological cell clustering in the ATLAS calorimeters and its performance in LHC Run 1*, Eur. Phys. J. C **77** (2017) 490, arXiv: 1603.02934 [hep-ex].

[94] ATLAS Collaboration, *Monte Carlo Calibration and Combination of In-situ Measurements of Jet Energy Scale, Jet Energy Resolution and Jet Mass in AT-LAS*, ATLAS-CONF-2015-037, 2015, URL: https://cds.cern.ch/record/2044941.

[95] M. Cacciari and G. P. Salam, *Pileup subtraction using jet areas*, Phys. Lett. B **659** (2008) 119, arXiv: 0707.1378 [hep-ph].

[96] ATLAS Collaboration, *Pile-up subtraction and suppression for jets in ATLAS*, ATLAS-CONF-2013-083, 2013, URL: https://cds.cern.ch/record/1570994.

[97] ATLAS Collaboration, *JES Public Plots for Moriond 2017*, JETM-2017-003, 2017, URL: https://atlas.web.cern.ch/Atlas/GROUPS/PHYSICS/PLOTS/JETM-2017-003.

[98] ATLAS Collaboration, *Expected performance of the ATLAS b-tagging algorithms in Run-2*, ATL-PHYS-PUB-2015-022, 2015, URL: https://cds.cern.ch/record/2037697.

[99] ATLAS Collaboration, *Measurements of b-jet tagging efficiency with the ATLAS detector using $t\bar{t}$ events at $\sqrt{s} = 13$ TeV*, JHEP **08** (2018) 089, arXiv: 1805.01845 [hep-ex].

[100] ATLAS Collaboration, *Optimisation of the ATLAS b-tagging performance for the 2016 LHC Run*, ATL-PHYS-PUB-2016-012, 2016, URL: https://cds.cern.ch/record/2160731.

[101] ATLAS Collaboration, *Reconstruction, Energy Calibration, and Identification of Hadronically Decaying Tau Leptons in the ATLAS Experiment for Run-2 of the LHC*, ATL-PHYS-PUB-2015-045, 2015, URL: https://atlas.web.cern.ch/Atlas/GROUPS/PHYSICS/PUBNOTES/ATL-PHYS-PUB-2015-045.

[102] ATLAS Collaboration, *Measurement of the tau lepton reconstruction and identification performance in the ATLAS experiment using pp collisions at $\sqrt{s} = 13$ TeV*, ATLAS-CONF-2017-029, 2017, URL: https://cds.cern.ch/record/2261772.

[103] ATLAS Collaboration, *Performance of missing transverse momentum reconstruction with the ATLAS detector using proton-proton collisions at $\sqrt{s} = 13$ TeV*, (2018), arXiv: 1802.08168 [hep-ex].

[104] I. Bird et al., *Update of the Computing Models of the WLCG and the LHC Experiments*, Technical Design Report LCG **2** (2014), URL: https://cds.cern.ch/record/1695401.

[105] T. Maeno, *PanDA: distributed production and distributed analysis system for ATLAS*, J. Phys.: Conf. Ser. **119** (2008) 062036.

[106] CDF Collaboration, *Search for the Standard Model Higgs Boson Produced in Association with Top Quarks Using the Full CDF Data Set*, Phys. Rev. Lett. **109** (18 2012) 181802, arXiv: 1208.2662 [hep-ex].

[107] ATLAS Collaboration, *Measurements of the Higgs boson production and decay rates and coupling strengths using pp collision data at $\sqrt{s} = 7$ and 8 TeV in the ATLAS experiment*, Eur. Phys. J. C **76** (2016) 6, arXiv: 1507.04548 [hep-ex].

[108] CMS Collaboration, *Search for the associated production of the Higgs boson with a top-quark pair*, JHEP **09** (2014) 087, arXiv: 1408.1682 [hep-ex].

[109] ATLAS Collaboration, *Search for the associated production of the Higgs boson with a top quark pair in multilepton final states with the ATLAS detector*, Phys. Lett. B **749** (2015) 519, arXiv: 1506.05988 [hep-ex].

[110] ATLAS Collaboration, *Search for the Standard Model Higgs boson produced in association with top quarks and decaying into $b\bar{b}$ in pp collisions at $\sqrt{s} = 8$ TeV with the ATLAS detector*, Eur. Phys. J. C **75** (2015) 349, arXiv: 1503.05066 [hep-ex].

[111] CMS Collaboration, *Search for a standard model Higgs boson produced in association with a top-quark pair and decaying to bottom quarks using a matrix element method*, Eur. Phys. J. C **75** (2015) 251, arXiv: 1502.02485 [hep-ex].

[112] ATLAS Collaboration, *Search for $H \rightarrow \gamma\gamma$ produced in association with top quarks and constraints on the Yukawa coupling between the top quark and the Higgs boson using data taken at 7 TeV and 8 TeV with the ATLAS detector*, Phys. Lett. B **740** (2015) 222, arXiv: 1409.3122 [hep-ex].

[113] ATLAS Collaboration, *Search for the Associated Production of a Higgs Boson and a Top Quark Pair in Multilepton Final States with the ATLAS Detector*, ATLAS-CONF-2016-058, 2016, URL: https://cds.cern.ch/record/2206153.

[114] ATLAS Collaboration, *Search for the Standard Model Higgs boson produced in association with top quarks and decaying into a $b\bar{b}$ pair in pp collisions at $\sqrt{s} = 13$ TeV with the ATLAS detector*, Phys. Rev. D **97** (2018) 072016, arXiv: 1712.08895 [hep-ex].

[115] E. Boos et al., *Generic user process interface for event generators*, (2001), arXiv: hep-ph/0109068.

[116] J. Alwall et al., *A Standard format for Les Houches event files*, Comput. Phys. Commun. **176** (2007) 300, arXiv: hep-ph/0609017.

[117] A. Hoecker et al., *TMVA – Toolkit for Multivariate Data Analysis*, CERN-OPEN-2007-007, 2007, arXiv: physics/0703039 [physics.data-an].

[118] T. Chen and C. Guestrin, *XGBoost: A Scalable Tree Boosting System*, KDD (2016) 785, arXiv: 1603.02754 [cs.LG].

[119] D. Dannheim et al., *PDE-Foam — A probability density estimation method using self-adapting phase-space binning*, Nucl. Instrum. Meth. Phys. A **606** (2009) 717, arXiv: 0812.0922 [physics.data-an].

[120] ATLAS Collaboration, *Search for supersymmetry in final states with two same-sign or three leptons and jets using* 36 fb^{-1} *of* $\sqrt{s} = 13$ *TeV pp collision data with the ATLAS detector*, JHEP **09** (2017) 084, arXiv: 1706.03731 [hep-ex].

[121] DØ Collaboration, *Extraction of the width of the W boson from measurements of* $\sigma(p\bar{p} \to W + X) \times B(W \to e\nu)$ *and* $\sigma(p\bar{p} \to Z + X) \times B(Z \to ee)$ *and their ratio*, Phys. Rev. D **61** (2000) 072001, arXiv: hep-ex/9906025.

[122] ATLAS Collaboration, *Estimation of non-prompt and fake lepton backgrounds in final states with top quarks produced in proton–proton collisions at* $\sqrt{s} = 8$ *TeV with the ATLAS Detector*, ATLAS-CONF-2014-058, 2014, URL: https://cds.cern.ch/record/1951336.

[123] ATLAS Collaboration, *Luminosity determination in pp collisions at* $\sqrt{s} = 8$ *TeV using the ATLAS detector at the LHC*, Eur. Phys. J. C **76** (2016) 653, arXiv: 1608.03953 [hep-ex].

[124] CMS Collaboration, *Evidence for associated production of a Higgs boson with a top quark pair in final states with electrons, muons, and hadronically decaying* τ *leptons at* $\sqrt{s} = 13$ *TeV*, CERN-EP-2018-017, 2018, arXiv: 1803.05485 [hep-ex].

[125] ATLAS Collaboration, *Measurements of Higgs boson properties in the diphoton decay channel with* 36 fb^{-1} *of pp collision data at* $\sqrt{s} = 13$ *TeV with the ATLAS detector*, CERN-EP-2017-288, 2018, arXiv: 1802.04146 [hep-ex].

[126] ATLAS Collaboration, *Measurement of the Higgs boson coupling properties in the* $H \to ZZ^* \to 4\ell$ *decay channel at* $\sqrt{s} = 13$ *TeV with the ATLAS detector*, JHEP **03** (2018) 095, arXiv: 1712.02304 [hep-ex].

[127] CMS Collaboration, *Observation of* $t\bar{t}H$ *production*, Phys. Rev. Lett. **120** (2018) 231801, arXiv: 1804.02610 [hep-ex].

[128] ATLAS Collaboration, *HL-LHC projections for signal and background yield measurements of the* $H \to \gamma\gamma$ *when the Higgs boson is produced in association with t quarks, W or Z bosons*, ATL-PHYS-PUB-2014-012, 2014, URL: https://atlas.web.cern.ch/Atlas/GROUPS/PHYSICS/PUBNOTES/ATL-PHYS-PUB-2014-012.

[129] ATLAS Collaboration, *Projections for measurements of Higgs boson signal strengths and coupling parameters with the ATLAS detector at the HL-LHC*, ATL-PHYS-PUB-2014-016, 2014, URL: https://cds.cern.ch/record/1956710.

[130] LHC Top Physics Working Group, *LHCTopWG Summary Plots*, 2018 (accessed June 15, 2018), URL: https://twiki.cern.ch/twiki/bin/view/LHCPhysics/LHCTopWGSummaryPlots.

[131] CMS Collaboration, *Search for top quark decays via Higgs-boson-mediated flavor-changing neutral currents in pp collisions at $\sqrt{s} = 8$ TeV*, JHEP **02** (2017) 079, arXiv: 1610.04857 [hep-ex].

[132] ATLAS Collaboration, *Search for top quark decays $t \to qH$ with $H \to \gamma\gamma$ using the ATLAS detector*, JHEP **06** (2014) 008, arXiv: 1403.6293 [hep-ex].

[133] ATLAS Collaboration, *Search for flavour-changing neutral current top quark decays $t \to Hq$ in pp collisions at $\sqrt{s} = 8$ TeV with the ATLAS detector*, JHEP **12** (2015) 061, arXiv: 1509.06047 [hep-ex].

[134] CMS Collaboration, *Search for the flavor-changing neutral current interactions of the top quark and the Higgs boson which decays into a pair of b quarks at $\sqrt{s} = 13$ TeV*, (2017), arXiv: 1712.02399 [hep-ex].

[135] Pierre Artoisenet et al., *Automatic spin-entangled decays of heavy resonances in Monte Carlo simulations*, JHEP **03** (2013) 015, arXiv: 1212.3460 [hep-ph].

[136] M. Czakon and A. Mitov, *Top++: A Program for the Calculation of the Top-Pair Cross-Section at Hadron Colliders*, Comput. Phys. Commun. **185** (2014) 2930, arXiv: 1112.5675 [hep-ph].

[137] PDF4LHC Working Group, *The PDF4LHC Working Group Interim Recommendations*, (2011), arXiv: 1101.0538 [hep-ph].

[138] A. D. Martin et al., *Uncertainties on alpha(S) in global PDF analyses and implications for predicted hadronic cross sections*, Eur. Phys. J. C **64** (2009) 653, arXiv: 0905.3531 [hep-ph].

[139] J. Gao et al., *CT10 next-to-next-to-leading order global analysis of QCD*, Phys. Rev. D **89** (2014) 033009, arXiv: 1302.6246 [hep-ph].

[140] A. L. Read, *Presentation of search results: the CL_S technique*, J. Phys. **G28** (2002) 2693.

[141] ATLAS Collaboration, *Expected sensitivity of ATLAS to FCNC top quark decays $t \to Zq$ and $t \to Hq$ at the High Luminosity LHC*, ATL-PHYS-PUB-2016-019, 2016, URL: https://atlas.web.cern.ch/Atlas/GROUPS/PHYSICS/PUBNOTES/ATL-PHYS-PUB-2016-019/.

[142] G. Apollinari et al., *High-Luminosity Large Hadron Collider (HL-LHC): Technical Design Report V. 0.1*, CERN Yellow Rep.: M. 2017, URL: https://cds.cern.ch/record/2284929.

[143] ATLAS Collaboration, *Letter of Intent for the Phase-II Upgrade of the ATLAS Experiment*, CERN, 2012, URL: https://cds.cern.ch/record/1502664.

[144] CMS Collaboration, *Projections for Top FCNC Searches in 3000/fb at the LHC*, CMS-PAS-FTR-13-016, 2013, URL: http://cds.cern.ch/record/1605885.

[145] CMS Collaboration, *ECFA 2016: Prospects for selected standard model measurements with the CMS experiment at the High-Luminosity LHC*, CMS-PAS-FTR-16-006, 2017, URL: https://cds.cern.ch/record/2262606.

[146] ATLAS Collaboration, *Letter of Intent for the Phase-I Upgrade of the ATLAS Experiment*, CERN, 2011, URL: https://cds.cern.ch/record/1402470.

[147] ATLAS Trigger Operation Group, *Trigger Operation Public Results*, 2018 (accessed June 15, 2018), URL: https://twiki.cern.ch/twiki/bin/view/AtlasPublic/TriggerOperationPublicResults.

[148] M. Aleksa et al., *ATLAS Liquid Argon Calorimeter Phase-I Upgrade Technical Design Report*, CERN, 2013, URL: https://cds.cern.ch/record/1602230.

[149] T. Kawamoto et al., *New Small Wheel Technical Design Report*, CERN, 2013, URL: http://cds.cern.ch/record/1552862.

[150] G. Aielli et al., *The ATLAS BIS78 Project*, CERN, 2016, URL: https://cds.cern.ch/record/2161109.

[151] M. Shochet et al., *Fast TracKer (FTK) Technical Design Report*, CERN, 2013, URL: http://cds.cern.ch/record/1552953.

[152] ATLAS Collaboration, *Technical Design Report for the Phase-I Upgrade of the ATLAS TDAQ System*, CERN, 2013, URL: http://cds.cern.ch/record/1602235.

[153] J. Anderson et al., *FELIX: a PCIe based high-throughput approach for interfacing front-end and trigger electronics in the ATLAS Upgrade framework*, JINST **11** (2016) C12023, URL: https://cds.cern.ch/record/2229597.

[154] ATLAS Collaboration, *ATLAS Pythia 8 tunes to 7 TeV data*, ATL-PHYS-PUB-2014-021, 2014, URL: https://cds.cern.ch/record/1966419.

[155] M. H. Seymour and A. Siodmok, *Constraining MPI models using σ_{eff} and recent Tevatron and LHC Underlying Event data*, JHEP **10** (2013) 113, arXiv: 1307.5015 [hep-ph].

[156] P. Z. Skands, *Tuning Monte Carlo Generators: The Perugia Tunes*, Phys. Rev. D **82** (2010) 074018, arXiv: 1005.3457 [hep-ph].

[157] J. Bellm et al., *Herwig 7.0/Herwig++ 3.0 release note*, Eur. Phys. J. C **76** (2016) 196, arXiv: 1512.01178 [hep-ph].

[158] D. J. Lange, *The EvtGen particle decay simulation package*, Nucl. Instrum. Meth. Phys. A **462** (2001) 152.

[159] P. Golonka and Z. Was, *PHOTOS Monte Carlo: A Precision tool for QED corrections in Z and W decays*, Eur. Phys. J. C **45** (2006) 97, arXiv: hep-ph/0506026.

[160] ATLAS Collaboration, *Modelling of the $t\bar{t}H$ and $t\bar{t}V(V = W, Z)$ processes for $\sqrt{s} = 13$ TeV ATLAS analyses*, ATL-PHYS-PUB-2016-005, 2016, URL: https://cds.cern.ch/record/2120826.

[161] ATLAS Collaboration, *Multi-boson simulation for 13 TeV ATLAS analyses*, ATL-PHYS-PUB-2016-002, 2016, URL: https://cds.cern.ch/record/2119986.

[162] ATLAS Collaboration, *Simulation of top-quark production for the ATLAS experiment at $\sqrt{s} = 13$ TeV*, ATL-PHYS-PUB-2016-004, 2016, URL: https://cds.cern.ch/record/2120417.

A. Monte Carlo simulation samples

The configurations of the Monte Carlo simulation samples, used in the presented searches for $t\bar{t}H$ and $t \to Hq$ in multileptonic final states, are summarised in table A.1 for all signal and background processes. Different parton-level generators, parton showering

Table A.1.: Configurations of Monte Carlo samples in searches for $t\bar{t}H$ and $t \to Hq$ in multileptonic final states. The samples for the estimate of systematic uncertainties are given in brackets for the $t\bar{t}H$, $t\bar{t}W$, $t\bar{t}Z$ and $t\bar{t}$. The alternative samples for $t\bar{t}$ are used in the estimate for the $t \to Hq$ signal.

Process	Generator	ME order	Parton Shower	PDF (PS)	Tune
$t\bar{t}H$	MG5_aMC [64]	NLO	Pythia 8 [72]	NNPDF 3.0 NLO [60]	A14 [154]
	(MG5_aMC)	(NLO)	(Herwig++ [73])	(CT10 [63])	(UE-EE-5 [155])
$t\bar{t}W$	MG5_aMC	NLO	Pythia 8	NNPDF 3.0 NLO	A14
	(Sherpa 2.1.1 [66–70])	(LO multileg)	(Sherpa)	(NNPDF 3.0 NLO)	(Sherpa default)
$t\bar{t}(Z/\gamma^* \to ll)$	MG5_aMC	NLO	Pythia 8	NNPDF 3.0 NLO	A14
	(Sherpa 2.1.1)	(LO multileg)	(Sherpa)	(NNPDF 3.0 NLO)	(Sherpa default)
$t\bar{t}t$, $t\bar{t}t\bar{t}$	MG5_aMC	LO	Pythia 8	NNPDF 2.3 LO [59]	A14
$t\bar{t}W^+W^-$	MG5_aMC	LO	Pythia 8	NNPDF 2.3 LO	A14
$tHqb$	MG5_aMC	LO	Pythia 8	CT10	A14
tHW	MG5_aMC	NLO	Herwig++	CT10	UE-EE-5
tZ	MG5_aMC	LO	Pythia 6 [71]	CTEQ6L1 [61, 62]	Perugia2012 [156]
tWZ	MG5_aMC	NLO	Pythia 8	NNPDF 2.3 LO	A14
s-, t-channel, Wt single top	Powheg-BOX v1 [65]	NLO	Pythia 6	CT10	Perugia2012
$t\bar{t}$	Powheg-BOX v2	NLO	Pythia 8	NNPDF 3.0 NLO	A14
	(Powheg-BOX v2)	(NLO)	(Herwig 7 [157])	(NNPDF 3.0 NLO)	(H7-UE-MMHT [155])
	(Sherpa 2.1.1)	(NLO)	(Sherpa)	(NNPDF 3.0 NLO)	(Sherpa default)
	(MG5_aMC)	(NLO)	(Pythia 8)	(NNPDF 2.3 NLO)	(A14)
$t\bar{t}\gamma$	MG5_aMC	LO	Pythia 8	NNPDF 2.3 LO	A14
$t\bar{t}$, $t \to Hq$	MG5_aMC	NLO	Pythia 8	NNPDF 3.0 NLO	A14
$VV(\to llXX)$, $qqVV$, VVV	Sherpa 2.1.1	MEPS NLO	Sherpa	CT10	Sherpa default
$Z \to ll$	Sherpa 2.2	MEPS NLO	Sherpa	NNPDF 3.0 NLO	Sherpa default

and hadronisation and parton distribution functions (PDFs) are combined as described in section 2.3.1. The underlying-event tuned parameters of the parton shower are given in the column 'Tune'. The PDF used for the parton shower (PS) is given in the table. The PDF for the parton-level generators is NNPDF 2.3 LO for samples using the A14 tune and it is CTEQ6L1 for samples using either the UE-EE-5, H7-UE-MMHT or the Perugia2012 tune. The heavy-flavour hadron decays are generated by EvtGen 1.2.0 [158] for Pythia 6 and Pythia 8 samples. Leading-logarithm photon emission is modelled by either the parton shower generator or PHOTOS [159].

The simulation of the $t\bar{t}H$, $t\bar{t}W$, $t\bar{t}Z$, multi-boson and top quark production samples is described in the references [160–162].

B. Pruning and smoothing

Two algorithms are used in order to decrease the time of fit workspace creation and the fit with only few impact on the final result. The parameters are tested in the following for an Asimov fit with $\mu_{t\bar{t}H} = 1$ including the $2\ell SS$, default 3ℓ and 4ℓ channels.

The first algorithm is the so called pruning. There are two pruning parameters, one for normalisation and one for shape. A normalisation (shape) pruning parameter of e.g. 1 % means, that all nuisance parameters are dropped for systematics with an overall size (all bins of the shape-uncertainty distribution) of less than 1 % of the concerning yield of this sample (of each bin). The scan of significance and workspace creation and fitting time is shown in figure B.1. The option of 1 % for both normalisation and shape prun-
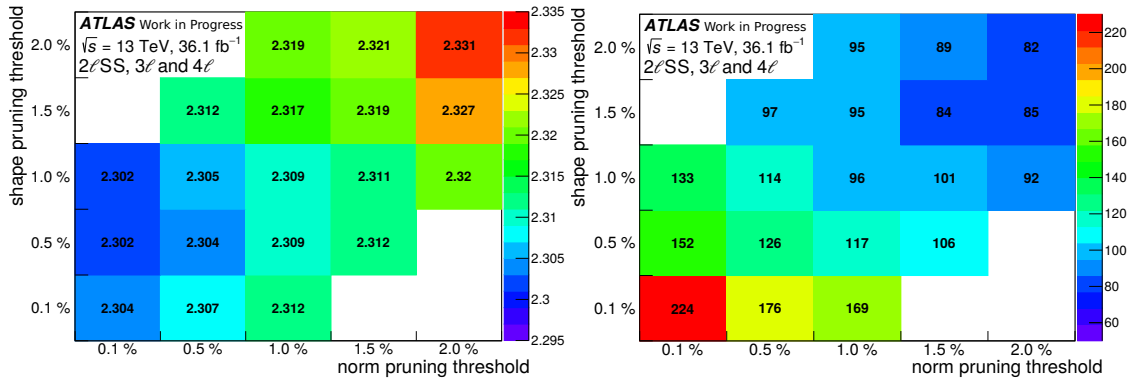

Figure B.1.: Scan of (left) expected significance and (right) workspace creation and fitting time in seconds for different settings for the norm pruning threshold (*x*-axis) and the shape pruning threshold (*y*-axis).

ing parameter performs best with acceptable workspace creation and fitting time of less than 100 seconds and almost no further drop in significance for lower thresholds. In the following it is used as default.

The second algorithm is the so called smoothing, which is used to decrease the fluctuations in shape systematics due to low statistics of the estimate templates. Figure B.2 sketches the steps of the smoothing algorithm. Firstly bins are merged with a statistical uncertainty greater than *X*. Then the number N of derivative changes in the distribution is reduced iteratively until $N \leq Y$. Here the parameters chosen are $X = 8\%$ and $Y = 4$.

A study was performed testing the application and non-application of the smoothing algorithm on different shape systematics. The impact of the different smoothing options
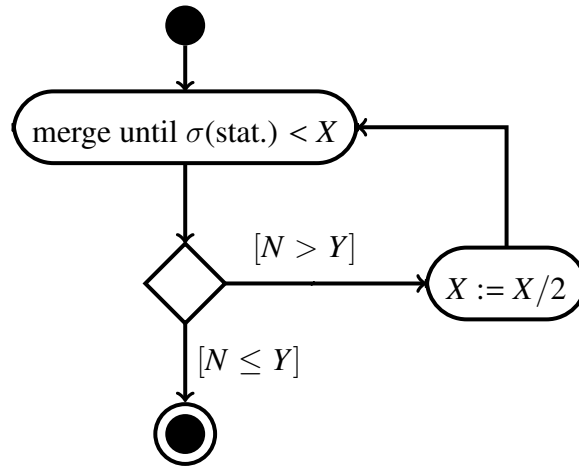
Figure B.2.: Scheme of the smoothing algorithm.

Table B.1.: Impact of different smoothing options on the expected significance and workspace creation and fitting time for 2ℓSS and 3ℓ channel as well as no-tau channels combination.

| Channel | Smoothing applied on ... | | | | |
	scales,PS,Gen trees weights data-driven	scales,PS,Gen trees weights	scales,PS,Gen trees	scales,PS,Gen	none
2ℓSS	1.84 (0m25s)	1.84 (0m25s)	1.83 (0m53s)	1.84 (1m46s)	1.84 (1m46s)
3ℓ	1.50 (0m53s)	1.50 (0m53s)	1.50 (1m38s)	1.51 (2m51s)	1.50 (2m56s)
no-tau combination	2.38 (1m28s)	2.38 (1m30s)	2.38 (2m60s)	2.39 (4m57s)	2.38 (5m01s)

on the expected significance is shown in table B.1. For the different smoothing options the exact same errors on the signal strength $\mu_{t\bar{t}H}$ and only minor changes in expected significances are observed. On the other hand the workspace creation and fitting times are much larger when less smoothing is applied, because many more shape-uncertainty NPs are kept after pruning. It is decided to use the smoothing for all shape systematics by default, as no significant change in significance is seen.

Abstract

After the Higgs boson discovery at the Large Hadron Collider (LHC), the focus of experimental particle physics is on the measurement of its interaction with other particles of the Standard Model (SM). The interaction strength with SM fermions is determined by the Yukawa coupling, which is proportional to the particle mass and therefore the largest for the top quark.

This doctoral thesis describes the search for the associated Higgs boson production with a pair of top quarks ($t\bar{t}H$) in a dataset of proton-proton collisions at a center-of-mass energy of $\sqrt{s} = 13\,\text{TeV}$ and with an integrated luminosity of $36.1\,\text{fb}^{-1}$, recorded by the ATLAS detector in 2015 and 2016. Seven final states, associated to different Higgs boson decays into vector bosons or tau leptons and containing at least two leptons, are optimised to get the best signal to background separation. An excess of events over the SM background is observed with a significance of 4.1 standard deviations, while 2.8 are expected. In combination with search results obtained for other Higgs boson decay channels, the $t\bar{t}H$ production has been discovered with the ATLAS detector using up to $79.8\,\text{fb}^{-1}$ of collision data at $\sqrt{s} = 7$, 8 and 13 TeV.

Flavour-changing neutral currents in top quark decays into a Higgs boson and a light up-type quark ($t \rightarrow Hq$) are strongly suppressed in the SM. New physics models can predict a $t \rightarrow Hc$ decay branching ratio of 0.15%. The search for these decays in final states with two or three leptons observes no signal. An upper limit on the $t \rightarrow Hc$ ($t \rightarrow Hu$) decay branching ratio at a 95% confidence level is set at 0.16% (0.19%) with an expected limit of 0.15% (0.15%).

To bypass the limitation of an insufficient amount of collision data, the LHC and its experiments foresee an ambitious upgrade plan. The current ATLAS Liquid Argon Calorimeter readout will be replaced to get an increased granularity to improve the trigger selectivity and avoid bandwidth saturation at high luminosity. A demonstrator system has been operated since 2015 and its performance studied with calibration and collision data.

Keywords: LHC, ATLAS, Higgs boson, top quark, $t\bar{t}H$, FCNC, multileptonic final states, Liquid Argon Calorimeters upgrade

Résumé

Après la découverte du boson de Higgs au Grand collisionneur de hadrons (LHC), la physique expérimentale des particules se concentre sur la mesure de son interaction avec d'autres particules du modèle standard (MS). La force de l'interaction avec les fermions du MS est déterminée par le couplage Yukawa, qui est proportionnel à la masse des particules et donc le plus élevé pour le quark top.

Cette thèse de doctorat décrit la recherche de la production du boson de Higgs associée à une paire de quarks tops ($t\bar{t}H$) dans un ensemble de données de collisions proton-proton à une énergie de centre de masse de $\sqrt{s} = 13$ TeV et avec une luminosité intégrée de $36,1$ fb^{-1}, enregistrée par le détecteur ATLAS en 2015 et 2016. Sept états finaux, correspondants à différentes désintégrations du boson de Higgs en bosons vecteurs ou en leptons taus et contenant au moins deux leptons, sont optimisés pour une meilleure séparation du signal par rapport au bruit de fond. Un excès d'événements par rapport au bruit de fond MS est observé avec une signification de 4,1 écarts types, tandis que 2,8 sont attendus. En combinaison avec des résultats de recherches avec d'autres canaux de désintégration du boson de Higgs, la production de $t\bar{t}H$ a été découverte par le détecteur ATLAS en utilisant jusqu'à $79,8$ fb^{-1} de données de collisions à $\sqrt{s} = 7, 8$ et 13 TeV.

Les courants neutres, qui changent de saveur dans la désintégration du quark top en un boson de Higgs et un quark léger ($t \rightarrow Hq$), sont fortement supprimés dans le MS. Des nouveaux modèles physiques peuvent prédire un rapport d'embranchement de $t \rightarrow Hc$ de 0,15%. La recherche de ces désintégrations, avec un état final à deux ou trois leptons, n'observe aucun signal. Une limite supérieure sur le ratio d'embranchement de $t \rightarrow Hc$ ($t \rightarrow Hu$) avec un niveau de confiance de 95% est observé à 0,16% (0,19%) avec une limite attendue de 0,15% (0,15%).

Pour contourner la limitation du nombre insuffisant des collisions, le LHC et ses expériences prévoient un plan de mise à niveau ambitieux. Le système de lecture actuel du Calorimètre à Argon Liquide ATLAS sera remplacé avec une granularité accrue pour améliorer la sélectivité du système de déclenchement et éviter la saturation de la bande passante à haute luminosité. Un système de démonstration est en service depuis 2015 et ses performances étudiées avec des données de calibrations et de collisions.

Mots clés : LHC, ATLAS, boson de Higgs, quark top, $t\bar{t}H$, FCNC, états finaux multileptoniques, mise à jour des Calorimètres à Argon Liquide